Towards a Strontium Optical Lattice Clock

Elizabeth M. Bridge

Department of Physics

University of Oxford

A thesis submitted for the degree of

Doctor of Philosophy

December 2012

I hereby declare that the work presented here as my own is my own, and in all other cases appropriate references are given.

Abstract

Towards a Strontium Optical Lattice Clock
Elizabeth M. Bridge
Linacre College, University of Oxford
Doctor of Philosophy in Physics
Michaelmas Term 2012

Due to the recent success, in terms of accuracy and precision, of a number of strontium optical lattice optical frequency standards, and the classification of the $5s^2\ {}^1\mathrm{S}_0$ to $5s5p\ {}^3\mathrm{P}_0$ transition in neutral strontium as a secondary definition of the SI unit of the second, many new strontium lattice clocks are under development. The strontium optical lattice clock (Sr OLC) at the National Physical Laboratory (NPL) is one such project. This thesis describes the design and build of the NPL Sr OLC, discussing the considerations behind the design. Details of the first cooling stage are given, which includes the characterisation of a novel permanent-magnet Zeeman slower by measurements of the longitudinal velocity distributions and loading of the MOT at 461 nm. Development of a narrow linewidth laser system at 689 nm is described, which is used for initial spectroscopy of the second-stage cooling transition. In particular, this work describes progress towards two independent ultra-narrow linewidth clock lasers.

The new generation of strontium lattice clock experiments have focused on characterising the systematic frequency shifts and reducing their associated fractional frequency uncertainties, as well as reducing the fractional frequency instability of the measurement. One focus of the Sr OLC at NPL is to help characterise the frequency shift of the clock transition due to black-body radiation (BBR), which is currently the largest contributor to the uncertainty budget of the measured clock frequency. Our approach, discussed here, is to make a direct, differential measurement of the shift with the atoms housed alternately in environments of differing temperatures. Better characterisation and control of the BBR frequency shift of the strontium clock transition is crucial for the future of the Sr OLC as a leading frequency standard.

I would like to dedicate this thesis to my loving parents Judy and Andy, who have loved and supported me throughout.

Thank you.

Acknowledgements

It is difficult to individually acknowledge all those who have helped me develop as a scientist and towards the completion of my D.Phil. I suppose my scientific career started as a young child with my love of puzzles and technical toys, and developed with encouragement from my parents and grandparents to be inquisitive and learn about the world around me. The first time I appreciated this interest to be classed as science was in year 6 when my teacher Ms Wyatt started up an after school science club which I greatly enjoyed. In secondary school my love of science grew with help from all my science teachers, but particularly Mr Nicholls and Mrs Gallagher. Mr Nicholls knows how to make physics fun and I soon learnt that my strongest scientific interest lay within physics. The choice of which university to study at was a difficult one, but I am happy to say I made the right decision. The staff at Durham University were very supportive and I owe particular thanks to my third and fourth year tutor Dr Simon Gardner, and my fourth year M.Sci. project supervisors Dr Matthew Jones and Prof Charles Adams. I would like to thank Matt for helping me achieve my first scientific publication and for encouraging me to gain confidence in my work and continue as a physicist by undertaking a D.Phil. I would also like to thank my friends at school and my physics buddies at university - Anna, Shelley, Tom, and Tom - for working with me and challenging me.

During the course of my D.Phil. many people have helped me. Technical staff at NPL I would particularly like to thank are Paul, Keith, and the guys in the Engineering Workshop for taking the time and care to machine the many parts I requested of them, as well as Pravin and Barry for their help with the electronics required for our apparatus. I have greatly benefited from my interactions with many scientific staff at NPL. I owe thanks to Dr Stephen Webster, Dr Rachel Godun, Dr Helen Margolis, Dr Luke Johnson, Dr Alastair Sinclair, Dr Guido Wilpers, Dr Hugh Klein, Dr Geoff Barwood, Dr Jeff Flowers, and Dr Chris Edwards for general support and advice on various aspects of the project, including optical cavities, laser locking, vacuum preparation, optcal frequency comb measurements, electronic design and the general fields of frequency metrology and atomic physics. The other students in my cohort - Steve, Ben, and Ian - provided a social environment that lead to many thought-provoking, and often slightly-heated, but enjoyable scientific discussions. Thank you to Prof Patrick Gill, the head of the group and one of my supervisors, for the opportunity to undertake such an educational D.Phil. Many thanks to my other supervisors Dr Anne Curtis and Dr Patrick Baird for supervision and support throughout my D.Phil. The experiment would not have progressed as far as it has without the help of the other scientists who have worked on it, these include Dr Anne Curtis, Dr Yuri Ovchinnikov, Dr Geoff Barwood, Dr Sean Donnellan, Prof Patrick Gill, and last but most importantly Ian Hill (now Dr). I would like to extend a special thanks to Ian, my lab buddy and good friend; we did it together!

Thank you to my parents and family for supporting me throughout, and when I loose faith, for reassuring me that I can do it! Thanks to my good friend Richard for his support and care throughout my D.Phil. and the times we shared. Last, but not least, thank you to Rachael and Nick for welcoming me into their home and for the tasty dinners we shared, sorry if I started an unwelcome trend!

Contents

List of Figures

Chapter 1

Introduction

For thousands of years the rotation of the Earth was the most stable and reliable time-keeper. Such natural cycles are the basis for today's calendar. One year is one Earth orbit around the Sun, a month (a 'moonth') is based on the Moon's orbit about the Earth, and a day is a rotation of the Earth upon its axis. The week is based on Man's need for routine and a regular break from labour. Its period is again based on stellar observations, there being approximately four weeks in a lunar cycle, and each day is named after one of the main seven objects in the night's sky. This is clearest in a combination of French and English: Lundi/Monday (la Lune/ the Moon), Mardi (Mars), Mercredi (Mercury), Jeudi (Jupiter), Vendredi (Venus), Saturday (Saturn) and Sunday (the Sun).

One of the first methods of keeping time would have been a simple method for counting the days in a year, enabling crops to be planted and harvested at the right time. Later on, when trade became important, it would make sense to agree a time and place for people to meet and trade; people would need to know on which day the market was held. As society became more complex, the importance of measuring time intervals became greater, from hours, to minutes, to seconds, and now fractions of nanoseconds.

1.1 Importance of time-keeping

One of the first notable demands from society for higher accuracy time-keeping was in the 1700's when the British government offered a reward for anyone who could build a chronometer that would allow seafarers to determine their longitude to within half a degree, thus reducing the risk of boats containing men and valuable cargo becoming shipwrecked or getting lost at sea. John Harrison took up the challenge and devoted his life to designing a chronometer that met the specifications; after 31 long years, a number of design iterations, and some political challenges, he was finally awarded his prize in 1773 when he was 80 years old [1]. Some examples of his carefully crafted chronometers can be found in the National Maritime Museum in Greenwich, London. Chronometers were used for air and sea navigation until the implementation of global satellite navigation at the end of the twentieth century. Accurate time-keeping is essential for the function of the global satellite navigation systems, because the time interval between signals is used to calculate a user's location. Each of the four satellite systems, GPS, GLONASS, COMPASS, and Galileo (some operational and some under development), have ~ 30 satellites, each containing at least one atomic clock.

Precise atomic time-keeping is essential for various economic activities, such as regulating the national grid, packet synchronisation over the internet, and time-stamping transactions in the financial sector to name a few. There are also numerous scientific applications such as measuring continental drift, deep space navigation, synchronising large telescope arrays, and testing fundamental physics such as the theory of gravity and looking for any temporal variation in the physical constants. Over the years advances in science and technology have allowed the development of higher stability and accuracy clocks. Society has evolved to first use, and then require, these improvements in time-keeping for

day-to-day operations. This is a clear example of an area where science and technology go hand in hand. Today atomic clocks are the most accurate time-keepers in the world, with an uncertainty of less than 1 second in 3.7 billion years (equal to a fractional frequency uncertainty of 8.6×10^{-18}) [2].

1.2 Atomic clocks

In 1955 Louis Essen and John V.L. Parry from the National Physical Laboratory demonstrated the first operation of an atomic frequency standard with higher accuracy than astronomical time [3; 4] [1]. The caesium atomic clock measured the frequency, ν_0 of the microwave radiation required to excite a particular electronic transition in atomic caesium. The energy separation E between the electronic ground $|g\rangle$ and excited $|e\rangle$ states is given by $E = h\nu_0$, where h is Planck's constant and ν_0 is the radiation frequency required to excite the transition, see figure 1.1. In order to be a good frequency reference, and thus a component of a good clock, the atomic transition needs to accept a narrow range of excitation frequencies, meaning it has a well-defined frequency value; we call this the transition linewidth $\delta\nu$. It would also ideally be insensitive to perturbations from external fields so that we could measure the correct ν_0 and not a shifted value. (In reality this is rarely the case, instead we characterise the shifts well, so we can extrapolate to the unshifted value). For example, to reduce sensitivity to magnetic fields the caesium atomic clocks use a transition between the hyperfine states $F = 3$, $m_F = 0$ and $F = 4$, $m_F = 0$. Such m_F values result in zero Zeeman shifts (to first-order) of the transition frequency. Today the most accurate caesium fountains have a fractional frequency uncertainty of $\sim 1 \times 10^{-16}$ [6], this means

[1] The world's first atomic frequency standard was actually based on the 23.87 GHz nitrogen inversion transition in ammonia molecules, but its accuracy could not match that of astronomical observations [5].

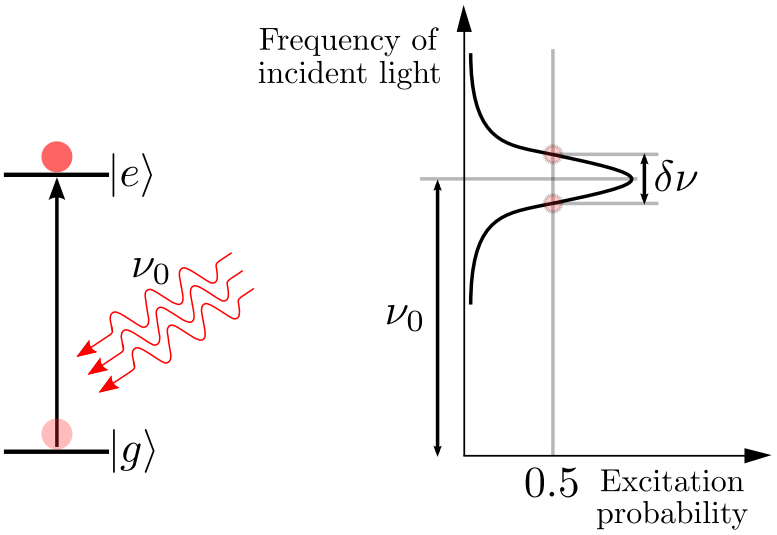

Figure 1.1: **Basics of an atomic clock** - Light of frequency ν_0 is used to excite atoms from state $|g\rangle$ to $|e\rangle$. The transition has a fixed frequency ν_0, with a linewidth of $\delta\nu$ (full width at half maximum).

they can measure the frequency of the 9.19 GHz transition with an uncertainty of $< 0.9\,\mu$Hz. Frequency (and hence time) is the most accurately measured SI unit.

1.3 The components of a clock

Since we are trying to make a 'clock' (we are actually making the frequency standard, or 'reference', part of the clock, but in the text we often refer to it as a clock) we should first discuss the essential components for any clock, whether it be a grandfather clock or an atomic clock. A clock consists of an oscillator, a counter and a reference.

Oscillator: Such as the pendulum of a grandfather clock, a quartz crystal in a wristwatch, or a narrow-linewidth laser in an optical frequency standard. A good oscillator has a high short-term stability and acts to 'keep' time in the short term (seconds to hours). A higher stability oscillator allows us to measure time more precisely, and generally higher frequency oscillators

have higher stability through its proportionality to the oscillators' quality factor, $Q = \nu_0/\delta\nu$, where ν_0 is the oscillator frequency and $\delta\nu$ is the full width at half maximum in the frequency domain (see figure 1.1).

Counter: This is generally the mechanism of cogs leading to the clock face, or if we are talking about microwave atomic clocks, such as the caesium fountain it will be an electronic device capable of counting the frequency of the microwave oscillations. For optical atomic clocks we cannot use electronic counters as these are not fast enough to count hundreds of terahertz, instead we use an optical frequency comb. See section 1.4.1 for more details.

Reference: This is the 'constant' reference which we use to steer the frequency of our oscillator back to the 'correct' value. For example, the Earth's rotation upon its axis gives us the length of a day, to which all clocks were referenced to up until 1956. At this point oscillators such as quartz had been engineered to become stable enough to detect alterations in the length of the solar day and it was evident that the Earth's rotation was slowing and could no longer be used as a stable reference. Between 1956 and 1967 the length of a second was referenced to ephemeris time, which used the motion of the Moon and the Earth. Since 1967 the second has been defined by International Atomic Time, which is a weighted collection of atomic clock references from around the world. The current SI definition states that:

> "The second is the duration of 9 192 631 770 periods of the radiation corresponding to the transition between the two hyperfine levels of the ground state of the caesium 133 atom. This definition refers to a caesium atom at rest at a temperature of 0 K."

Technological developments over the last few decades have lead to optical frequency standards exceeding the stability of the caesium fountains that define the second, so we find ourselves in a position again where the stability and certainty of the oscillator frequency exceed that of the reference and it appears the second may need to be re-defined again in the near future.

Noting the slowing of the Earth's rotation, we should also consider the long term stability of our 'constant' reference. Frequency metrologists are looking for temporal variation in the fine structure constant $\alpha \simeq 1/137$, to which some optical frequency standards are particularly sensitive [7; 8; 9; 10; 11]. The fine structure constant governs the interaction between charged particles, and so variations would affect the energy, and frequency, spacing between the atomic transitions that make up our clock references. The upper limit of the fractional temporal variation is currently accepted to be $\dot{\alpha}/\alpha = (-1.6 \pm 2.3) \times 10^{-17}$ /year [11].

1.4 Going into the optical domain

Traditionally atomic clocks use electronic transitions with frequencies in the microwave range. The use of optical transitions has the potential to improve clock performance due to their higher oscillator frequencies, which increase the quality factor ($Q = \nu_0/\delta\nu$) and hence decrease the fractional frequency instability, usually expressed as the Allan deviation $\sigma_y(\tau)$:

$$\sigma_y(\tau) \simeq \frac{1}{Q}\frac{1}{\sqrt{N}}\sqrt{\frac{t_c}{\tau}} \tag{1.1}$$

where N is the number of atoms, τ is the measurement averaging time, and t_c is the cycle time.[1] This idea of increasing the clock's 'ticking' frequency has led to a new generation of atomic clocks that use a spectrally narrow optical transition as the reference frequency. These are typically based on alkali-earth and alkali-earth-like atoms. Optical transitions have a frequency $\sim 10^4$ to 10^5 times higher than the microwave frequency used in caesium clocks, and assuming all other parameters are equal, the fractional frequency instability could decrease by the same factor.

This concept is more easily explained using the analogy of a ruler for measuring distances. A metre ruler with no divisions can only reliably measure lengths to around a precision of half a meter. If, however, we now have a metre ruler with 100 centimetre divisions marked on, we can now measure lengths with a precision of around half a centimetre - 100 times higher resolution. It works the same with time, if our frequency-ruler has $\sim 10^4$ times more divisions we should be able to get the same increase in measurement precision.

Up until about 15 years ago optical frequency standards were little more than just a "nice idea", because counting, or measuring, optical frequencies was very difficult. In 1996 Schnatz et al. published the first phase coherent absolute frequency measurement of visible radiation [12]. They used an extensive frequency chain, consisting of many phase-locked frequency oscillators in multiple adjoining laboratories, to bridge the frequency gap between the 9.2 GHz of the caesium frequency standard to the 456 THz of the calcium frequency standard. This frequency chain took many years to build and required a committed crew of workers to maintain each system during the frequency comparison. In 1999 the first opti-

[1] Equation 1.1 represents the theoretical fractional frequency instability of an oscillator limited by quantum projection noise. It assumes white frequency noise, which averages down as $1/\sqrt{\tau}$. In practice the quality factor Q is limited by the linewidth of the local oscillator rather than the atomic transition linewidth.

cal frequency comb used a mode-locked Ti:sapphire laser to bridge the 18.4 THz gap between a frequency-quadrupled methane-stabilised He-Ne laser and the caesium D_1 line at 335 THz [13]. Developments in this field were rapid, and only a year later the first octave-spanning, self-referenced frequency comb was operational, allowing measurements of a 282 THz frequency directly in terms of the caesium frequency standard [14]. Optical frequency combs are now readily used for optical frequency measurements and are even available as commercial products from companies such as Menlo Systems GmbH.

1.4.1 Optical frequency combs

Optical frequency combs are the 'counters' in optical atomic clocks. They are pulsed laser systems, which, like any other laser pulsed in the time domain, has a comb of equally spaced modes in the frequency domain [15], see figure 1.2. The comb mode frequency spacing, also referred to as the repetition rate ν_{rep}, is referenced to a microwave frequency standard such as a hydrogen maser or a caesium fountain primary frequency standard. In order to be a useful frequency ruler a technique called self-referencing must be used to measure the carrier envelope offset frequency ν_{ceo} of the comb modes; this is often achieved with an octave-spanning optical frequency comb, see [14] for more details. The optical frequency to be measured is co-aligned with an optical comb mode which is close in frequency, and the beat frequency ν_{beat} (usually tens of Megahertz) between the two is measured. The optical frequency of the laser is then calculated by:

$$\nu_{\mathrm{laser}} = \nu_{\mathrm{ceo}} + N_{\mathrm{mode}}\,\nu_{\mathrm{rep}} \pm \nu_{\mathrm{beat}} \tag{1.2}$$

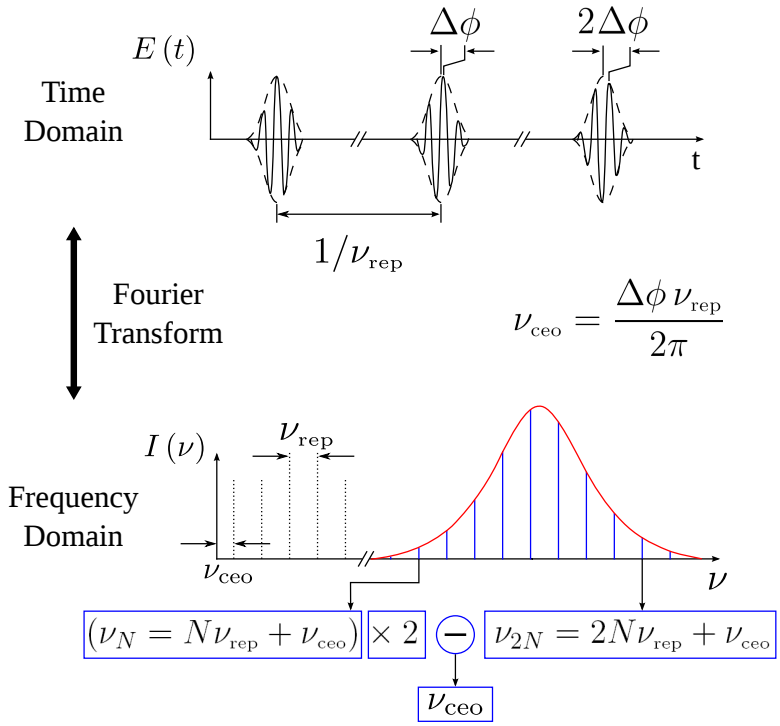

Figure 1.2: **Optical frequency comb** - Time domain and frequency domain of an octave-spanning, mode-locked optical frequency comb.

where N_{mode} is the integer mode number (usually an unknown quantity but can be calculated by changing the comb mode spacing and repeating the measurement).

1.4.2 Accuracy versus precision

It is worth taking a moment here to clarify the difference between the terms 'accuracy' and 'precision', and how these relate to the terms 'uncertainty' and '(in)stability', since these are used in the frequency standard community.

Precision is a measure of how repeatable a set of results are. If one takes a series of measurements (of time, length, mass or some other quantity) and the results are repeatable then they are said to be precise, but this does not necessarily mean they are accurate. Accuracy refers to the lack of deviation from the *true* value. For example, one uses five different sets of weighing scales to measure the

mass of an object. If the different sets of weighing scales all record the same or similar mass, then this measurement is repeatable, so it is described as precise, but it is not necessarily accurate. The scales could be faulty, they could have been used incorrectly, or they could be poorly calibrated to the internationally accepted SI unit of the kilogram. The only way a measurement can be *accurate* is if it is true to the accepted value.

Within the field of frequency standards the term 'stability' (or instability, which is more commonly used) is used as a quantitative way to describe the precision of a set of frequency measurements over time and is usually given as a fractional frequency instability. A frequency instability value includes a combination of measured frequency fluctuations due to time-varying systematic effects (e.g. laser noise in an optical frequency standard) and apparent frequency fluctuations due to statistical uncertainties (often a dominating contribution in single ion optical frequency standards). When quoting a frequency instability it is important to quote the time period for which that instability is applicable. For example, a narrow-linewidth laser which is frequency stabilised to an optical cavity could have a fractional frequency instability of 2×10^{-15} at 1 second (representing a linewidth on the order of a Hertz at this time-scale), but over a longer time period the laser frequency might drift, increasing the fractional frequency instability to around 1×10^{-14} at 100 seconds.

The fractional frequency uncertainty of a measurement describes the accuracy to which the measurement is made. This is an indication of the scientists' confidence that their result is an accurate measurement of the frequency of the unperturbed transition. Obviously no laboratory on Earth would enable a direct measurement of an unperturbed transition (with no frequency shifts caused by external magnetic and electric fields), because such measurements would need to

be made in a laboratory that was impermeable to the Earth's magnetic field and at a temperature of absolute zero! Instead scientists choose to make a number of frequency measurements in differing, well-characterised conditions (e.g. at a number of different magnetic field strengths, or over a range of probe laser beam intensities) such that the trend in the data can be extrapolated back to approximate the unperturbed value. An estimate to the certainty of this value is carefully made by taking all known possible perturbations into account and an estimated fractional frequency uncertainty is published along with the unperturbed 'clock' frequency.

1.4.3 Divalent atoms for optical frequency standards

Neutral alkaline-earth atoms have a favourable electronic structure for the development of optical atomic frequency standards. They have a spectrally-broad transition ($\gamma_{\mathrm{nat}} \simeq 10\,\mathrm{MHz}$), which is suitable for rapid first-stage laser-cooling to around a millikelvin, and a spectrally-narrow transition which can be used for second-stage laser cooling to a few microkelvin (or for the clock transition in some atomic species). They also have an ultra-narrow transition frequency suitable for use as the frequency reference in optical frequency standards.

1.4.4 Atoms versus ions

Currently optical ion clocks containing one, or two (for quantum logic clocks), ions in a RF electrical trap have the lowest fractional frequency uncertainty; the best to date is reported to be 8.6×10^{-18} from an Al^+ ion clock at NIST [2]. This ultra-low uncertainty is achievable because aluminium has very low sensitivity to external electro-magnetic fields. Ions can be cooled and trapped in a well-controlled environment with only low levels of perturbation affecting the

frequency of the clock transition. However, normally only one clock ion is trapped and so for a high signal-to-noise ratio, as required for a low fractional frequency instability (equation 1.1), a long averaging time is necessary. Optical clocks based on neutral atoms have the potential to overcome this problem by utilising up to $N = 10^6$ trapped atoms at a time, but until recently the best stability achieved by neutral atom clocks has been approximately equal to that of ion clocks [2; 16; 17]. The frequency instability of neutral atom clocks is limited by the Dick effect, and the quantum projection noise floor is yet to be reached in these systems [18]. The Dick effect is explained in section 2.3.2.1, it can be suppressed by reducing the dead time in the clock cycle [17; 18] and by reducing the linewidth of the clock laser [19]. Using state of the art laser systems Nicholson et al. [20] have recently demonstrated a record-breaking fractional frequency instability of $\sim 1 \times 10^{-17}$ after 1000 s averaging time in a neutral atom strontium optical lattice clock. This stability surpasses that achieved with ion clocks by over a factor of 10, and is within a factor of 2 of the quantum projection noise floor for the system [20].

At present optical atom clocks are still rapidly developing and show great potential, but are behind optical ion clocks in terms of fractional frequency uncertainty. The best published result to date is from the strontium lattice clock at JILA where they achieve a fractional frequency uncertainty of 1.5×10^{-16} [21]. The largest contributing factors to the frequency uncertainty in neutral atom optical clocks are from uncertainties in frequency shifts due to the black-body radiation of the environment and from inter-atomic collisions [21], both of which are actively being investigated to characterise the shifts further and reduce the uncertainties [19; 22; 23; 24].

1.4.5 Ballistic atom optical clocks

The first neutral atom optical clocks used calcium atoms [25]. The atoms were laser-cooled and trapped in a magneto-optical trap (MOT) with the dipole-allowed transition at 423 nm. The 657 nm spectrally-narrow intercombination line, with a natural linewidth of ~ 400 Hz, proved to be suitable as a clock transition for the frequency standard. Using the Bordé-Ramsey spectroscopy technique the frequency of the transition was resolved to the order of the natural linewidth, with a fractional frequency instability of 5×10^{-14} at 1 second [26]. To reduce the Stark and Zeeman frequency shifts caused by the laser light and magnetic field, respectively, of the MOT, the MOT fields were switched off for the duration of the clock interrogation pulses. This left the cold collection of atoms free to ballistically expand and fall under gravity, causing Doppler shifts and providing only a limited interrogation time before the atoms moved out of view. The inability to accurately measure the frequency of the clock transition in a trapped state limited the potential of this system as a frequency standard. Ideally the atoms should be cold and tightly confined, but with the clock frequency unperturbed by external fields. A solution to this problem was first proposed by Katori in 2001 [27] in the form of an engineered light-shift trap, where the atoms are confined using light of the 'magic' wavelength, which leaves the frequency of the clock transition unperturbed.

1.4.6 The 'magic' wavelength

At the 6th Symposium on Frequency Standards and Metrology, Katori proposed to trap strontium atoms in an engineered light-shift trap [27]. This far-off-resonant dipole trap would be of a 'magic' wavelength such that the scalar AC-Stark shift observed by the atoms was equal in both the ground and excited states

of the clock transition. In this way, the frequency of the clock transition could be measured in a seemingly unperturbed state while the atoms remain cold and trapped. This idea was further developed to trap the atoms in a 'magic' wavelength lattice, where the atomic confinement is comparable to the wavelength of the probe light; this resulted in (almost) Doppler- and recoil-free spectroscopy within the Lamb-Dicke regime [28; 29].

This significant step of shift-free trapping of atoms has allowed neutral atom optical clocks to compete with the single ion optical clocks in terms of fractional frequency stability and uncertainty. Optical neutral atom standards have the benefit of high atom numbers, so they can average down very quickly to achieve high stabilities at short time-scales. Frequency comparisons between the two strontium lattice clocks at JILA have achieved a fractional frequency instability of 1×10^{-17} in 1000 s [20]. The best recorded fractional frequency uncertainty of a neutral strontium optical lattice clock is 1.5×10^{-16} [21]. The fractional frequency uncertainty of the aluminium ion standard currently surpasses that of neutral atom clocks due to the absence of inter-atomic interactions and aluminium's ultra-low sensitivity to external electric and magnetic fields [30]. Aluminium ion clocks currently hold the record for the world's best fractional frequency uncertainty at 8.6×10^{-18} [2], with a fractional frequency instability of $\sim 1 \times 10^{-16}$ at 1000 s. In the future, one might expect neutral atom optical frequency standards to be the short-term, high-stability flywheels, essential for day-to-day frequency and time measurements, and the optical ion clocks to be the long-term, low-uncertainty standards used to define the unit of time.

To date a number of neutral atom optical lattice clocks have been developed around the world, including those given in table 1.1.

Species	Transition	Best reported fractional frequency uncertainty	Laboratories
^{87}Sr (I = 9/2)	$^1S_0$–$^3P_0$	1.5×10^{-16} [21]	Univ. of Tokyo, Japan [31] JILA, Colorado [21] LNE-SYRTE, France [32] LENS, Italy [33] PTB, Germany [34] NPL, UK [35] NIM, China [36] Univ. of Birmingham, UK [37] NRIPRM, Russia [38]
^{171}Yb (I = 1/2)	$^1S_0$–$^3P_0$	3.4×10^{-16} [39]	NIST, Colorado [39] NMIJ, Japan [40]
^{174}Yb (I = 0)	$^1S_0$–$^3P_0$	1.5×10^{-15} [41]	NIST, Colorado [41]
^{88}Sr (I = 0)	$^1S_0$–$^3P_0$	2.9×10^{-15} [42]	Univ. of Tokyo, Japan [42] LNE-SYRTE, France [43]
^{199}Hg (I = 1/2)	$^1S_0$–$^3P_0$	5.7×10^{-15} [44]	LNE-SYRTE, France [44] Univ. of Tokyo, Japan [45]
^{40}Ca (I = 0)	$^1S_0$–$^3P_1$	7.5×10^{-15} [46]	NIST, Colorado [46] PTB, Germany [47] Univ. of Western Australia [48]
^{24}Mg (I = 0)	$^1S_0$–$^3P_{1,0}$	2.5×10^{-12} [49]	Univ. Hannover, Germany [50]

Table 1.1: **Neutral atom optical clocks** - details and references for known neutral atom optical clock projects either running or under construction. All are optical lattice clocks, other than the NIST and PTB Ca standards, which are ballistic atom clocks.

1.5 Frequency standards at the National Physical Laboratory

The National Physical Laboratory (NPL) has a number of microwave and optical frequency standards at various stages of development. These include two caesium fountains, a rubidium fountain, two commercial hydrogen masers, two ytterbium ion clocks, three strontium ion clocks, and a strontium optical lattice clock, together with three optical frequency combs to act as the reference to link the optical frequencies to the microwave frequencies. This thesis is about the development of the strontium optical lattice clock. Strontium was chosen as a suitable alkaline-earth atom because of its favourable nuclear and electronic structure and the convenience of all the required transition frequencies for cooling, trapping and probing the clock transition being accessible with diode lasers.

1.6 Project outline

The work in this thesis is part of a laboratory project to design, build, characterise, and operate a neutral strontium optical lattice optical frequency standard; this is a large scale project involving a team of several members. The personnel concerned with the development of the apparatus were the author of this thesis, I.R. Hill (now Dr), Dr Y.B. Ovchinnikov, and Dr E.A. Curtis. The project had been running for less than two years at the start of this D.Phil. studentship, and was still in the very early stages of the design and build. The vast majority of the experimental set-up discussed in this thesis was built (or in some cases, modified) within the duration of this D.Phil., providing a very hands-on experience.

The remainder of this thesis gives an outline of the strontium optical lattice clock project at the NPL. In particular, chapter 2 gives a more detailed overview of

the key techniques involved in making an accurate and precise strontium optical lattice frequency standard. I begin to discuss technical aspects of the project in chapter 3, where I describe the strontium vapour source, and first-stage laser-cooling and trapping; including some of our work with permanent-magnet Zeeman slowers. Chapter 4 covers the narrow-linewidth laser system built for second-stage laser-cooling of the strontium atoms, with preliminary atomic spectroscopy of the narrow-linewidth transition. This chapter also includes details of the 'magic' wavelength optical lattice laser system and the proposal for the transport optical lattice for direct measurement of the frequency shift of the 'clock' state due to black-body radiation. Chapter 5 contains the focus of the work for this thesis; we discuss in detail the physics and engineering behind the narrow-linewidth 'clock' laser systems, and the results of this work-in-progress.

Although the author was actively involved in nearly all aspects of this project, the majority of the contribution was towards the work with the narrow-linewdth laser systems discussed in chapter 4 and in detail in chapter 5.

Chapter 2

Strontium optical lattice clock

In order to make our frequency standard we wish to measure the precise energy separation (and hence frequency, $\nu_0 = E/h$) of the 'clock' electronic states ($5s^2\,{}^1\mathrm{S}_0$ and $5s5p\,{}^3\mathrm{P}_0$) of neutral strontium. To enable us to measure the unperturbed frequency precisely and accurately, the atoms need to be slow-moving (i.e. cold, to reduce Doppler shifting and broadening of the transition frequency), tightly confined (allowing for recoil-free spectroscopy and suitably long interrogation periods), and in a near-non-perturbative environment (so that external fields, for trapping or otherwise, only shift the frequency of the transition by a small, characterisable amount). Alkaline-earth and alkaline-earth-like atoms such as strontium and ytterbium have a near-ideal electronic structure for such a task with suitable transitions for cooling and for the 'clock' measurement. They also have 'magic' wavelengths, for quasi-non-perturbative trapping. NPL decided to work with strontium because all of the necessary laser wavelengths for atom manipulation and control are accessible with either diode or solid state lasers, and it is currently unclear which atom will make the best frequency standard.

As we can see from table 1.1 there are a number of groups working on strontium optical lattice frequency standards, with five groups having published an

absolute frequency measurement of the $5s^2\,{}^1\mathrm{S}_0$ to $5s5p\,{}^3\mathrm{P}_0$ clock transition in ^{87}Sr. On this project at NPL we have not only been able to use the experience gained by these groups to help us with the basic design of our experimental apparatus, but have also had the opportunity to work on new ideas and methods for the strontium optical lattice clock operation.

2.1 Atomic structure of strontium

Strontium is in group II of the periodic table, making it an alkaline-earth metal; it shares many of its properties with other alkaline-earth and alkaline-earth-like atoms such as magnesium, calcium, mercury, and ytterbium. Neutral strontium has 38 electrons. When in the ground state these occupy up to the $5s$ level, which houses the two valence electrons. There are four stable, naturally occurring isotopes of strontium, as shown in table 2.1 with their natural abundances. The even numbered isotopes (^{84}Sr, ^{86}Sr, and ^{88}Sr) are bosonic in nature with nuclear spin $I = 0$, the remaining stable isotope (^{87}Sr) is fermionic with nuclear spin $I = 9/2$ and hence exhibits hyperfine structure.

Upon excitation the atom is transferred from the ground state ($5s^2\,{}^1\mathrm{S}_0$) to the first excited state ($5s5p\,{}^{(2S+1)}\mathrm{P}_J$). Sr exhibits either a singlet state ($S = 0$, excitation to $5s5p\,{}^1\mathrm{P}_1$) or a triplet state ($S = 1$, excitation to $5s5p\,{}^3\mathrm{P}_{0,1,2}$). The transition to the singlet state is electric dipole allowed with a natural linewidth ($\gamma = \Gamma/2\pi$) $\gamma = 30.2\,\mathrm{MHz}$ (state lifetime $\simeq 5.3\,\mathrm{ns}$) and a vacuum wavelength $\lambda = 460.86\,\mathrm{nm}$; it is used for rapid cooling of the atoms towards the Doppler limit of $T_D = 730\,\mu\mathrm{K}$ and state detection in the clock read-out. The transitions to the triplet states are all spin-forbidden in the LS-limit (they involve a spin flip of the excited electron which breaks the selection rule $\Delta S = 0$), but excitation to the $5s5p\,{}^3\mathrm{P}_1$ state is partially allowed by spin-orbit coupling. This results

Isotope	Relative Abundance (%)	Nuclear Spin
^{84}Sr	0.56	I = 0
^{86}Sr	9.86	I = 0
^{87}Sr	7.00	I = 9/2
^{88}Sr	82.58	I = 0

Table 2.1: **Isotopes of strontium** - with their relative abundances and nuclear spin [53].

in a small natural linewidth, $\gamma = 7.5\,\mathrm{kHz}$ (state lifetime $\simeq 21\,\mu\mathrm{s}$), at a vacuum wavelength $\lambda = 689.4\,\mathrm{nm}$. Cooling on this narrow transition ($5s^2\,{}^1\mathrm{S}_0 - 5s5p\,{}^3\mathrm{P}_1$) is limited by the recoil momentum of the photons to $T_r = 230\,\mathrm{nK}$, and is used for further cooling of the atoms beyond the Doppler limit of the first cooling transition.

The last transition to note here is that from the ground state to the lower lying triplet state ($5s^2\,{}^1\mathrm{S}_0 - 5s5p\,{}^3\mathrm{P}_0$), this is not only spin forbidden ($\Delta S \neq 0$) but is also forbidden by the fact that it is a $J = 0$ to $J = 0$ transition. In the odd isotope (with $I = 9/2$) the nuclear spin induces mixing of $5s5p\,{}^3\mathrm{P}_0$ with the $5s5p\,{}^3\mathrm{P}_1$ and $5s5p\,{}^1\mathrm{P}_1$ states resulting in a very small natural linewidth, $\gamma \simeq 1\,\mathrm{mHz}$, at a vacuum wavelength $\lambda = 698.4\,\mathrm{nm}$. The even isotopes have no nuclear spin to induce this hyperfine interaction, so the transition remains inaccessible without the aid of external applied fields to artificially induce a transition linewidth. (For more information on this the reader should refer to [51]). This $5s^2\,{}^1\mathrm{S}_0 - 5s5p\,{}^3\mathrm{P}_0$ transition is used to define the 'clock' frequency since its ultra-narrow linewidth means the transition frequency is very well-defined and the state lifetime is long ($\sim 140\,\mathrm{s}$ for ^{87}Sr [52]).

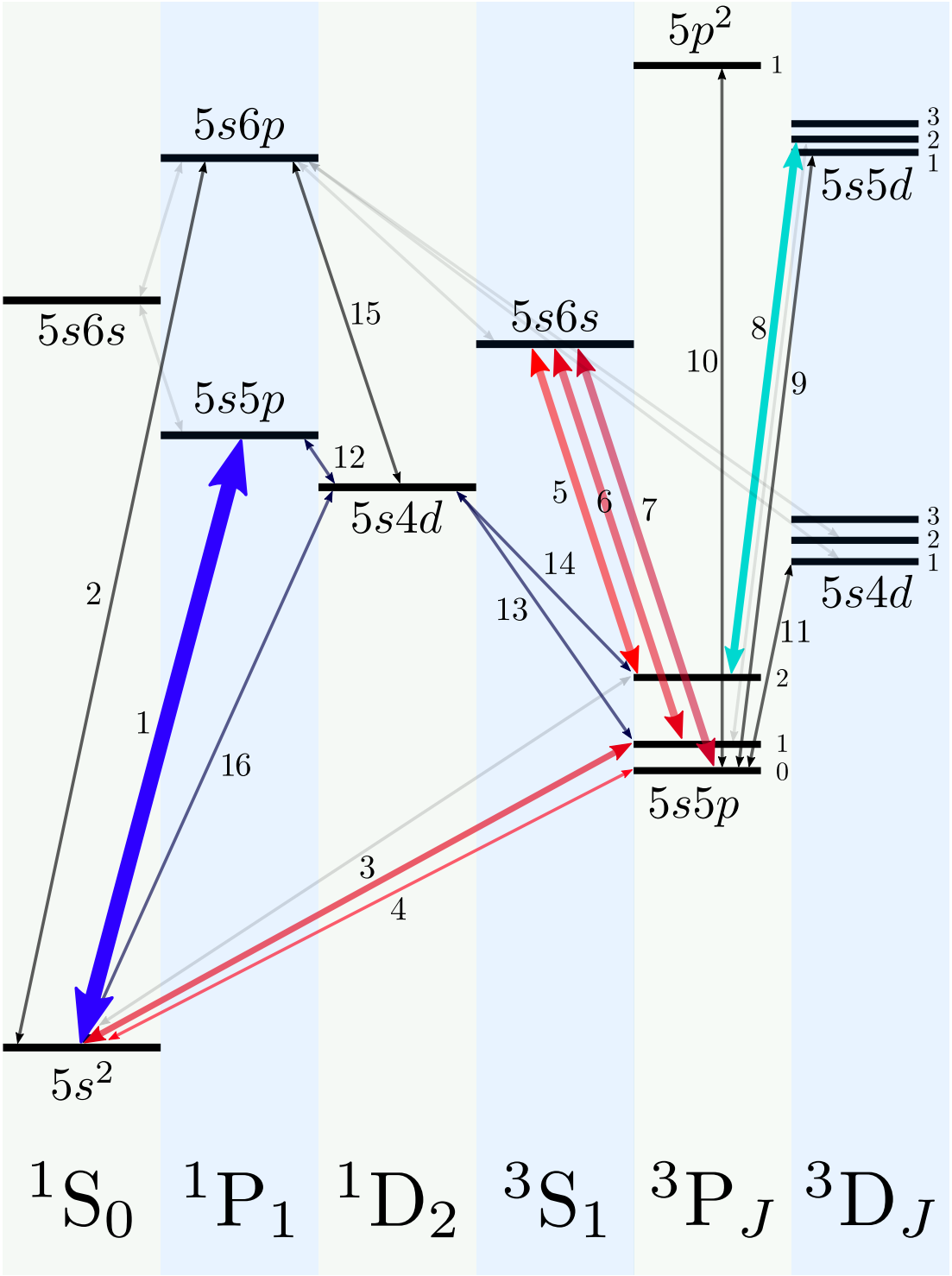

Figure 2.1: **Energy levels of lower-lying strontium transitions** - vacuum wavelengths and transition rates are given in table 2.2.

Transition	Wavelength, λ (nm)	Decay rate, Γ ($10^6\,\mathrm{s}^{-1}$)
1	460.86	190.01 [54]
2	293.27	1.9
3	689.45	0.0469
4	698.4	^{87}Sr: $\sim 7 \times 10^{-9}$ [52]
5	707.21	42
6	688.02	27
7	679.29	8.9
8	496.93	12.8
9	483.34	33
10	474.33	39
11	2603.1	0.2712 [55]
12	6.5×10^3	3.85×10^{-3} [56]
13	1.8×10^3	2.2×10^{-3} [57; 58]
14	1.9×10^3	1.1×10^{-3} [57; 58]
15	717	9
16	496 [56]	70×10^{-6} [57; 58]

Table 2.2: **Neutral strontium transition wavelengths and decay rates** - values calculated from [53] unless otherwise stated. Wavelengths given are for in vacuum.

2.2 Cooling and trapping strontium

The relevant electronic energy levels of strontium are shown in figure 2.1 with their transition wavelengths and rates in table 2.2. There are a small number of different loading schemes that can be used for cooling and trapping the strontium atoms and for subsequent loading into the lattice for 'clock' interrogation. Here I describe the sequence we will use with the aid of figure 2.1 and table 2.2.

First we use a laser at 461 nm (driving transition 1) to rapidly slow the atoms using a Zeeman slower and then trap and cool them in a magneto-optical trap (MOT) to a temperature of a few millikelvin. This transition is almost closed, but has a small decay (approximately 1 in 50 000) from the excited state to $5s4d\,^1\mathrm{D}_2$ (via transition 12); from here 65 % of the atoms subsequently decay to $5s5p\,^3\mathrm{P}_1$ (transition 13) and then back to the ground state in $\sim 21\,\mu\mathrm{s}$ (transition 3); a further 32 % decay to the metastable state $5s5p\,^3\mathrm{P}_2$ (transition 14), and the remaining 2 % decay directly back to the ground state very slowly [58] (transition 16). The atoms would remain shelved in the $5s5p\,^3\mathrm{P}_2$ state if it were not for the repump laser at 707 nm used to pump them rapidly up to the $5s6s\,^3\mathrm{S}_1$ (transition 5), from here the atoms decay back to all three of the $5s5p$ triplet states (transitions 5, 6, and 7). Those in the $^3\mathrm{P}_1$ state decay back to the ground state, those in the $^3\mathrm{P}_2$ state are repumped again and those that decay to the metastable $^3\mathrm{P}_0$ state are repumped using a laser at 679 nm (transition 7) and undergo the same cycle. Both repump lasers are applied during the loading of the 461 nm MOT to increase loading rate, atom number, and atom density, but they are not applied during the Zeeman slowing process because this stage is much faster and very few atoms are lost by the decay to the $5s4d\,^1\mathrm{D}_2$ state.

After quick and efficient loading into the 461 nm MOT the atoms will be transferred in to a MOT at 689 nm (transition 3) where they will be cooled to a

few microkelvin, cold enough for trapping in a lattice at the 'magic' wavelength of 813 nm. Once in the lattice the atoms may be further cooled (motional sideband cooling technique [29; 59]) and state prepared ($m_F = \pm 9/2$ for ^{87}Sr) using the 689 nm transition [59; 60]. The atoms will then be probed with the 'clock' laser at 698 nm (transition 4) with the required intensity and duration for a π-pulse (Rabi pulse) [61] to drive a significant fraction of the atoms from the ground state to the excited $5s5p\,^3\mathrm{P}_0$ state. At this point we expect to have a few thousand cold atoms held in the lattice trap, some in the ground state and some shelved in the excited state. We wish to know the fraction of excited state atoms so that we can alter our laser frequency or pulse duration accordingly, see section 2.3. The unexcited fraction of atoms will be driven out of the trap with the 461 nm laser and the fluorescence used to derive atom number in the ground state. The excited fraction will be repumped (transitions 7 and 5) and will decay back to the ground state, where they are to be interrogated with the 461 nm laser to determine the number (and total fraction) of excited state atoms.

2.3 Making a 'clock' measurement

Following the sequence detailed in section 2.2 we are in a position to drive the 'clock' transition, but how do we measure the 'clock' frequency? This is done by stabilising (also referred to as 'locking') the clock laser frequency to that of the strontium clock transition ($^1\mathrm{S}_0 - {}^3\mathrm{P}_0$).

2.3.1 'Locking' to the clock transition

In an ideal system a π-pulse exactly at the clock transition frequency would result in 100 % excitation of the clock transition, and a π-pulse half the linewidth from

line-centre would result in 50 % excitation. The distribution follows a Lorentzian line-shape:

$$\rho_E = \rho_{max} \frac{\gamma^2}{4\Delta^2 + \gamma^2} \tag{2.1}$$

where ρ_E (ρ_{max}) is the (maximum) excited state fraction, Δ is the detuning from line-centre and γ is the natural linewidth of the transition (full-width at half maximum). We will ignore power broadening for now.

In order to lock our laser frequency to that of the atomic line centre we detune the laser frequency by $-\gamma/2$ so that we get $\rho_E/\rho_{max} = 0.5$ excitation fraction (point 1a in figure 2.2), and then step the frequency to $+\gamma/2$ above line centre to again achieve $\rho_E/\rho_{max} = 0.5$ excitation fraction (point 2a in figure 2.2). If our laser frequency drifts we will measure uneven excitation fractions (for example points 1b and 2b in figure 2.2), the difference between the excitation fractions tells us the magnitude and direction of the frequency correction we need to apply to our laser to stay centred on the atomic line; this correction is applied to the laser frequency via an acousto-optic modulator (AOM). Continually repeating this method locks the laser frequency to that of the atomic transition and the frequency of the continuously-running laser can be measured using an optical frequency comb, which is referenced to the hydrogen maser.

2.3.2 The 'clock' cycle

Using the scheme described above, cold atoms are lost from the lattice trap on each 'clock' cycle, i.e. every time we measure the excited state fraction of atoms, so we will have some dead-time between each measurement while we re-load cold atoms into the lattice. This dead time limits the stability of our lattice clock by contributing to our cycle time t_c (see equation 1.1), so it is desirable to keep this as short as possible, while still taking enough time to cool a sufficient

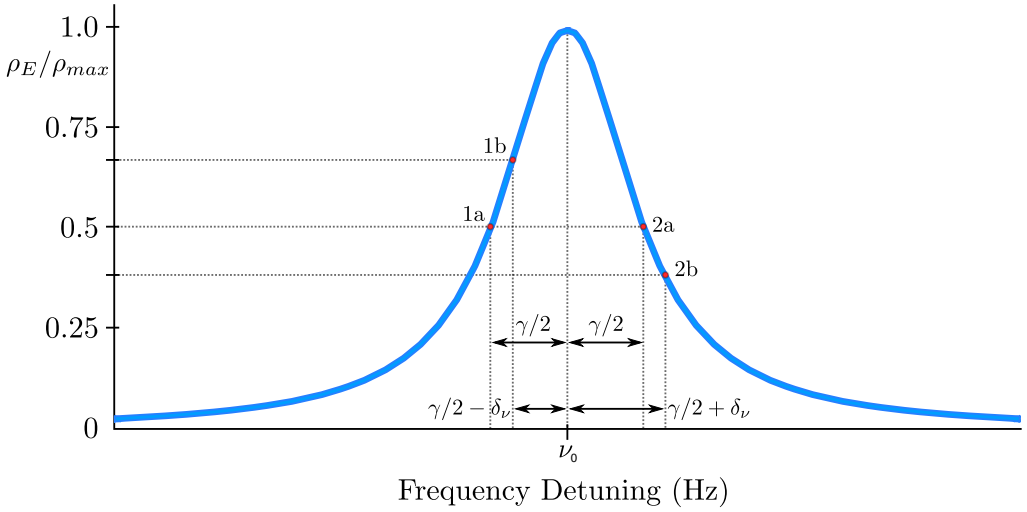

Figure 2.2: **Locking to the transition** - Clock laser frequency is stepped $\gamma/2$ (on the order of $\sim 1\,\text{Hz}$) either side of ν_0 and the excitation fraction measured. If the laser drifts by an amount δ_ν then the measured excitation fractions differ and the laser frequency drift is corrected.

number of atoms N. Loading cycles vary, depending on the aim of a particular set of measurements, but a typical measurement cycle for PTB's Sr optical lattice clock, for example, is outlined by Falke et al. [34]. Here we summarise the clock sequence (with approximate timings).

1. **First stage cooling ($\sim 300\,\text{ms}$)** - Zeeman slowing and 461 nm MOT
2. **Second stage cooling A ($\sim 90\,\text{ms}$)** - Broadband cooling in 689 nm MOT
3. **Second stage cooling B ($\sim 50\,\text{ms}$)** - Narrowband cooling in 689 nm MOT
4. **Lattice loading** - during all above MOT loading and cooling stages
5. **Sideband cooling ($\sim 45\,\text{ms}$)** - (optional) with 689 nm light
6. **Spin state preparation ($\sim 1\,\text{ms}$)** - with B-field and 689 nm light
7. **Rabi π-pulse ($\tau \gtrsim 5\,\text{ms}$)** - with 698 nm laser. The pulse intensity and duration are altered to achieve a π-pulse. Narrower linewidth lasers can achieve longer pulse durations due to their longer coherence times.

8. **Ground state clear-out ($\sim$ 5 ms)** - single short pulse of 461 nm light to clear out the ground state (for clock readout normalisation)
9. **Repump excited state ($\sim$ 10 ms)** - single pulse of 679 nm and 707 nm repump lasers to return excited state atoms to the ground state
10. **Clock readout ($\sim$ 5 ms)** - single pulse of 461 nm light to clear out the ground state. Fluorescence detection determines excitation fraction

Total cycle time ($t_c \simeq$ 600 ms)

2.3.2.1 Dick effect

The relation given earlier for the fractional frequency instability (equation 1.1) is the quantum projection noise limit of the atomic reference, this assumes no laser noise contribution and white frequency noise on the measurement, which averages down as $1/\sqrt{\tau}$. However, in reality the stability achievable is limited by the linewidth of the clock laser (limiting the Q-factor of the measurement) and furthermore the Dick effect [18; 62; 63]. The Dick effect arises from the periodic sampling of the clock laser noise. Low frequency sampling of the high frequency laser noise acts to alias the noise down to lower frequencies and increases the measurement instability. This effect is more noticeable in lattice clocks compared to ion clocks because of the lower measurement time τ as compared to the total cycle time t_c, referred to as the duty cycle ($d = \tau/t_c$). Higher duty cycles act to average out the noise quicker and reduce the instability, this is the approach being worked on by Lodewyck et al. at LNE-SYRTE [64], see section 2.3.2.2. Alternatively, one can reduce the noise by narrowing the linewidth of the clock laser to decrease the instability of the measurement; this is the approach that Ye's group at JILA have focused on to reach their record fractional frequency instability of $< 1 \times 10^{-17}$ in 1000 s [20].

2.3.2.2 Non-destructive read-out method

In order to reduce the cycle dead time, the Dick effect, and hence the fractional frequency instability of the clock measurements Lodewyck et al. [64] are developing a non-destructive clock readout technique that leaves the majority of the atoms trapped in the lattice: after short pulses from the repump and sideband cooling lasers the atoms are ready to be probed with the clock laser again. This method significantly reduces the cycle time from hundreds of milliseconds to tens of milliseconds, although complete reloading of the lattice is required after every few cycles.

The non-destructive method utilises the phase shift experienced by off-resonant light as it interacts with atoms. The accumulated phase shift is proportional to the number of interacting atoms and is related to the detuning from resonance. Laser light at $\sim 461\,\mathrm{nm}$, slightly detuned from the resonance feature, directed through the atomic cloud will accumulate a phase shift proportional to the number of atoms in the ground state (atoms in the excited state will not add a phase shift because they have no resonance features close to 461 nm), the phase shift is measured using a Mach-Zehnder interferometer. The excited atoms are then de-excited using the repump lasers and the phase shift due to the total atom number measured. The ratio of the two measured phase shifts gives the ratio of the excited to ground state atoms. Lodewyck et al. demonstrate that at lattice depths of $\sim 120\,E_R$ (E_R = recoil energies, see section 4.2) more than 80 % of atoms remain trapped in the lattice after each non-destructive readout, and deeper lattices have a greater efficiency. It is estimated that using this method with a Ramsey interrogation technique might achieve fractional frequency instabilities below $2 \times 10^{-16}\,\tau^{-1/2}$ [18]. For more information on this method see the following publications [18; 64; 65].

2.3.2.3 Frequency measurement instabilities (Allan deviation)

Allan deviation is a tool that is used in the frequency metrology field to represent graphically the noise characteristics of a frequency measurement as a function of time [66]. It describes the fractional frequency instability of the frequency standard at different time-scales and gives us some insight to the mechanisms causing instabilities, or alternatively allows us to make the appropriate choice of frequency reference for a particular measurement. The rate at which an instability averages down depends on the source of the noise. Examples of relevant frequency measurement techniques are given below with their typical noise characteristics:

Direct optical-optical comparisons: these typically present white frequency noise, so average down as $1/\sqrt{\tau}$. The initial instability depends on the linewidth of the lasers. If we assume two 698 nm lasers with sub-Hertz linewidth at one second (linewidths are typically quoted at one second), these will have a frequency stability of $\lesssim 2 \times 10^{-15}$ at one second. If the lasers are only locked to optical reference cavities the instability will reach a floor and start moving back up after ~ 10 s; alternatively, if the lasers are also locked to the atomic transition their instability may continue to average down beyond a thousand seconds.

The optical frequency comb: in the current NPL set-up the noise typically averages down as $1/\tau$ when measuring an optical-optical frequency ratio, starting at $\sim 7 \times 10^{-16}$ at one second [67].

The hydrogen maser: to which the optical frequency comb is usually referenced, is a relatively stable short-term oscillator and runs all day, every day with little maintenance. Hydrogen masers present white phase noise, which averages down quickly, as $1/\tau$. A typical hydrogen maser at NPL has a

stability of around 5×10^{-13} at one second, and reaches its noise floor of $\sim 10^{-15}$ after a few thousand seconds [67].

The caesium fountain: (used for absolute frequency measurements) has a typical fractional frequency instability of $\sim 10^{-15}$ after a day of averaging [68]. For absolute frequency measurements of the optical frequencies the hydrogen maser is used to the link the optical frequency comb to the caesium fountain primary frequency standard. The maser provides the frequency reference for both the optical frequency comb's frequency synthesisers and counters, and the microwave source used to drive the atomic excitation in the caesium fountain.

These instability trends are summarised in the plot in figure 2.3.

2.4 Systematic frequency shifts

In order to make a reliable frequency measurement of the clock transition that we can compare to those from other laboratories, we need to analyse carefully our systematic frequency shifts and their uncertainties. Shifts can be due to a number of perturbing fields including, but not exclusively AC-Stark shifts from the probing clock laser and the trapping lattice laser, first and second order Zeeman shifts from magnetic fields, Stark shifts from the black-body radiation (BBR) of the environment, and density related shifts due to interactions with neighbouring trapped atoms. If a shift can be determined with good certainty then it does not cause a problem, for example the AC-Stark shift due to the clock laser can be measured at a range of laser powers and extrapolated to zero with a relatively high certainty. It is the uncertainty in our applied frequency corrections that limit our publishable fractional frequency uncertainty. The largest fractional frequency un-

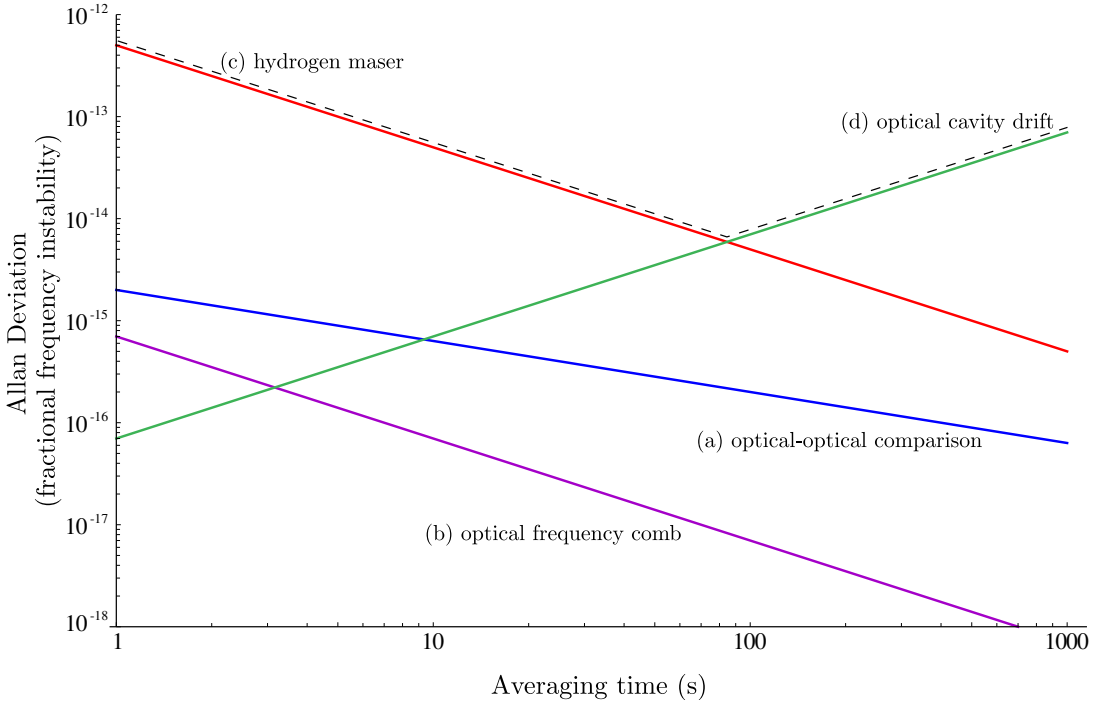

Figure 2.3: **Example Allan deviation plots** - example plots shown for a range of frequency measurements: (a) direct optical-optical comparison of two Hertz linewidth 698 nm lasers locked to suitably stable atomic transitions, $\sigma = 2 \times 10^{-15}\tau^{-1/2}$; (b) noise contribution from the NPL optical frequency comb in its current set-up, $\sigma = 7 \times 10^{-16}\tau^{-1}$; (c) hydrogen maser instability, $\sigma = 5 \times 10^{-13}\tau^{-1}$, (d) 698 nm clock laser locked to an optical reference cavity with a linear drift rate of 30 mHz/s, $\sigma = 7 \times 10^{-17}\tau$. The instability of a frequency measurement will always take the value of the highest contributor at a given time-scale. For example, using the maser-referenced optical frequency comb to measure the frequency of a 698 nm clock laser locked to an optical reference cavity with a linear drift rate of 30 mHz/s, as we have done for figure 5.24, would give an Allan deviation similar to that overlaid with the dashed black line.

certainties of published absolute frequency measurements of the strontium clock transition to date are due to shifts from black-body radiation (i.e. uncertainty in the shift coefficient and the atomic environment) and density related shifts from atomic interactions [21; 34]. Ye's group at JILA have been concentrating their efforts on understanding and addressing the density related shifts [19; 22]. Our project at NPL and the strontium lattice clock project at PBT are concerned with characterising and reducing the uncertainty in the AC-Stark shift due to black-body radiation.

2.4.1 AC-Stark shift

The application of an alternating electromagnetic field causes a perturbation of the energy of an electronic state known as the AC-Stark shift. The energy shift of a state a is given by:

$$\delta E_a^{Stark} \simeq -\frac{1}{2}\alpha_a(\nu)\langle E^2\rangle (+\text{... higher order terms}) \tag{2.2}$$

where $\alpha_a(\nu)$ is the polarisability of state a and $\langle E^2\rangle$ is the mean square of the applied electric field, which relates to the electric field maximum E_0 and the light intensity I by:

$$\langle E^2\rangle = \frac{E_0^2}{2} = \frac{I}{\epsilon_0 c} \tag{2.3}$$

where ϵ_0 is the permittivity of free space and c is the speed of light in a vacuum. The polarisability of a state is given by:

$$\alpha_a(\nu_L) = \frac{2}{h}|d|^2 \frac{\nu_0}{\nu_0^2 - \nu_L^2} \tag{2.4}$$

where ν_0 is the transition frequency from the state a, ν_L is the frequency of the applied light and $|d|$ is the transition dipole matrix element. For multi-level systems we need to sum over all levels k that contribute to the polarisability (i.e. every transition from state a):

$$\alpha_a(\nu_L) = \frac{2}{h}\sum_k |d_{ak}|^2 \frac{\nu_{ak}}{\nu_{ak}^2 - \nu_L^2} \tag{2.5}$$

The dipole matrix element $|d_{ak}|$ is related to the transition rate Γ_{ak} by:

$$\Gamma_{ak} = \frac{4\pi\nu_{ak}^3}{3\epsilon_0 hc^3}|d_{ak}|^2 \tag{2.6}$$

The frequency shift of a particular transition from state a to b is worked out by calculating the difference between the polarisabilities of the ground and excited state ($\Delta\alpha(\nu_L) = \alpha_b(\nu_L) - \alpha_a(\nu_L)$):

$$\Delta\nu_{ab}^{Stark} \simeq -\frac{1}{2h}\Delta\alpha(\nu_L)\langle E^2\rangle \tag{2.7}$$

2.4.1.1 The 'magic' wavelength

In order to calculate the magic wavelength we need to find the frequency of light that causes the two clock states to have the same scalar polarisability, and hence the same frequency shift to first order. There will be many such frequencies, which we can categorise into two groups; those that are red-detuned from the main 461 nm transition and trap the atoms in the high intensity regions of the lattice, and those which are blue-detuned from the 461 nm transition and trap in the low intensity lattice regions. We also require the gradient of the polarisability curves to be low to reduce the magic wavelength stability requirements. The details for calculating α for the two clock states are given in [55], this approach gives an

estimate of the magic wavelengths (the accuracy of which is determined by the knowledge of the transition rates, some of which are not known particularly well) before the wavelengths are experimentally determined. There are two shallow-gradient 'magic' wavelengths accessible with current laser technology; the red-detuned wavelength at $\lambda_{\mathrm{red}} = (813.428 \pm 0.001)\,\mathrm{nm}$ [31; 69; 70]; and the blue-detuned wavelength at $\lambda_{\mathrm{blue}} = (389.889 \pm 0.009)\,\mathrm{nm}$ [71].

For true confinement with a blue-detuned lattice one requires a three-dimensional geometry to trap the low-field-seeking atoms, whereas for the red-detuned lattice one can use a range of lattice geometries from one-dimensional to three-dimensional. To date all strontium lattice clock experiments use red-detuned magic wavelength lattices, with confinement typically in one-dimension, although JILA use two-dimensional confinement to achieve high densities [22], and the group in Tokyo have tried a three-dimensional geometry [42]. The additional complexities of producing the laser light and providing the three-dimensional geometry for a blue-detuned lattice mean we are yet to see much experimental progress along this direction (except for the measurement of the magic wavelength quoted above [71]). However, trapping the atoms in the lower intensity regions means that we see a reduction in the higher-order intensity-related shifts and their associated uncertainties, compared to the red-detuned magic wavelength lattice.

For the red-detuned magic lattice the higher order lattice effects dominate the lattice-induced fractional frequency uncertainty of the clock transition; these include vector and tensor polarisabilities, hyperpolarisability and multipolar effects, and are explained and characterised for λ_{red} by Westergaard et al. [16]. For one-dimensional lattice configurations up to a depth of $U_0 = 150\,E_R$ (recoil energies) the lattice-induced fractional frequency uncertainty is shown to be below

10^{-17} [16]. This is sufficient for today's optical lattice clocks with fractional frequency uncertainties limited to $\sim 10^{-16}$ by black-body radiation shifts [21], but future generations of lattice clocks may choose to benefit from the reduction of higher-order shifts associated with blue-detuned lattices. The predicted fractional frequency uncertainty of the clock transition due to the hyperpolarisability effects (the dominating higher-order effect) of a blue-detuned magic wavelength lattice is as low as $\sim 2 \times 10^{-19}$ [71]. We can reasonably conclude that experimental progress with blue-detuned magic wavelength lattices will continue, and will be crucial for lattice clocks of the future.

In our experiment we intend to use the red-detuned magic wavelength in a one-dimensional lattice geometry. The clock frequency sensitivity to lattice wavelength deviation from the 'magic' value, per trap depth U_0 in recoil energies E_R, is measured in [70] to be $\sim 8\,\mathrm{Hz/nm}/(U_0/E_R)$, this is equivalent to approximately $18\,\mu\mathrm{Hz/MHz}/(U_0/E_R)$. With our expected trap depth of $\sim 120\,E_R$ (see section 4.2) we need to control our lattice wavelength to better than 20 MHz to be sure of a fractional frequency uncertainty of lower than 1×10^{-16}, or 2 MHz for uncertainties of better than 1×10^{-17}.

2.4.1.2 Frequency shift due to black-body radiation

We can also use the equations in section 2.4.1 to calculate the Stark shift due to the black-body radiation (BBR) the atom 'sees' from its environment, but rather than applying a single frequency ν_L of light we are applying a whole BBR spectrum. Planck's Radiation Law gives the radiative energy density $\rho(\nu)$ at the frequency ν for a given black-body temperature T:

$$\rho(\nu) = \frac{8\pi h}{c^3} \int_0^\infty \frac{\nu^3}{\exp\left(\frac{h\nu}{k_B T}\right) - 1} \mathrm{d}\nu \tag{2.8}$$

We can integrate over all frequencies and relate $\rho(\nu)$ to the mean square field [23]:

$$\langle E^2_{\mathrm{BBR}}(\nu)\rangle = \frac{\rho(\nu)}{\epsilon_0} = \frac{8\pi^5 k_B^4}{15\epsilon_0 h^3 c^3} T^4 = c_1 T^4 \tag{2.9}$$

This can be substituted into equation 2.2:

$$\delta\nu_a^{\mathrm{BBR}} \simeq -\frac{1}{2h}\alpha_a(\nu)\, c_1 T^4 \tag{2.10}$$

We use Wein's Displacement Law ($\lambda_{\mathrm{peak}} T = 2.898 \times 10^{-3}\,\mathrm{m{\cdot}K}$) to find the wavelength of the peak of the BBR spectrum. At $T = 300\,\mathrm{K}$, $\lambda_{\mathrm{peak}} = 9.66\,\mu\mathrm{m}$, which is significantly longer than the relevant transition frequencies to and from both the $^1\mathrm{S}_0$ and $^3\mathrm{P}_0$ states of our atom, so we can make the approximation that the perturbation is mainly static, with a small dynamic correction $\eta_a(T)$ [72]:

$$\delta\nu_a^{\mathrm{BBR}} \simeq \frac{c_1}{2h}\alpha_a(0)\, T^4 [1 + \eta_a(T)] \tag{2.11}$$

The total frequency shift of the $^1\mathrm{S}_0$ - $^3\mathrm{P}_0$ transition is:

$$\Delta\nu^{\mathrm{BBR}} = \delta\nu^{\mathrm{BBR}}_{^3\mathrm{P}_0} - \delta\nu^{\mathrm{BBR}}_{^1\mathrm{S}_0} \tag{2.12}$$

The polarisabilities of the $^1\mathrm{S}_0$ and $^3\mathrm{P}_0$ states due to BBR were theoretically determined for Sr, Yb, Ca, and Mg by Porsev and Derevianko, and the frequency shift and its uncertainty evaluated at $T = 300\,\mathrm{K}$ in [72]. The same parameters are calculated for Hg by Hachisu et al. in [45]. The estimated frequency shifts and uncertainties at 300 K are summarised in table 2.3. Sr has the largest shift and the second largest uncertainty behind Yb. Mg and Hg have smaller sensitivities to BBR, and so are attractive species for use in optical lattice clocks, but progress with these species is slowed by the less well developed laser technology at the

Species	ν_0 ($\times 10^{14}$ Hz)	$\Delta\nu^{\mathrm{BBR}}$ (Hz)	$\Delta\nu^{\mathrm{BBR}}/\nu_0$ ($\times 10^{-16}$)	Ref.
Sr	4.29	-2.354 ± 0.032	-55 ± 0.7	[72]
Ca	4.54	-1.171 ± 0.017	-26 ± 0.4	[72]
Yb	5.18	-1.25 ± 0.13	-24 ± 3	[72]
Mg	6.55	-0.258 ± 0.007	-3.9 ± 0.1	[72]
Hg	11.3	-0.181	-1.6	[45]

Table 2.3: **Estimated BBR frequency shifts** - showing theoretically calculated room temperature BBR shifts and their uncertainties for divalent atomic species currently used in optical lattice clocks. Small corrections to some of these shifts have since been made, see details in section 2.4.1.2.

required wavelengths for cooling, trapping and probing.

Static polarisability measurements. The variable η in equation 2.11 represents a small, temperature dependant dynamic correction to the static shift, for example at $T = 300\,\mathrm{K}$ the static shift in Sr was predicted to be $(-2.248 \pm 0.031)\,\mathrm{Hz}$ with the dynamic contribution to the shift being $(-0.107 \pm 0.011)\,\mathrm{Hz}$ [23] (totalling the $-2.354\,\mathrm{Hz}$ shift shown in table 2.3). From the relative sizes of the static and dynamic shifts and their uncertainties we can see that the static component is the largest contributing factor. Better knowledge of this static component will enable us to reduce the fractional frequency uncertainty of the BBR induced frequency shift. Groups at PTB and NIST have worked on making experimental measurements of the static polarisability of Sr [23; 24] and Yb [73] atoms respectively. Each group made a set of carefully designed capacitor plates to apply a DC electric field across the atoms trapped in the lattice. They measured the frequency shift for a range of applied fields and deduced the static polarisability and frequency shift along with their relative uncertainties. By improving the knowledge of the static polarisabilities they limit the fractional frequency uncertainty of the BBR shift at room temperature to that of the dynamic contribution, which

is 2.6×10^{-17} for Sr [23]. In reality the shift uncertainties are limited by a lack of knowledge of the temperature of the environment, a 1 K uncertainty at 300 K results in fractional frequency uncertainties of $\sim 7 \times 10^{-17}$ for Sr and $\sim 3 \times 10^{-17}$ for Yb.

Dipole matrix element measurements. Improvements to the total BBR frequency shift uncertainty can be made by better knowledge of the transition frequencies and decay rates that go into the polarisability calculations (ν_{ak} and $|d_{ak}|$ in equation 2.4). The largest contributions are from transitions in the infra-red region of the spectrum, because they couple more strongly to the BBR spectrum. Alkaline-earth-like atoms have an infra-red transition from the excited clock state ($5s5p$ in Sr) $^3\mathrm{P}_0$ to the ($5s4d$ in Sr) $^3\mathrm{D}_1$ state (transition 11 in figure 2.1). The Yb lattice group at NIST [74] and the Sr lattice group at PTB [24] have been working on making improvements to the knowledge of the relevant dipole matrix elements. The approaches used are direct measurement [74] and remodelling the polarisability by confining the known values (α^{static}, α^{magic} etc.) and allowing the dipole matrix element under consideration to be a free parameter [24; 74]. This approach reduces the fractional frequency uncertainty of the BBR shift at room temperature, due to knowledge of the coefficients in equation 2.11, to 1.1×10^{-18} in Yb [74], and 5×10^{-18} in Sr [24]. This means that the uncertainties are now heavily limited by lack of knowledge of the BBR environment in which the atoms are housed.

The accepted BBR shift for Sr at $T = 300\,\mathrm{K}$ is now $(-2.2777 \pm 0.0023)\,\mathrm{Hz}$, consisting of the static contribution of $(-2.130186 \pm 0.000060)\,\mathrm{Hz}$, and the dynamic contribution of $(-0.1477 \pm 0.0023)\,\mathrm{Hz}$ [24]. This is somewhat different to the value given in table 2.3 from [72] due to refinement of the parameters used in the calculation and a small error in the calculations performed in [72]. Small

corrections will ultimately need to be applied to the absolute frequency values published between 2006 and 2012 (e.g. $\sim +\ 76\,\mathrm{mHz}$ for Sr), but the frequencies will still remain in agreement with one another.

Total BBR shift measurements. At NPL we are making an experimental apparatus to measure directly the total BBR frequency shift for Sr atoms. We intend to benefit from the $\sim T^4$ dependence of the BBR shift, shown in equation 2.10, by increasing the environment temperature to increase the frequency shift. We have designed our system to have two black-body environments (i.e. tubes), see figure 4.6, which will be stabilised to different temperatures. The atoms will be moved into the 'hot' ('cold') tube by a transport lattice and a frequency measurement made; this measurement will be compared to that made in the other, 'cold' ('hot'), tube.

With this method we should be able to confirm experimentally the calculated value in reference [24] with a predicted fractional frequency uncertainty in the 10^{-17} range. More details of our intended approach are given in section 4.3 and [55].

Minimisation. As with our plan to take advantage of the the $\sim T^4$ dependence by heating the environment to make a measurement of the BBR induced frequency shift, the opposite can be done to significantly reduce the magnitude of the shift and its uncertainty. Even with good knowledge of the BBR induced frequency shift, [74] demonstrates that at room temperature knowledge of the temperature distribution which the atoms can 'see' limits the certainty of the frequency shift. As we mentioned earlier, at 300 K a temperature uncertainty of 1 K equates to a fractional frequency uncertainty of $\sim 3 \times 10^{-17}$ for Yb and $\sim 7 \times 10^{-17}$ for Sr. If we go to cryogenic temperatures we get a reduction in the fractional frequency

uncertainty for the same level of temperature certainty. At 77 K a temperature uncertainty of 1 K equates to a fractional frequency uncertainty of $\sim 1 \times 10^{-18}$ for Yb [73] and Sr [24].

2.5 Current status of our experiment

At present in our experiment we have developed the apparatus and techniques to enable us to follow these steps up to the point where we are just about to start trapping in the 689 nm MOT. We have most the laser systems required of clock operation built, stabilised, characterised and ready for use. Details of our vapour source, Zeeman slowing, and first stage MOT can be found in chapter 3. Our 689 nm laser set-up and plan for second stage cooling, along with details of our magic wavelength lattice laser are given in chapter 4. The focus of the work for this thesis is towards the clock laser set-ups; this work is detailed in chapter 5.

Chapter 3

Preparing the cold atomic vapour

In the previous two chapters we have introduced the concept and purpose of a strontium optical lattice clock. Over the next few chapters we will describe the details of how we are building the strontium optical lattice optical frequency standard at the National Physical Laboratory. This chapter describes how we create a high strontium vapour pressure, produce an atomic beam, and then use laser cooling on the 461 nm transition to slow, cool, and trap the atoms at a few millikelvin above absolute zero, to make a cold atomic vapour. This process must be both efficient and rapid to meet the goal of trapping $\sim 10^7$ cold atoms within a time of ~ 300 ms. In subsequent chapters we detail the apparatus being built for further cooling of the atoms in order to trap them in an optical lattice at temperatures of a few microkelvin, where they will be interrogated with the clock laser.

3.1 Strontium vapour

In this section we cover the physics behind producing a strontium atomic vapour. We discuss strontium vapour cells, and discover the need for an atomic beam

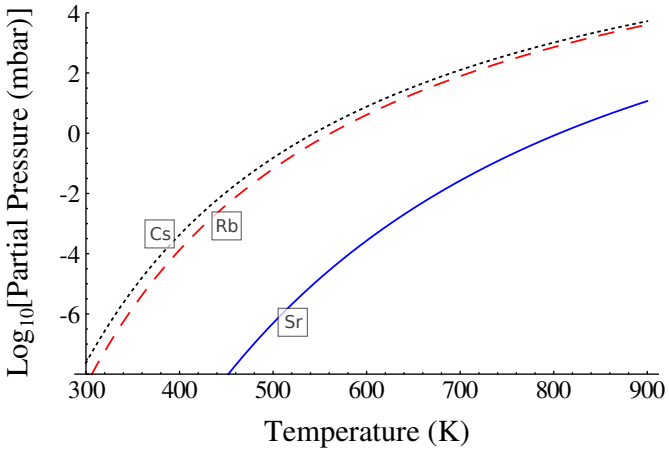

Figure 3.1: **Vapour pressures** - of caesium [75], rubidium [75], and strontium [76]. To achieve room temperature vapour pressures of caesium and rubidium, strontium needs to be heated to around 450 K.

apparatus, before we go on to characterise the strontium atomic beam built in our laboratory.

The vapour pressure of a substance is the equilibrium pressure between its solid or liquid form and its vapour form, and it varies with temperature and substance. Figure 3.1 shows a plot of the vapour pressure of strontium compared to rubidium and caesium, elements that for historic and practical reasons have been extensively studied by atomic physicists. We can see that to achieve the room temperature vapour pressure of the alkali elements rubidium or caesium, the alkaline-earth element strontium, similarly to ytterbium and calcium, needs to be heated to around 450 K. We might initially think that we can use a simple strontium vapour cell for trapping and studying cold strontium, like those used for rubidium and caesium. Naively one could assume we simply heat the cell more to get the required vapour pressure; unfortunately this leads to problems. Firstly, strontium reacts with the silicates in glass [77; 78] turning standard optical windows opaque. An alternative is to use sapphire windows, as in the strontium vapour cells described in [57] and [77], or to have a buffer gas or containment

region of the strontium to keep it away from the windows, as described in [79; 80; 81]. The second problem comes from the resulting background pressure in a vapour cell, in order to trap atoms in an optical lattice trap for sufficient time to interrogate the clock transition (ideally a few seconds lattice lifetime) the background pressure needs to remain low. In a strontium vapour cell the collision rate from background gas will be far too high for this. A third problem in trying to make a strontium optical lattice clock in a vapour cell is due to black-body radiation quenching of the clock state. Figure 2.1 shows a 2.6 μm transition from the excited clock state to the $5s4d\,^3D_1$ state (transition 11), which decays to the ground state via the $5s5p\,^3P_1$ state. At elevated temperatures (typically $\sim 600\,K$) a significant portion of the black-body radiation spectrum is resonant with this transition, quenching the lifetime of the excited clock state (usually $\sim 140\,s$) to less than $\sim 300\,ms$ at $600\,K$ [55].

3.1.1 Strontium atomic beam

A solution for producing a sufficient strontium vapour in a suitable environment is to use an atomic beam source, where the strontium is contained in a heated region of the vacuum apparatus and is allowed to escape (effuse) into the lower pressure region through a small opening. With further beam aperturing this can result in a near-collimated atomic beam. Many strontium experiments, including ours, use adaptations of this same basic idea. They typically use a crucible containing a few grams of strontium with some combination of single and multi-channel nozzles for beam collimation. The crucible is typically heated to around $700\,K$ - $900\,K$, while the nozzle is $\sim 50\,K$ hotter to avoid blockages. Our oven design is shown in figure 3.2. We use mineral-insulated heater wire from Thermocoax Ltd. inside our vacuum chamber to heat the crucible and nozzle efficiently. By

applying direct heating inside the vacuum we are able to benefit from the vacuum's insulation and heat our oven to $\sim 900\,\mathrm{K}$ by applying only 2.0 A, 14 V, while the outside vacuum chamber only reaches temperatures of $\sim 330\,\mathrm{K}$. We have two K-type thermocouples for monitoring the temperature of the crucible and nozzle, although after a short time these became contaminated with strontium and now read erroneously. The original oven had a multi-channel nozzle containing $\sim 50 \times 200\,\mu\mathrm{m}$ diameter, 10 mm long stainless steel capillary tubes with a further aperture $\sim 5\,\mathrm{cm}$ further downstream, but the nozzle became blocked by the copper surrounding it (see figure 3.2 (d)), which was eroded by the strontium (strontium is known to react with copper). The oven lasted for about a year of continual use before the nozzle became blocked or the oven became depleted - it is not clear which happened first. Upon refilling the oven, the multi-channel nozzle broke, and due to the lack of immediate availability of replacements, a new nozzle design containing a single 1 mm diameter, 11 mm long hole drilled into a stainless steel piece, was implemented. To aid beam collimation we now have an additional 1 mm aperture 10 cm downstream from the oven nozzle exit, and between these two we have a small vacuum cross piece, see figure 3.3. The cross is used for atomic beam characterisation and for alignment of the slowing beam. We have attempted transverse laser-cooling of the atoms in this region, resulting in no significant increase in atomic flux downstream in the experimental chamber, and have successfully carried out fluorescence spectroscopy on the narrow 689 nm transition (see section 4.1.3), indicating we could use this region for frequency stabilisation of the second-stage cooling laser.

We can compare our single channel nozzle oven to that published by Schioppo et al. [82]. Comparing the heating efficiency of the two ovens we can see that our oven is more efficient in terms of temperature reached per unit of electrical power;

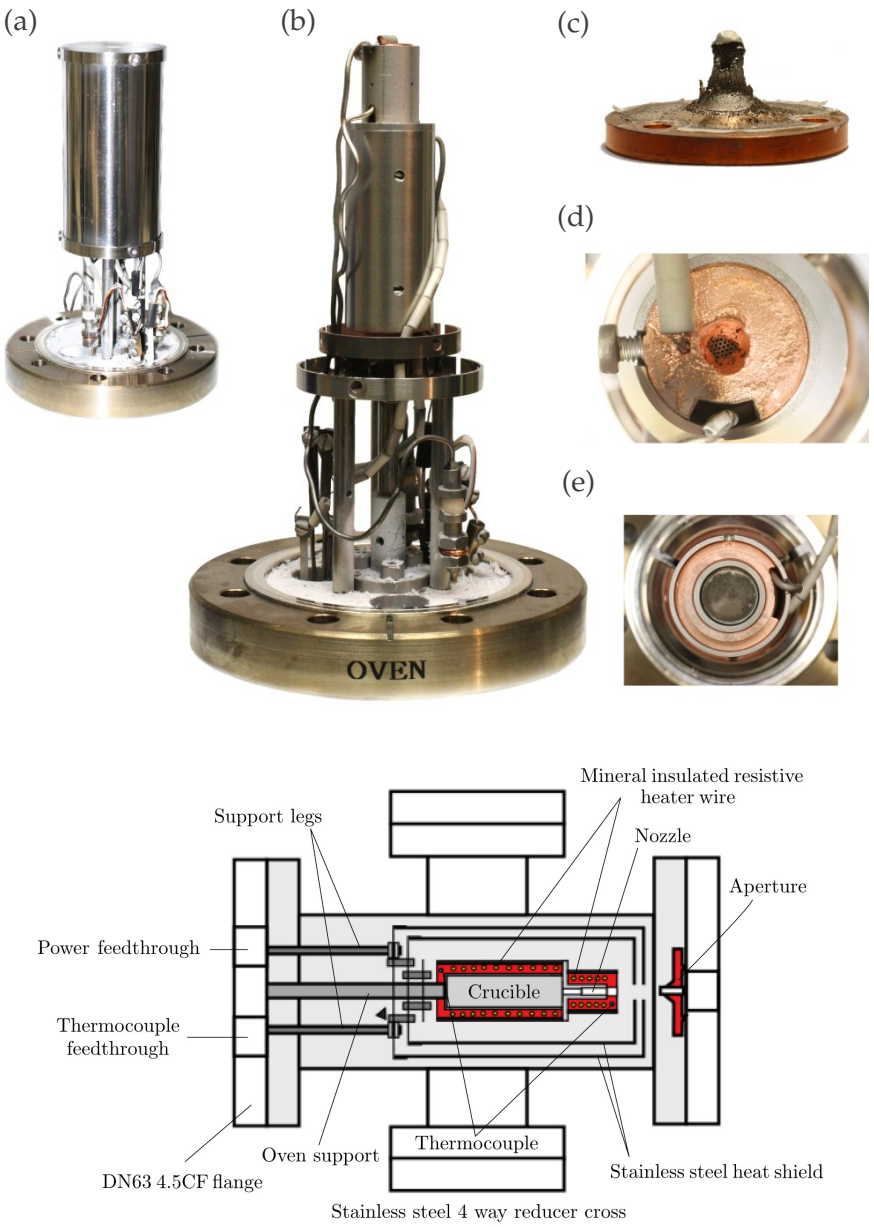

Figure 3.2: **NPL strontium oven** - (Top) Photographs of the oven after first full use; (a) fully assembled, including thermal radiation shielding; (b) with shielding removed, showing separate nozzle and crucible heater wires and thermocouples; (c) external copper aperture showing the build-up of strontium over the course of one oven lifetime; (d) semi-blocked stainless steel multi-channel nozzle with corroded copper surround; (e) view inside crucible with nozzle removed. (Bottom) Oven schematic. Figure taken from [55], with thanks to I.R. Hill.

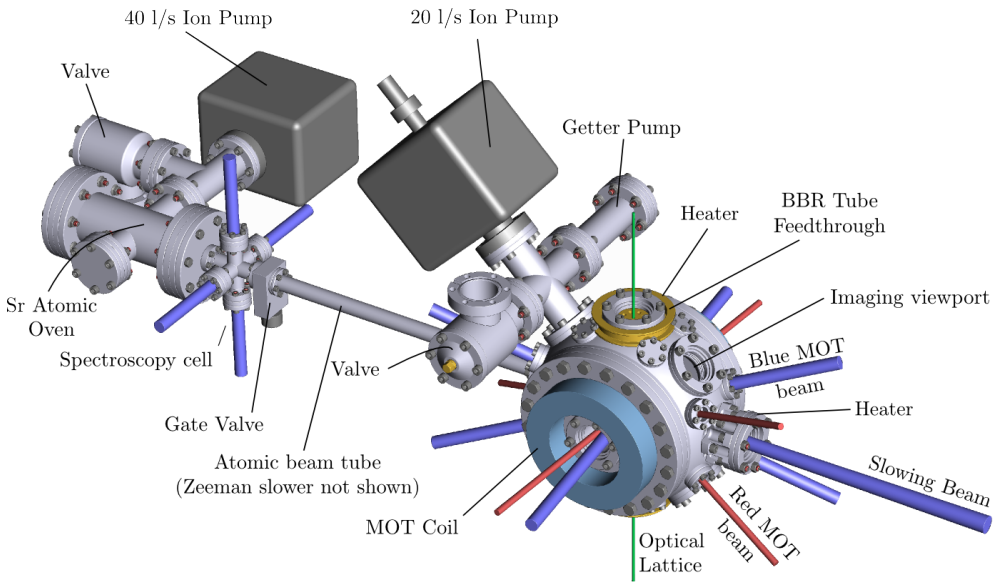

Figure 3.3: **Main vacuum chamber** - Schematic of main atomic vacuum system, showing geometry of cooling and trapping beams. The Zeeman slower sits around the long central tube. Drawing taken from [55], with thanks to I.R. Hill.

reaching 600 °C with 28 Watts of electrical heating compared to Schioppo's 450 °C with 36 Watts of heating. However, if we compare the atomic flux densities we can see that Schioppo's oven is more efficient in terms of the collimated atomic beam output; with 10^{13} atoms/s/cm^2 compared to our 3×10^{10} atoms/s/cm^2. The large difference in atomic flux densities is due to the nozzle geometry; the multi-channel nozzle design used in [82] achieves in a highly collimated atomic beam with divergence half angle ~ 37 mrad, whereas our single channel nozzle results in a more divergent beam (divergence half angle > 150 mrad) that is apertured to achieve a collimated beam with a divergence half angle of ~ 16 mrad (calculated from a measured transverse fluorescence FHWM of 34 MHz). The lower operating temperature and larger strontium reservoir in [82] (6 grams compared to our 3.5 grams) means that Schioppo's oven should last significantly longer than ours, they estimate 10 years of operation. From this comparison we can see that our vacuum and heater design is efficient in terms of heating the strontium, but we

would benefit significantly in terms of atomic flux and oven lifetime if we were to go back to using a multi-channel nozzle design.

3.1.2 Atomic velocity distribution

In this section we characterise the atomic velocity distribution of atoms exiting the oven and compare this to the Maxwell-Boltzmann theory. We will see that the thermal distribution has very few atoms at low velocities. This then leads us on to a discussion of laser cooling and Zeeman slowing which is presented in sections 3.2 and 3.2.1. This technique facilitates the slowing of a large number of the thermal atoms to within the capture velocity of our first-stage magneto-optical trap.

As we wish to know the distribution of velocities in our atomic beam we should first consider the Maxwell-Boltzmann distribution of a thermal cloud of atoms, where the speed probability density function is given by:

$$f(v) = \sqrt{\frac{2}{\pi}\left(\frac{m}{k_B T}\right)^3} v^2 \exp\left(\frac{-mv^2}{2k_B T}\right) \tag{3.1}$$

where m is the atomic mass, k_B is Boltzmann's constant, T is the absolute temperature of the sample and v is the atomic speed. We now wish to consider only the atoms that escape from our oven. The chance of a particular atom escaping from the oven is proportional to its velocity, so we have to multiply the above distribution through by v. The normalised atomic beam intensity distribution for effusion is given by:

$$I(v) = I_0 \left(\frac{m}{k_B T}\right)^2 v^3 \exp\left(\frac{-mv^2}{2k_B T}\right) \tag{3.2}$$

where I_0 is the full atomic beam intensity. Characteristic velocities of this distri-

bution are given in [83]:

Most probable velocity $v_p = 1.22\sqrt{\frac{2k_BT}{m}}$

Average velocity $\overline{v} = 1.33\sqrt{\frac{2k_BT}{m}}$

RMS velocity $v_{RMS} = 1.41\sqrt{\frac{2k_BT}{m}}$

Velocity-calibrated atomic intensity distributions for the two nozzle configurations of our oven are shown in figure 3.4 with a Maxwell-Boltzmann distribution fit. These data are taken by scanning a resonant 461 nm probe beam at an angle of 55° to the direction of atomic trajectory (an angle that is corrected for in the velocity calibration) and the resulting fluorescence detected. We must remember that if we look at atomic fluorescence to determine the longitudinal velocity distribution we need to multiply the fluorescence spectrum through by the atomic velocity v to take into account the shortened interaction time of the faster atoms with the probing laser beam. From the results shown in figure 3.4 we can see that the multi-channel nozzle better fits the ideal distribution than the single-channel nozzle. This is because it is a better approximation of an effusive source. For a source to be categorised as effusive the mean free collision path must be greater than or equal to the characteristic length (radius or length depending on the flow regime) of the circular nozzle through which the atoms are escaping [83], meaning there are few collisions within the nozzle. Neither velocity distribution is particularly better or worse for Zeeman slowing, but it is important to know the initial distribution in order to later characterise the Zeeman slowing efficiency.

Atomic Dispensers An alternative approach to using a crucible oven is to use an atomic dispenser, such as those sold by Alvatec GmbH. These are directly heated by applying a current through them ($\sim$15 A for the 500 mg strontium

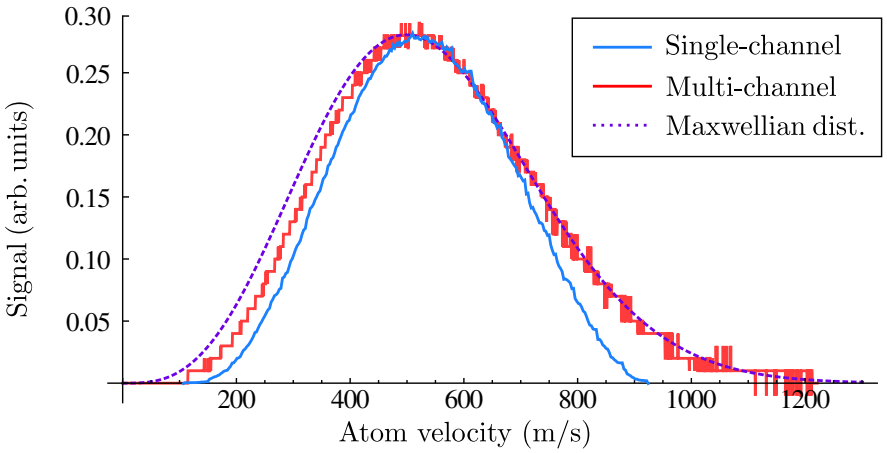

Figure 3.4: **Atomic velocity distributions from atomic oven** - Longitudinal velocity distributions for single-channel and multi-channel nozzle configurations, as detailed in sections 3.1.1 and 3.1.2, with corresponding Maxwell-Boltzmann distribution. Atomic source temperature for both cases is $\sim 900\,\mathrm{K}$.

dispensers), and they heat up in a matter of seconds, compared to the heating time of ~ 2 hours for our crucible oven. The atomic dispensers are much simpler to incorporate into a vacuum system than a crucible oven, and have been shown to last for over a year of regular use [79]. They are also suited to making a much more compact vacuum system, which is one of the requirements for the development of optical clocks for use in space. The main disadvantage is that the atomic dispensers produce an atomic jet, rather than the nicely collimated atomic beam the crucible oven creates, and so cannot be used to feed a Zeeman slower directly. One could conceive adapting the dispenser to have a multi-channel nozzle at the output, but in reality this is likely to get blocked due to the technical difficulties of heating this independently of the dispenser's main body. The strontium lattice clock project at the University of Birmingham is aiming to use strontium dispensers to feed a 2D MOT, which will capture and collimate the atoms for loading into a 3D MOT [84]. The strontium Rydberg project at Durham University is working towards a compact strontium source consisting of a dispenser-fed pyramid MOT [85]. At the time of writing, neither experiment has yielded re-

sults, so we cannot comment on their efficacy compared to standard crucible oven sources.

3.2 Laser cooling and trapping

We are producing our atomic vapour beam in a crucible oven at around 900 K, which gives a most probable atomic velocity of $\sim 500\,\mathrm{m/s}$ with a velocity profile resembling equation 3.2 (see figure 3.4). Since we wish to trap our atoms in an optical lattice potential of depth $\sim 20\,\mu\mathrm{K}$ (equivalent to a speed of $\sim 6\,\mathrm{cm/s}$), we first need to slow (in one dimension), and then cool (in three dimensions) our atoms. This is accomplished with the aid of laser cooling techniques developed since the idea of using photon momentum to slow atoms was first proposed in 1975 by Hänsch and Schawlow [86], and Wineland and Dehmelt [87] simultaneously. A nice history of the development of the field is given in [88].

Light can be thought of as either particles or waves. A photon is a particle of light and has energy $E_{ph} = h\nu = hc/\lambda$ and momentum $\vec{p_{ph}} = \hbar\vec{k}$, where h ($\hbar$) is Plank's constant (divided by 2π), $\vec{k}$ is the wave-vector of the light $|\vec{k}| = k = 2\pi/\lambda$, and ν, c, and λ are the frequency, speed, and wavelength of light respectively. We will imagine a simple two-level atom with an electric-dipole-allowed transition between the two electronic states, which have energies E_g and E_e, and the atom has a momentum $\vec{p_{at}} = m\vec{v}$, where m is the atom mass and $\vec{v}$ is the atom velocity. If this atom is initially stationary in a beam of photons, then it can absorb a photon with energy $E = E_e - E_g$, which excites the atom from the ground to the excited state (or the excited state to the ground state via stimulated emission). Conservation of linear momentum dictates the atom absorbs the photon's momentum, $\vec{p_{at}} = m\vec{v} + \hbar\vec{k}$, receiving a 'kick' in the direction of the photon's travel. After a time $\tau = 1/\Gamma$ the excited atom decays back to the

ground state, emitting a photon of energy $E_e - E_g$, momentum $p_{ph} = \hbar k$, and the atom recoils with equal and opposite momentum. At first glance it appears we are exactly back where we started, except for one significant difference; this photon is emitted in a random direction by spontaneous emission. Multiple, N_{ph}, absorptions and emissions will result in an isotropic emission pattern (this is not always the case, but is assumed here for the purpose of this example) with the net emission momentum cancelling out to zero, but the net absorption momentum being $\vec{p} = N_{ph}\vec{p_{ph}}$, acting to push the atom in the direction of photon travel.

If we now consider an atom with velocity v in the opposite direction to that of the photons, we can now see how light can be used to slow atoms. There are two important points we cannot neglect here. Firstly, since the atom is travelling towards the photons it will observe their frequency and energy to be Doppler shifted to $\nu_D = (1 + v/c)\,\nu_0$ and $E_D = h\,(1 + v/c)\,\nu_0$. So in order to remain on resonance we need to detune the frequency of our light so that it matches that which the atoms require. Secondly, after sufficient absorption and emission cycles the atom will have slowed enough so that it is no longer on resonance with the light and can no longer absorb any more photons. How quickly this happens depends upon the intensity of the laser beam and the linewidth of the transition, $\gamma = \Gamma/2\pi = 1/2\pi\tau$. The linewidth γ not only controls how quickly the atoms can absorb the photons and decay back to the ground state, it also indicates the frequency range over which the atom will absorb photons. The absorption profile of the atom has a Lorentzian lineshape, with a full-width at half maximum (FWHM) equal to γ, given by:

$$A\,(\nu) = A_0 \frac{\gamma^2}{4\Delta_\nu^2 + \gamma^2} \tag{3.3}$$

where $\Delta_\nu = \nu_D - \nu_{at}$ is the detuning of the light from the centre of the atomic

resonance. For our first cooling transition at 461 nm, with a natural linewidth of $\gamma = 30.2\,\mathrm{MHz}$, the Doppler cooling range (full-width at half-maximum) for a single frequency photon source is characterised by $\gamma\lambda \simeq 14\,\mathrm{m/s}$. The force applied by a laser beam is given by:

$$\vec{F}_{\mathrm{scatt}} = \frac{1}{2}\hbar\vec{k}\Gamma\frac{\gamma^2 s}{4\Delta_\nu^2 + \gamma^2(s+1)} \tag{3.4}$$

where $s = I/I_{\mathrm{sat}}$ is the saturation parameter, I is the intensity of the laser beam and I_{sat} is the saturation intensity for the transition, given by:

$$I_{\mathrm{sat}} = \frac{\pi hc\Gamma}{3\lambda^3} \tag{3.5}$$

For full formalisation of the theory of laser cooling the author refers the reader to texts such as those by C.J. Foot [61] or H.J. Metcalf and P. van der Straten [89].

3.2.1 Zeeman Slowing

In this section we cover the basic physics behind Zeeman slowing and consider the specific details of slowing different isotopes of strontium.

We wish to slow the thermal atoms in our atomic beam, with a most probable velocity of $\sim 500\,\mathrm{m/s}$, to $\sim 30\,\mathrm{m/s}$, which is within the capture velocity of our magneto-optical trap. Now that we have the basics of laser cooling, there is one more step we need to include, namely how to keep the laser on resonance sufficiently long so that we can cool beyond the $\gamma\lambda$ limit. The most intuitive way to do this, and hence the first that was tried, is to sweep the frequency of the laser so that it matches the frequency of the slowing atoms; this is called chirped cooling [90]. There are two points that need to be considered here if one were planning

to utilise this technique in the current experiment. Firstly, the laser needs to be swept over a relatively large frequency range; $\sim 1\,\mathrm{GHz}$ for slowing $\sim 500\,\mathrm{m/s}$ atoms down to $\sim 30\,\mathrm{m/s}$. This is not necessarily difficult, but can complicate the optical set-up somewhat if other fixed frequency beams are required for this transition (e.g. for the magneto-optical trap, see section 3.2.2). Secondly, the cold atoms arrive grouped together and there is a period of time between each group during which the laser is scanned back to the starting frequency to collect the next cluster of atoms. As we discussed previously in section 2.3.2 we require fast cycle times for high stability frequency standards, so this technique would prove problematic. A second method, which is more easily implemented, is called Zeeman slowing [91]. This method utilises the Zeeman effect. A spatially-varying, applied magnetic field shifts the electron energy levels within the atom such that as the atoms move along the length of the slower, and are slowed by the counter-propagating laser light, the transition frequency is tuned and kept on resonance with the fixed frequency laser beam. The magnetic field profile can be calculated such that the Zeeman shift compensates for the Doppler shift at each point along the slower. The frequency of the transition with an applied magnetic field B is shifted to:

$$\nu_B = \nu_0 + \frac{g_J m_J \mu_B B}{h} \tag{3.6}$$

where g_J is the Landé g-factor, m_J is the quantum angular momentum of the atom's energy state and $\mu_B = \frac{e\hbar}{2m_e}$ is the Bohr magneton, with e the electron charge and m_e the electron mass.

If the atoms are to undergo constant deceleration we can equate ν_D and ν_B and use the spatially dependent equation for constant acceleration $v = \sqrt{v_0^2 + 2az}$, where v_0 is the initial velocity, a is the acceleration (which is a negative number), and z is the distance along the slowing path. From these relations we can show

that the required magnetic field is:

$$B = \sqrt{v_0^2 + 2az}\frac{h\nu_0}{cg_J m_J \mu_B} \tag{3.7}$$

which gives a field profile similar to that shown in figure 3.10. If we choose a starting velocity v_0 (say 420 m/s) and a final velocity v_f to which we wish to slow to (say 30 m/s) the length of our Zeeman slower is:

$$L_0 = \frac{v_f^2 - v_0^2}{2a} \tag{3.8}$$

Remember this is assuming constant acceleration throughout the slower, which in practice means we have a collimated slowing laser beam and we are neglecting the effects of absorption on the laser beam intensity. The acceleration due to the scattering of a near-resonant laser beam on an atom is given by dividing equation 3.4 through by the mass of the atom m. When we talk about Zeeman slowing we are usually referring to a slowing laser beam of intensity comparable to the saturation intensity. The maximum acceleration for a given atomic transition with a particular intensity of slowing beam is:

$$\vec{a}_{\max}(z) = \frac{F_{\max}(z)}{m} = -\frac{1}{2}\frac{\hbar\vec{k}\Gamma}{m}\frac{s(z)}{s(z)+1} \tag{3.9}$$

where, if desired, the intensity can be spatially dependent to take into account a converging laser beam and/or intensity losses due to scatting events. Maximum acceleration requires the laser light to be exactly on resonance with the atomic transition, i.e. we are sitting on the top of the scattering curve shown in figure 3.5. This is an unstable situation, in the sense that if there were any discrepancies in our theoretical and experimental environments the atoms could easily slip off

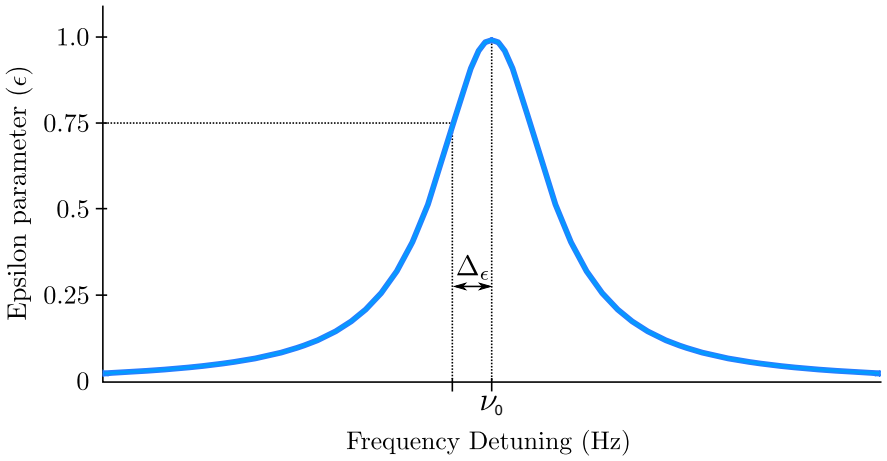

Figure 3.5: **Epsilon parameter for Zeeman slowing** - Epsilon controlled by laser beam detuning. Maximum stable deceleration is achieved at the steepest part of the curve, where $\epsilon = 0.75$.

resonance by being decelerated too much or too little. Those that underwent too little deceleration would be lost from the slowing process. Following this argument we typically choose a conservative acceleration $a = \epsilon a_{\max}$ [92], where ϵ takes a value between 0 and 1, as shown in the acceleration plot in figure 3.5. Maximum stable deceleration is achieved with $\epsilon = 0.75$, and our Zeeman slowers, detailed in section 3.3.2, are usually on the cautious side with $\epsilon = 0.6$. The resulting acceleration can be put into equations 3.7 and 3.8 to calculate the magnetic field profile and the required Zeeman slower length.

The required detuning to provide the desired acceleration can be calculated from the equation for ϵ:

$$\epsilon = \frac{a}{a_{\max}} = \frac{\gamma^2(s+1)}{4\Delta_\epsilon^2 + \gamma^2(s+1)} \tag{3.10}$$

Rearranging gives us:

$$\Delta_\epsilon = \frac{\gamma}{2}\sqrt{\frac{(s+1)(1-\epsilon)}{\epsilon}} \tag{3.11}$$

Slowing beam detuning: Above we have all the equations necessary for designing our Zeeman slower. It is usual to apply a bias field to the magnetic field profile calculated in equation 3.7, as we see in figure 3.10, in order to minimise the magnitude of magnetic field required, and the resulting field sits approximately centred around $B = 0$. It is important to note here that we can only do this for slowing of atoms whose ground state energy levels are near-degenerate in zero magnetic field. For example, this will not work for lithium, because the ground state structure means some atoms get lost in a dark state at the zero-field crossing point.

The total slowing beam detuning required for the Zeeman slower is a contribution of: that required to compensate for the applied bias magnetic field = $\Delta_{B\text{bais}}$; that required to achieve the final velocity = Δ_D; and that given in equation 3.11 to achieve the required deceleration parameter ϵ.

$$\begin{aligned} \Delta_{tot} &= \Delta_{B\text{bais}} - \Delta_D - \Delta_\epsilon \\ &= \frac{g_J m_J \mu_B B_{\text{bais}}}{h} - \frac{\nu_0 v_f}{c} - \frac{\gamma}{2}\sqrt{\frac{(s+1)(1-\epsilon)}{\epsilon}} \end{aligned} \tag{3.12}$$

The magnetic fields for Zeeman slowing are usually produced by carefully designed tapered solenoids. In our experiment we are testing a range of Zeeman slowers based on arrays of permanent-magnetic dipoles. Details of different Zeeman slowers we have designed and used are given in section 3.3.2 along with experimental results. A more detailed theory behind the design of our permanent-magnet Zeeman slowers is given in the publications by Y.B. Ovchinnikov [92; 93; 94].

3.2.1.1 Slowing different isotopes of Sr

We wish to make a strontium optical frequency standard using firstly ^{88}Sr, and then with the lower abundance ^{87}Sr. It is therefore imperative that the Zeeman slower facilitates the slowing of both isotopes equally well. Here we cover the physics necessary for calculating the Zeeman shifts of each isotope to confirm equivalent slowing is theoretically achievable. We also experimentally confirm this in section 3.3.3.1.

The bosonic isotopes of strontium have a zero nuclear spin and hence have a single ground state, $5s^2\,{}^1\mathrm{S}_0$, and an excited state, $5s5p\,{}^1\mathrm{P}_1$ that can be split into three distinct energy levels, $m_J = -1, 0, +1$ by application of a magnetic field. The magnitude of the splitting is set by m_J and B in equation 3.6. We cool using cycling of the excitation and decay between the ground state and the $m_J = -1$ excited state, which has a Landé g-factor of 1 (from equation 3.13, where $g_S \simeq 2$ and $g_L = 1$), giving a frequency shift of $\Delta\nu = -1.4\,\mathrm{MHz/Gauss}$. (1 Gauss = 10^{-4} Tesla).

$$g_J = g_L \frac{J(J+1) - S(S+1) + L(L+1)}{2J(J+1)} + g_S \frac{J(J+1) + S(S+1) - L(L+1)}{2J(J+1)} \tag{3.13}$$

Slowing and cooling the fermionic isotope, ^{87}Sr, is more complicated because the nuclear spin, $I = 9/2$, adds extra detail to the electronic energy level structure. In zero magnetic field the ground state has angular momentum $F = 9/2$, resulting in 9 degenerate sub-levels with $m_F = -9/2$ to $+9/2$. The excited state has three separate hyperfine states with angular momentum $F = 7/2, 9/2$ and $11/2$, which each have degenerate sub-levels $m_F = -F$ to $+F$ in zero magnetic field. For slowing and cooling we use the F to $F+1$ transition from the $F = 9/2$ ground state to the $F = 11/2, m_F = -11/2$ excited state. The Landé g-factors

for the ground and excited state are given by:

$$g_F = g_J \frac{F(F+1) - I(I+1) + J(J+1)}{2F(F+1)} + g_I \frac{F(F+1) + I(I+1) - J(J+1)}{2F(F+1)} \tag{3.14}$$

where [95]:

$$g_I = \frac{\mu_N}{\mu_B} \frac{\hbar}{\langle \mathbf{I} \rangle} (-1.0924)(1 - \sigma_d) \tag{3.15}$$

$$g_I = \frac{m_e}{m_p} \frac{1}{|I|} (-1.0924)(1 - 0.00345) \tag{3.16}$$

μ_N is the nuclear magneton, m_p is the proton mass, σ_d is the diamagnetic correction [95], $\langle \mathbf{I} \rangle$ is the expectation value of the nuclear spin vector operator, and $|I| = 9/2$ is the nuclear spin. For the ground state the Zeeman splitting is very small, giving a maximum separation of only $\sim 1.66\,\mathrm{kHz/G}$, well within the 30.2 MHz natural transition linewidth for the magnetic field range used, meaning we can treat the ground state as degenerate. For the excited state, equation 3.14 gives $g_F \simeq 11/2$, which gives a $g_F m_F$ product equal to -1, the same as for the bosonic isotopes, meaning that we can use the same magnetic field profile for Zeeman slowing the fermionic and bosonic isotopes.

3.2.2 Magneto-Optical Trapping

Once we have slowed our strontium atoms down to $\sim 30\,\mathrm{m/s}$ we wish to trap and cool them; for this we use a magneto-optical trap (MOT). A MOT consists of six laser beams in three orthogonal directions paired with their counter-propagating partners, centred on a quadrupole magnetic field, which has zero-field at the trap centre. This technique was first demonstrated by Raab et al. in 1987 [96]. The laser beams are all detuned an equal amount, approximately $\Delta_{MOT} \simeq -1.3\gamma$, and the polarisations are chosen such that the scatting force always acts towards

trap centre. We explain the operation of the MOT with the aid of figure 3.6, where the energy levels given are for trapping of the bosonic isotopes. In this one-dimensional picture we can see that an atom sitting to the right of trap centre experiences a positive magnetic field, which shifts the energy levels of the excited state, and the frequency required for excitation, by the amount given in equation 3.6. The $m_J = +1$ state is pushed further away from resonance and the $m_J = -1$ state is pulled onto resonance with the laser beam. In order to excite the atom, selection rules dictate that σ^- polarisation light is required, which is provided by laser beam 2. If we look at atoms sitting to the left of trap centre, the reverse is true, they experience a negative magnetic field, so the $m_J = +1$ state is pulled into resonance and the light polarisation required to excite is σ^+, which is provided by laser beam 1. At each location the laser beam that would push the atoms further from trap centre is off resonance from one $m_J = \pm 1$ state and has the wrong polarisation to excite the other, so the atoms remain trapped. The trapping force is given by $F_{\text{scatt}} = ma_{\text{scatt}}$:

$$\vec{F}_{\text{scatt}} = \frac{1}{2}\hbar\vec{k_+}\Gamma\frac{\gamma^2 s}{4\Delta_+^2 + \gamma^2(s+1)} + \frac{1}{2}\hbar\vec{k_-}\Gamma\frac{\gamma^2 s}{4\Delta_-^2 + \gamma^2(s+1)} \tag{3.17}$$

where the effective detunings Δ_+ and Δ_- are given by $\Delta_{\text{MOT}} + \Delta_D + \Delta_B$:

$$\Delta_+ = \Delta_{\text{MOT}} - v/\lambda + \mu' B/h \tag{3.18}$$

$$\Delta_- = \Delta_{\text{MOT}} + v/\lambda - \mu' B/h \tag{3.19}$$

where $\mu' = g_J m_J \mu_B$.

The magnetic field is usually provided by a pair of coils in the anti-Helmholtz configuration, which provide a near linear magnetic field close to the trap centre, such that $B \simeq z\, dB/dz$. The condition for anti-Helmholtz arrangement is that

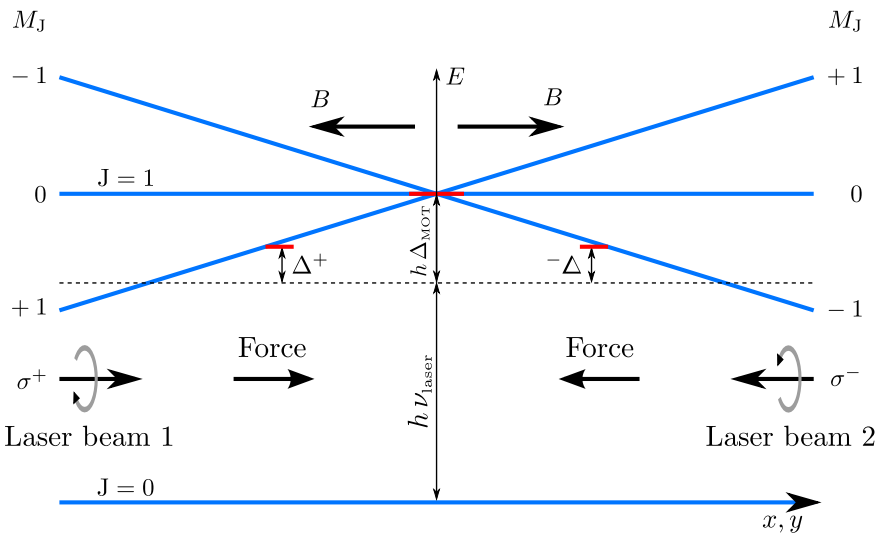

Figure 3.6: **Magneto-optical trap mechanism** - 1D diagram of MOT mechanism for $J = 0 \rightarrow J = 1$ transition, such as in bosonic ^{88}Sr. Section 3.2.1.1 explains how it can also apply for the fermionic isotope of ^{87}Sr. Figure adapted from [55].

the identical coils are separated by a distance equal to the coil radius and with the currents travelling in opposite directions. The Biot-Savart law can be used to calculate the magnetic field along the z-axis of the coil pair:

$$B_z = \frac{\mu_0 N_I I R^2}{2\left(R^2 + (z + R/2)^2\right)^{3/2}} - \frac{\mu_0 N_I I R^2}{2\left(R^2 + (z - R/2)^2\right)^{3/2}} \tag{3.20}$$

where $\mu_0 = 4\pi \times 10^7$ is the permeability of free space, N_I is the number of turns of wire on a coil, I is the current through the wire, and R is the coil radius. The origin of the z-axis is centred axially and radially between the pair of coils. The shape of the magnetic field along the z-axis of such a coil pair is shown in figure 3.7. The magnetic field along the radial axis can be shown to have the same profile, but half the magnitude by Maxwell's equation $\nabla \cdot B = 0$; giving $\frac{\partial B_x}{\partial x} = \frac{\partial B_y}{\partial y} = -\frac{1}{2}\frac{\partial B_z}{\partial z}$.

We intend to load the slow atom peak ($v_f \simeq 30\,\mathrm{m/s}$) exiting our Zeeman slower into our MOT, so we need to know the maximum velocity of atoms which the

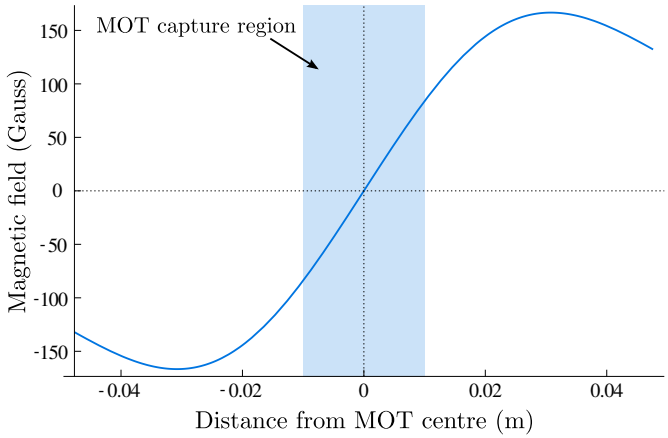

Figure 3.7: **Anti-Helmholtz coil pair magnetic field** - The MOT capture region is set by the laser beam size; it contains a near-linear magnetic field.

MOT can capture; the MOT capture velocity v_c. Assuming our MOT magnetic field has a gradient which can efficiently slow atoms (similar to choosing a suitable field gradient and ϵ parameter for the Zeeman slower as described in section 3.2.1), we can use equation 3.8 with L_0 replaced by the dimension of the capture region, approximately the diameter of the MOT laser beams $= 2r_c$, to estimate the MOT capture velocity:

$$v_c = 2\sqrt{a_{scatt} r_c} \tag{3.21}$$

See figure 3.7. Since we are looking for fast, efficient loading of our MOT we should design our Zeeman slower to have a slow atom peak that falls within the capture velocity of the MOT. This is easily fine-tuned by varying the detuning of the slowing beam, as we will see in section 3.3.2.

3.3 First-stage cooling (461 nm)

The $5s^2\,{}^1\mathrm{S}_0 - 5s5p\,{}^1\mathrm{P}_1$ first-stage cooling transition of strontium, at 461 nm, is particularly suitable for cooling due to a number of attractive features. The broad transition linewidth of $\gamma = 30.2$ MHz (transition decay time of $\tau = 5.3$ ns)

allows for rapid transition cycling, and hence cooling. The ground state has the advantage of having no electronic angular momentum in the even isotopes and only a small hyperfine splitting in the odd isotope, which is well within the transition natural linewidth for the range of magnetic fields used. This means that, unlike the alkali-atoms, there is no loss of atoms due to optical pumping within this transition, and so repump lasers are not required at 461 nm. The transition is almost closed for repeat cycling, with only ~ 1 in 50 000 atoms lost via decay to the $5s4d\,^1\mathrm{D}_2$ state, of which $\sim 2/3$ of the atoms decay to the $5s5p\,^3\mathrm{P}_1$ state and back to the ground state within 21 µs. The remaining $\sim 1/3$ are shelved in the metastable $5s5p\,^3\mathrm{P}_2$ state, which has a lifetime of around 17 minutes [97]. Due to the lack of significant ground state structure and the small loss of atoms via the $5s4d\,^1\mathrm{D}_2$ state, it is possible to slow and cool atomic strontium without the use of repumping lasers. However, we will see in section 3.3.1 that the addition of repump lasers to return the atoms shelved in the $5s5p\,^3\mathrm{P}_2$ state to the ground state can significantly increase the number of atoms trapped in the magneto-optical trap (MOT).

The laser light for driving the 461 nm transition is provided by a commercial extended cavity diode laser (ECDL), tapered amplifier and frequency-doubler system. Our Toptica DL100-TA-SHG regularly provides ~ 300 mW of power, with the only maintenance being occasional tweaking of the beam alignment within the laser system. The laser benefits from feed-forward electronics between the piezo voltage and the diode current, providing a wide mode-hop-free tuning range. The principal negative aspects of this laser system are the spatial beam quality that results from the frequency doubling process and the beam pointing instability, which is thought to be due to thermal lensing effects within the frequency doubling crystal. Both of these effects previously caused problems in our experiment, but

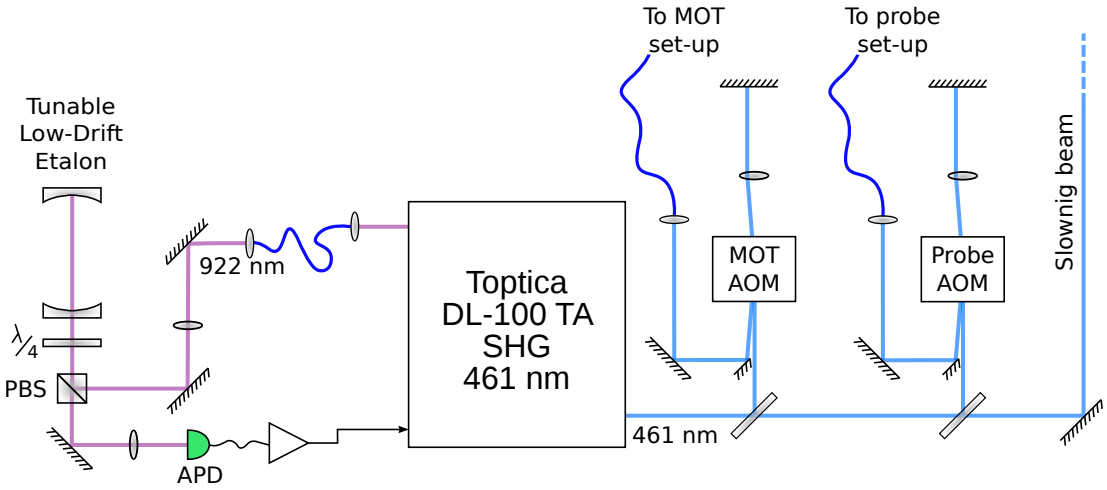

Figure 3.8: **Optical set-up for first-stage cooling** - The 922 nm lasing frequency is locked to the tunable reference cavity, which is set to give a slowing beam detuning of -490 MHz. The probe beam AOM is double passed at a frequency of $+245$ MHz to give an on-resonance probe beam. The probe light is sent to a portable (Thorlabs C1506/M, 72 mm x 72 mm) intensity and polarisation stabilisation platform containing polarisation optics and a pick-off to a photodiode feeding a servo-loop to the AOM RF drive power. The MOT beam AOM is double passed at a frequency of $+225$ MHz to give MOT beams at -40 MHz detuning from resonance. The MOT light is sent, via optical fibre, to a raised optical table where it is intensity stabilised, with a similar scheme to the probe beam, and then split into its three beams for the MOT.

have now been resolved to a satisfactory level through the use of additional lenses for beam shaping and optical fibres to couple the light from the laser to the experiment.

The 922 nm light from the ECDL is frequency-stabilised to a low finesse ($\mathcal{F} = 450$) tunable optical reference cavity, of the Stephen Webster / NPL design, using the Pound-Drever-Hall (PDH) technique [98]. The cavity is in a temperature-stabilised vacuum chamber and is not locked to the atomic transition. However, this could be implemented at a later date using a 461 nm absorption or fluorescence signal from the spectroscopy cell discussed at the end of section 3.1.1. In the mean time this cavity arrangement has demonstrated a satisfactorily low drift rate of a few MHz/day.

The decay rate of the 461 nm transition is $\Gamma = 190 \times 10^6\,\mathrm{s}^{-1}$, giving a saturation intensity of $40.38\,\mathrm{mW/cm^2}$ and a Doppler cooling limit of 730 μK. We use 70 mW of light at a detuning of around -490 MHz to 'Zeeman slow' our atoms from ~ 420 m/s to ~ 30 m/s, i.e. to within the capture velocity of our MOT. For the MOT we use 3×3.5 mW retro-reflected beams at a detuning of -40 MHz. We also have a low power, intensity-stabilised, resonant probe beam for finding the resonance frequency and characterising the atomic beam. The optical set-up for achieving the necessary frequency detunings is shown in figure 3.8.

3.3.1 Repump lasers (679 nm and 707 nm)

As explained in sections 2.1 and 3.3 atoms are shelved in the $5s5p\,^3\mathrm{P}_2$ metastable state during cooling and trapping with the 461 nm light. The shelved atoms need to be repumped to allow them to return to the ground state and be available for further cooling. Repump laser(s) can be used during the MOT loading to enhance trapped atom number and density. There are a number of repump schemes in use in different cold strontium experiments and it was part of the work of this project to decide which repump scheme we should adopt:

1. **497 nm** transition from $5s5p\,^3\mathrm{P}_2$ to $5s5d\,^3\mathrm{D}_2$. This transition has a natural linewidth of $\gamma = 2$ MHz and decays to the $^3\mathrm{P}_2$ and $^3\mathrm{P}_1$ states with lifetimes of $\tau = 78.1$ ns and 20.8 ns respectively. This repump transition is used by Poli et al. [99]. They use a frequency-doubled diode laser to provide 4 mW of power at 497 nm.

2. **3012 nm** transition from $5s5p\,^3\mathrm{P}_2$ to $5s4d\,^3\mathrm{D}_2$. This transition has a natural linewidth of $\gamma = 12.6$ kHz and decays to the $^3\mathrm{P}_2$ and $^3\mathrm{P}_1$ states with lifetimes of $\tau = 12.7$ μs and 3 μs respectively. This repump transition is used by

Mickelson et al. [100]. They use a $\lambda = 1060\,\text{nm}$ fibre laser to seed a laser based on optical parametric oscillation; this provides 4 mW of power at 3012 nm.

3. **707 nm and 679 nm** transitions from $5s5p\,^3\text{P}_2$ to $5s4d\,^3\text{S}_1$ and $5s5p\,^3\text{P}_0$ to $5s4d\,^3\text{S}_1$, respectively. Due to the excited state angular momentum of $\text{J} = 1$, the excited atoms can decay back to all three of the $5s5p$ triplet states, which means a second laser is required at 679 nm to repump the atoms that become shelved in the $^3\text{P}_0$ state. The natural linewidths of the 707 nm and 679 nm transitions are $\gamma = 6.7\,\text{MHz}$ and $\gamma = 1.4\,\text{MHz}$, respectively. The excited state decays to the $^3\text{P}_2$, $^3\text{P}_1$ and $^3\text{P}_0$ states with lifetimes of $\tau = 25.2\,\text{ns}$, 38.6 ns and 111.5 ns, respectively. This repump scheme is used in a number of laboratories [34; 101; 102; 103]. A few milliwatts of laser light at each frequency is usually provided by ECDLs.

The repump scheme chosen for our experiment is option 3; using the 707 nm and 679 nm transitions. Despite the marginally faster repumping provided by the 497 nm transition (option 1) and the added complexity of requiring a second laser for repumping, this two-laser scheme is desirable for our experiment because we require a clock-state repump laser (679 nm or other) later on in the clock cycle; i.e. so we need to build a second laser anyway. Furthermore, red wavelength ECDLs are easier to build and maintain than a frequency-doubled diode system. The laser light for these two wavelengths is provided by two home-built ECDLs with home-built drive electronics. The laser diodes are anti-reflection coated and wavelength selected 685 nm and 705 nm central lasing wavelength diodes. These were purchased from Toptica and Laser 2000. Each ECDL produces $> 5\,\text{mW}$ of light, and these beams are combined into a 633 nm optical fibre; this delivers $\sim 1\,\text{mW}$ of each to the 461 nm MOT. The frequency of the 707 nm laser is

stabilised to a HighFinesse WSU-10 wavemeter, which has a short-term stability of ~ 1 MHz when calibrated, via Labview feedback control to the ECDL diffraction grating piezo. The wavemeter tends to drift from its calibration by around 10 MHz during a working day, so we usually recalibrate at least once a day. Given the narrower natural linewidth of the 679 nm transition, this method would not be ideal for frequency stabilisation of this laser, so we lock it to a resonant mode of a mid-to-low finesse optical reference cavity using the Pound-Drever-Hall (PDH) technique. We use the same tunable optical cavity as is used for stabilising the frequency of the 922 nm laser used to produce the 461 nm light; this way the cavity can later be referenced to the 461 nm fluorescence. We use a combination of dichroic optics and different modulation frequencies to isolate the PDH locks from one another, see section 4.2.1.

3.3.2 Permanent-magnet Zeeman slowers

Usually Zeeman slowers consist of a carefully designed tapered solenoid to produce the magnetic field required for Zeeman slowing. They typically use a few Amps of electric current to produce the desired magnetic field and often require water-cooling. Following the brief theory behind Zeeman slowing given in section 3.2.1 and the more detailed theory of reference [92], our team has designed, built, and characterised a number of permanent-magnet Zeeman slowers. The main advantage of using permanent-magnets to create the magnetic field instead of the more traditional tapered solenoid approach is that no power source or water cooling are necessary. The magnetic field produced by tapered solenoid Zeeman slowers is orientated longitudinally to the direction of travel of the atomic beam. We have permanent-magnet Zeeman slowers with magnetic fields orientated either transversely or longitudinally to the direction of the

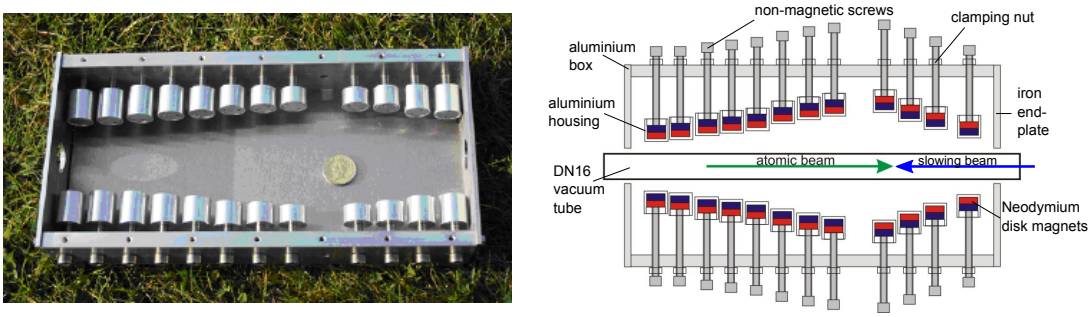

Figure 3.9: **Transverse-field permanent-magnet Zeeman slower** - Photograph of the 'standard' version (with no extension piece) of our light-weight Zeeman slower, and a schematic giving details of the design.

atomic beam. The permanent-magnet Zeeman slowers with the transverse magnetic field can be very simple in design (an example of which is shown in figure 3.9), and extremely light-weight ($< 2\,\mathrm{kg}$), significantly lighter than $\gtrsim 10\,\mathrm{kg}$ typical of a tapered solenoid with its power supply and cooling equipment. Such permanent-magnet slowers may be particularly suitable for future neutral atom optical clocks in space [104; 105; 106]. The transverse field slowers require twice the slowing laser beam power of the equivalent longitudinal field slowers. This is because the optical polarisation must be orthogonal to the magnetic field in order to drive the electron into the excited state, but we still need the correct orientation of circularly polarised light to excite from the $m_J = 0$ ground state to the $m_J = -1$ excited state. In order to meet these requirements twice the laser power with a linear polarisation (superposition of half σ^+ and half σ^-) orthogonal to the magnetic field orientation is used. Our experimental parameters require this to be $\sim 70\,\mathrm{mW}$.

Transverse-field permanent-magnet Zeeman slowers have further advantages over their longitudinal-field counterparts. Firstly, their simple design facilitates quick and easy fine-tuning of the magnetic field profile for optimum slowing. This can be completed either in situ or by simply removing it from the system as we

do. We use a travelling Hall probe to measure the magnetic field and tune the magnet positions accordingly. This method allows us to match the magnetic field almost perfectly to the desired profile (see figure 3.10) in a short amount of time. Secondly, the orientation of the magnetic dipoles in the transverse-field slowers results in rapid decay of the magnetic field magnitude following the end of the Zeeman slower. This negates the need for a compensation coil before the MOT, as is typically necessary to prevent the longitudinal-field slowers distorting the MOT magnetic field. The magnetic field profile shown in figure 3.10 is typical of the transverse-field Zeeman slowers, this shows the magnetic field decaying to approximately zero in $< 5\,\mathrm{cm}$ from the end of the Zeeman slower. Finally, due to the essentially 2-D nature of the magnet arrangement for the transverse-field Zeeman slower, the appropriate vacuum apparatus could facilitate transverse cooling of the atomic beam along the length of the slower. This would reduce the atomic losses due to atomic beam expansion from the transverse velocity contribution, and would result in a higher number of atoms captured in the MOT.

The design of the transverse-field Zeeman slower used for our initial characterisation is described in [93]. It is designed to slow strontium atoms from $\sim 412\,\mathrm{m/s}$ to $\sim 25\,\mathrm{m/s}$ over a length of 25 cm with a 70 mW convergent laser beam at 461 nm and an epsilon parameter value of 0.6. The convergent laser beam means that the laser intensity, and hence the acceleration are dependent on z, the position within the slower. This can be incorporated into equation 3.9 and those that follow. The resulting magnetic field has a magnitude ranging over $\sim 600\,\mathrm{G}$ along its 25 cm length, so a bias field of $\sim 300\,\mathrm{G}$ is added so that it spans from around $-300\,\mathrm{G}$ to $+300\,\mathrm{G}$. For this Zeeman slower a total slowing beam detuning of $\Delta_{tot} = -490\,\mathrm{MHz}$ is expected to give an exit velocity of $\sim 25\,\mathrm{m/s}$. The detuning

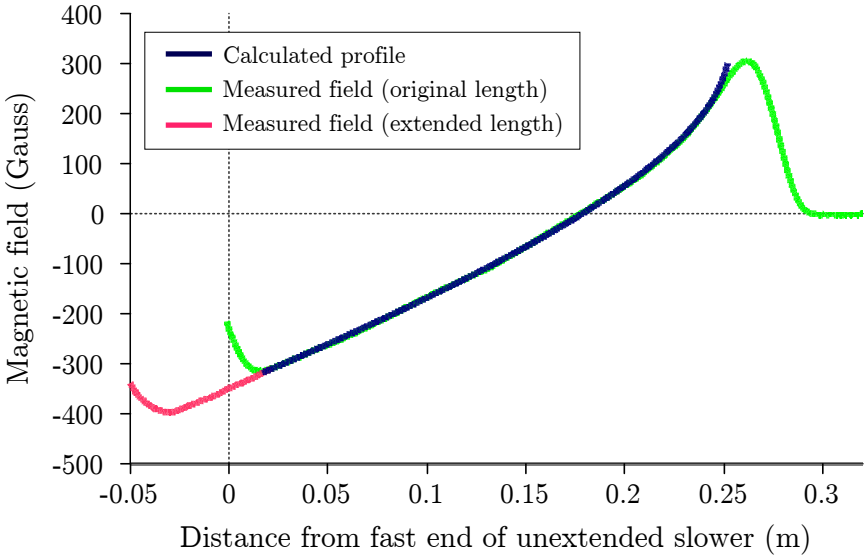

Figure 3.10: **Magnetic profile of transverse-field Zeeman slower** - Blue line is the ideal magnetic field profile from theoretical calculations. The green line is the measured magnetic field for the transverse-field Zeeman slower shown in figure 3.9. The red line is the measured magnetic field for the transverse-field with its 'fast' extension piece added. As we can see, the measured fields match the ideal field very well.

contributions are $\Delta_{B\text{bais}} = -419\,\text{MHz}$, $\Delta_D = -54\,\text{MHz}$, and $\Delta_\epsilon = -17\,\text{MHz}$.

We have the option to extend the length of this 'standard' transverse-field Zeeman slower with an extension piece added to the 'fast' end of the slower (see figure 3.10). This extends the length to 28 cm and capture velocity to $\sim 480\,\text{m/s}$, allowing us to increase the slow atomic flux by $\sim 30\,\%$ - experimentally confirmed by relative atom numbers in a magneto-optical trap. We have also designed [94], built, and tested a longitudinal-field permanent-magnet Zeeman slower for strontium. This has a length of $\sim 20\,\text{cm}$, with a magnetic field ranging from $-300\,\text{G}$ to $+300\,\text{G}$, and an epsilon parameter value of 0.6. We still use a 70 mW slowing beam, this time of circular (σ^-) polarisation. This configuration of magnetic field and polarisation orientation means that the whole of the available power is utilised (compared to only half in the transverse slowers).

The Zeeman slowers' magnetic fields are tuned by hand using a calibrated Hall probe on a linear actuator until the magnetic field matches the desired profile, see figure 3.10. The tunability of the transverse-field permanent-magnet Zeeman slowers mean that we are able to experiment with a range of field gradients (epsilon parameters) and bias fields. We are able to measure the resulting longitudinal atomic velocity distributions and MOT loading properties over a wide range of parameters.

3.3.2.1 Longitudinal Atomic Velocity Distributions

We wish to measure the longitudinal velocity distribution of the atomic beam to begin characterising the Zeeman slowers. In order to measure the distribution with and without Zeeman slowing we recorded the atomic fluorescence while scanning a resonant probe laser beam. In order to measure a significant portion of the thermal velocity distribution, the probe beam needs to be scanned by around 2 GHz while keeping the slowing beam at a fixed detuning from the atomic resonance. In the first instance we tried to use an EOM (electro-optic modulator) to scan a sideband over the required frequency range, but the EOM crystal soon became cloudy, thought to be due to photo-degradation of the crystal, and the resulting beam quality became very poor. Our second and successful approach was to borrow the 461 nm laser light from a neighbouring laboratory, with thanks to A. Sinclair and G. Wilpers. This laser system is a home-built ECDL and frequency-doubler. The light was coupled into an optical fibre, the output power of which was around 200 μW and was intensity stabilised by feeding back to the drive power of an AOM. The laser frequency was scanned using the piezo on the diffraction grating of the ECDL. In our laboratory the laser was aligned through the atomic beam in the 'experiment chambers' of our vacuum

apparatus, as shown in figure 3.11, at an angle of: (a) 90° to the atomic beam for finding the centre of the resonance feature, or (b) 55° for measuring the velocity distribution. The exiting laser beam was: (a) co-aligned with a portion of the slowing laser beam to check the beat frequency (frequency difference) between the resonant probe beam and the slowing beam, or (b) aligned into a scanning optical cavity for frequency calibration of the scan. The linear polarisation of the probe laser beam was set 90° to that of the slowing laser beam to increase the signal-to-noise ratio at the detector. The fluorescence signal was detected on a large area photodiode and high gain transimpedance amplifier, with a further offset and amplifier circuit, or by using a CCD camera. To begin with, fluctuating scatter from the 70 mW slowing beam swamped the fluorescence signal from the $< 200\,\mu$W probe beam. This problem was caused by pointing instability of the 461 nm Toptica system and was solved by coupling the slowing light through an optical fibre and intensity stabilising the output by modulating the drive power of an AOM (acousto-optic modulator) before the fibre input. The full optical set-up is shown in figure 3.11.

An example longitudinal velocity distribution is shown in figure 3.12; the y-axis is a direct measure of the fluorescence in the detection region. As previously explained in section 3.1.2, the nature of the detection under-represents the higher velocity atoms, and to gain an atomic flux from this we would need to multiply through by the atomic velocity. We have left the data in this form for clarity of the features. As we can see from the graph, we have a slow atom peak at around 30 m/s and the residual Maxwell-Boltzmann distribution above ~ 300 m/s. There is also a second mid-to-slow atom peak at ~ 120 m/s; the possible origins of this are discussed below. We took a number of such velocity distributions for a range of slowing beam powers and detunings, and experimented with a few different

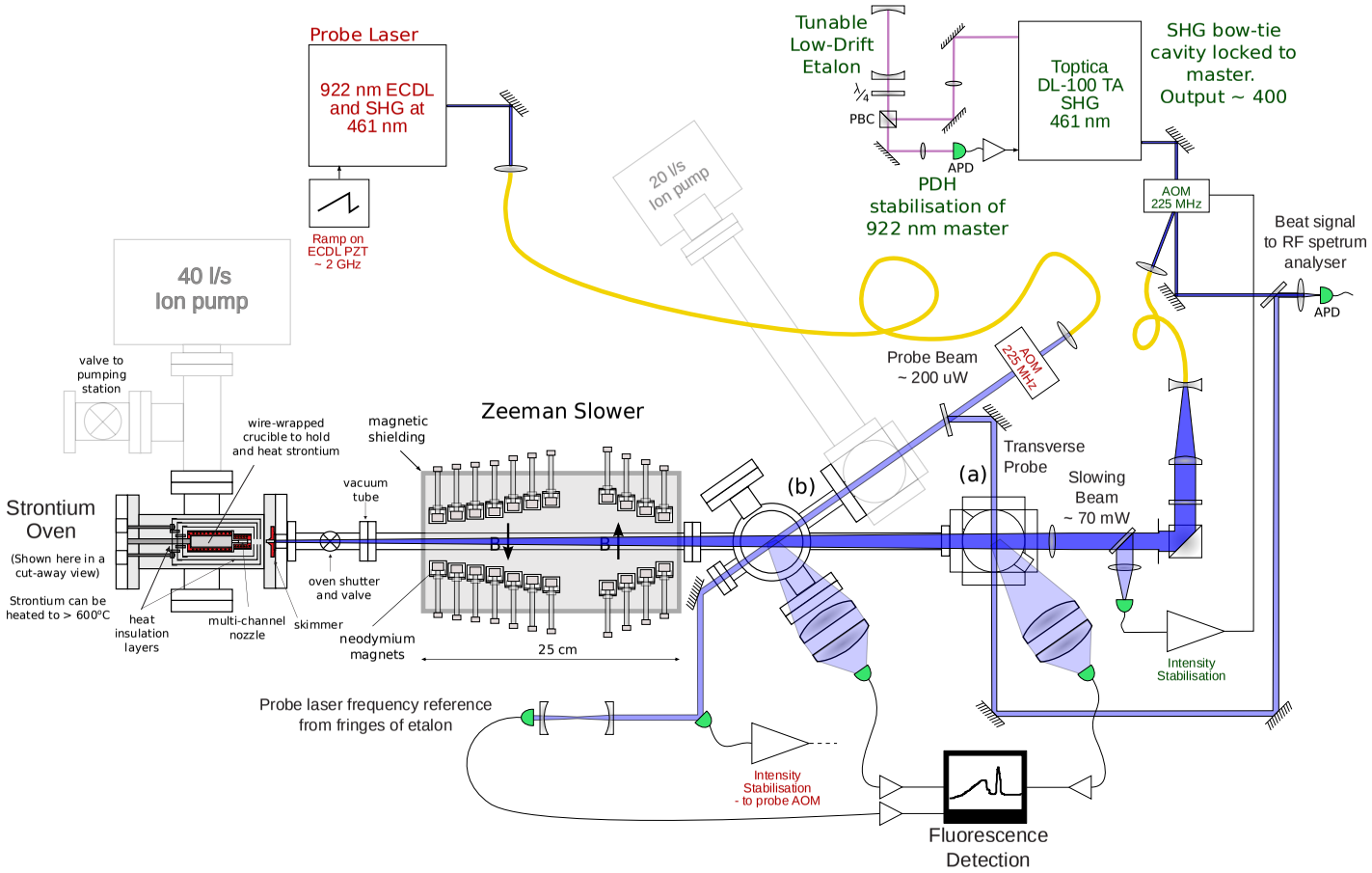

Figure 3.11: **Optical set-up for measuring longitudinal velocity distributions** - Velocity distributions of atoms exiting the Zeeman slower are measured using the above set-up. The intensity stabilised slowing beam is provided by our 461 nm Toptica laser locked to the resonant mode of our low-drift tunable etalon. The probe light for measuring the distribution is provided by a laser on loan from a neighbouring laboratory, delivered by optical fibre. (Figure courtesy of I.R. Hill.)

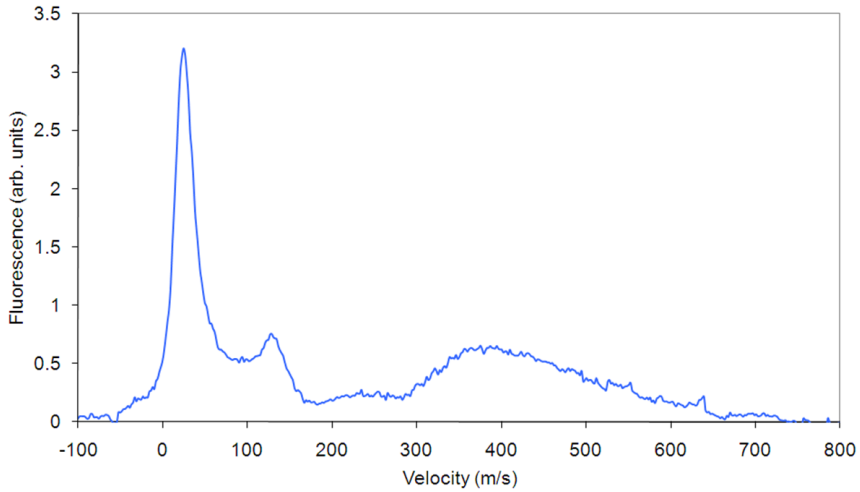

Figure 3.12: **Longitudinal velocity distribution of atoms exiting Zeeman slower** - Example distribution recorded by scanning a resonant probe beam at an angle of 55° from the direction of the atomic beam ((b) in figure 3.11). Fluorescence signal detected on a CCD camera. Atomic flux can be obtained by multiplying the distribution through by the velocity v.

magnetic field gradients (ϵ parameters), as well as a prototype longitudinal-field permanent-magnet Zeeman slower. The majority of the data we discuss here are from the longitudinal velocity distributions for the original transverse-field Zeeman slower.

Since ^{88}Sr is the most abundant isotope ($\sim 83\,\%$, see table 2.1) the slowing distributions are taken with the intention of efficiently slowing this isotope, however there will be some fluorescence from the other isotopes (the detunings of which are given in table 3.1). We also need to ensure that the Zeeman slower, with its bias field causing the low-field region around the zero-crossing, efficiently cools ^{87}Sr. This is successfully demonstrated with MOT atom numbers as discussed in section 3.3.3.1.

We would like to confirm that the Zeeman slower behaves as our theory predicts, and find the optimum operating parameters for Zeeman slowing strontium atoms for our experiment. Over the next few pages we discuss the results and

conclusions from two such experiments; we investigate the effects of the slowing laser beam detuning and power.

Slow atom velocity as a function of slowing beam detuning. The velocity of the slow atom peak as a function of slowing beam detuning is measured for detunings ranging from $-480\,\mathrm{MHz}$ to $-770\,\mathrm{MHz}$, the data for which are shown in figure 3.13. The exit field for this Zeeman slower was $\sim 245\,\mathrm{G}$, slightly smaller than the previously given value of 300 G. This means we would expect a slow atom peak of $\sim 25\,\mathrm{m/s}$ at a detuning of about $-415\,\mathrm{MHz}$. A very basic interpretation of the system, where the atoms are slowed only in the intended section of the Zeeman slower, and the detuning of the slowing beam affects only the velocity contribution Δ_D to the total detuning Δ_{tot} (equation 3.12), would lead us to expect the trend to be linear, with a gradient equal to the transition wavelength $\lambda \simeq 461\,\mathrm{nm}$, shown as trend line (a) in figure 3.13. We can see (in figure 3.13) that this naive approach does not fit the data, in fact we observe significantly greater slowing than first expected. In order to identify the source of this discrepancy we modelled the slowing process using a 3D Monte-Carlo simulation (work of I.R. Hill). The simulation showed that further deceleration of the atoms occurred in the 'extraction' of the atoms from the Zeeman slower. From the magnetic field profile shown in figure 3.10 we can see that beyond the end of the desired magnetic field profile, in what we call the "extraction region", the magnetic field is initially slow to change, then rapidly decays to zero. In the first part of the 'extraction', where the end field is maintained, we will expect to see some additional slowing from the resonant slowing-beam. This additional slowing contribution accounts for a reduction in velocity of $\sim 30\,\mathrm{m/s}$ beyond that expected from the naive model; this is shown by line (b) in figure 3.13. We can see this interpretation fits the data better, but still not fully; the data demonstrates a trend of higher gradient than

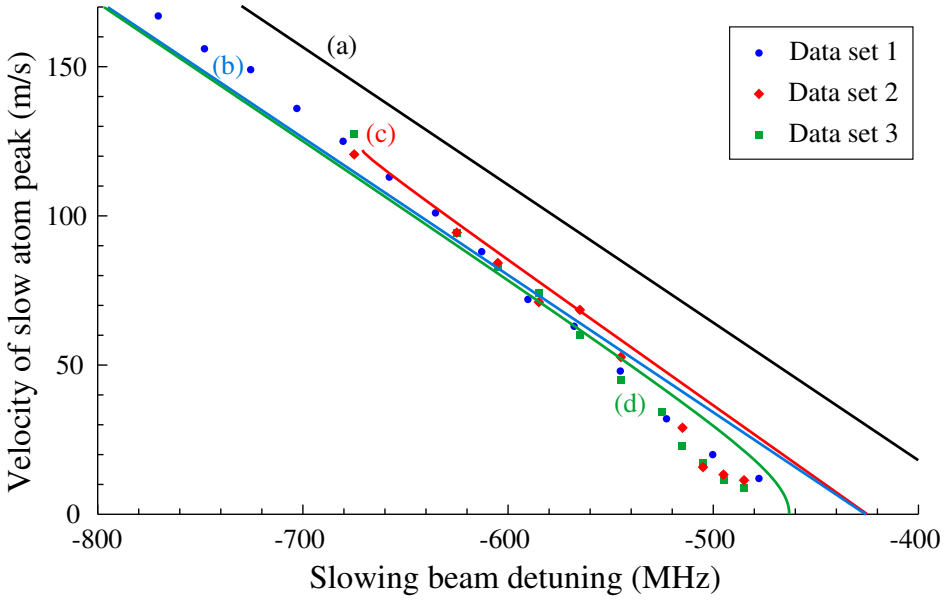

Figure 3.13: **Zeeman slower: slow atom velocity vs. slowing beam detuning** - A scanning resonant probe beam is used to measure longitudinal velocity distributions of atoms exiting the transverse-field permanent-magnet Zeeman slower for a range of slowing beam detunings. The velocity of the slow atom peak is measured and plotted here against the slowing beam detuning. Data sets 1 and 2 are for Zeeman slowers with an epsilon parameter of 0.6, whereas the Zeeman slower used for data set 3 has an epsilon parameter of 0.8. The fit curves (a - d) are described in the main text.

our basic model, and at slower velocities we see a still greater loss of velocity.

By changing the detuning of the slowing beam we are shifting the range of velocities we expect to capture: greater detunings slow a higher velocity class of atoms by an equal amount ($\delta v = v_0 - v_f$) along the length of the slower. This interpretation is incomplete. The atoms are slowed by the same amount δv in the same length L_0, but they are travelling faster, so the process is quicker and the acceleration needs to be greater in order to achieve this. Our model should take into account the associated shift in acceleration, and hence ϵ, that the change in detuning causes. This leads to an approximately linear trend with a steeper gradient, as shown by trend line (c) in figure 3.13. To account for the greater drop of velocity at lower velocities we look to the probe beam for an explanation. The

probe beam, although very low power, is resonant with the atoms, so provides an additional velocity-dependent deceleration. This contribution is modelled by substituting the appropriate parameters into equation 3.4, and is shown as curve (d) in figure 3.13.

Although our explanation does not go the full way to accounting for the observed trend of the velocity of the slow atom peak over the measured range of slowing beam detunings, our analysis has demonstrated our permanent-magnet Zeeman slowers offer efficient slowing of atomic strontium and has high-lighted the additional slowing due to the 'extraction' of the atoms from the slower. We have also demonstrated that a resonant probe beam is only partially suitable for measuring such velocity distributions, and since we are ultimately concerned with how many atoms, and at what rate, we can load into our MOT, we should use MOT loading data to optimise our Zeeman slower parameters.

Slow atom velocity and number as a function of slowing beam power. Longitudinal velocity distributions were taken for slowing beam powers ranging from 10 mW to 90 mW; the resulting velocity of the slow atom peak is shown in figure 3.14. We can see that increased slowing beam power decreases the velocity of the slow atom peak, it is not immediately obvious why this trend occurs. We can imagine that if we decrease the slowing beam power below optimum we will not scatter enough photons to provide the necessary force to decelerate the atoms sufficiently to stay in the slowing process, so we 'drop' atoms along the length of the Zeeman slower. This explains the reduction in atom number at lower powers we see in figure 3.15, and is evident when looking at the individual atomic velocity distributions. The change in the velocity of the slow atom peak is caused by a more subtle effect, which only became clear by studying the results of the Monte-Carlo simuation.

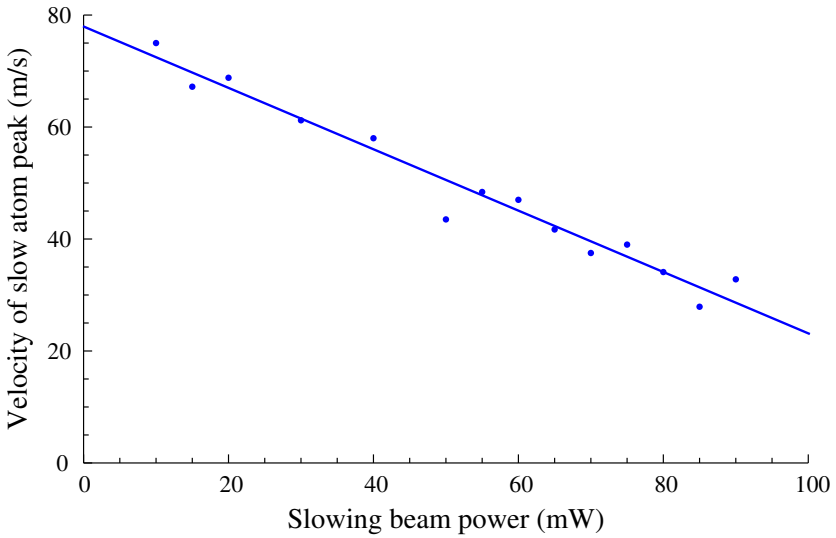

Figure 3.14: **Zeeman slower: slow atom velocity vs. slowing beam power** - Increasing the slowing beam power increases the amount of additional slowing we see in the 'extraction' of the atoms from the Zeeman slower, and hence decreases the final velocity v_f of the slow atom peak. The linear fit applied to this graph follows the form $v_f = AP + B$, where $A = -0.548\,\mathrm{m/s/mW}$ and $B = 77.92\,\mathrm{m/s}$ are the least-squared best fit parameters.

The magnetic field profile of the Zeeman slower defines the acceleration, a, which the atoms are to follow to remain resonant with the slowing beam, so a in equation 3.10 is fixed. By changing the slowing beam power we are altering the maximum acceleration $a_{\max}$ and hence ϵ (see equation 3.10) and Δ_ϵ in equation 3.11. This changes the balance of the various detuning contributions that make up Δ_{tot} in equation 3.12; when the slowing beam power increases, Δ_ϵ increases, so Δ_D decreases, resulting in a lower final velocity. We can easily calculate the change in velocity this effect will cause using the equations in section 3.2.1. We find, for example, that for slowing beam powers of 50 mW compared to 90 mW we expect a difference of $\sim 4\,\mathrm{m/s}$ at all points along the length of the slower, this agrees with the outcome of the Monte-Carlo simulation. However, the velocity distribution data in figure 3.14 shows a $\sim 20\,\mathrm{m/s}$ difference when comparing these two slowing beam powers. The Monte-Carlo simulation can go some way

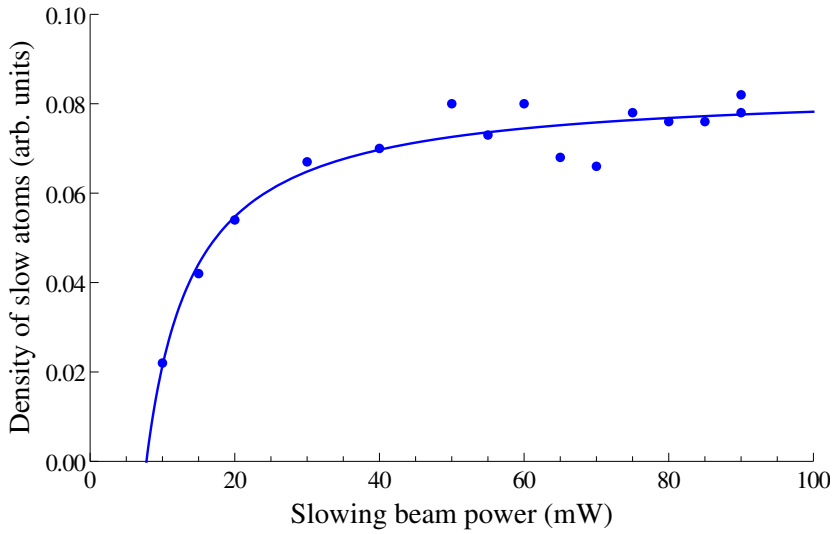

Figure 3.15: **Zeeman slower: slow atom density vs. slowing beam power** - Increasing slowing beam power results in a saturation of the density of slow atoms. The fit curve follows an equation $C\frac{D(P-E)}{D(P-E)+1}$, where C to E are fit parameters and P is the slowing beam power.

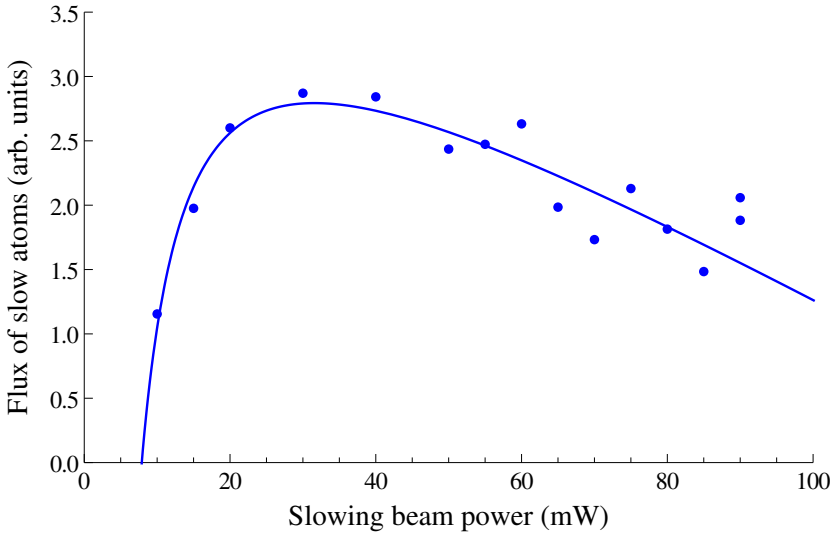

Figure 3.16: **Zeeman slower: slow atom flux vs. slowing beam power** - Increasing slowing beam power results in a saturation of the density and a decrease in velocity of slow atoms. The fit curve is that from figure 3.15 multiplied by the linear velocity dependence from figure 3.14: $C\frac{D(P-E)}{D(P-E)+1}(AP+B)$, where A to E are fit parameters and P is the slowing beam power.

to explain this discrepancy. As with the detuning dependencies discussed in the previous section, the effects of the 'extraction' of the atoms from the Zeeman slower are significant; in the first part of the 'extraction', where the end field is maintained for a short period, the higher laser beam powers offer more significant slowing. The simulation shows that in the first 1.5 cm beyond the end of the intended slowing region we see additional slowing; this results in a velocity difference of ~ 10 m/s for the 50 mW and 90 mW slowing beams, compared to the ~ 4 m/s difference observed along the whole length of the intended slowing region. The effect is still not large enough to agree with the data, but this can simply be explained by the 'extraction' region of the Zeeman slower being longer in reality than in the model. At high enough slowing beam powers we would expect to see some saturation of this effect, this is not seen in our data because we do not have enough power available, but we can see these effects in the results from the simulation.

We can also look at the measured number of slow atoms over the range of slowing beam powers, either in terms of density (fluorescence peak height), see figure 3.15, or flux (fluorescence $\times$ velocity peak height), see figure 3.16. In figure 3.15 we can see the slow atom density saturates, meaning that above ~ 50 mW adding more power does not slow many more atoms, but from figure 3.14 we can see that it continues to make them slower. Increasing the laser power continues to increase the acceleration over the full range of available powers, but below ~ 50 mW there is not enough power to maintain efficient slowing for the given magnetic field gradient, and atoms are dropped along the length of the slower. We have confirmed this effect by looking at the profiles of the individual velocity distributions.

Figure 3.16 shows the atomic flux passing through the detection region as a

function of slowing beam power, this is the atomic density (proportional to the detected fluorescence) multiplied by the atomic velocity. In figure 3.15 we see the density of slow atoms saturate, and as we continue to increase the power they slow further, resulting in fewer atoms per second passing through the detection region (i.e. a lower atomic flux). If we were to increase the power further we should see atoms being decelerated so much that they do not make it to the detection region, because they have zero or negative longitudinal velocity and travel back towards the atomic source.

This analysis is more qualitative than quantitative, but it has given us important information about our Zeeman slowing apparatus. As with the velocity vs. detuning data shown in figure 3.13, optimisation of the slowing beam power should be done by measuring the atom numbers and loading rates of the magneto-optical trap, since this is what we wish to optimise. Later data taken by other members of the group, measuring the MOT loading as a function of slowing beam power, showed saturation effects just starting to appear at the higher ($\sim 80\,\mathrm{mW}$) slowing beam powers. This is likely due to the compromise between the velocity of the atoms and the fall-off in atomic flux seen in figures 3.14 and 3.16.

Origin of the second peak: In all of our longitudinal atomic velocity distribution data, such as figure 3.12, we see a second peak of atoms at mid-to-low velocities. In trying to identify the origin of this unexpected peak we came up with a number of hypotheses to be tested. Initially we thought it could be the cooling of a second isotope, either ^{86}Sr or ^{87}Sr, but further analysis of the relative peak heights and the velocity difference between the two peaks at different detunings made this unlikely. The next step was to make sure we were not dropping atoms somewhere along the Zeeman slower, either due to a sharp change in magnetic field or at the point where the magnetic field crosses zero. We tested

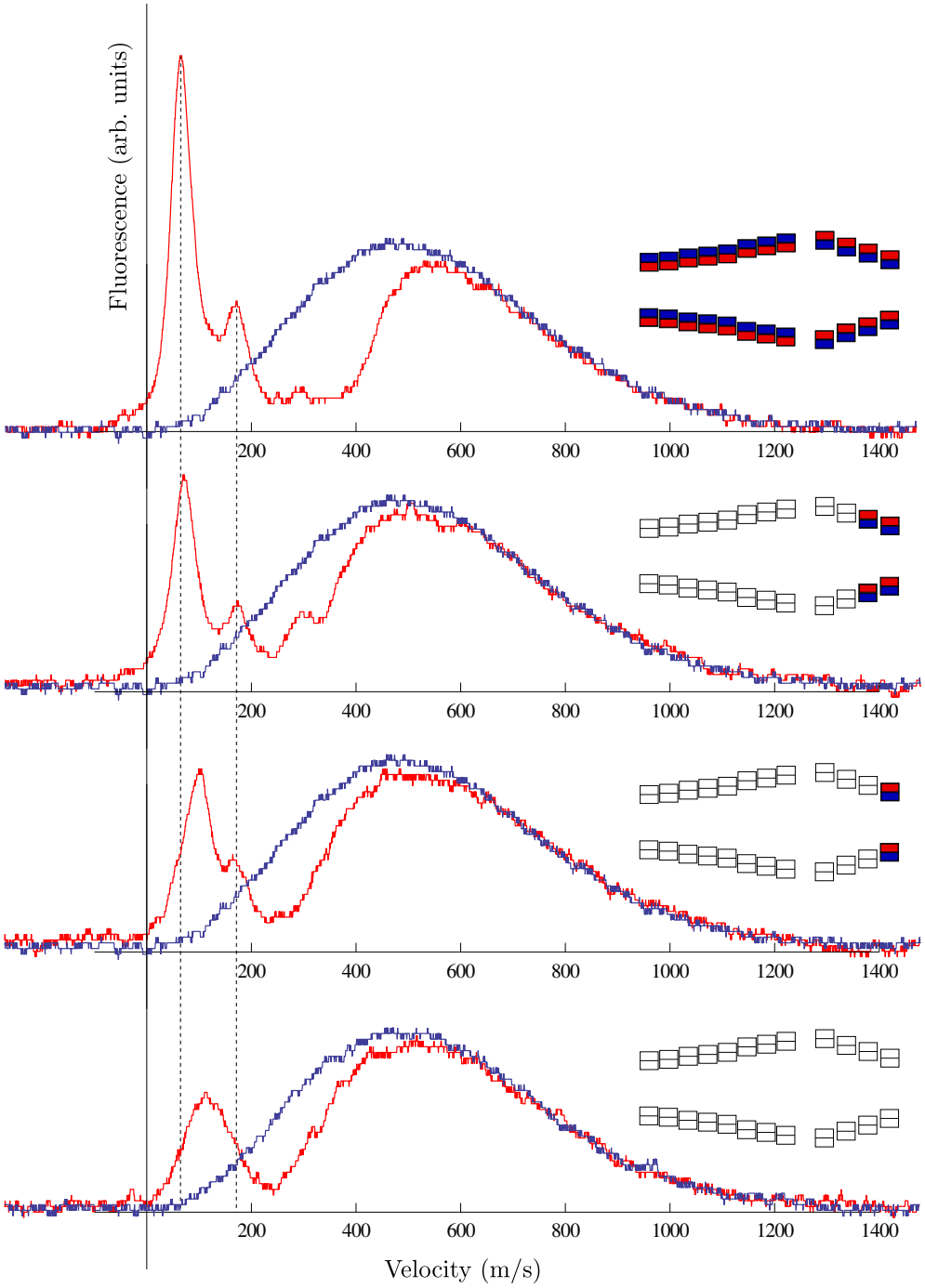

Figure 3.17: **Zeeman slower velocity distributions** - With varying numbers of magnets, as indicated by figures on the right-hand side. (Distributions taken in MOT chamber, location (b) in figure 3.11.) With only two magnets remaining we see the two slow-atom peaks merge into one at the velocity associated with slowing in zero magnetic field.

this by removing pairs of magnets in turn, starting at the fast end of the Zeeman slower. We observed two slow-atom peaks all the way up to and including a Zeeman slower containing only the last pair of magnets (at the slow end), where the peaks were starting to merge (see figure 3.17). After removal of the last two magnets the peaks merged together at the velocity associated with slowing in zero magnetic field. This tells us the origin of the second peak is due to slowing in zero magnetic field, either where the magnetic field profile crosses zero or after the Zeeman slower, an effect we call "post-cooling". This peak cannot be attributed to the driving of the $^1S_0$ to $^1P_1$ $m_J = 0$ transition, which is insensitive to first order Zeeman shifts, because the linear polarisation of the slowing beam is the wrong orientation to drive this transition (the light polarisation is orthogonal to the direction of the magnetic field). It is difficult to isolate the effects of the "zero-crossing" and "post-cooling", and it is possible that both are contributing. However, we believe the effect due to the zero-crossing to be small, or non-existent, because there do not seem to be any significant loss mechanisms that could cause it. The magnetic field axis is poorly defined in this zero-crossing region, and so there may be some excitation of the $m_J = 0$ and $m_J = +1$ states, but the rapid decay to the degenerate ground state means that these atoms are quickly picked back up by the cooling cycle and are not lost from the process. We conclude that the vast majority of the atoms in the second peak are from post-cooling effects unrelated to the efficiency of the Zeeman slowing, but we do not yet have solid proof of this.

Zeeman slower efficiency: In order to characterise how well the Zeeman slowers are working and to be able compare them with other Zeeman slowers, an estimate of the slower efficiency is required. To work out the maximum slowable atomic flux from our atomic beam we need to take into account the longitudi-

nal atomic velocity distribution and the losses from the cooling cycle due to the decay of atoms from the $5s5p\,^1\mathrm{P}_1$ state to the $5s4d\,^1\mathrm{D}_2$ state (transition 12 in figure 2.1), which has a branching ratio of approximately 1 in 50 000. We will also need to consider the capture velocity of the Zeeman slower and the initial velocity distribution of the atomic beam.

The total atomic beam flux, from the single-channel-nozzle oven and aperture configuration, is measured to be 10^{11} atoms/s by absorption imaging of a weak, resonant, transverse probe beam. The longitudinal velocity distribution of the atoms emerging from the oven is measured by fluorescence imaging of an angled, weak, scanning probe beam (see figures 3.4 and 3.11). This fluorescence profile represents the atomic density and can be converted into atomic flux by multiplying the profile through by the velocity (to take account of the reduced interaction time of the faster atoms with the probe beam); the integral under this whole profile is equal to the total atomic flux of 10^{11} atoms/s. We can fit the appropriate Maxwell-Boltzmann curve to this atomic flux profile (as we have in figure 3.4). Next we need to take into account the atomic losses from the cooling cycle due to decay via the $5s4d\,^1\mathrm{D}_2$ state (see figure 2.1 and table 2.2); higher velocity atoms require more photon interactions to reduce their velocity to 25 m/s, so are more likely to be lost. The probability of an atom remaining in the cooling process, i.e. not being lost due to the branching ratio to the $5s4d\,^1\mathrm{D}_2$ state is:

$$P(v) = \left(1 - \frac{\Delta p_{\mathrm{atom}}(v)}{p_{\mathrm{photon}}} \frac{\Gamma_{12}}{\Gamma_1}\right) \tag{3.22}$$

where Γ_{12} and Γ_1 are the decay rates of transitions 12 and 1, respectively (see figure 2.1 and table 2.2 for values), $p_{\mathrm{photon}} = h/\lambda_1$ is the (461 nm) photon momentum, and $\Delta p_{\mathrm{atom}}(v) = m_{\mathrm{atom}}(v - 25)$ is the velocity dependant change in momentum required to slow the atoms (of mass m_{atom}) from their initial veloc-

ity v to their final velocity of 25 m/s. The modified velocity profile is shown in figure 3.18, where curve (a) shows the calibrated atomic flux fit, and curve (b) shows the modified distribution (curve (a) multiplied by $P(v)$). We can integrate this modified curve (as shown in figure 3.19) to calculate the maximum slowable atomic flux. We find that our oven configuration (defined by its geometry and temperature) can provide a maximum slow atom flux (given a perfect Zeeman slower) of 9.6×10^9 atoms/s, which is 9.6 % of the total atomic flux. In order to increase this fundamental efficiency of our apparatus we would need a better design of oven; one that produced a similar atomic flux at a lower temperature, such as the one built by Schioppo et al. [82]. Using the information given in [82] (oven temperature = 450 °C, total atomic flux = 1.2×10^{12} atoms/s, and that the oven nozzle is operating in the collision-free regime) we can use the same approach as in figures 3.18 and 3.19 to estimate the maximum slowable atomic flux to be 1.2×10^{11} atoms/s, which is 10.3 % of the total atomic beam flux. These numbers compare favourably to those for our apparatus, and make it clear that in the future we should go back to a multi-channel nozzle design for our oven, as we had before it broke (see section 3.1.1).

We can still use our current oven configuration to calculate the slowing efficiency of our permanent magnet Zeeman slowers. By integrating curve (b) in figure 3.18 between $v = 25$ m/s and 412 m/s (the Zeeman slower capture velocity) we find the maximum slowable atomic flux of our oven and Zeeman slower configuration to be 7.5×10^9 atoms/s. By integrating over the slow atom peak of our longitudinal velocity distributions, up to a typical MOT capture velocity of 50 m/s, we can obtain the slow atom flux achieved by our Zeeman slowers. We find this to typically be 3×10^9 atoms/s for a transverse-field permanent magnet Zeeman slower. This is around 40 % of the maximum slowable atomic flux, and

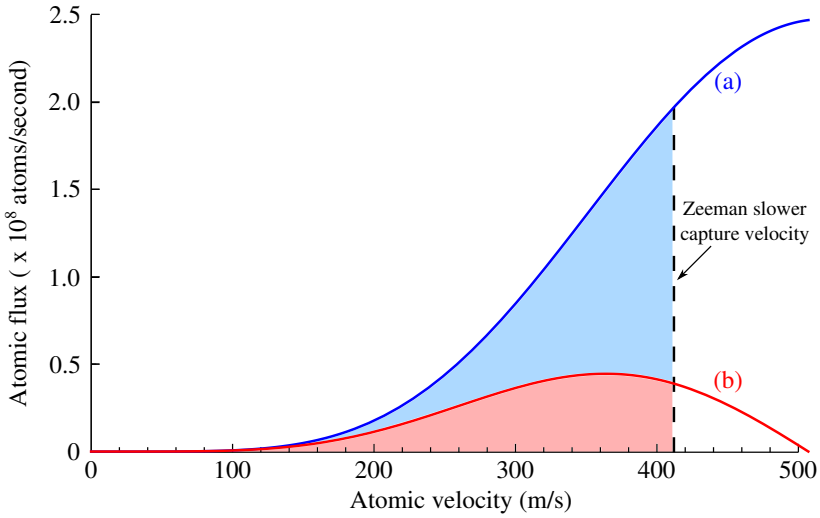

Figure 3.18: **Zeeman slower efficiency calculation demonstration** - This plot shows (a) the calibrated Maxwell-Boltzmann atomic velocity distribution fit of the atoms escaping from the oven, and (b) the modified distribution which takes into account the loss of atoms from the cooling cycle via the $5s4d\,^1\mathrm{D}_2$ state. The capture velocity of the Zeeman slower is indicated by the black dashed line. The red shaded area shows the maximum atomic flux achievable with a perfect Zeeman slower.

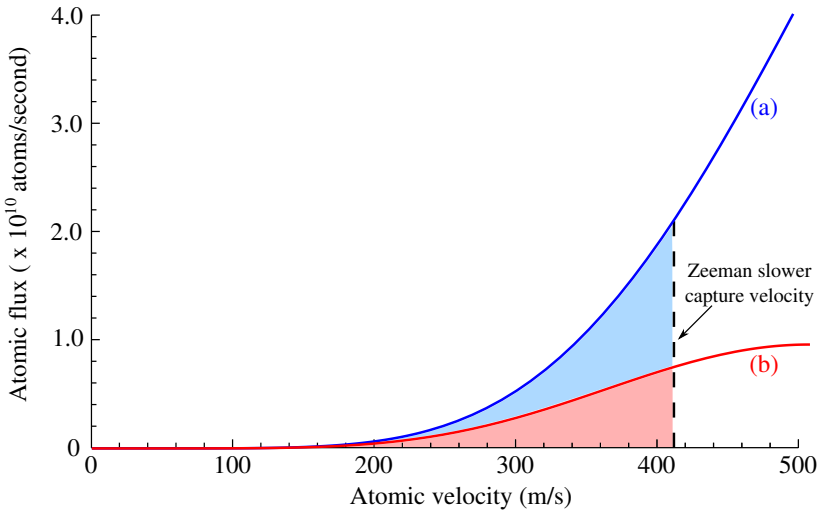

Figure 3.19: **Cumulative atomic flux profiles** - This plot shows (a) the cumulative Maxwell-Boltzmann fit from figure 3.18, and (b) the cumulative modified distribution from figure 3.18. For our oven configuration, the maximum cumulative fluxes for (a) and (b) are 10^{11} atoms/s and 9.6×10^9 atoms/s respectively, therefore a perfectly designed Zeeman slower could only slow a maximum of 9.6 % of the total atomic flux. This percentage value could be increased with a better design of oven, that had a similar atomic flux at a lower temperature, such as the one built by Schioppo et al. [82].

3 % of the total atomic flux. It is unrealistic to expect to measure an accurate Zeeman slower efficiency in this way, but this estimate demonstrates the Zeeman slowers are working at a decent efficiency level.

3.3.3 First-stage Magneto-Optical Trap

Typical operation parameters for our first-stage magneto-optical trap (MOT) are as follows: three $\sim 3.5\,\mathrm{mW}$ retro-reflected beams with a $1/e^2$ beam waist (radius) of $\sim 5\,\mathrm{mm}$ at a detuning of $-40\,\mathrm{MHz}$; the magnetic field gradient along the axial direction at trap centre is $\sim 40\,\mathrm{G/cm}$. We routinely load the MOT from Zeeman-slowed atoms, typically trapping around 2×10^7 atoms with a 1/e loading time of $\sim 20\,\mathrm{ms}$ without repump lasers (measured by fluorescence imaging).

To produce the magnetic field required for the MOT, a pair of wire-wound coils of radius 4.75 cm and separation 19.75 cm are used. Each coil has approximately 450 windings of polyester-coated 0.9 mm diameter copper wire, through which ~ 17 Amps are run to produce a magnetic field of $\sim 40\,\mathrm{G/cm}$ in the MOT region. This configuration of magnetic coils does not match the ideal anti-Helmholtz condition, because the coils were originally designed to be used for a different vacuum chamber configuration, but this does not overly affect the MOT. The coils were also never intended for switching on and off rapidly, so have a high number of turns and consequently a high inductance, resulting in a slow field-decay time of $\sim 8\,\mathrm{ms}$. We are yet to demonstrate whether these coils are suitable for loading from the 461 nm MOT to the 689 nm MOT and then into the lattice. Due to inefficient water-cooling the percentage cycle time during which the coils are on during any given experimental sequence must be carefully planned to avoid overheating. For clock frequency measurements we do not want our cycle time dictated by the MOT coils, so we plan to replace them in the near future.

3.3.3.1 Cooling All the Isotopes?

We need to demonstrate the Zeeman slower works as well for ^{87}Sr as it does for ^{88}Sr, as we intend to make clock frequency measurements with each isotope. It may be that the ^{87}Sr atoms undergo optical pumping in the low magnetic field region close to the field zero-crossing and are lost from the cooling cycle. To show equivalent slowing for all isotopes we load into the 461 nm MOT and compare the peak atom number for each isotope to the natural abundance values. In order to cool and trap isotopes other than ^{88}Sr, detuning of the cooling and trapping beams needs to be adjusted accordingly. The ^{87}Sr $5s5p\,^1\mathrm{P}_1$ $F = 11/2$, $m_F = -11/2$ state is detuned -51.9 MHz from the ^{88}Sr excited state (see table 3.1). This offset detuning needs to be added to both the slowing beam and the MOT beams. Tuning the length of the optical reference cavity to which we frequency stabilise the 922 nm light (see section 3.3 for details) allows us to scan over the trapping range for the different isotopes, and detection of the MOT fluorescence produces the graph shown in figure 3.20. The ratio of heights of the peaks (relative atom numbers) for ^{88}Sr : ^{87}Sr : ^{86}Sr is $1 : 0.0854 : 0.132$, this is close to that of the ratio of natural abundance of each isotope ($1 : 0.0848 : 0.119$), demonstrating that our transverse-field Zeeman slowers work as well for the ^{87}Sr isotope as they do for the bosonic isotopes.

3.3.3.2 MOT loading with repump lasers

We recall that the repump lasers reduce the MOT loss rate caused by shelving in the $^3\mathrm{P}_2$ and $^3\mathrm{P}_0$ states, so application of the repump lasers to the MOT should result in an increased number of atoms. By applying the 707 nm repump laser to the MOT (to clear out the $^3\mathrm{P}_2$ state) we see an atom number enhancement of ~ 3. With both the 707 nm and 679 nm repump lasers incident on the MOT simulta-

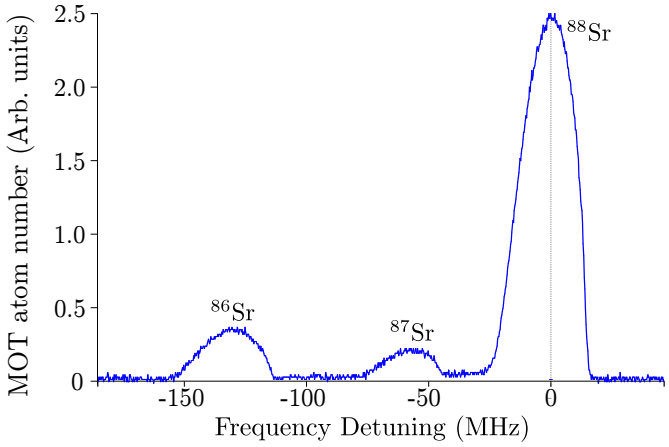

Figure 3.20: **Isotope scan of 461 nm MOT** - The cooling and trapping laser frequency is scanned and the fluorescence from the MOT measured. The relative peak heights for ^{88}Sr : ^{87}Sr : ^{86}Sr are $1 : 0.0854 : 0.132$, which is close to that of the ratio of natural abundance of each isotope ($1 : 0.0848 : 0.119$). This demonstrates the Zeeman slower and MOT work effectively for all Sr isotopes of interest. The frequency detuning is measured from the peak of the ^{88}Sr MOT.

Isotope	Relative Abundance (%)	I	F	Shift (MHz)
^{84}Sr	0.56	I = 0	-	-270.8
^{86}Sr	9.86	I = 0	-	-124.5
			7/2	-9.7
^{87}Sr	7.00	I = 9/2	9/2	-68.9
			11/2	-51.9
^{88}Sr	82.58	I = 0	-	0

Table 3.1: **Isotope abundances and detunings for 461 nm cooling** - with their nuclear and angular momentum quantum numbers [107].

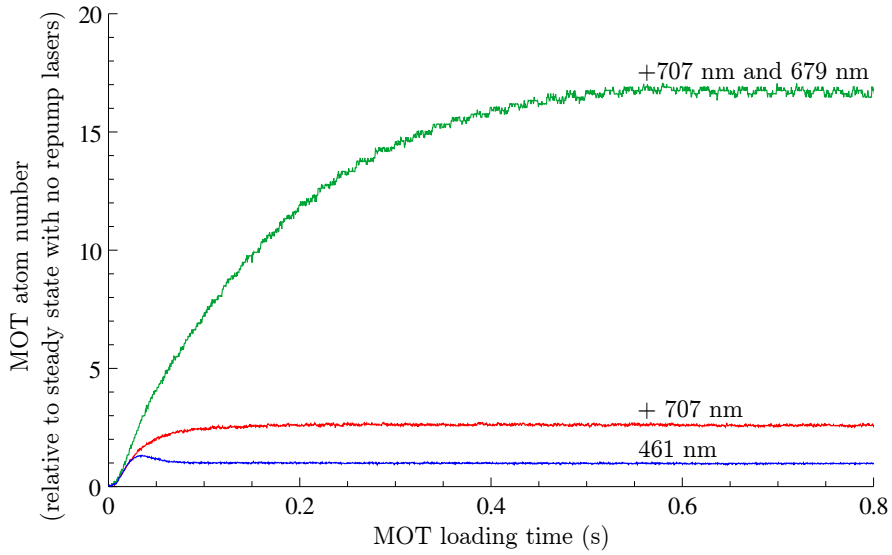

Figure 3.21: **MOT loading with repump lasers** - MOT fluorescence data demonstrating MOT atom number enhancements of ~ 3 with the 707 nm repump laser and ~ 17 with both the 707 nm and 679 nm repump lasers. The overshoot shown in the lower curve is due to settling of the MOT magnetic field after switch-on.

neously we observe an atom number enhancement of ~ 17. These enhancement factors are similar in comparison to those achieved by other groups working with Sr [101]. Figure 3.21 shows loading curves for the 461 nm MOT with and without repump lasers. We measure the MOT fluorescence on a photodiode, and assume the fluorescence is proportional to the number of atoms in the MOT. We can see that inclusion of the repump lasers results in longer loading times, and therefore higher atom numbers, before the system reaches an equilibrium.

3.4 Conclusions

We have shown that our strontium source, Zeeman slower, and first-stage magneto-optical trap work together to cool and capture $\sim 2 \times 10^7$ atoms. We have demonstrated efficient cooling of the necessary strontium isotopes with our novel transverse-field permanent-magnet Zeeman slowers and standard magneto-optical trap. We

have presented an initial analysis and explanation of Zeeman slowing characteristics for a range of parameters.

We have further data, not presented here, from our Zeeman slower and MOT set-up showing MOT atom numbers as a function of various Zeeman slowing parameters; this allows us to find our optimum parameters for MOT loading and work out our MOT capture velocity. This work is not presented here because the author was not directly involved in these experiments, although a complete overview of our work with permanent-magnet Zeeman slowers is due to be published soon.

Further work for this section of the experimental set-up is as follows:

- replace MOT coils to achieve faster switching time and efficient water cooling
- optimise MOT density and temperature with the repump lasers
- attempt loading into second-stage MOT (see chapter 4 for details on the 689 nm laser system).

Chapter 4

Further cooling and trapping of atomic strontium

After Zeeman slowing the thermal atomic beam and trapping and cooling in the first-stage magneto-optical trap at 461 nm, we have a cloud of $\sim 2 \times 10^7$ Sr atoms at a temperature of a few millikelvin. Our lattice trap depth is $\sim 20\,\mu$K, so we need to utilise the narrow linewidth transition at 689 nm to cool the atoms further, so that they can be efficiently loaded and trapped in the lower lying energy levels of the optical lattice. The 689 nm transition has a natural linewidth of $\gamma = 7.5$ kHz, giving a transition rate of $4.7 \times 10^4\,\mathrm{s}^{-1}$, a saturation intensity of $2.98\,\mu\mathrm{W/cm}^2$, and a recoil cooling limit of ~ 230 nK. Narrow cooling transitions such as this have the characteristic feature of the frequency shift due to the recoil momentum from the photon (equal to 9.5 kHz) being larger than the natural transition linewidth, meaning that the cooling is recoil-, rather than Doppler-, limited. This chapter outlines the trapping and cooling requirements for the 689 nm transition and details the laser set-up required. It also contains details of the optical lattice trap and the black-body radiation shift measurement proposal. Extensive details of the laser frequency stabilisation to the optical reference cav-

Isotope	Angular momentum states	Frequency (kHz)	Reference
^{86}Sr	J = 0 → J' = 1	434 828 957 494 (10)	[108]
	F = 9/2 → F' = 7/2	434 830 473 270 (55)	[109]
^{87}Sr	F = 9/2 → F' = 9/2	434 829 343 010 (50)	[109]
	F = 9/2 → F' = 11/2	434 827 879 860 (55)	[109]
^{88}Sr	J = 0 → J' = 1	434 829 121 312.334(53)	[110]

Table 4.1: **Second cooling transition frequencies** ($5s^2\,{}^1\mathrm{S}_0 - 5s5p\,{}^3\mathrm{P}_1$) - for different isotopes and hyperfine states of strontium.

ity via the Pound-Drever-Hall technique are not covered here because they are explained in depth in chapter 5.

4.1 Second-stage cooling (689 nm)

In order to drive the 689 nm, 7.5 kHz wide transition efficiently we need a laser with a linewidth narrower than that of the transition. In order to achieve this we use the Pound-Drever-Hall (PDH) technique [98] to stabilise our laser frequency to that of a resonant mode of a high finesse optical reference cavity. We discuss the PDH technique in detail in section 5.2, and talk specifically about the implementation for the 689 nm laser in section 4.1.2.

The experimentally determined frequencies of the 689 nm transition for the different isotopes and hyperfine states are shown in table 4.1. For trapping and cooling the bosonic isotopes we wish to drive the single J = 0 → J' = 1 transition, as we do for cooling on the 461 nm transition (see figure 3.6). The main difference here is how the very narrow transition linewidth affects the cooling. The $\gamma\lambda$ Doppler cooling limit for single frequency light driving the 461 nm transition is $\sim$ 14 m/s (refer back to section 3.2), for the 689 nm transition it is only $\sim$ 5 mm/s (one photon absorption)! The narrow transition linewidth provides us with a

very low cooling limit, but also a very low capture velocity range. To transfer a significant portion of the atoms from the 461 nm MOT (with a temperature of a few millikelvin and a most probable atomic speed of $\sim 1\,\mathrm{m/s}$) to the 689 nm MOT we need to find a way to address more of the atomic velocity distribution than a single narrow-frequency line does alone. We choose to do this by spectrally broadening the 689 nm cooling light. This can be achieved by frequency modulating the cooling light on the acousto-optic modulator (AOM) (see figure 4.1) so that the spectrum covers most of the velocity distribution of the $\sim 2\,\mathrm{mK}$ atom sample. Groups typically cool with this broadband light for $\sim 90\,\mathrm{ms}$ before switching to single frequency cooling and slowly ramping up the magnetic field gradient from around $\sim 3\,\mathrm{G/cm}$ to $\sim 10\,\mathrm{G/cm}$ [111; 112].

4.1.1 Trapping ^{87}Sr

Since this work is not essential for this thesis we will not explain it in full detail, but will give an overview to portray the necessity of the stirring laser. More detailed explanations are given in [113] and the theses of Ludlow [114] and Boyd [70].

As we detailed and demonstrated in section 3.3.3.1, cooling and trapping ^{87}Sr on the 461 nm transition is little harder than for the ^{88}Sr isotope. The main difference is the lower natural abundance, which means we have a lower MOT loading rate, and so trap fewer atoms before loss and loading rate equilibrium is reached. Repumping is slightly more complicated because the nuclear spin of ^{87}Sr adds hyperfine structure to the $5s5p\,^3\mathrm{P}_2$ and $5s6s\,^3\mathrm{S}_1$ states, so swept or frequency modulated repump lasers are required to repump all the states efficiently. Trapping and cooling on the 689 nm transition is more complicated, because the narrow transition linewidth means the ground state sublevels are no longer ef-

fectively degenerate as they are for the broad 461 nm transition. The diagram of energy levels in our MOT is no longer as simple as in figure 3.6. Attempting to cool solely on the $F \rightarrow F+1$ transition would result in loss of atoms from the MOT, because the Zeeman splitting of ground and excited state energies is different due to the differing g_F values of the ground and excited state. This means that the detuning of the cooling light is not resonant for the excitation of all possible ground spin states, and atoms get pumped into dark states that are no longer cooled and escape from the trap. To avoid this an additional stirring laser is used on the $F = 9/2 \rightarrow F' = 9/2$ transition [113]. This mixes up the population of the spin states to give a more even distribution for efficient cooling on the $F = 9/2 \rightarrow F' = 11/2$ transition.

4.1.2 Optical reference cavity for 689 nm

The optical reference cavity for stabilising the frequency of the 689 nm laser is a horizontally mounted, 10 cm long, ultra-low expansion glass (ULE), cylindrical geometry cavity, with both mirrors having a radius of curvature of 30 cm. The finesse at 689 nm was measured by locking the laser to the cavity and using an acousto-optic modulator (AOM) to rapidly ($< 1\,\mu$s) switch off the light and measure the decay of the cavity transmission. The time constant of this exponential decay gives the cavity finesse (see sections 5.3.3 and 5.3.3.1 for more details). We measure the decay time to be $(6.9 \pm 0.2)\,\mu$s, which equates to a finesse of $65\,000 \pm 2\,000$ and a cavity linewidth of (23.1 ± 0.1) kHz. If we assume we can (relatively) easily lock the laser to within 1 % of the cavity fringe width, this will result in a laser linewidth of ~ 230 Hz, which is perfectly narrow enough to drive the $\gamma = 7.5$ kHz linewidth transition efficiently.

The optical reference cavity is housed in a vacuum chamber utilising mainly

standard steel Conflat vacuum pieces, a 2 l/s ion pump and a Viton angle valve. The vacuum apparatus maintains a steady pressure of 8×10^{-8} mbar. The windows for optical access are wedge-shaped, anti-reflection coated, and are attached using indium as a cold-weld seal at an additional orthogonal tilt to the wedge. The wedged and tilted nature of the windows ensures there are no parallel reflecting surfaces (no matter how small the reflection from the anti-reflection coating) and prevents unwanted parasitic etalons (see section 5.2.2.2 for more information on parasitic etalons). The vacuum chamber is externally temperature-stabilised to around 22.5 °C using a tuned PI (proportional-integral) temperature controller that drives a current though constantan heater wire wound around the vacuum chamber. The bridge amplifier circuits for the in-loop and monitor thermistors are housed very close to the vacuum chamber to prevent amplifications of noise picked up on the small thermistor signals, and to provide a temperature stabilised environment for the remaining bridge components. The PI gains were chosen by first mapping out the Bode plot of the system's temperature response and then choosing appropriate capacitor and resistor values to complement this. This characterisation technique for choosing appropriate PID parameters for temperature servo loops was developed in our lab and is described further in section 5.1.1.1. We find it a quick and efficient method for temperature stabilisation, and here it provides better than 10 mK temperature stability over a 24 hour period; this is good considering it is quite a simple system, consisting of a single layer of active stabilisation with one additional passive layer (a foam-lined aluminium box) between it and the laboratory environment.

4.1.2.1 Cavity mode frequencies

From the cavity length we can use equation 5.12 to calculate the free spectral range (FSR) of the cavity to be $\sim 1.5\,\text{GHz}$. We have measured the frequency of two TEM_{00} resonant modes by locking the laser to the cavity and using the optical frequency comb, housed in an adjacent laboratory, to compare our locked laser frequency to the microwave frequency of the hydrogen maser. The frequency of the cavity modes are: (a) $(434\,829\,569 \pm 3)\,\text{MHz}$, and (b) $(434\,828\,066 \pm 3)\,\text{MHz}$, giving a measured $\text{FSR} = (1.503 \pm 0.004)\,\text{GHz}$, with typical drift rates of around $2\,\text{Hz/s}$. Such high drift rates are attributed to thermal expansion and contraction of the cavity spacer. At this rate our laser will drift a full linewidth of the transition within one hour, making experimental operations tricky. There are two main reasons for our high drift rate: firstly the cavity only has a single layer of temperature control, which is in air, so susceptible to convection currents and changes in laboratory temperature and is only stable to 10 mK. An additional actively temperature controlled shield inside the vacuum would enable us to improve the temperature control to around a millikelvin over a 24 hour period, but in order to do this we will need to redesign our vacuum chamber. Secondly, we are not taking advantage of the ULE's zero coefficient of thermal expansion (CTE). At a particular temperature T_c (usually close to room temperature) the CTE of ULE passes through zero. Stabilising our cavity temperature at, or close to, this point has major advantages in terms of frequency stability, because the fractional frequency of the cavity mode scales as T^2 from T_c (see section 5.3.1.1 for more details). This cavity was originally part of a different experiment; from data they took we know T_c for this cavity is around $0\,^\circ\text{C}$. Being stabilised to a temperature so far away from its T_c easily explains the drift rates we have been observing, but cooling the cavity down to $0\,^\circ\text{C}$ would not be a simple task. We would not

only need to exchange the heater wire set-up for a peltier cooling system, but we would also need a second layer of temperature stabilisation inside the vacuum system, because cooling past the dew point ($\sim 10\,^{\circ}\mathrm{C}$ at standard temperature, pressure and humidity) would result in water condensing on the vacuum system.

At present we are just about to start trapping the atoms with this laser, so we can probably manage with this high drift rate, because we will only be using it on short time-scales. Soon we will need to use this laser system on longer time-scales; we have a few options for implementing longer-term drift correction. A slow lock to a strontium vapour cell would be an obvious option, but we would need to buy or build a vapour cell and lock electronics. Our preferred option is to use the second clock laser optical reference cavity and PDH lock the laser to this rather than the intended cavity. The second clock laser reference cavity is intended to aid with characterisation of the clock lasers and will not be used in day-to-day operations. We intend to set the 689 nm and 698 nm lasers up so that either one can be locked to the cavity. It is probably possible to lock both lasers to the cavity at the same time by using different modulation frequencies and separating the PDH error signals after the APD, but this could make one or both of the locks worse than ideal. We intend to send the 689 nm light to the 698 nm set-up via an optical fibre and use a beam splitter to combine the beams for alignment into the reference cavity. See chapter 5 for more details on the clock cavities and 698 nm optical set-ups. The frequency drift of this clock cavity is less than 500 Hz in 4 hours and is mainly linear, so should be easy to correct for using an AOM. If necessary an additional atomic reference may be implemented in the future for drift correction on even longer time-scales.

In our present set-up, in order to bridge the frequency gap between the optical cavity modes and that required for cooling and trapping in the 689 nm MOT we

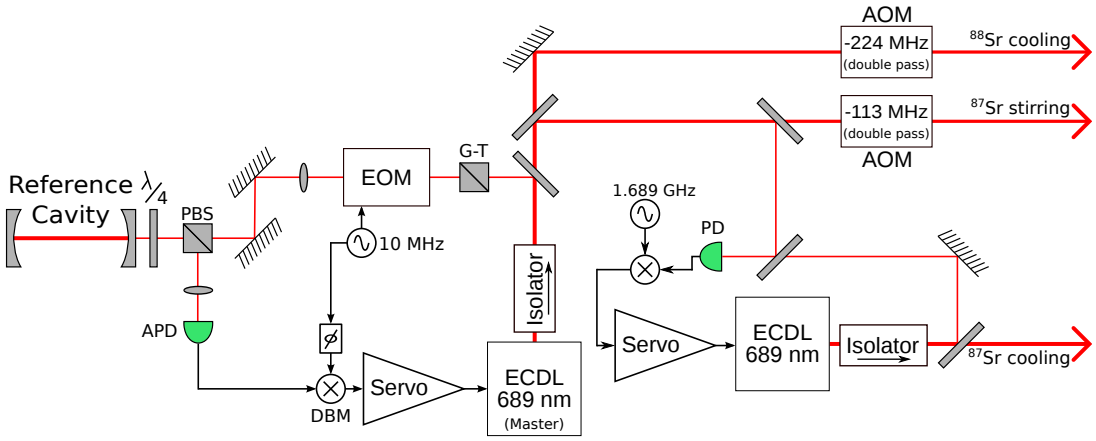

Figure 4.1: **Proposed 689 nm optical set-up** - The left-hand half of the drawing is the PDH lock of the master ECDL to the optical reference cavity. The right-hand half derives the correct frequencies for cooling and trapping the ^{87}Sr and ^{88}Sr isotopes by the use of double-passed AOMs and an offset lock. Key of terms: ECDL = extended cavity diode laser; G-T = Glan-Thompson polariser; EOM = electro-optic modulator; PBS = polarising beam splitter cube; $\lambda/4$ = quarter waveplate; (A)PD = (avalanche) photodiode; DBM = double balanced mixer; AOM = acousto-optic modulator. The use of these components for PDH locking is explained further in section 5.2.

plan to use the AOM scheme detailed in figure 4.1. To cool and trap ^{88}Sr we need to lock to cavity mode (a) and shift the laser frequency by -448 MHz; we do this by using a double passed -224 MHz AOM. For cooling and trapping ^{87}Sr we require the stirring laser frequency, which will be obtained by locking to the same cavity mode and using a double-passed AOM at -113 MHz, and the cooling laser frequency, which will be obtained by offset locking a slave laser frequency to that locked to the optical cavity with an offset of -1.689 GHz. With the addition of an injection-locked slave laser we would have enough laser power to switch rapidly between cooling ^{88}Sr and ^{87}Sr, which we may require for analysis of frequency shifts on the clock transition. A schematic of the planned optical and electronic set-up is all shown in figure 4.1. To date we have implemented the optics and cavity locking electronics for cooling and trapping ^{88}Sr (without the additional slave laser and AOM so far); we have also built a second ECDL

for the ^{87}Sr cooling slave. The first laser is PDH locked to the cavity, and the linewidth estimated to be less than 1 kHz by looking at the magnitude of the noise on the in-loop error signal. The ECDL was quite sensitive to noise on the optical table and the laser would be knocked out of lock by people setting up other optical systems. We identified the sensitive part of the set-up as the ECDL and have started to implement some passive isolation between it and the main optical table.

4.1.3 Preliminary atomic spectroscopy at 689 nm

In an attempt to replicate the measurements published in [108; 109; 110; 115] atomic fluorescence spectroscopy was performed in the small spectroscopy cross directly down stream from the strontium oven, described in section 3.1 and shown in figure 3.3. The experimental set-up is shown in figure 4.2. The light from the free-running ECDL (not locked to the optical reference cavity) is double passed through an AOM with a fixed modulation frequency and coupled into a polarisation maintaining optical fibre to the spectroscopy cross. After the fibre a $\lambda/2$ waveplate is used to orientate the light polarisation horizontally and a polarising beam splitter cube used to clean up the polarisation and ensure its orientation. There is a small pick off to a photodiode (Thorlabs DET100A/M, with a 50 Ω load to ground giving a bandwidth of 10 MHz), which is used with a comparator circuit and single integrator to stabilise the light intensity by feeding back to the RF drive power of the AOM with a Mini Circuits voltage variable attenuator (part number ZX73-2500+). The intensity noise jitter at the output of the fibre is reduced from $\sim 10\,\%$ to $< 1\,\%$.

The output beam from the fibre has a power of 95 µW and a $1/e^2$ radius of 0.4 mm, giving a peak laser beam intensity of $I_0 = 38\,\mathrm{mW/cm^2} \simeq 13\,000\,I_{sat}$.

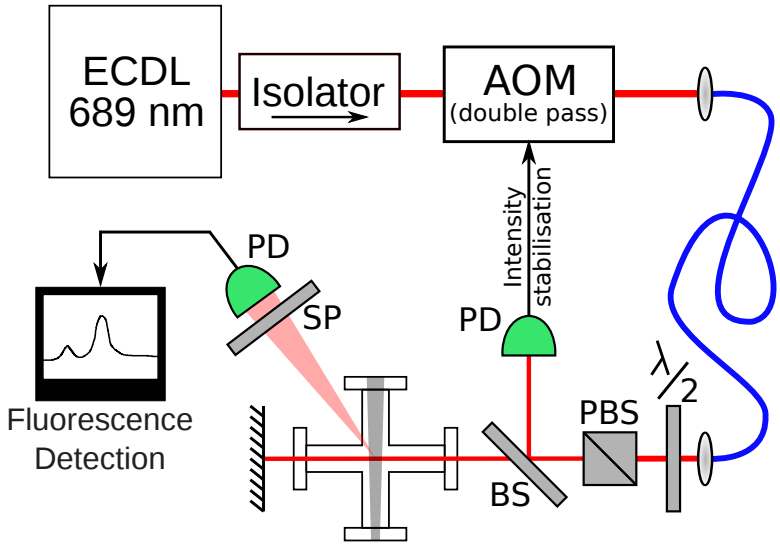

Figure 4.2: **689 nm fluorescence spectroscopy optical layout** - outlining the key components in the spectroscopy experiment. Key of terms: ECDL = extended cavity diode laser; AOM = acousto-optic modulator; $\lambda/2$ = half waveplate; PBS = polarising beam splitter cube; BS = beam splitter; PD = photodiode; SP = short-pass optical filter ($\lambda_{\text{cutoff}} \simeq 700\,\text{nm}$).

This will power broaden the 7.5 kHz transition linewidth to around 850 kHz. The laser frequency is scanned over $\sim 500\,\text{MHz}$ by ramping the voltage applied to the piezo disk on the ECDL diffraction grating, and the scan is calibrated with a 1 MHz resolution wavemeter (HighFinesse WSU-10), with an estimated error of $\lesssim 5\,\text{MHz}$ on a 500 MHz scan. The period of a full scan was around 9 seconds. The fluorescence signal was detected on a large area photodiode with a built-in high gain transimpedance amplifier and a further voltage offset (to subtract the background signal) and amplifier stage to increase the signal-to-noise at our recording stage. A short-pass optical filter (similar to Thorlabs FES700) was used in front of the photodiode to reduce the large background signal due to infra-red radiation from the hot oven. The resulting captured fluorescence signal is shown in figure 4.3. The full width at half maximum (FWHM) of the lineshape is $\sim 30\,\text{MHz}$, and the separation between the ^{88}Sr and ^{86}Sr peaks is $(163 \pm 3)\,\text{MHz}$, in agreement with the experimentally determined isotope shift of 163.8 MHz [108].

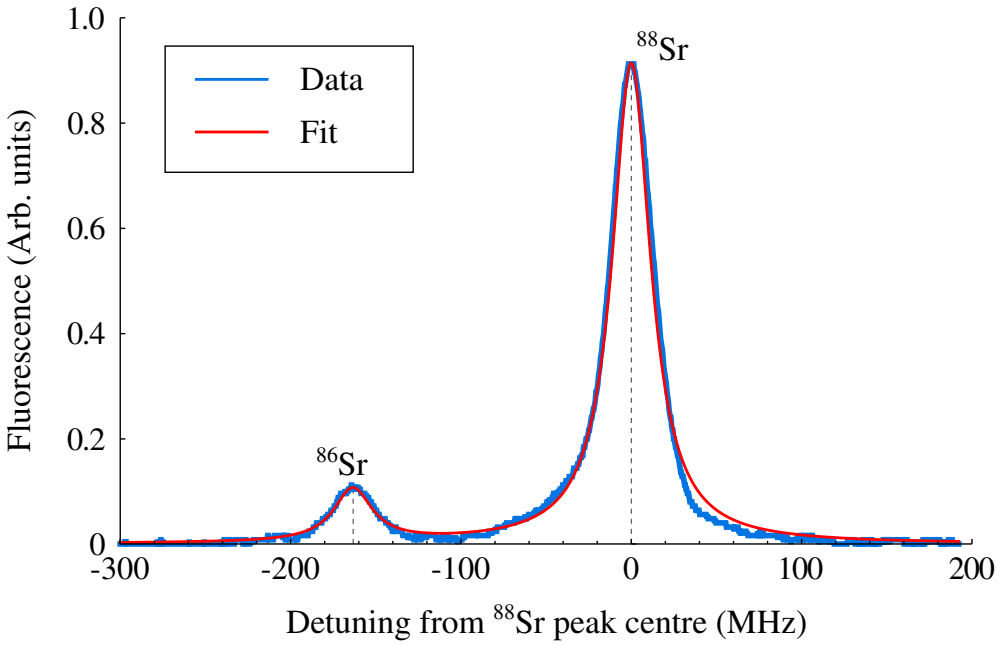

Figure 4.3: **689 nm fluorescence spectroscopy** - from a single (repeatable) scan of the unlocked 689 nm probe beam across the transverse velocity distribution. The fluorescence is detected by an amplified photodiode. The ^{88}Sr and ^{86}Sr peaks are at the expected detunings, and have the anticipated peak heights, relative to one another. The fitted profile is the sum of two Lorentzians, with the fit parameters given in table 4.2. The reasons for fitting a Lorentzian to this data are given in the text.

Parameter	Expected	Best fit value
^{88}Sr−^{86}Sr frequency shift	$-163.8\,\mathrm{MHz}$	$-(163 \pm 3)\,\mathrm{MHz}$
^{88}Sr relative abundance	$89.3\,\%$	$(90 \pm 1)\,\%$
^{86}Sr relative abundance	$10.7\,\%$	$(10 \pm 1)\,\%$
Profile linewidth	$< 130\,\mathrm{MHz}$	$\sim 27\,\mathrm{MHz}$

Table 4.2: **689 nm fluorescence spectroscopy** - best fit values compared to expected values from literature or calculated values.

The profile of the line-shape will be broadened from its natural 7.5 kHz wide Lorentzian profile by a number of broadening mechanisms. We have already mentioned power broadening, which is due to saturation of the transition by the incident laser power. The power broadened lineshape follows that of equation 3.4, where the FWHM is given by $\gamma\sqrt{1+s}$ [61]. We expect the extent of this broadening mechanism to be $\lesssim 850$ kHz for the laser beam intensity used. A second broadening mechanism is due the short interaction time between the atoms and the laser, and is referred to as transit time broadening. The short interaction time, t_{trans}, Fourier limits the frequency resolution of the spectroscopy and results in a linewidth of $\nu_{\text{trans}} \simeq 1/(2\pi\, t_{\text{trans}})$ [116]. For our particular case (with atoms at ~ 900 K, a most probable velocity of ~ 500 m/s, and therefore a transit time of $\sim 1.6\,\mu$s) the transit time broadening is ~ 100 kHz. A third broadening mechanism is due to the laser linewidth. The laser is not locked to an optical reference cavity during this spectroscopy, and so it is estimated that the linewidth is somewhere between a few hundred kilohertz and a megahertz. The fourth and most significant broadening mechanism is due to the Doppler effect. The atomic beam is approximately collimated by the nozzle of the oven, but there is still some transverse velocity contribution in the direction of the probe beam, which causes Doppler broadening. For a three-dimensional atomic cloud the velocity distribution is Gaussian, and hence so is the resulting Doppler broadened distribution, which follows $\nu_D = \nu_0\, v/c$. In an atomic beam the profile of the Doppler broadened line shape is more complicated, and is discussed in detail in [117]. Ultimately the lineshape depends of the flow regime of the nozzle configuration and is non-trivial to calculate. We can make an estimate of the scale of the Doppler broadening mechanism by simply calculating the possible extent of the transverse velocity distribution from the nozzle geometry and assuming, for simplicity, that

there are no atomic collisions. A most probable velocity of 500 m/s and a nozzle half-angle of $\theta_{1/2} = \tan^{-1}(1/11)$ results in a transverse velocity distribution of ± 45 m/s, which is equivalent to a Doppler width of ~ 130 MHz. This width is larger than the ~ 30 MHz measured by the spectroscopy, which shows, as we expected, this simple calculation is not suitable for making a realistic approximation for the extent of the transverse velocity profile.

The profile that best fits the spectroscopic data is a Lorentzian lineshape. There is no physical justification given here for why a Lorentzian lineshape would fit the fluorescence profile, other than that the atomic collisions within the nozzle may result in such a disribution. The fit is given more for comparison and to demonstrate the profile asymmetry, which is evident on the ^{88}Sr peak. This asymmetry is thought to be due to clipping of the atomic beam by the aperture after the nozzle (see figure 3.2). Table 4.2 compares the best fit parameters with those expected from calculations or literature. We can see that the measured isotope shift and relative abundances agree with the literature values.

After taking the single beam fluorescence data shown in figure 4.3, the beam is then retro-reflected so that we can observe the Lamb dip, where saturation causes a reduction in fluorescence from the centre of the velocity profile. This technique is insensitive to the transverse velocity of the atoms, so allows us to see beyond the Doppler broadened profile. The observed Lamb dip is shown in figure 4.4. The linewidth of this is ~ 1.5 MHz, which we assume to be limited by the laser linewidth. Ideally we would like to scan over the Lamb dip while the laser is locked to the optical reference cavity. With the laser locked its linewidth should be less than the natural atomic linewidth, so the linewidth of our spectroscopy should be limited by power broadening. By reducing the laser beam intensity we should be able to approach the transit time broadening linewidth limit. Unfortunately,

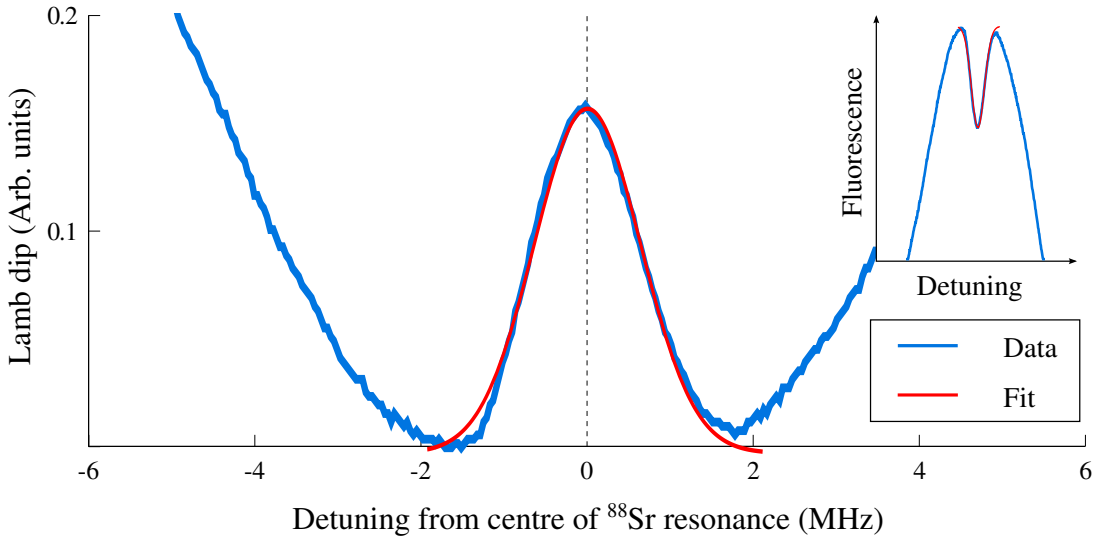

Figure 4.4: **689 nm fluorescence spectroscopy Lamb dip** - single scan with Gaussian fit. Insert shows fluorescence data from which the main graph is obtained.

due to experimental difficulties we did not have time to repeat this experiment with a locked laser.

4.2 Magic wavelength lattice

We wish to confine the atoms in a one-dimensional, red-detuned optical lattice trap at the magic wavelength, as described in section 2.4.1.1. From previous work we know the magic wavelength is around $\lambda_L = 813.428\,\text{nm}$ [31; 69; 70], and the AC-dipole polarisability of the ground and excited clock states are calculated to be $\alpha_a \simeq 300 \times 4\pi\epsilon_0 a_0^3$ [55], where ϵ_0 is the permittivity of free space and a_0 is the Bohr radius. The laser light at 813 nm is provided by an ECDL and tapered amplifier. The ECDL is a home-built design, similar to that described in section 5.1. The pivot point for the diffraction grating is designed to give a wide mode-hop-free tuning range, which is measured to be around 40 GHz (approximately 0.1 nm at this wavelength). The output coupling mirror (see section 5.1 for a

picture and details) enables gross tuning of the laser frequency with only a very small displacement of the outgoing beam, meaning optics, including single core optical fibres, stay aligned over a wide tuning range. This mode-hop-free tuning together with the maintained beam alignment will be invaluable in our experiment as we seek to confirm the magic wavelength, by making clock measurements at a range of different lattice wavelengths. The ECDL output power is around 30 mW.

The tapered amplifier is a commercial unit from Toptica. It is designed to take a seed power of ~ 15 mW and output ~ 500 mW. This light will be overlapped and coupled into an optical fibre with the 698 nm clock laser for delivery to the atomic apparatus (see figure 4.7). We expect to have a minimum of ~ 150 mW of 813 nm light at the atomic vacuum chamber which we will focus down to a beam waist of $w_0 \simeq 50\,\mu$m and retro-reflect to make the one-dimensional lattice trap. From these parameters we can calculate our lattice depth:

$$U_0 = -\alpha_a \frac{4P}{\epsilon_0 c \pi w_0^2} \tag{4.1}$$

where P is the retro-reflected lattice power ~ 300 mW. It is usual to quote the lattice depth in terms of temperature or recoil energies of the lattice photons. The recoil energy is given by:

$$\begin{aligned} E_R &= \frac{p^2}{2m} \\ &= \frac{h^2}{2m\lambda_L^2} \end{aligned} \tag{4.2}$$

where p is the photon momentum and m is the mass of an atom. The temperature of the trap is given by:

$$T_{trap} = \frac{2U_0}{nk_B} \tag{4.3}$$

where k_B is Boltzmann's constant, and n is the number of degrees of freedom, which in this case is two. Our anticipated lattice parameters give a lattice depth of $\sim 120\, E_R$, which is equivalent to $\sim 20\,\mu\text{K}$.

To be able to trap atoms in this lattice effectively, we need to cool them to temperatures well below $20\,\mu\text{K}$ in our second-stage MOT (the temperature of the optical lattice ground state will be approximately $2\,\mu\text{K}$). The trapped atoms will slosh around within the trap potential, which approximates a harmonic well. Along the axial direction the trap potential follows a $\sin^2$ function as: $U_L(z) = U_0 \sin^2(k_L z)$, which for small perturbations from the trap centre is equal to $U_L(z) = U_0 (k_L z)^2$, where $k_L = 2\pi/\lambda_L$ is the lattice wavenumber. In the radial direction the trap follows $U_L(r) = U_0 \left[-2\,(r/w_0)^2\right]$. We can equate each of these to the harmonic oscillator potential to estimate the trap oscillation frequencies ν_z and ν_r: $U_{HO} = \frac{1}{2} m \omega_x^2 x^2 \equiv \frac{1}{2} m (2\pi\nu_x)^2 x^2$, where m is the atomic mass and x is z or r. The resulting trap frequencies are then:

$$\nu_z = \sqrt{\frac{2U_0}{\lambda^2 m}} \tag{4.4}$$

$$\nu_r = \sqrt{\frac{U_0}{\pi^2 w_0^2 m}} \tag{4.5}$$

For our estimated trap depth, this approximates the axial frequency to be $\sim 76\,\text{kHz}$ and the radial frequency to be $\sim 280\,\text{Hz}$. The tight confinement in the axial direction offers Lamb-Dicke confinement in one-dimension, with resolved sidebands at $\sim 76\,\text{kHz}$ spacing. In order to benefit from this we must align our clock laser collinear with the lattice trap, which is why we initially intend to deliver our lattice and clock light via the same optical fibre.

4.2.1 Frequency stabilisation of magic wavelength lattice laser

In section 2.4.1.1 we saw that for our expected trap depth we need to control the lattice wavelength to better than 20 MHz to be sure of a fractional frequency uncertainty of lower than 1×10^{-16}, or 2 MHz for uncertainties of better than 1×10^{-17}. We plan to achieve this by locking the laser to an optical cavity which is referenced to the atoms themselves; this way we can be sure we are at the correct wavelength (within some error) without needing to repeatedly make measurements with the optical frequency comb. The optical cavity we plan to use is the same tunable cavity as is used to lock the 679 nm repump laser and the 922 nm light for the 461 nm laser. The locking scheme is outlined in figure 4.5. To combine the beams for alignment into the optical cavity and to separate the PDH locking signals, we use dichroic optics. We also use different modulation frequencies for the different locks, so that any residual beams hitting the wrong lock photo-detectors do not affect the lock signals because they are electrically filtered out immediately after the detectors.

At present, to reference this cavity to the atoms we lock the 922 nm light to the cavity and manually adjust the cavity length (by tuning the voltage to the electrostrictive actuators) to obtain maximum fluorescence on the 461 nm transition (with the on-resonance probe beam, shown in figure 3.8, applied orthogonal to the direction of the atomic beam). This method is satisfactory for day-to-day use of the 461 nm laser because the cavity only drifts a few megahertz a day, but it is starting to become a problem for use of the 679 nm repump laser. The linewidth of the 679 nm transition is ~ 1.4 MHz, and the cavity can drift beyond this in around an hour. It is also not ideal to have a drifting cavity for the lattice laser lock. In future we intend to lock the cavity to a stable reference, either by

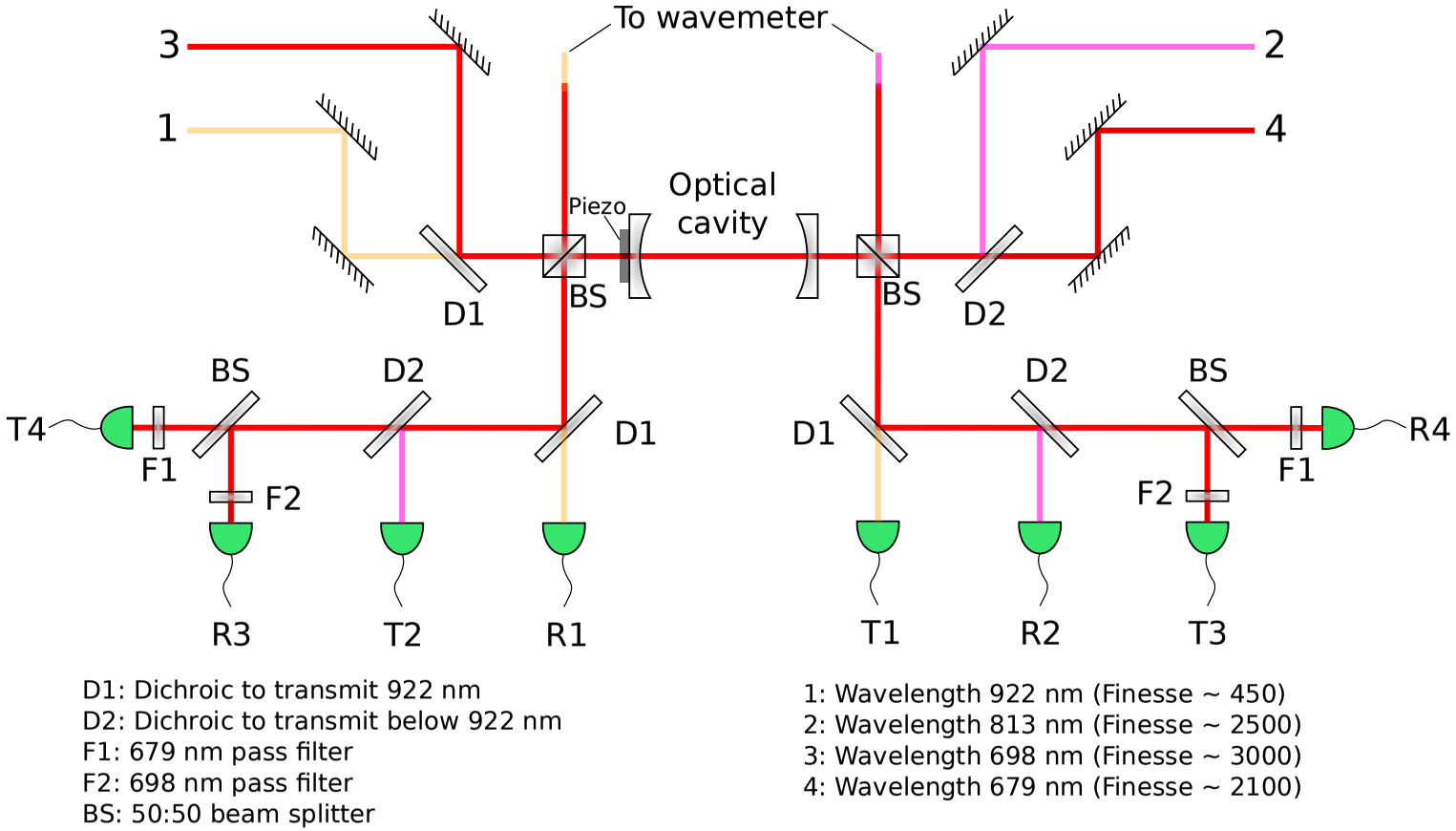

Figure 4.5: **Multi-wavelength lock schematic** - Proposed lock schematic for locking four wavelengths to one tunable optical reference cavity. At present the 922 nm and 679 nm lasers are locked and the 813 nm laser is being set up. The 698 nm laser shown here is an option we are considering to stabilise the cavity length in the longer term. Figure adapted from [55], with thanks to I.R. Hill.

locking the 461 nm laser frequency to the atomic resonance feature, and locking the length of the optical cavity to the 922 nm laser light, or by locking the cavity to the clock laser, which is in turn locked to its low drift cavity. The clock laser light could be sent to the cavity as the fourth wavelength in figure 4.5, and would provide a frequency reference with a drift less than 3 kHz in 24 hours.

4.3 BBR shift measurement proposal

As explained in section 2.4.1.2, at NPL we are making an experimental apparatus to directly measure the total BBR frequency shift for Sr atoms. We intend to benefit from the BBR shift's $\sim T^4$ dependence, shown in equation 2.10, by increasing the temperature of the atomic environment to increase the frequency shift. We have designed our system to have two black-body environments (tubes) (see figure 4.6), which will be stabilised to different temperatures. The atoms will be moved into the 'hot' ('cold') tube by a transport lattice and a frequency measurement made. This measurement will be compared to one made in the other, 'cold' ('hot'), tube. The frequency difference between the two measurements will be ~ 5 - 10 Hz, depending on the temperatures chosen, and in practice will be measured by the shift in AOM frequency required to jump between the two situations. For accurate measurement of the frequency shift, the AOM drive frequency will be referenced to the hydrogen maser.

To transport the atoms into and out of the tubes we considered using an electro-mechanical translation stage to move the lattice optics and transport the atoms while they are trapped in the magic wavelength lattice, but we decided against this for two reasons. We wished to benefit from the reduced tunnelling between sites provided by a vertically-orientated lattice [118], and we wished to keep the duty cycle low (on the order of a second) to benefit from the increase

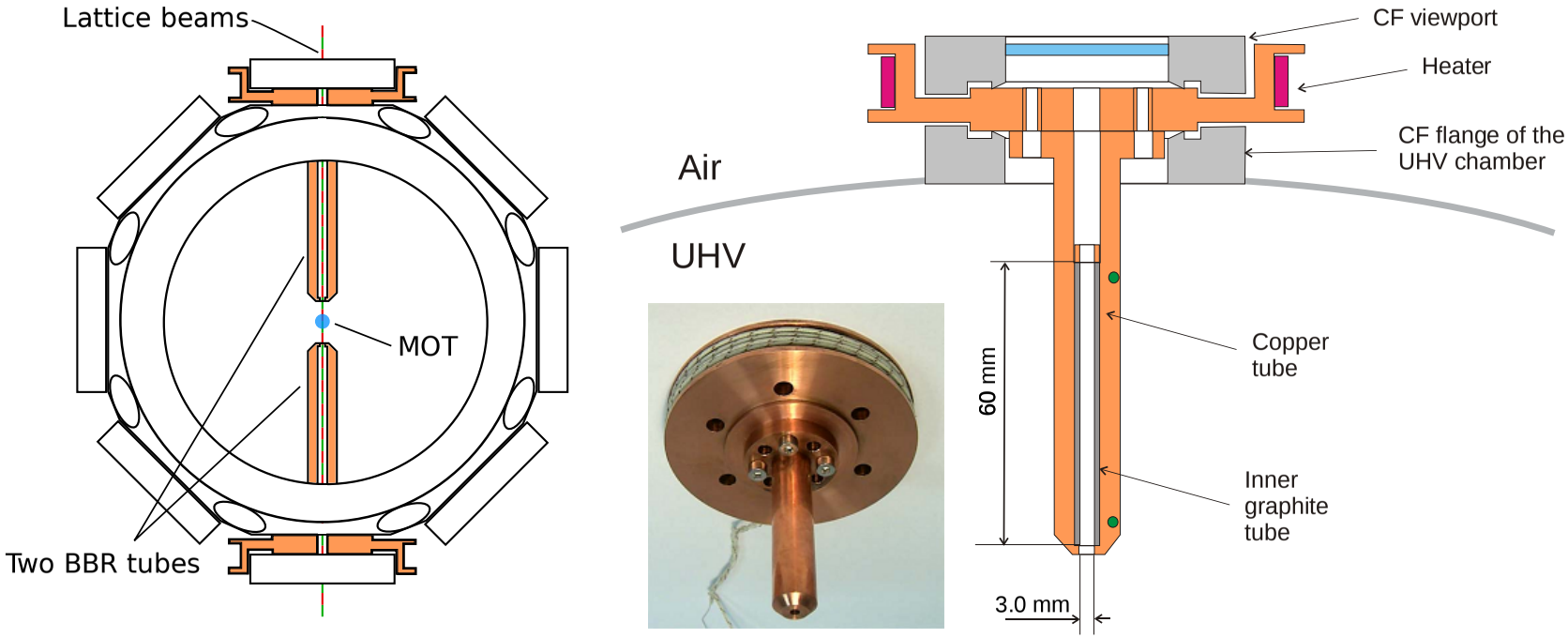

Figure 4.6: **BBR shift measurement apparatus** - Two black-body environments (tubes) made from copper, to benefit from its high thermal conductivity, with graphite inserts to create black-body environments for the atoms. The two tubes are held at different temperatures to facilitate a differential measurement of the frequency shift of the clock state due to black-body radiation. The atoms are trapped and cooled in the two-stage MOT before being loaded into the 532 nm lattice for transport into the centre of one of the BBR tubes. See text for full explanation.

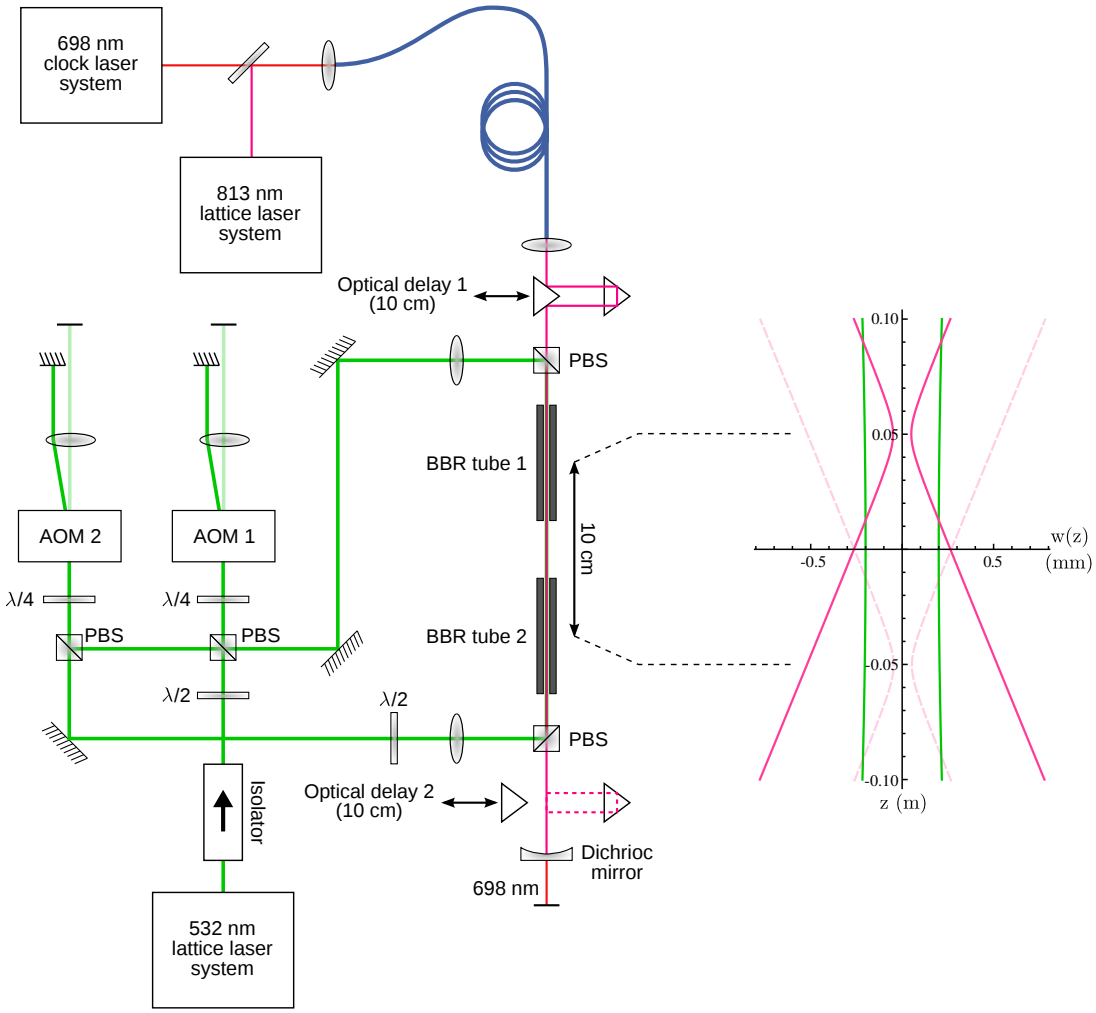

Figure 4.7: **Optical lattice set-up for BBR shift measurement** - The 532 nm lattice has a large waist and Rayleigh range to allow for effective trapping in both BBR tubes. The 813 nm lattice has a much smaller waist and Rayleigh range for tighter confinement during the clock excitation, with an optical delay line to move the beam waist from one BBR tube to the other between measurements. The AOMs control the frequency of each 532 nm lattice beam for transportation of the atoms trapped in the lattice. Figure taken from [55], with thanks to I.R. Hill.

in stability this provides. We could not find an electro-mechanical translation stage to meet such requirements. Instead we chose to transport the atoms using a travelling optical lattice. The lattice will be formed of two counter-propagating laser beams, the frequency of which can be independently controlled. Detuning the frequency of one of the transport lattice beams will provide a travelling wave to move the atoms. The lattice beam frequencies will be controlled by double-passed AOMs (see figure 4.7), with the transport velocity dictated by $\Delta\nu$, the frequency difference between the two beams:

$$v_{\text{trans}} = \frac{\lambda}{2}\Delta\nu \tag{4.6}$$

We plan to transport the atoms a distance of 5 cm within 20 ms, with a maximum acceleration of $\sim 40\,g$ and a maximum velocity of $\sim 4\,\text{m/s}$.

Due to lack of power at the magic wavelength ($\sim 500\,\text{mW}$ at 813 nm) and the large distance we wish to move the atoms ($\sim 10\,\text{cm}$ in total) we decided to use a separate lattice to transport the atoms and transfer them into the magic lattice for excitation of the clock transition. This transport lattice does not need to be at the magic wavelength, so can be at a wavelength where high power lasers are readily available, providing it is still red-detuned from the main 461 nm transition to provide trapping in the high intensity regions of the lattice. It is also important that the chosen wavelength traps both ground and excited states of the clock transition with near equal depth, since we wish to transport the atoms back to the chamber centre after clock excitation for state interrogation.

We have chosen a 10 W, 532 nm Verdi laser to provide the light to make our transport lattice. The polarisabilities for the two clock states are given in table 4.3, and the trap depths for each state can be worked out using equation 2.2 or 4.1. Choosing this shorter wavelength also makes it easier to achieve a long

λ (nm)	Waist (μm)	Power (mW)	Rayleigh range (cm)	State	Polarisability (atomic units)	Trap depth (E_R)	Trap depth (μK)
813	50	300	0.97	$^1S_0$	285	120	20
				$^3P_0$	285	120	20
532	200	3000	23.6	$^1S_0$	760	85	33
				$^3P_0$	420	47	18

Table 4.3: **Lattice trap parameters** - Approximate proposed values for lattice traps at 813 nm (magic wavelength lattice) and 532 nm (transport lattice).

Rayleigh range for good trapping along the whole 10 cm transport length:

$$z_R = \frac{\pi w_0^2}{\lambda} \tag{4.7}$$

where w_0 is the laser beam waist (radius) at the focus. A shorter Rayleigh range is needed for tighter confinement in the magic wavelength lattice, the focus of which needs to be in the centre of the interrogation region, see figure 4.7. The proposed order of sequence is as follows:

1. Trap and cool atoms in the chamber centre (first and second MOTs)
2. Load atoms into 532 nm transport lattice
3. Transport atoms up (down) 5 cm to centre of hot (cold) BBR tube
4. Transfer atoms to focus of 813 nm magic wavelength lattice
5. Excite a fraction of the atoms with the clock laser
6. Transfer atoms back into 532 nm transport lattice
7. Transport atoms back to chamber centre and perform state interrogation
8. Switch in (out) optical delay line
9. Repeat with second cold (hot) BBR tube.

In order to repeat this sequence in the second tube the location of the 813 nm lattice focus will need to be moved. We plan do do this with an optical delay line, as shown in figure 4.7.

4.4 Conclusions

In this chapter we have detailed our plans and proposals for second-stage cooling and the necessary lattice trapping required for clock frequency measurements and the study of the black-body radiation shift. We have detailed the experimental progress made on these fronts, the majority of which has been towards developing and testing the 689 nm laser system. The work involved in building and locking this 689 nm laser system became the test-bed for design and build of the 698 nm clock laser systems as detailed in chapter 5. The combination of the work with these narrow linewidth laser systems and the experiments run on the permanent magnet Zeeman slowers, along with helping to develop the over-all project plans, make up the majority of the author's contribution to the work discussed in this thesis.

The next step with regard to the parts of the experiment covered in this chapter is to begin loading ^{88}Sr into the narrow-line MOT. We do not anticipate this step being easy, and expect it to take some time to optimise the MOT parameters for best atom number, density and temperature. While we are working on this we will build the stirring laser set-up, lock the 813 nm laser to the optical reference cavity, and set up the remainder of the lattice optics. We need to demonstrate that the lattice transport proposal is feasible in terms of loading from one lattice to the other, maintaining a high proportion of trapped atoms in the 'hot' BBR tube with its consequential higher vacuum pressure, and transporting a mixture of ground and excited state atoms without distortion of the excited state frac-

tion. Once we have atoms trapped in the 813 nm lattice we can begin to excite the clock transition, for which we need a narrow-linewidth clock laser. Experimental details of the clock laser set-ups are discussed in depth in the next chapter.

Chapter 5

Narrow linewidth clock lasers at 698 nm

As detailed in chapter 2 the linewidth of the clock transition in neutral strontium is around 1 mHz in ^{87}Sr (or user-defined in ^{88}Sr [119]). This transition linewidth sets the theoretical quantum projection noise limit for our frequency standard (see equation 1.1), but, as discussed in section 1.4.4, the achievable stability is limited by the clock laser noise.

The most frequency-stable lasers used in optical clock set-ups today have linewidths of around a hundred millihertz [120], a value which is predominately limited by thermal noise on the optical reference cavity mirrors - we will go into more details on this later. The wavelength of these lasers is stabilised to high finesse optical reference cavities via the Pound-Drever-Hall technique [98].

In this chapter we cover details of the narrow-linewidth lasers we are building to drive our clock transition, with details of the equipment and techniques required to achieve such narrow laser linewidths. In particular we discuss the extended cavity diode lasers (section 5.1) which are locked to ultra-stable, high finesse, optical reference cavities (section 5.3) via the Pound-Drever-Hall technique

(section 5.2). We go into detail on the stages of the experiment accomplished so far and discuss the proposed steps for completion of the work. We are building two complete, independent systems to enable us to characterise our lasers, and in particular, measure the locked laser linewidth via beat frequency comparison.

5.1 Extended cavity diode lasers

The clock transition wavelength is $\sim 698.4\,\text{nm}$ (in vacuum). Laser diodes are commercially available at or around this wavelength, providing powers up to $\sim 30\,\text{mW}$. Laser diodes typically have a natural lasing range of a few nanometres, this can be tuned a small amount by adjusting the temperature of the diode. Typically the front facet of the laser diode acts as a low reflectivity mirror providing optical feedback to the lasing medium. The length of this low finesse optical cavity (along with other characteristics of the gain medium) defines the wavelengths at which the diode will preferentially lase. One could tune the temperature of this diode to encourage it to lase at the required wavelength, but in practice the short cavity length (a few millimetres) and the competing modes in this cavity make for an unstable laser.

The most common way to improve the stability of a laser diode (in the first instance) is to extend the cavity length and to feedback only a single frequency to the laser diode gain medium. Extending the cavity length (usually from a few millimetres to a few centimetres) reduces the effect that small changes in the cavity length have on the wavelength:

$$\frac{\Delta L}{L} = \frac{\Delta \lambda}{\lambda} = -\frac{\Delta \nu}{\nu} \tag{5.1}$$

Using a low reflectivity mirror as the extended cavity reflector would still have the

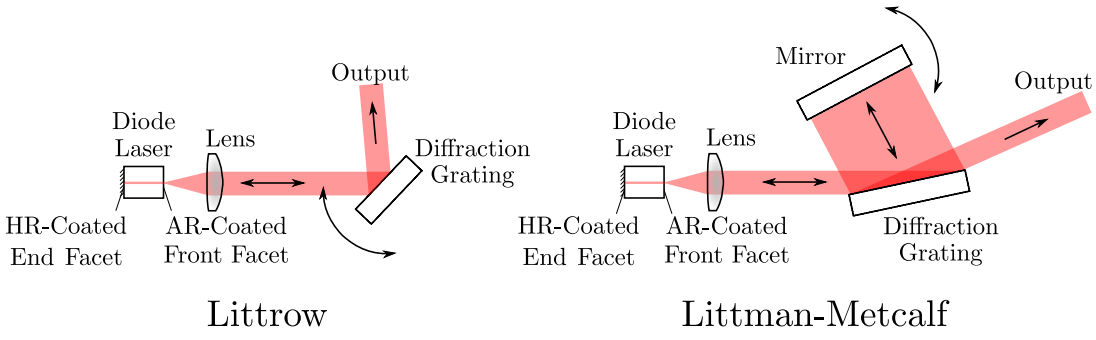

Figure 5.1: **Littrow and Littmann-Metcalf ECDL configurations** - the ECDLs used in this thesis are all of the Littrow configuration.

problem of competing cavity modes, so instead we use an angle-selected narrow-band diffraction mode from a diffraction grating. There are two commonly used configurations for ECDLs with diffraction grating feedback; Littman-Metcalf and Littrow, both of which are shown in figure 5.1.

The Littrow configuration is the simplest design, with the first diffraction order directed back to the diode and the zeroth order reflected out of the ECDL for use in the experiment. This provides single frequency feedback to the laser diode and generally results in single-mode lasing with a linewidth on the order of a few hundred kilohertz. The main drawback of this configuration is that tuning of the diffraction grating angle to change the laser wavelength has the undesirable consequence of changing the angle of the output beam, making it necessary to realign the optical set-up. This is only usually a problem when gross frequency tuning is taking place during the initial set up of the ECDL, but this can still cause great frustration to the user. This can be solved by coupling an output mirror to the diffraction grating, as shown in figure 5.2. The output mirror (fixed in location with respect to the diffraction grating) translates a change in angle to a tiny spatial translation of the laser beam position. This requires little or no realignment of the optical set-up, as demonstrated by our laser design (detailed in section 5.1.1) which tunes a number of nanometres while maintaining alignment

into a single core optical fibre to a wavemeter. This aspect of the design is very useful for our lattice laser, as discussed in section 4.2, which we will need to tune over a wide range of wavelengths while maintaining alignment into the tapered amplifier and optical reference cavity.

The Littman-Metcalf configuration also solves the beam steering problem described above as well as having the additional benefit of narrower wavelength selection. The laser light is diffracted off the grating twice (first order diffraction to the mirror, then first order diffraction back to the diode) before feeding back to the diode. This double diffraction results in a narrower inherent linewidth of the ECDL. The disadvantage with this design is that it results in lower output beam powers due to the light lost to the zeroth order diffraction on the second pass of the diffraction grating.

Despite the efforts made to enable the user to select the lasing frequency of their laser diode there is still a problem of competing modes due to reflections from the diode front facet. These competing modes can cause the laser frequency to be pulled away from the required lasing frequency and cause the laser to mode-hop and behave in an undesirable manner. In order to aid single-mode lasing an anti-reflection coating is usually applied to the diode front facet, reducing the reflectance to around 10^{-3} to 10^{-5} depending on the quality of the coating.

5.1.1 Clock ECDL Design

The ECDL design is by I.R. Hill [55] and is shown in figure 5.2. The main design features are the near-monolithic aluminium cavity for reduced vibration sensitivity and increased temperature stability, the output coupling mirror, and the diffraction grating arm pivot point being positioned at the mode-hop-free tuning point [121]. This optimal choice of pivot point allows us to tune the laser

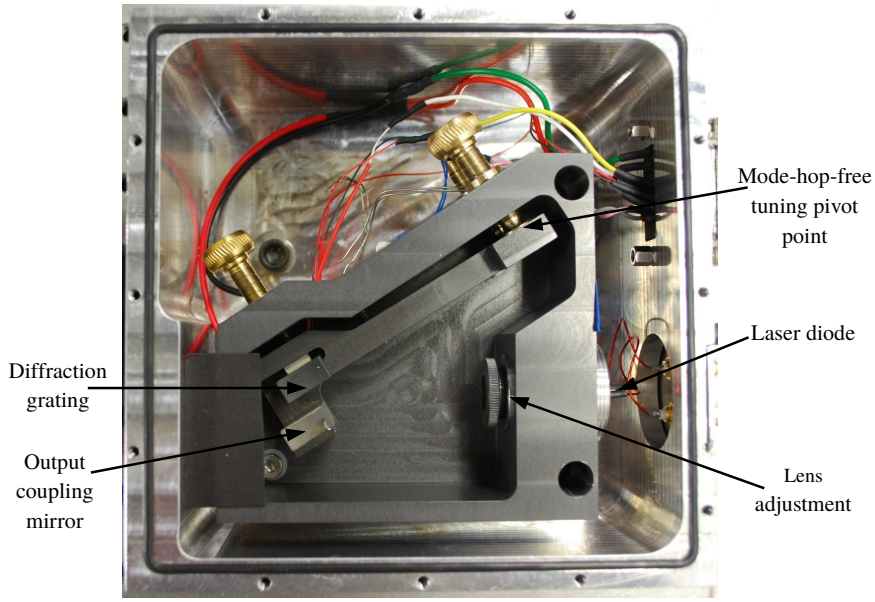

Figure 5.2: **Clock extended cavity diode laser** - Photograph of constructed ECDL.

up to 50 GHz mode-hop-free with no current feed-forward to the diode; making this competitive with commercial ECDL designs. The lens adjustment is more user friendly than any commercial design we have seen. It uses a fine thread to adjust the distance from the laser diode and has no x or y adjustment. We have not found the lack of x or y adjustment a problem, in fact we have found these extra degrees of freedom difficult to reliably tune in other ECDL designs. The ECDL is housed in a near-hermetically sealed aluminium box, the lack of air flow around the ECDL aids the temperature control and reduces refractive index changes (effective length changes) within the cavity. These ECDLs have been shown to have a free-running linewidth of less than 100 kHz (by heterodyne beat note comparison), see figure 5.3, and are also stable in the long term, drifting only a few MHz in about an hour.

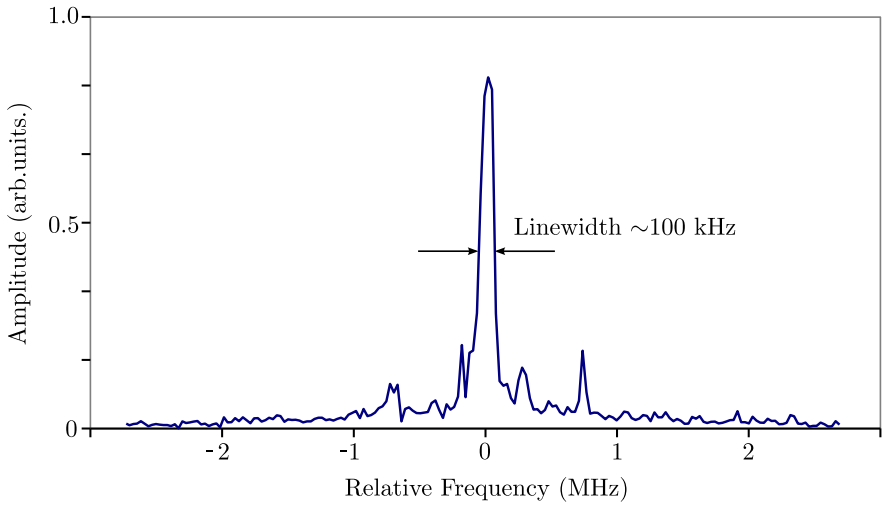

Figure 5.3: **Beat note between two free-running (unlocked) clock ECDLs** - Beat linewidth is typically $\sim 100\,\text{kHz}$, which is likely due to technical noise from the drive electronics. If we assume equal noise contributions from each laser and an approximate profile of a Gaussian this gives us a free-running ECDL linewidth of 70 kHz ($100/\sqrt{2}$).

5.1.1.1 ECDL Electronics

The laser diode temperature is controlled by the peltier between the ECDL and the ECDL box. There are two thermistors (one for the feedback circuit and one for monitoring) and one controller containing the rest of the Wheatstone bridge, bridge amplifier, PI (proportional-integral) feedback loop, transistor power stage and the linear power supply, see figure 5.4. The PI gain settings were calculated using the transfer function method we developed. This method was first suggested to us by S.A. Webster for choosing laser lock gains, and was developed and tested by us for selecting the gains for temperature control servos. To find the transfer function of the system one simply by-passes the PI section of the electronics and measures the system response (gain and phase) at the bridge amplifier output while the output stage is driven by sine waves at a range of frequencies. Recording the system response (at the bridge amplifier output) al-

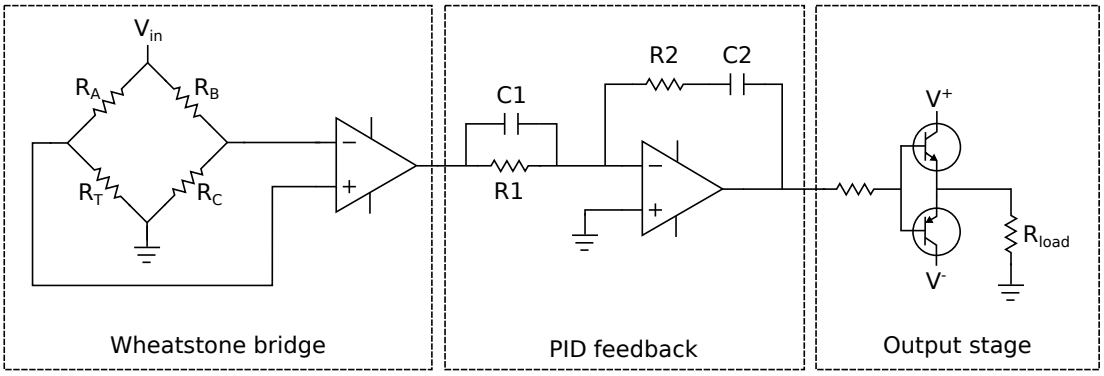

Figure 5.4: **Temperature controller schematic** - Temperature controllers for the ECDLs, cavity vacuum chambers and other apparatus are based on this layout. The Wheatstone bridge is balanced if $\frac{R_T}{R_A} = \frac{R_C}{R_B}$ (R_T is the thermistor), otherwise the amplifier sends a non-zero voltage to the PID section. It is wise to place at least some of the Wheatstone bridge resistors (R_A, R_B, and R_C) in a temperature stable environment, as temperature changes with cause resistance changes, which change the set-point of the temperature controller. For the clock cavity vacuum temperature control, described in section 5.3.4.3, resistor R_C is housed in the temperature stabilised environment. For the 689 nm cavity temperature control the whole bridge and amplifier circuit are housed in the temperature-stabilised environment, see section 4.1.2. The gains for the PID feedback are carefully chosen to suit the system being temperature controlled (see sections 5.1.1.1 and 5.3.4.3). The output stage will vary depending on the system being controlled; here R_{load} represents a peltier for heating or cooling, alternatively a single ended output stage with resistive heater wire can be implemented.

lows us to construct a Bode plot for our set-up. The theoretical gain and phase response of the PI feedback section of the circuit can be calculated based on the resistor and capacitor configuration e.g. the gain and phase for the PID section of the circuit shown in figure 5.4 is given in equations 5.2 and 5.3 respectively.

$$|G| = -\sqrt{\left(\frac{C_1}{C_2} + \frac{R_2}{R_1}\right)^2 + \left(\omega C_1 R_2 - \frac{1}{\omega C_2 R_1}\right)^2} \tag{5.2}$$

$$\phi = \tan^{-1}\left(\frac{\omega C_1 R_2 - \frac{1}{\omega C_2 R_1}}{\frac{C_1}{C_2} + \frac{R_2}{R_1}}\right) \tag{5.3}$$

Using equations 5.2 and 5.3 and the measured system response we calculate

the total gain and phase (multiply gains and add phases) response we expect for the whole set-up based on the chosen values of R_1, R_2 and C_2 (set C_1 to zero and remove the capacitor if no D is required). The resistor and capacitor values in the calculation are tuned until we get the desired gain and phase response. The ideal response is to have high gain at low frequencies and to make sure the gain rolls off to below unity when the total phase reaches $-180°$ (a gain of greater than unity beyond the 180° phase point will result in oscillations). We also need to ensure suitable gain and phase margins are maintained close to the $-180°$ phase point to ensure feedback loop stability. It is usual to allow a 45° phase margin and maybe a small gain margin. For our Bode plots see figure 5.5.

The PI parameters for the clock ECDL temperature controllers were calculated using this method and the first calculated values ($R_1 = 2.2\,\mathrm{M\Omega}$, $R_2 = 1.5\,\mathrm{M\Omega}$ and $C_2 = 66\,\mu\mathrm{F}$) gave a temperature stability of better then 50 mK over 24 hours. The short term stability (around 1 hour) was better than 5 mK, and removing the ECDL box lid had little effect on the temperature other than to make the signal slightly noisier. On longer time scales we observed temperature jumps of $\sim 50\,\mathrm{mK}$ at random intervals, these could be due to temperature fluctuations in the bridge resistors (including set-point potentiometer) or ground level fluctuations. We have since seen significant changes in the set-point temperature (up to 1 °C!) from removing the side panels of the case housing the electronics. This effect is due to the warm power supply being housed in the same case as the bridge resistors, which have some temperature dependence. This is not an ideal set-up and we intend to rectify this in the near future.

We have used our transfer function technique to good effect for temperature stabilising a number of systems (including various ECDLs and the 689 nm optical cavity vacuum chamber), it has proven to be significantly faster to implement and

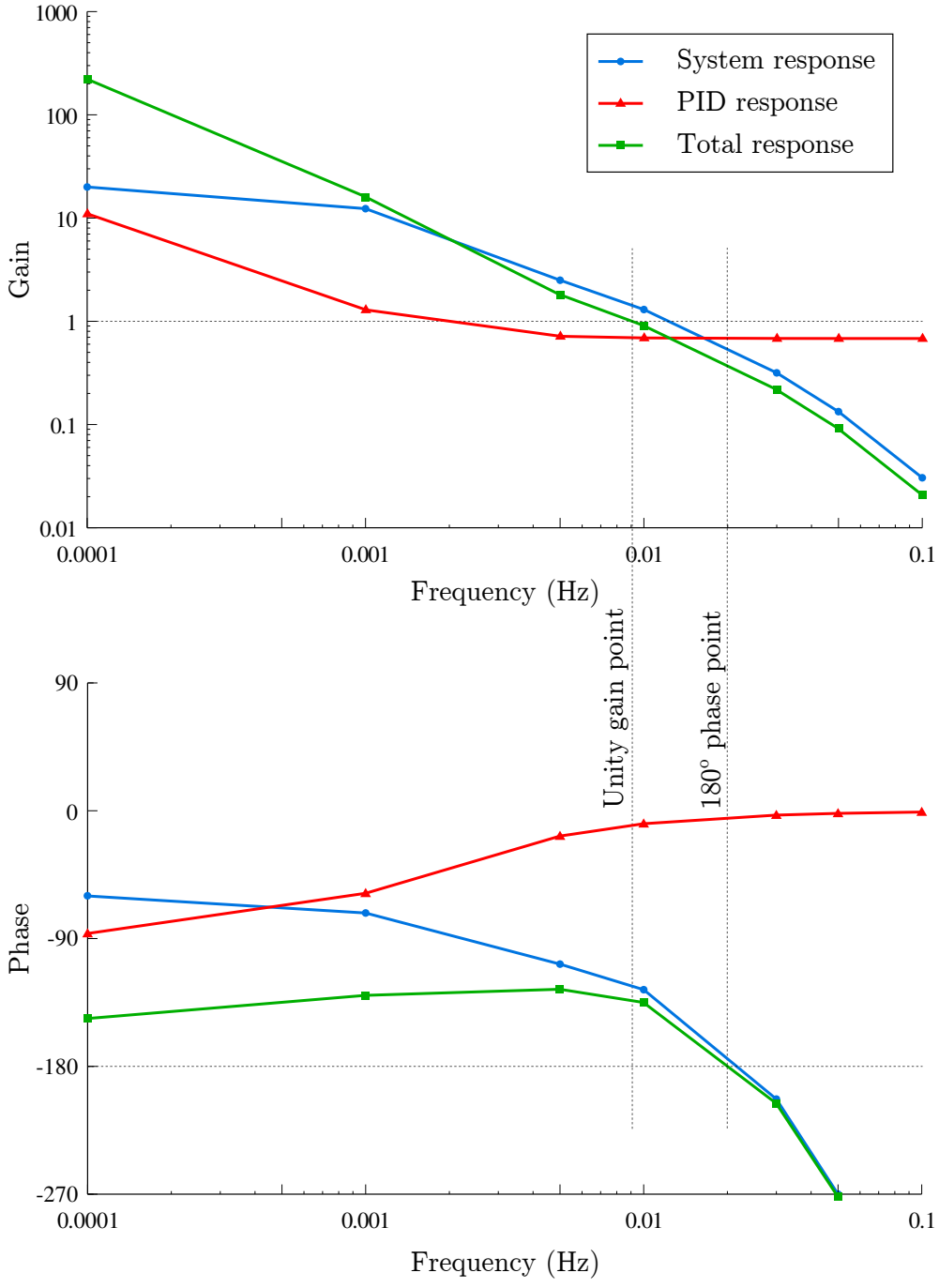

Figure 5.5: **Bode plots for ECDL temperature control** - Gain and phase response of the system as a function of frequency; plus the calculated PI feedback response and the calculated combined total.

gives more stable temperature control than the closed-loop Ziegler Nichols method outlined in section 5.3.4.3. We also use this same transfer function technique for choosing the gain parameters for our PDH (Pound Drever Hall [98]) stabilisation of the laser frequencies, see section 5.2.1.4 for more details.

5.2 Pound-Drever-Hall laser locking

Our extended cavity diode lasers (ECDLs) have a free-running lasing linewidth of around 70 kHz at one second and a drift rate of a few megahertz per hour. With appropriate active feedback to the laser diode and the ECDL diffraction grating angle it should be possible to reduce this linewidth to less than one Hertz at one second and the drift rate to around one hundred Hertz an hour (this drift rate is usually predominantly linear, so can also be corrected for once characterised, see section 5.4). In order to narrow the laser linewidth and to stabilise the frequency drift we use the Pound Drever Hall frequency stabilisation technique [98] to 'lock' the laser frequency to that of a resonant mode of an optical reference cavity. The optical reference cavity is explained in section 5.3. In summary the cavity provides a very stable, spectrally narrow frequency reference.

The Pound Drever Hall technique is already explained very well in a number of alternative references: [98] is the original paper; for a conceptual outline see [122] and [123]; for a hands-on guide see [124]. Here we will outline the basic concept and spend more time on the experimental and technical details necessary for achieving a stable and robust lock.

For mid-to-low finesse cavities, aligning our laser into the optical cavity and scanning its frequency will give transmission modes similar to those shown in figure 5.14. For higher finesse cavities it is essentially the same, but the laser linewidth is broader than the cavity linewidth, so power build-up inside the cavity

fluctuates and the transmission signal becomes jittery. If for now we imagine a lower finesse cavity, then when our laser is exactly on resonance with one of the cavity modes the cavity transmission will be a maximum. If the laser frequency drifts slightly the transmission will decrease, the magnitude of the decrease tells us how far off resonance we have moved. We wish to use this change in transmission to correct for the laser frequency drift, but due to the symmetry we do not know which way the laser frequency has moved. If we dither our laser frequency we will see the transmission increase and decrease at the dither frequency, and a comparison of the phase of the transmission signal and the dither signal will tell us which way our laser has drifted, so in which direction we need to apply the correction. This is the gist of Pound-Drever-Hall locking, but instead of dithering the frequency we modulate the phase of the light (at a frequency of a few megahertz) and we use the cavity reflection signal rather than the cavity transmission, so when on resonance we see a minimum in place of the maximum.

5.2.1 Clock laser set-ups

The optical set-up used for Pound-Drever-Hall locking is shown in figure 5.6. Describing the optical set-up in order we have the ECDL, described in section 5.1.1, followed by an anamorphic prism pair to shape the beam, an optical isolator to prevent unwanted optical feedback to the laser diode, then a half-waveplate and a polarising beam-splitter cube to split the light power for the various parts of the experiment. For the PDH locking we only need a few microwatts of light incident on the first cavity mirror, but to set up the optics and initial lock it is easier to start with slightly more power. We require at least 1 mW of light going into the fibre to the optical frequency comb laboratory and ~ 1 mW into the fibre for the atomic spectroscopy. The light directed to the optical reference

cavity is double-passed through AOM1; this AOM (acousto-optic modulator) will be used to correct for the cavity drift relative to the atoms (see "Locking to the clock transition" in section 2.3.1) and for intensity stabilisation of the light to the optical reference cavity (see section 5.2.1.5). The electro-optic modulator (EOM) is used to phase modulate the light at a frequency of $\sim 10\,\mathrm{MHz}$ for the PDH locking (see section 5.2.1.2). The Glan-Thompson (GT) polariser prior to the EOM cleans up the light polarisation and ensures alignment to the EOM crystal axis, see section 5.2.2.1 for more details. The lens is for mode-matching the incident laser beam mode to that of the cavity for efficient coupling (for information on mode-matching the reader is referred to the work of Kogelnik and Li [125]). The polarising beam splitter (PBS) cube and the quarter waveplate are used to separate the reflected cavity light from the incident light. The reflected light, which contains the lock signal, is directed onto a fast photodiode, here we use a home-built avalanche photodiode (APD), but one could equally use a commercial product, such as Thorlabs PDA10A-EC or similar. The cavity transmission is also monitored for simple diagnostics and to tell if the laser is locked; for this we use fast amplified photodiodes (for example, part numbers TSL12S to TSL14S from TAOS). It is also useful to observe the cavity transmission on a CCD camera, especially during the set up stages. The CCD shows the Laguerre-Gaussian modes of the cavity transmission, which are a useful aid for initial alignment to the high finesse cavity and to confirm the laser is aligned and locking to the TEM_{00} mode.

We have kept the beam path as short as we can to reduce the effect of beam pointing instabilities due to mechanical drift of the optics mounts. The laser, optics, and optical reference cavity are compactly mounted on a $50\,\mathrm{cm} \times 60\,\mathrm{cm}$ optical breadboard, which is part of an active vibration isolation (AVI) platform from Table Stable Ltd. (see figure 5.18 (d)). The AVI actively reduces vibrations

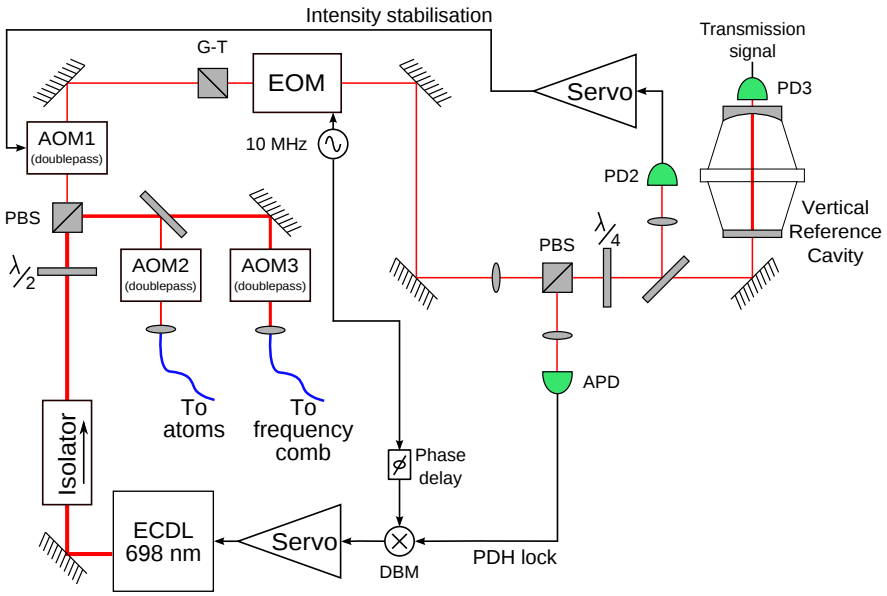

Figure 5.6: **Clock laser set-up** - Showing significant optical and electrical elements of the set-up. Key of terms: ECDL = extended cavity diode laser; $\lambda/2$ and $\lambda/4$ are half and quarter waveplates; PBS = polarising beam splitter cube; AOM = acousto-optic modulator; G-T = Glan-Thompson polariser; EOM = electro-optic modulator; PD = photodiode; APD = avalanche photodiode; PDH = Pound Drever Hall technique; DBM = double balanced mixer. Red lines indicate laser beam paths, black lines indicate electronic signal paths, blue lines are polarisation maintaining optical fibres. More details of the "servo" are given in figure 5.9.

in the 1 Hz - 200 Hz range, reducing laser noise, and hence linewidth, within this frequency range. Once the system is complete we will design a box to go around the entire set-up to reduce temperature and air pressure fluctuations, and acoustic vibrations, all of which affect the lock performance and long-term stability.

5.2.1.1 AOM configuration

We have designed the AOM configuration shown in fibre 5.6 to provide the appropriate frequency and intensity of light to the relevant areas of the experiment. AOM1 is used to intensity-stabilise the light to the optical reference cavity. The purpose of AOM3 is for fibre-phase-noise cancellation of the laser light sent to the optical frequency comb laboratory. The optical fibre naturally imprints phase-noise on the light, acting to broaden the sub-hertz linewith laser to a linewidth of a few tens or hundreds of hertz after a few metres of optical fibre [126]. The technique of fibre-phase-noise cancellation is described by Ma et al. [126], where they demonstrate noise cancellation to millihertz accuracy.

AOM2 is used to bridge the frequency gap between that of the locked ECDL and the atomic clock transition frequency. We will feedback to the drive power of AOM2 to stabilise the intensity of the light reaching the atoms and feedback to the frequency for fibre-phase-noise cancellation. We will also switch the frequency of this AOM to jump from one side of the atomic transition to the other, as described in section 2.3.1. The frequency correction required to 'lock' the laser to the atoms (see section 2.3.1) can be applied to AOM2 or, preferably AOM1. In order to make an accurate clock frequency measurement it is imperative that the frequencies of AOM2 and AOM3 are well known at all times i.e. the frequency difference between the light reaching the atoms and that measured by the optical frequency comb. It is for this reason we recommend using AOM1 for the lock feedback, leaving the

frequencies of AOM2 and AOM3 fixed apart from the jumping signal applied to AOM2.

The AOM frequencies will be controlled by direct digital synthesisers (DDS) which will be referenced to the hydrogen maser. The DDS we have chosen for this application is part number AD9912 from Analog Devices; it has a 14 bit, 1 giga-sample per second digital to analog converter and a 48 bit frequency-tuning word, offering 4 µHz resolution.

5.2.1.2 EOM for phase modulation

The electro-optic modulator phase modulates the light, at $f_m \simeq 10\,\mathrm{MHz}$ in our case, with a modulation depth $\delta \simeq 1$. The mathematics of phase modulation is covered in [15] and [123]; we will not go into it in detail here. A phase-modulated cosine wave can be represented as follows:

$$A = A_0 \cos\left[2\pi\nu t + \delta\cos\left(2\pi f_m t\right)\right] \tag{5.4}$$

where A is the electric field amplitude, ν is the laser frequency, and t is time. With a significant amount of re-arranging and re-working, and setting $\delta \leqslant 1$ [15] we can write this as:

$$A \simeq A_0\left[J_0\left(\delta\right)e^{i2\pi\nu t} + J_1\left(\delta\right)e^{i2\pi(\nu+f_m)t} - J_1\left(\delta\right)e^{i2\pi(\nu-f_m)t} + ...\right] + c.c.... \tag{5.5}$$

where J_n are the n th order Bessel functions. In the frequency domain this represents a carrier with sidebands at the modulation frequency and its harmonics. As we can see, the first-order sidebands created by phase-modulation are 180° out of phase with one another, with one of them in phase with the carrier. Choosing our modulation depth to be approximately equal to one ($\delta \simeq 1$) results in first-order

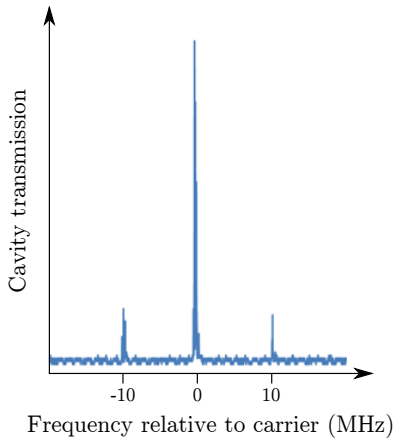

Figure 5.7: **Phase modulated light spectrum** - High finesse cavity transmission signal showing carrier and first-order sidebands. Measured by scanning the free-running laser frequency across the cavity mode.

sidebands that are $\sim 33\,\%$ of the carrier power and second-order sidebands that are only $\sim 2\,\%$ of the carrier power. Due to their small size and negligible effect we can neglect second-order and higher-order sidebands. Scanning our phase modulated light across a cavity mode allows us to see the frequency spectrum of the light, see figure 5.7 for an example.

The EOM is custom built for NPL by Leysop, it contains two Brewster-cut ADP crystals. Brewster-cut crystals are preferable for their low reflection levels from each surface, this helps prevent parasitic etalons, see section 5.2.2.2, and residual amplitude modulation caused by multiple crystal passes [127], see section 5.2.2.1. The EOM is driven by a FET (field-effect transistor) oscillator circuit, which is driven by a high voltage DC supply. The modulation depth can be controlled by changing the drive voltage to the FET oscillator.

5.2.1.3 PDH error signal

To produce the PDH error signal the reflected cavity light is detected on the APD, see figure 5.6, and this signal is demodulated at the double balanced mixer

(DBM) by mixing it with the modulation frequency used to drive the EOM. Mathematically, mixing the appropriate phase signals, results in an error signal of the form [15]:

$$\xi(\Delta\nu) \propto \frac{f_m^2\,(\gamma/2)\,\Delta\nu\left[(\gamma/2)^2 - \Delta\nu^2 + f_m^2\right]}{\left[\Delta\nu^2 + (\gamma/2)^2\right]\left[(\Delta\nu + f_m)^2 + (\gamma/2)^2\right]\left[(\Delta\nu - f_m)^2 + (\gamma/2)^2\right]} \tag{5.6}$$

where γ is the cavity mode linewidth (or atomic transition linewidth if we are locking to an atomic line). Figure 5.8 shows an experimental realisation of this asymmetric error signal. It is important to get the relative phase correct before mixing to produce an appropriate error signal, so a tunable phase delay is placed between the EOM drive electronics and the mixer. The phase delay can simply be a long length of RF cable, or we use a Mini Circuits phase shifter (part number JSPHS-12 on evaluation board TB-122). The correct error signal is found by scanning the laser over the cavity fringe and adjusting the phase delay while observing the resulting demodulated signal. The optimum error signal is achieved 90° out of phase with the point where the carrier part of the error signal disappears, see [15] and [124] for pictures and more details on this. Depending on the phase set-point there are two such error signals, one which has the correct phase to cause the laser to lock to the carrier and the other, which is 180° out, will attempt to lock to the sidebands.

5.2.1.4 PDH lock electronics

The basic electronics required for PDH locking are shown in figure 5.6. The EOM drive electronics are explained in sections 5.2.1.2 and 5.2.2.4; the phase delay is a Mini Circuits JSPHS-12, the APD is a home-built NPL design, the double balanced mixer is a Mini Circuits ZRPD-1+ and the servo electronics are home-built. The servo electronics, also referred to as the loop filter, are outlined

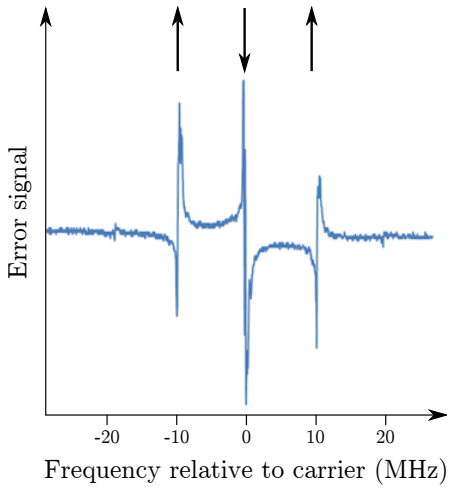

Figure 5.8: **PDH error signal** - Demodulated PDH error signal showing carrier discriminator out of phase with sideband discriminators. Taken by measuring the DBM output as the free-running laser frequency is scanned over the cavity mode.

in figure 5.9; they process the PDH signal so that it has the required offsets and gains for locking. The first stage of signal manipulation is to apply a variable, stable voltage offset to the error signal to cancel electrical offsets. Secondly we have a PID gain stage, then the signal is split to separately drive the laser diode current and the ECDL diffraction grating piezo voltage. The laser diode receives fast-feedback (up to hundreds of kilohertz or a megahertz bandwidth) via the current controller modulation input. This does the majority of the work for the lock so it is important to maintain a high bandwidth for this portion of the feedback. The ECDL diffraction grating piezo receives the slow-feedback (up to $\sim 1\,\mathrm{kHz}$ bandwidth) via another double integrator stage. This is for slower drift corrections and does not contribute to the bandwidth of the lock.

Careful choice of the PID gains in the fast section of the lock is essential for a good laser lock (achieving narrow linewidth and perturbation insensitivity). For this we use a very similar method to that described in section 5.1.1.1 for choosing the gains of a temperature servo. To find the frequency response of the laser (the diode and its current controller) we align the laser into a low finesse cavity (a

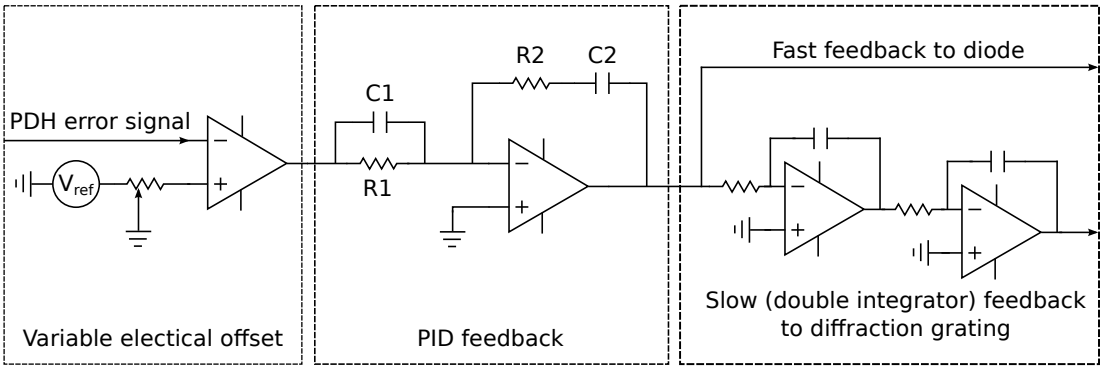

Figure 5.9: **PDH lock electronics** - Schematic outlining circuitry contained in the "servo" shown in figure 5.6.

finesse of a few hundred or less is ideal) and set the laser frequency so that we are sitting on the side of a cavity fringe. We apply a small sine wave modulation to the laser diode current and measure the amplitude and phase of the resulting modulation of the cavity transmission (or reflection). The observed photodiode signal is in units of V/V (voltage change per volt input), we can convert this to the desired units of Hz/V (frequency change per volt input) by calibrating the cavity discriminator slope. We measure the response for a range of frequencies, ensuring that we remain on the approximately linear part of the cavity fringe slope, and construct the bode plots as shown in figure 5.10. The high-finesse cavity used in the lock acts as a low-pass filter, with a cut-off frequency equal to half the cavity mode linewidth [123]. The PID servo (loop filter) response is calculated using equations 5.2 and 5.3. The calculated and measured gains are multiplied together, and the phases added, to give the total system gain and phase response (see figure 5.10). The resistor and capacitor values for the PID feedback circuit are changed in the calculation until a suitable total response is achieved (see section 5.1.1.1 for more details on this step). These components are then put into the loop filter. The laser lock is very sensitive to the gain parameters, so it is likely it will not lock immediately. In anticipation of this,

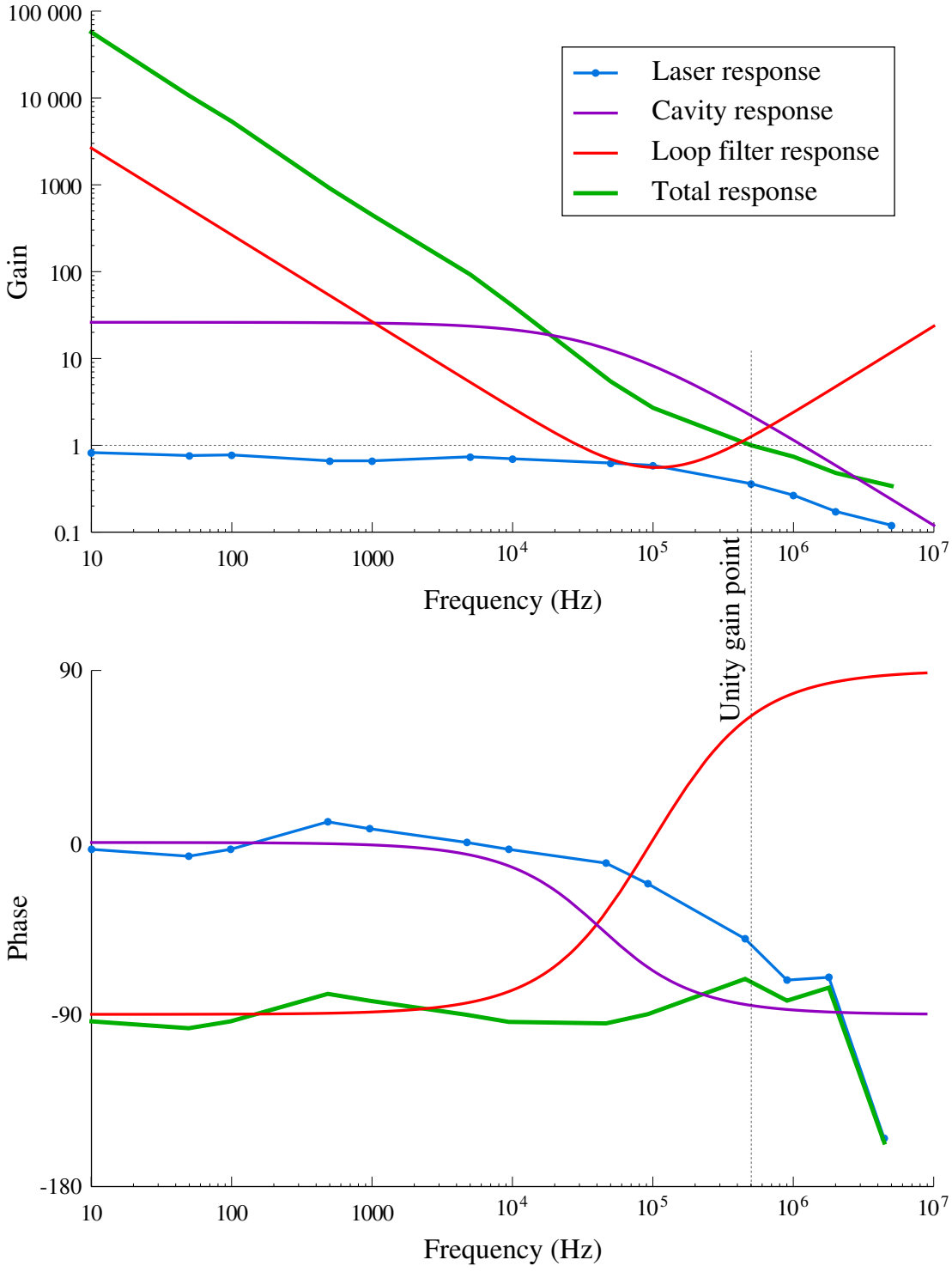

Figure 5.10: **Bode plots for laser locking** - Frequency dependent gain and phase response of the laser, optical reference cavity, loop filter locking electronics and the combined total.

some of the gain resistors are deliberately chosen to be potentiometers, and by tuning these we will start to see the laser locking. It is easiest to do the initial tuning of the laser lock gains while the laser is scanning over the cavity mode, usually scanning the laser by $\sim 40\,\mathrm{MHz}$ at a frequency of $\sim 5\,\mathrm{Hz}$, and observing the cavity transmission. Once the laser locks to the cavity we can turn the scan off and optimise the lock parameters while the laser is locked. To do this we monitor the in-loop error signal from the lock photodiode (PD2 in figure 5.6) on a spectrum analyser and the cavity transmission (photodiode PD3 in figure 5.6) on an oscilloscope. The aim is to lower the cavity transmission noise, while keeping the transmission high (at the top of the cavity peak), and to broaden the lock bandwidth and reduce the low frequency noise from the in-loop error signal trace (see figure 5.11).

Figure 5.11 shows a typical in-loop error signal trace for the locked clock laser. From figure 5.11 (a) we can see the servo bandwidth is approximately 120 kHz, which is not particularly wide (some laser locks have bandwidths of a few megahertz), but importantly, it is significantly wider than the 70 kHz linewidth of the unlocked laser. If we reduce the frequency span of this measurement (figure 5.11 (b)) we can see the low frequency lock noise, in particular we can identify peaks at 50 Hz and its harmonics. The 50 Hz peaks (and any others identified) need addressing, because they are adding noise to the locked laser; 50 Hz is likely due to electronic pick-up (poor shielding of the electronics, signal path, or the laser diode) or due to ground loops. We should be able to identify the reason for these peaks and significantly reduce or eliminate them.

Once the laser is locking with feedback to the diode current alone, we switch in the feedback to the diffraction grating piezo. The gains for the piezo integrators are less critical so are found by trial and error by switching in different capacitor

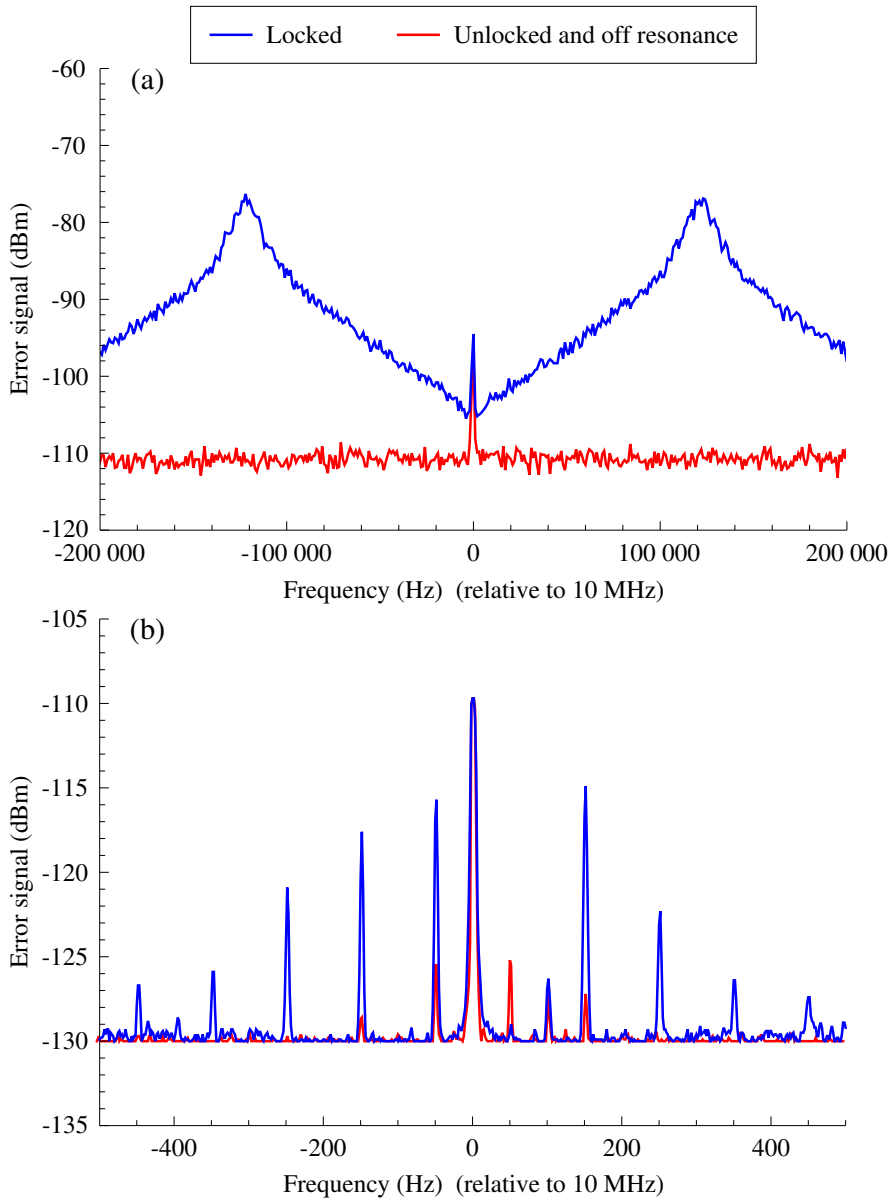

Figure 5.11: **In-loop error signal noise profiles** - We measure the lock photodiode signal (PD2 in figure 5.6) on a spectrum analyser. These traces are centred around the modulation frequency (10 MHz in our case); this frequency offset has been removed here for ease of plotting. (a) shows the full span of the error signal noise. The distance between the centre of the trace and the top of the servo bump gives an indication of the lock bandwidth, ~ 120 kHz in this case. (b) shows the same lock signal over a smaller frequency range. This shows up any low frequency noise, such as the 50 Hz and its harmonics we see here. These in-loop error signal measurements will only identify discrepancies between the laser frequency and the cavity mode frequency, it will not show up any noise the cavity is imprinting on the laser, but this is likely to be comparatively small at this stage of locking.

and resistor combinations.

From here on it is an iterative process to narrow the laser linewidth further with small changes to the loop filter gains for the fast-feedback. We have completed the majority of the work for locking this laser, but have not finished the lock optimisation yet. This last step is far easier with two locked laser systems, so we intend to finish building the second system first.

5.2.1.5 Intensity stabilisation

Since we have carefully and systematically chosen our feedback gains it is important that they remain constant. Day-to-day changes in laser power will change the size of the error signal, and hence the overall gain setting of the feedback, as will power changes that result from the feedback signal to the laser diode current. These can be removed from the lock servo by stabilising the intensity of the light sent to the optical reference cavity. Our optical set-up has been built with this in mind, and although we have not implemented it in this set-up yet, we have used it in other laser systems. We will use photodiode PD2 in figure 5.6 to feed a voltage variable attenuator (Mini Circuits part number ZX73-2500+) to control the RF drive power, and hence the diffraction efficiency, of AOM1.

5.2.2 Lock errors

In order to benefit from the exceptional frequency stability provided by the high finesse optical cavity we need to ensure not only that our laser lock is good, but that our PDH error signal is free from noise and offsets. An offset on our error signal, whether it be optical or electrical in origin, will result in the laser locking to some point away from the cavity fringe centre, and if this offset varies in time so will our 'locked' laser frequency.

Electrical offsets come from components such as operational amplifiers in the servo loop and the double balanced mixer. These offsets are usually relatively stable and can be cancelled using the voltage offset stage before the loop filter. However, they may have some temperature dependence, so towards the latter stages of lock optimisation it is important to check for offset variations and it may be necessary to passively or actively control the temperature of some components.

A second source of error signal offset is from optical offsets caused by residual amplitude modulation (RAM) [128] and parasitic etalons. We see these effects on our lock, their sources need to be identified and eliminated during the first stages of lock optimisation. We talk about RAM and parasitic etalons in more detail in the sections below.

5.2.2.1 Residual amplitude modulation

Light that is purely phase modulated has first order sidebands that are 180° out of phase from one another. This means when the laser frequency is tuned away from the cavity resonance the APD sees no signal at the modulation frequency f_m because the beat frequency contributions from the carrier mixing with each sideband have opposite phase and cancel out. When the laser is on resonance with the cavity there is a signal at frequency f_m, this is the PDH lock signal. On the other hand, purely amplitude modulated light has the carrier and all sidebands in phase with one another, so with the laser frequency away from cavity resonance the APD always sees a signal at the modulation frequency f_m. Demodulating this signal will result in a DC, non-zero, voltage, commonly referred to as an optical offset. The demodulated PDH error signal would still be visible above this voltage offset and we could naively add a compensatory voltage to bring the base level back to zero volts. However any change in the modulation depth due

to temperature or other effects would cause this optical offset to change, affecting the lock point and hence the frequency of the 'locked' laser.

We are phase modulating our light, so should see no signal at frequency f_m on the APD when the light is off resonance from the cavity mode, but any amplitude modulation contributions, however small, will show up as a signal at f_m, which when demodulated will result in an offset to our error signal and shift of the lock point. More problematically, varying amplitude modulation contributions will cause our laser frequency to drift around. Optical offsets caused by residual amplitude modulation (RAM) are a common problem in laser stabilisation [128], so it is important for us to identify, and eliminate where possible, sources of RAM. We diagnose the corrections necessary for reduced RAM by looking at the APD output at the modulation frequency when the laser is off resonance from the cavity mode.

The largest source of RAM is from the EOM. Although it is designed to be a phase modulator, this is only true for perfectly linearly polarised light aligned exactly with the crystal axis. Light with polarisation misaligned from the crystal axis undergoes polarisation modulation, which is converted to amplitude modulation by any polarising optics, such as the Brewster-cut crystal face of the EOM or the PBS cube before the cavity. A Glan-Thompton polariser with an extinction ratio of $100\,000:1$ (Thorlabs part number GTH10M-B) is placed before the EOM in a fine-adjustment rotation mount (Thorlabs part number PRM1/M) to clean up the light polarisation and ensure it is well aligned to the EOM crystal axis. Implementing this in place of the previously used PBS cube reduces the RAM by about an order of magnitude and increases the stability significantly, but it does not achieve complete elimination. The processes that contribute to EOM RAM are not fully understood [127; 129], but we know that beam polarisation, beam

alignment through the EOM crystal, and EOM temperature are all important. We have mounted our EOM on top of a peltier to allow us to implement active temperature stabilisation at a later stage of the lock optimisation. In addition we may decide to implement active RAM cancellation techniques such as those that adjust the relative refractive index of the crystal axes by feeding back to the EOM temperature [128] or an additional DC voltage applied across the EOM crystal [130].

The second largest source of RAM is from RF pick-up of the modulation frequency by the laser drive electronics, see also section 5.2.2.3. This can directly modulate the diode current and cause some unwanted RAM. In order to reduce this pick-up we have tried to enclose the source of the RF by shielding our EOM with a metal box (which also acts as the heat sink for the temperature control) and the FET oscillator is also housed in a metal box. The amount of pick-up is very sensitive to the grounding of the FET oscillator box. The level of pick-up onto the laser diode is now small enough that its effect is not visible above the noise floor.

5.2.2.2 Parasitic etalons

Parasitic etalons arise from any parallel optical surfaces along the beam path coupling to make a weak cavity, usually between optics such as the PBS cube and the first cavity mirror or between crystal faces within the EOM. Parasitic etalons cause a frequency and time dependent error signal offset, such as that shown in figure 5.12, which acts to cause fluctuations in the frequency of the 'locked' laser. In figure 5.14 the two dashed lines represent 'resonant modes' of low finesse etalons with 'mirror' reflectances of 4 % (that of glass) and 1 % (close to that of an anti-reflection coated optic). The period of the oscillation

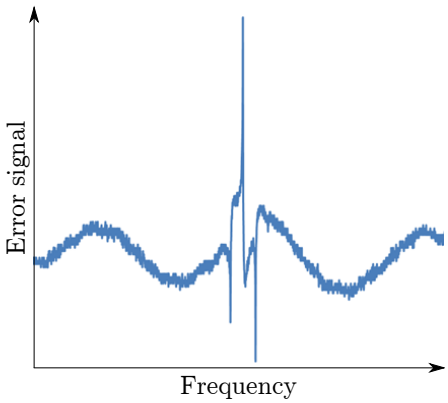

Figure 5.12: **Parasitic etalon** - PDH error signal shown on top of the parasitic etalon feature. Recorded by measuring the DBM output as the free-running laser frequency is scanned over the cavity mode. The carrier and sidebands accumulate a different phase contribution due to their position within the parasitic etalon resonance, causing them to sit at different voltage offsets.

is determined by the length of the cavity, which for the poor cavities we are speaking of, is varied by air currents, temperature changes and vibration of the optics. These length changes contribute to shift the frequency of the parasitic etalon compared to that of the high finesse cavity mode. This results in the error signal bobbing around on top of the moving parasitic etalon waveform below (as in figure 5.12), making a very unstable 'locked' frequency.

Large parasitic etalons are easy to remove by misaligning the necessary optics in the beam path so that there are no parallel surfaces. The EOM crystal is Brewster-cut to avoid etalons from the crystal surfaces, and the cavity vacuum chamber windows are wedged and attached at an angle. The parasitic etalon in figure 5.12 was caused by coupling between the retro-reflecting mirror used to double-pass AOM1 and the first cavity mirror. The etalon was removed by replacing the retro-reflecting mirror with a right-angled prism.

It can be difficult to find and remove all effects due to parasitic etalons, but useful steps towards further reduction include:

- ensuring good reflection efficiency from the final PBS cube and quarter

waveplate configuration;

- building a box around the optical set-up to reduce temperature and air pressure fluctuations;
- using a lower modulation frequency, so that the carrier and sidebands sit closer to one another compared the the parasitic etalon wavelength. This reduces the RAM-type effect due to the phase difference between the sidebands.

Some of which we have already incorporated, while for the others there are plans for future implementation.

5.2.2.3 Electrical grounding

Poorly constructed electrical grounding can be detrimental to the laser linewidth. We have observed that incorrect grounding of the laser diode drive electronics can cause the free-running laser linewidth to broaden from the $\sim 100\,\mathrm{kHz}$ shown in figure 5.3 to $\sim 1\,\mathrm{MHz}$! Ground loops cause problems with pick-up, particularly of $50\,\mathrm{Hz}$ mains noise, and in our case the $10\,\mathrm{MHz}$ modulation frequency. It is usually best to try to avoid ground loops, which are often inadvertently created by the shielding of signal cables connecting the different parts of the lock electronics. We find there are no obvious rules for optimal grounding and some ground loops have no observable affect on the system, so the desired grounding is found by trial and error. Particular care is taken when grounding the box for the FET oscillator that drives the EOM, as failure to achieve a suitable ground leads to pick-up of the modulation frequency by the laser diode, causing amplitude modulation and a lock offset.

5.2.2.4 EOM drive electronics

The FET oscillator used to drive the EOM produces not only the desired modulation frequency, but also many harmonics of this frequency, all of which contribute to the modulation of the light. This is not ideal for PDH locking because it can produce optical offsets on the error signal which affect the lock point. The frequency of the oscillator also drifts a small amount. It is unclear if this drift will definitely cause problems in the finished lock set-up, but it will cause a varying optical offset if there are any residual parasitic etalons in the set-up, and may cause the error signal to vary in size and shape due to differing phase delays for different modulation frequencies. It is desirable to drive the EOM with a fixed single frequency, so we plan to implement some suitable electronic upgrades into the set-up in the near future. We intend to build a resonant LC transformer driven by a simple frequency synthesiser, such as a DDS (direct digital synthesiser) circuit. In our laboratory we have access to a 10 MHz maser referenced signal to which we can lock the RF synthesisers, making the required stability of the modulation frequency easily achievable.

5.2.2.5 PDH lock electronics: further considerations

Filtering signals: The electronics required for locking are outlined in the schematic in figure 5.6. It is important to make sure each part of the signal path has only the required frequency contributions in order to keep the lock signal clean. For example, we saw in section 5.2.2.1 that amplitude modulation of the light at the modulation frequency f_m, which is hard to eliminate completely, creates in an additional signal on the APD at the frequency f_m. It also results in an undesired peak at $2f_m$ due to mixing of the first-order sidebands. Residual $2f_m$ harmonics from the EOM drive electronics will demodulate this $2f_m$ peak at

the double balanced mixer (DBM) resulting in unwanted noise on our DC error signal. For this reason it is important we heavily filter the signal from the EOM drive oscillator before the mixer; for this we use a low-pass filter. We also have the option to use a band-pass filter on the signal from the APD to ensure we are only mixing signals at the modulation frequency. However, filters with cut-off frequencies too close to the signal frequency add a delay time to the signal, which lowers the bandwidth of our lock servo, so it is often desirable not to use them in the signal line.

The DBM outputs two signals, one at DC (the desired error signal) and one at $2f_m$. There may also be some leakage of the modulation frequency to the DBM output. The loop filter electronics act as a lowpass filter, so ideally these f_m and $2f_m$ signals do not get fed back to the laser diode, but high frequency oscillations such as these can cause unforeseen problems with the electronics, so it is often best to filter them out. At present we are using a 5 MHz lowpass filter at the DBM output, the cut-off frequency of which should be sufficiently far from the signal so as not to limit the bandwidth too much, but we may in future move to narrowband notch filters at the modulation frequency and its harmonics. These notch filters may also be suitable for use on the APD output to reduce $2f_m$ and higher harmonic signals, but the phase delay at f_m must be sufficiently low.

Increasing piezo bandwidth: It is desirable to increase the bandwidth of the feedback to the diffraction grating piezo to take up the lower frequency range of the feedback to the laser diode. Any feedback to the laser diode will result in the desired frequency control, but it will also act to modulate the laser beam power. This intensity modulation is reduced by the intensity stabilisation at AOM1, but it is more effective to decrease it directly by applying more of the mid-range frequency feedback to the piezo rather than the diode. The laser diode

still receives the faster feedback, because the achievable piezo bandwidth will be a maximum of only a few kilohertz, and will be limited by the combination of mechanical design, piezo capacitance and the bandwidth and power of the drive electronics (for more details on increasing piezo bandwidths see [131]). In our set-up the piezo bandwidth extends out as far as $\sim 15\,\text{kHz}$, but is limited by the drive electronics to $\sim 200\,\text{Hz}$. Building drive electronics with a higher current capability would increase this bandwidth. We may decide to implement such an approach in the future.

5.3 Optical reference cavity

The lasing frequency of each 'clock' ECDL is stabilised to the centre of a resonant mode of a high finesse optical reference cavity using the Pound-Drever-Hall technique [98], to provide short-term stability (narrowing of the instantaneous linewidth) and long-term stability (reducing/characterising the drift during measurement of the atomic frequency).

Fractional length changes in our optical reference cavity are equal to the fractional frequency changes of the resonant cavity modes, and hence the stabilised laser (equation 5.1). To demonstrate the cavity requirements, the frequency of a 698 nm laser locked to a 10 cm long cavity would change by about 4 Hz if the cavity length were to change by only 1 fm (the size of an atomic nucleus)! This fractional length change is equivalent to the distance between the Earth and the Sun changing by just 1.5 mm. These particularly strict length stability requirements sound impossible to achieve, but years of hard work by a number of scientists have made this possible and a number of groups have achieved sub-hertz linewidth lasers at 1 second as a result (fractional frequency instabilities at the 10^{-15} level) [132; 133; 134].

We should consider what effects will change our cavity length (or effective length):

Temperature changes cause expansion or contraction of the cavity material.

Vibrations cause changes in mirror location and spacing.

Refractive index changes in the gas between the cavity mirrors change the effective cavity length.

We can go to great lengths to isolate our optical reference cavity from its environment (e.g. sub-millikelvin cavity temperature stability, in an evacuated chamber, mounted on a vibration isolation platform, in an acoustically isolated laboratory), but the rewards from these efforts are limited. A more scientifically profitable approach is to design a reference cavity that is insensitive to external perturbations such as vibrations and temperature fluctuations by suitable choice of cavity material and geometry. After significant work in these areas the length stability of optical reference cavities (and hence the frequency stability of stable lasers) is ultimately limited by thermal noise to parts in 10^{16} [135; 136]. (We shall discuss thermal noise further in section 5.3.1). In the next few sections we go into more detail of the important considerations when designing an optical reference cavity and look at some of the significant advances in the field.

5.3.1 Cavity material

The choice of cavity material is based largely on the coefficient of thermal expansion (CTE) and, for the cavity mirrors, transparency of the material at the desired wavelength. There are a small collection of optically transparent designer materials whose CTE passes through zero close to room temperature, these are Zerodur (a non-porous lithium aluminium silicon oxide glass ceramic made by Schott),

ULE (Ultra-Low Expansion glass 7972 made by Corning; this is a titania-doped silicate), and Cer-Vit (a glass ceramic made by Owens-Illinois, discontinued in 1978). Super Invar (an iron-nickel-cobalt alloy) also has a zero CTE close to room temperature, although its opacity makes it not suitable for optical cavity mirrors, it has nevertheless been tested for use as a cavity spacer for space applications [137]. In 1976 Berthold and Jacobs published a set of comprehensive measurements of the CTE temperature dependence of low CTE materials [138].

With the use of materials with such low ("$0 \pm 30 \times 10^{-9}$ /°C from 5 °C to 35 °C with a 95 % confidence level" [139]) CTEs, the limiting factor of cavity length fluctuations (and hence short-term laser stability) is attributed to thermal noise (Brownian motion) of the cavity mirrors [140; 141]. There are two main ways to reduce thermal noise; the most obvious of which is to reduce the cavity's temperature. Materials such as sapphire [142; 143] and silicon [136] have CTEs close to zero at cryogenic temperatures, but the added complexity and expense of cooling to cryogenic temperatures means that until recently we have seen few experiments in this area. We cannot move on from here without referring to the recent work of Kessler et al. at PTB where they stabilise a 1.5 µm laser to an all-silicon reference cavity held at 124 K (its zero CTE temperature). This low cavity temperature leads to a significantly reduced thermal noise floor and a world-leading laser linewidth of 40 mHz at 1 second [136]! However, silicon is opaque to optical wavelengths and so is not immediately applicable in our clock apparatus, but it may be possible to implement it via a frequency doubling stage into the optical regime or by transferring the frequency stability via an optical frequency comb [144].

A second approach is to reduce the thermal noise by using mirror substrate materials with higher mechanical quality factors (Q), meaning that less mechani-

cal energy is converted to thermal energy. Numata et al. measured the mechanical quality factors of commonly used cavity materials Zerodur ($Q = 3.1 \times 10^3$) and ULE ($Q = 6.1 \times 10^4$) along with fused silica ($Q \sim 10^6$) [140]. They run a number of calculations to simulate the effects of mechanical loss with a number of spacer and mirror materials and geometries, e.g. ULE spacer and mirror substrate, ULE spacer with fused silica mirror substrate, and Zerodur spacer and mirror substrate. The recommendations from this paper are to replace the ULE mirrors with a fused silica substrate (keeping the ULE spacer for its low CTE at room temperature) to gain a factor of ~ 2 in the fractional frequency stability, and to increase the laser beam spot size on the mirror surfaces to reduce localised heating, giving a total gain in fractional frequency stability of ~ 3. Laser beam spot size can be increased by using mirrors with a larger radius of curvature and a longer cavity length. A longer cavity also has the benefit of reduced *fractional* length changes from thermal noise. A number of groups are now pursuing narrower linewidth lasers from longer cavities e.g. 29 cm at NIST [135], 30 cm at NPL [145], 39.4 cm at JILA [19], and 100 cm at NIMJ [146]. Following on from an increase in laser beam spot size on the mirror surfaces to reduce localised heating, groups have experimented with locking to higher-order cavity modes rather than the usual TEM_{00}, or using different beam shapes altogether [147; 148]. To the author's knowledge no experimental results have yet been published on these alternative procedures.

The largest contributor to the thermal noise of the cavity is from the mirror substrates rather than the cavity spacer [136; 140], and following the recommendation in [140] there has been a recent move to groups making cavities with ULE spacers and fused silica mirrors [135; 141]. The optical contacting of the different materials distorts the overall cavity CTE [141; 149], but careful cavity design,

such as an additional ULE ring on the back face of the fused silica substrate [141; 150], or designer doping of the ULE spacer [135], can confine the zero-CTE temperature close to room temperature. With this approach the thermal noise floor has been reduced to $\sim 2\times10^{-16}$, with resulting laser linewidths of $<$ 250 mHz at 1 second [120; 135].

5.3.1.1 Temperature requirements of ULE

The two 'clock' cavities in use in our experiment have 7.75 cm long ULE spacers and optically contacted ULE-substrate mirrors. We intend to temperature stabilise them close to where their CTE crosses zero to take full advantage of this characteristic of the material. The linear coefficient of thermal expansion, α is the fractional change in length of the material per unit temperature change, ΔT, and is expressed in equation 5.7.

$$\alpha = \frac{1}{\Delta T}\frac{\Delta L}{L} \tag{5.7}$$

Published data for the direct measurement of the CTE of ULE suggests that near room temperature it follows an equation of the form: [149]

$$\alpha(T) = (k_0 + 2.21\,T - 0.0122\,T^2) \times 10^{-9}\,/\,^{\circ}\mathrm{C} \tag{5.8}$$

where T is the temperature in degrees Celsius and k_0 is a constant that varies between ULE batches. We find that if k_0 is set to equal -50 then the above equation fits very well to the measured CTE temperature dependence reported in figure 4 of [138], see figure 5.13.

Since the T^2 dependence is small in equation 5.8 we can approximate α to

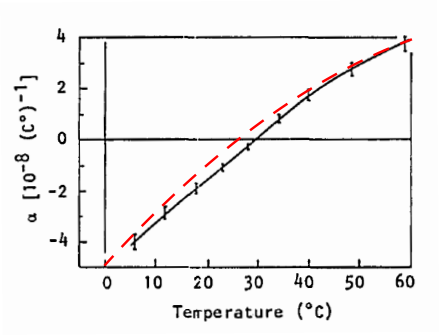

Figure 5.13: **ULE coefficient of thermal expansion (CTE)** - CTE data plot from [138] overlaid (in red dashes) with the fit from CTE equation 5.8 [149] for comparison.

have a linear dependence on T with the gradient from equation 5.7 being:

$$\frac{\Delta\alpha}{\Delta T} \approx \frac{1}{(\Delta T)^2}\frac{\Delta L}{L} \approx 2.21 \times 10^{-9} \,/\, ^\circ\mathrm{C}^2 \tag{5.9}$$

Re-arranging this and using the relation in equation 5.1 gives us the expected fractional frequency change of our laser with changes in temperature close to the zero-CTE temperature, T_c:

$$-\frac{\Delta\nu}{\nu} = \frac{\Delta L}{L} \approx 2 \times 10^{-9}(T - T_c)^2 \tag{5.10}$$

This T^2 dependence of laser frequency demonstrates the importance of stabilising the temperature at or close to the zero-CTE point. If we are stabilised at the temperature of zero CTE and the temperature of the cavity drifts by 1 mK then the resulting frequency shift of our 698 nm laser will be $\sim$0.9 Hz. If, on the other hand we are stabilised 5 °C from the temperature of zero CTE and the temperature of the cavity drifts by 1 mK then the resulting frequency shift of our 698 nm laser will be $\sim$9 kHz!

The temperature of the CTE zero-crossing depends on the ULE material and varies from batch to batch. To find the temperature of zero-CTE for each of our

cavities we need to make a series of frequency measurements of the laser locked to the same cavity mode over a range of cavity temperatures. This technique is demonstrated in [151] and details of our experimental procedure and results are in section 5.4.

5.3.2 Cavity geometry

Careful choice of cavity geometry can ensure that our cavity length is insensitive to perturbing vibrations (particularly those along the axial length of the cavity). Over the last ~ 10 years significant steps have been taken in this field to ensure that cavity vibrations are not the limiting factor in the stability of the cavity length. Prior to this work, groups went to great lengths to create layer upon layer of vibrational damping for the cavity, such as those described in [132]. The largest contributor to cavity vibrations are from vertical vibrations of the mounting surface (the floor or optical table). The most intuitive way to gain insensitivity to these is by mounting the cavity vertically, supported at the mid-plane [134; 152; 153; 154]. Mid-plane mounting leads to vertical vibrations causing the top and bottom mirrors to move by equal amounts, thus not affecting the cavity length. Fractional frequency vibration sensitivities achieved are $7 \times 10^{-11}\,/\mathrm{ms}^{-2}$ [134] and $1.4 \times 10^{-11}\,/\,\mathrm{ms}^{-2}$ [154]. Since active and passive vibration isolation platforms can achieve vibration reduction down to $\sim 5 \times 10^{-7}\,\mathrm{ms}^{-2}/\sqrt{\mathrm{Hz}}$, this equates to frequency fluctuations on the order of $10\,\mathrm{mHz}\,/\sqrt{\mathrm{Hz}}$, which is an order of magnitude below the thermal noise of the best room-temperature cavities today. However, with vertical cavities comes a compromise over the cavity length, shorter vertical cavities benefit from lower fractional length changes from vibrations, but a higher contribution from thermal noise. Since thermal noise is today's limiting factor, and the general trend is to opt for longer optical reference cavities,

most groups are choosing to mount their cavities horizontally.

This second approach of mounting the cavity horizontally with carefully chosen mounting points [155; 156] to reduce sensitivity to vibrations has lead to the development of a number of long cavities as described at the end of section 5.3.1. A cavity mounted horizontally sags under its own weight, but careful choice of mounting points can allow the sag to occur while leaving the cavity length invariant. This idea was first proposed by T. Rosenband and successfully implemented independently by T. Nazarova [155] and S.A. Webster [156]. Finite element analysis is used to calculate the ideal mounting points for length invariance and after construction a small number of iterations are required to get the mounts in exactly the right location [156]. Fractional frequency vibration sensitivities achieved in this way are $3 \times 10^{-11}\,/\mathrm{ms}^{-2}$ [155] and $1.3 \times 10^{-11}\,/\mathrm{ms}^{-2}$ [156], which equate to fractional frequency instabilities well below the thermal noise level at close to room temperature.

Today the field is focused towards developing cavities for use in space where there is no significant gravitational force, but where forces can occur in any direction; this requires sturdy cavity mounting without the aid of gravity. Cavity geometries in consideration are spherical - rigidly mounted at two points on its diameter $\sim 37^\circ$ from cavity axis [157] - and cubic, with tetrahedral mounting that leaves the cavity insensitive to mounting forces [158].

5.3.2.1 Measuring cavity vibration sensitivity

To measure the sensitivity of our cavity to vibrations in the horizontal and vertical planes we intend to apply calibrated vibrations in different directions and monitor the frequency fluctuations of the locked laser. The two optical systems are each built on independent active vibration isolation (AVI) platforms, which

have "shake" functionality built in. The AVIs allow us to shake the optical reference cavities in three or four (depending on the model) directions. Before building the optical set-ups on the AVIs we calibrated the shake functions using a seismometer. We measured the acceleration produced in each direction for a set of shake sine wave amplitudes and frequencies. We chose six different shake frequencies between 1 Hz and 100 Hz. The frequencies chosen were selected based on those that produced low cross-coupling between the different orientations (i.e. if we shake vertically we have low coupling to the horizontal directions), and we deliberately did not choose frequencies that are harmonics of each other.

To measure frequency fluctuations resulting from the applied vibrations we plan to beat the locked laser with a locked reference laser and measure the beat frequency fluctuations. We have not performed the cavity vibration sensitivity tests because we do not have two finished systems to compare. Upon performing the tests we may find the vibration sensitivity to be higher than expected. If this is the case we can apply small masses to the mid-plane ring of the cavity to change the centre of mass. This is an iterative process, during which we will re-measure the sensitivity and modify the mass further if necessary.

5.3.3 Cavity finesse

An optical cavity can be largely characterised by its mirror reflectance, R, and the distance (length), L, between these mirrors. Conservation of energy requires that light incident on a cavity mirror is either reflected, transmitted, absorbed or scattered, which leads to the equation:

$$R + T + A + S = 1 \tag{5.11}$$

where R is the reflectance, T is the transmittance of the mirror, and A and S are losses due to absorption and scattering, respectively. The free spectral range of the cavity, $\Delta\nu$, (the frequency spacing between identical resonance modes) is defined by the cavity length:

$$\Delta\nu = \frac{c}{2Ln} \tag{5.12}$$

where c is the speed of light and $n\,(\simeq 1)$ is the refractive index of the gas/vacuum between the mirrors.

The cavity finesse is a measure of the quality of the cavity mirrors. Finesse, $\mathcal{F}$, is defined by the mean reflectance of the two mirrors as in equation 5.13 [159].

$$\mathcal{F} = \frac{\pi}{2\arcsin(\frac{1-R}{2\sqrt{R}})} \tag{5.13}$$

When R is close to unity the MaClaurin series expansion is used to approximate this to give the equation in its usual form:

$$\mathcal{F} \approxeq \frac{\pi\sqrt{R}}{1-R} \tag{5.14}$$

The linewidth of the cavity modes, $\delta\nu$ (to which we stabilise our laser) is related to the cavity finesse and free spectral range by equation 5.15.

$$\mathcal{F} = \frac{\Delta\nu}{\delta\nu} \tag{5.15}$$

Since we are stabilising our laser frequency to the centre of a cavity fringe, see figure 5.14, narrowing the modes will (up to a limit) result in a narrower laser linewidth. Equations 5.12 to 5.15 show us that narrower cavity modes can be achieved with longer cavity lengths and higher reflectance mirrors. Longer cavity lengths also benefit us by equation 5.1; small changes in cavity length result in

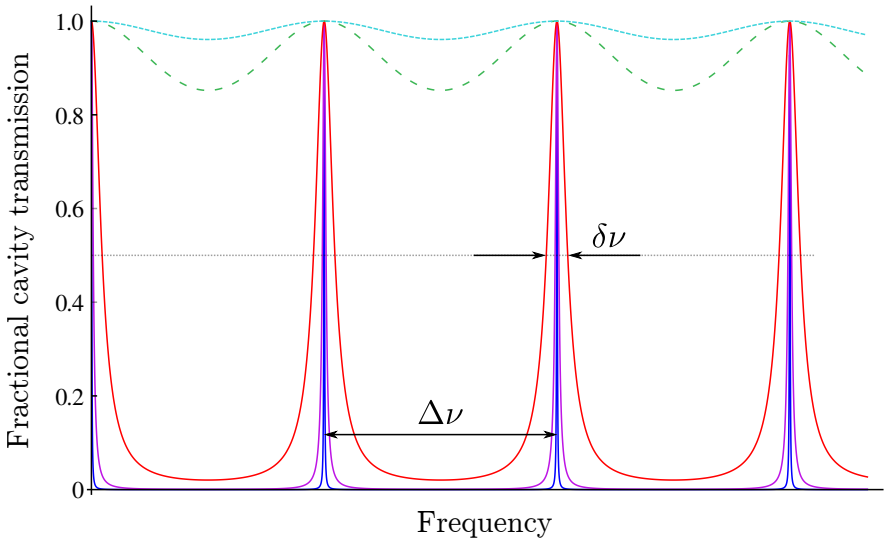

Figure 5.14: **Cavity transmission modes** - showing the fractional cavity transmission for an ideal cavity (no mirror losses and perfect mode matching) for a range of mirror reflectances with the mode linewidth $\delta\nu$ and separation $\Delta\nu$ indicated. Mirror reflectances, R: blue = 0.99, purple = 0.95, red = 0.75, dashed green = 0.04 (reflectance of glass), dashed cyan = 0.01. The two dashed curves are shown to indicate the effect parasitic etalons within the Pound-Drever-Hall optical set-up, see section 5.2 for more details.

smaller changes in wavelength. This is why a number of groups are beginning to work with longer cavities [19; 135; 145; 146]. Longer cavities introduce their own technical challenges with their larger vacuum systems, greater demands on the temperature control and stricter requirements on the geometrical design to reduce vibration sensitivity.

5.3.3.1 Measuring cavity finesse

For low finesse cavities, particularly where the laser linewidth is narrower than the cavity modes, equation 5.15 can be used to calculate the cavity finesse. Aligning a laser into a low finesse cavity will result in a transmission spectra similar to that shown in figure 5.14 (when either the laser frequency or the cavity length is scanning), $\delta\nu$ and $\Delta\nu$ are both easy to read from this on an oscilloscope for

example. For higher finesse cavities, where the laser linewidth is broader than that of the cavity modes the cavity transmission becomes jittery as the amount of light coupling into the cavity fluctuates rapidly. In this case it is not possible to simply measure $\delta\nu$, so an alternative method is used - cavity ringdown. Cavity ringdown allows us to measure the mirror reflectance (and hence the finesse using equation 5.14) by observing the decay of light 'trapped' inside the cavity. Light on resonance with a cavity mode will constructively interfere in the space between the cavity mirrors and will build up inside the cavity. When a laser is locked to a cavity mode this can be observed - a few microwatts of incident light can build up to over a Watt of intra-cavity power. This 'trapped' light intensity does not build up to infinity because transmission and mirror losses mean that a small amount is lost with each round trip of the cavity. If the incident light to the cavity is blocked (or the frequency is changed so that it is no longer on resonance with the cavity mode) the built-up light decays with each mirror interaction, and this exponential decay can be monitored with a fast photodiode. This is the essence of cavity ringdown.

The characteristic cavity decay time, τ_c, is the time it takes for the intra-cavity power to decay to $1/e$ of its original value. τ_c is the measurable quantity we wish to relate to the cavity finesse.

$$P(t) = P_0 e^{-t/\tau_c} \tag{5.16}$$

The bounce number, $\mathcal{B}$, describes the number of reflections (or bounces) a photon undergoes before it has a $(1 - 1/e)$ chance of escape. This is equal to the cavity decay time divided by half the round trip time, $t_r/2$, (i.e. the time for the photon

to travel from one mirror to the other).

$$\mathcal{B} = \frac{2\tau_c}{t_r} \tag{5.17}$$

$$t_r = \frac{2L}{c} \tag{5.18}$$

Referring back to equation 5.11 we can write R in terms of the cavity decay, $\mathcal{D}$, and relate this to the measurable cavity decay time, τ_c:

$$\begin{aligned} R &= 1 - (T + S + A) \\ &= 1 - \mathcal{D} \\ &= 1 - \frac{1}{\mathcal{B}} \\ &= 1 - \frac{L}{\tau_c c} \end{aligned} \tag{5.19}$$

Finally this leads us to be able to calculate the cavity finesse by substituting equation 5.19 into equation 5.14. Typical cavity decay times for mid-high finesse cavities are a few to tens of microseconds.

In order to experimentally realise this procedure we need to be able to: (a) lock the laser frequency to that of the cavity mode, (b) rapidly ($< 1\,\mu$s) switch the laser beam off or change its frequency by an appropriate amount, and (c) detect the cavity transmission on a DC coupled fast photodiode with a bandwidth greater than ~ 10 MHz and a gain high enough to give a reasonable signal to noise. Our optical layout is shown in figure 5.6. The laser frequency is locked to the TEM_{00} resonant mode of the optical cavity and the transmission measured on the DC photodiode (PD3). AOM1 is used to rapidly switch off the laser light to the cavity and the transmission decay is captured on a digital storage oscilloscope.

Results: Cavity #1 was put in its all-aluminium vacuum chamber (see section 5.3.4) and was temperature stabilised before locking the laser to it in order to perform cavity ringdown. We were expecting the cavity finesse to be a few hundred thousand. The supplied datasheet showed a single mirror transmittance T of ~ 5 ppm at our clock wavelength; this should give a cavity decay time of a few tens of microseconds and a cavity transmission on the order of 20 %, depending on the mirror losses and the cavity mode-matching. The first sign that something was not right was the very low transmission through the cavity. With the laser locked to the TEM_{00} mode we observed ~ 0.03 % transmission rather than the expected 20 %. After improving the cavity mode-matching, the PDH lock gains, and re-checking the alignment of the laser beam into the cavity, the maximum transmission observed was 0.14 %. Measuring this level of transmitted power, $\sim 1\,\mu$W, with a good signal to noise on a high bandwidth photodetector was not an easy task, but once achieved this confirmed the cavity finesse was poor due to very high scattering losses. The cavity decay time was measured to be $\tau_c = (3.5 \pm 0.1)\,\mu$s (see figure 5.15), which gives a cavity finesse of $43\,000 \pm 1\,000$, a cavity mode linewidth of (45 ± 1) kHz, and cavity mirror losses of ~ 70 ppm (see table 5.1). Such high mirror losses could be caused by contamination of the whole mirror surface or by a single speck of dust. To check this the laser was locked to a different cavity mode, TEM_{01}, so that we were using different parts of the mirror surfaces. The ringdown time for this mode was the same as the first, suggesting general contamination of the whole mirror surface.

It was unclear to us what had caused the mirror contamination. It could have been supplied like that or it could have been something that happened to the mirrors after installation into the vacuum chamber. Great care had been taken of the cavity throughout the whole process and we could not identify any

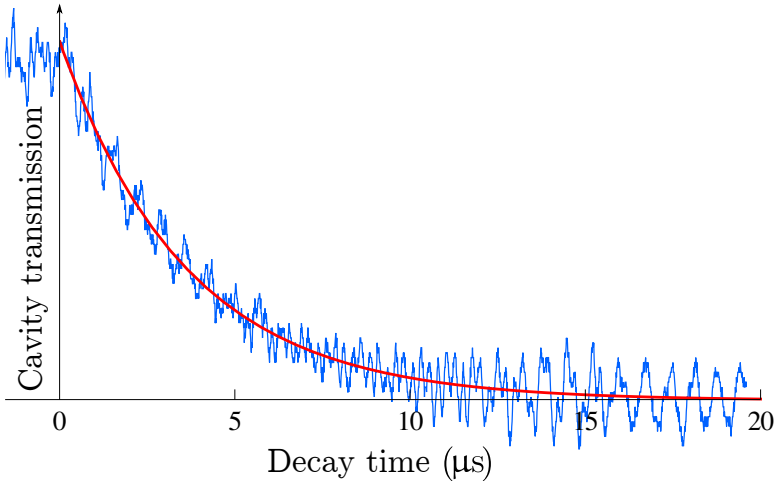

Figure 5.15: **Cavity ringdown measurement of 698 nm vertical cavity # 1** - with exponential decay fit. Exponential decay time of fit is $\tau_c = (3.5 \pm 0.1)\,\mu s$, giving a cavity finesse of $43\,000 \pm 1\,000$. Signal-to-noise ratio is poor due to the very low cavity transmission. Multiple ringdown measurements taken to confirm fit parameters and their uncertainty.

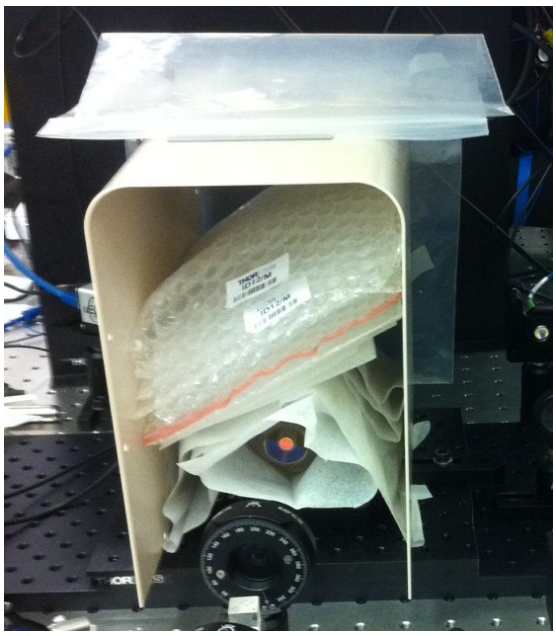

Figure 5.16: **Cavity ringdown set-up** - showing cavity # 2 mounted on v-blocks on the main experimental table. This set-up was used for initial cavity finesse measurements.

problems with our procedure. It was important for us to know the finesse of the second optical reference cavity (# 2) in order to make decisions on how to proceed. Both cavities were purchased together, but the second one was still in its protective packaging and had never been opened. We decided not to put cavity # 2 into vacuum in case it was something within the vacuum system causing the contamination, perhaps the Viton seals, but instead we would try to lock to the cavity with it in air. We mounted the cavity horizontally, balanced on two v-blocks on the main optical table. In order to reduce air pressure fluctuations within the cavity, we left the sticky tape over the bore holes, and we covered the cavity with bubble-wrap and a metal enclosure to help reduce air flow and maintain a constant temperature. The cavity housing arrangement is shown in figure 5.16. We used the same laser and lock electronics as for the first cavity, we redirected the light though an optical fibre to this second set-up and adjusted the PDH lock gains. Once the light was mode-matched and aligned into the cavity, locking did not take long. The cavity transmission intensity was a lot higher, at around 10 %, indicating a healthy cavity finesse, but it was fluctuating a lot due to air pressure changes between the cavity mirrors. This did not cause any problems for the ringdown measurements because once the input light is switched off the ringdown curve is smooth; effective cavity length fluctuations only affect light coupling into the cavity, not light that has already been built up. We measured the cavity ringdown time to be $(34.7 \pm 0.6)\,\mu s$ (see figure 5.17), which gives a cavity finesse of $422\,000 \pm 7\,000$, a cavity mode linewidth of $\sim 4.6\,kHz$, and cavity mirror losses of $\sim 2.5\,ppm$ (see table 5.1).

Cavity # 2 proved to be better than expected, so it is likely we inadvertently contaminated the mirrors of cavity # 1. We still do not know if the contamination is due to the Viton in the vacuum chamber, or because of problems with the ion

Parameter	Horizontal cavity for 689 nm	Vertical cavity # 1 for 698 nm	Vertical cavity # 2 for 698 nm
Cavity length	~ 10 cm	~ 7.75 cm	~ 7.75 cm
Free spectral range	1.503 (3) GHz	1.932 (4) GHz	~ 1.934 GHz
Transmission decay time, τ_c	6.9 (2) µs	3.5 (1) µs	34.7 (6) µs
Cavity finesse	65 000 (2000)	43 000 (1000)	422 000 (7000)
Cavity mode linewidth	23.1 (7) kHz	45 (1) kHz	~ 4.6 kHz
Locked transmitted power	-	~ 0.14 %	~ 10 %
Ideal transmitted power	-	~ 0.45 %	~ 44 %
Cavity mirror losses	-	~ 70 ppm	~ 2.5 ppm

Table 5.1: **High finesse cavities summary of values** - The free spectral range is measured for the first two cavities and estimated by equation 5.12 for vertical cavity # 2. The transmission decay time is measured as described in the text. The cavity finesse is calculated by equations 5.19 and 5.14. The cavity mode linewidth is calculated by equation 5.15. The locked transmission power is measured with a power meter. The ideal cavity transmission is calculated by $\left(\frac{T}{1-R}\right)^2$, where T is the mirror transmittance given on the datasheet and R is the mirror reflectance measured in ringdown, and any reduction from this value of the measured transmission is due to imperfect spatial mode-matching of the laser beam to the cavity. The cavity mirror losses are calculated from equation 5.11 once R has been calculated from ringdown.

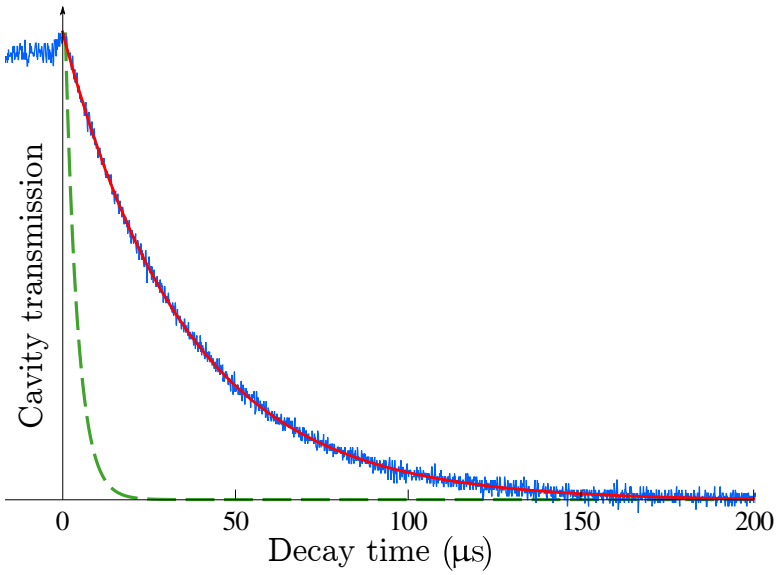

Figure 5.17: **Cavity ringdown measurement of 698 nm vertical cavity # 2** - with exponential decay fits for cavities # 1 (green dashed line) and # 2 (red solid line) shown for comparison. Exponential decay time of fit for cavity # 2 is $\tau_c = (34.7 \pm 0.6)$ μs, giving a cavity finesse of $422\,000 \pm 7\,000$.

pump (the first pump failed after a year, this may have deposited a layer of dirt onto the mirrors), or if there is some other cause. For this reason we made the decision to re-design the vacuum system to remove the majority of the Viton and to make it using all metal seals so that the ion pump can easily maintain the pressure, see section 5.3.4. While we are building up the second system we are continuing to use cavity # 1 in its current state. Once the second system is complete and the laser locked we will attempt to clean the mirrors of cavity # 1. The mirrors are optically contacted, but can be removed by carefully pinching them in a vice packed with lead for cushioning. The mirrors will be placed in isopropanol in an ultrasonic bath, and once clean, optically contacted back onto the spacer [160].

5.3.4 Cavity vacuum system

The optical reference cavities are used under ultra-high vacuum for two reasons. Firstly, refractive index changes in air, due to changes in pressure and humidity, result in undesirable fluctuations of the effective cavity length. Secondly, the use of a vacuum aids the temperature stability of the cavities by eliminating convection currents and increasing the time constant of the system, allowing better active control.

5.3.4.1 Frequency sensitivity to pressure fluctuations

At the beginning of section 5.3 we mentioned that the effective cavity length is sensitive to refractive index changes of the gas between the cavity mirrors. In order to estimate the changes in effective cavity length we would like to relate refractive index changes to pressure fluctuations, since pressure is a measurable quantity in the vacuum systems. However, according to the ideal gas law, for a fixed amount of gas, such as we have in a sealed vacuum system, changes in temperature will change the pressure inside the chamber, but this pressure change will not affect the refractive index, and hence the effective cavity length. In the following section we estimate the effect of pressure changes on the effective cavity length, and hence the frequency of the locked laser, but these are only relevant at a fixed temperature. We also assume the residual gas inside the vacuum chamber has a composition similar to that of air.

The refractive index of air n_{air} is given by the following relation [161]:

$$n_{air} \simeq 1 + \left(\frac{0.0472326}{173.3 - 10^{-12}/\lambda^2} \right) \frac{100P\left[1 + 100P\left(60.1 - 0.972T\right) \times 10^{-10}\right]}{96095.43\left(1 + 0.003661T\right)} \quad (5.20)$$

where λ is the wavelength in units of m, P is the pressure in units of mbar and

T is the temperature in °C. For a given wavelength $\lambda = 698.4\,\text{nm}$, at a constant temperature $T = 25\,°\text{C}$, this approximates a linear function of P:

$$n_{air} \simeq 1 + 2.63 \times 10^{-7} P \tag{5.21}$$

The effective cavity length Ln_{air} determines the cavity free spectral range by equation 5.12:

$$\nu_{FSR} = \frac{c}{2Ln_{air}} \tag{5.22}$$

which is proportional to the frequency of the locked laser. The fractional frequency shifts are equal so that:

$$\frac{\Delta\nu}{\nu} = \frac{\Delta\nu_{FSR}}{\nu_{FSR}} = \left(\frac{1}{n_2} - \frac{1}{n_1}\right) \simeq -2.63 \times 10^{-7} P \tag{5.23}$$

For a frequency instability of $< 1\,\text{Hz}$ we require pressure fluctuations below the $10^{-8}\,\text{mbar}$ level. Ideally we would house our optical reference cavity at a pressure of around $10^{-7}\,\text{mbar}$ or lower, thus allowing fluctuations at the 10 % level to maintain sub-hertz deviations. As we will see below our first cavity is housed at a pressure of $7 \times 10^{-6}\,\text{mbar}$, so this requires fluctuations below the 0.2 % level. We have no direct way of measuring the pressure stability to this degree of precision, but it is likely the pressure stability is not good enough. As we discuss later, we are building a second vacuum system, which should achieve a lower background pressure, and hence lower fluctuations.

5.3.4.2 Our vacuum designs

We have two separate vacuum chamber designs, one used for each cavity. The first chamber is an all-aluminium vacuum chamber and inner temperature shield, as shown in figure 5.18. Aluminium is chosen for the material of both the inner

temperature shield and the outer vacuum chamber because of its high thermal conductivity, allowing for a higher bandwidth temperature servo and a more uniform temperature environment for the cavity. The temperature of the cavity and its mirrors is determined by conduction from the inner temperature shield and radiation from the environment it can 'see', i.e. mostly the inner temperature shield, but also the outer vacuum chamber and the laboratory to a small degree. The windows are attached using indium wire, which cold-welds to the glass and aluminium during initial compression, and the rest of the vacuum seals use Viton o-rings (Viton is a brand name for a fluoroelastomer commonly used in vacuum o-rings). Metal seals (such as indium or the commonly used ConFlat flanges with copper gaskets) provide the best vacuum seals and allow vacuums of $\sim 10^{-11}$ mbar to be reached in a suitably designed vacuum chamber. ConFlat flanges use two steel knife edges that cut into a copper gasket to make the air-tight seal; these knife edges cannot be made with aluminium because it is too soft. This type of seal can be implemented into an aluminium vacuum chamber if the aluminium knife edge is coated with CrN, TiN, or electroless nickel to toughen it and an aluminium gasket is used in place of the copper one. Unfortunately this route is very expensive, for example one CrN coated aluminium DN160CF blank flange costs $\sim £760$ from a well-known vacuum company compared to $\sim £70$ for the stainless steel version, putting it out of our price range.

The Viton seals we use in this aluminium vacuum chamber are easy to use and are re-sealable, but they limit the vacuum pressure which can be achieved because of their elevated out-gassing and permeation rates compared to metal seals. Viton is unfortunately very good at absorbing solvents and slowly releasing them into the vacuum system, limiting the vacuum pressure achievable for a given pumping speed. A new Viton o-ring should be cleaned and pre-baked

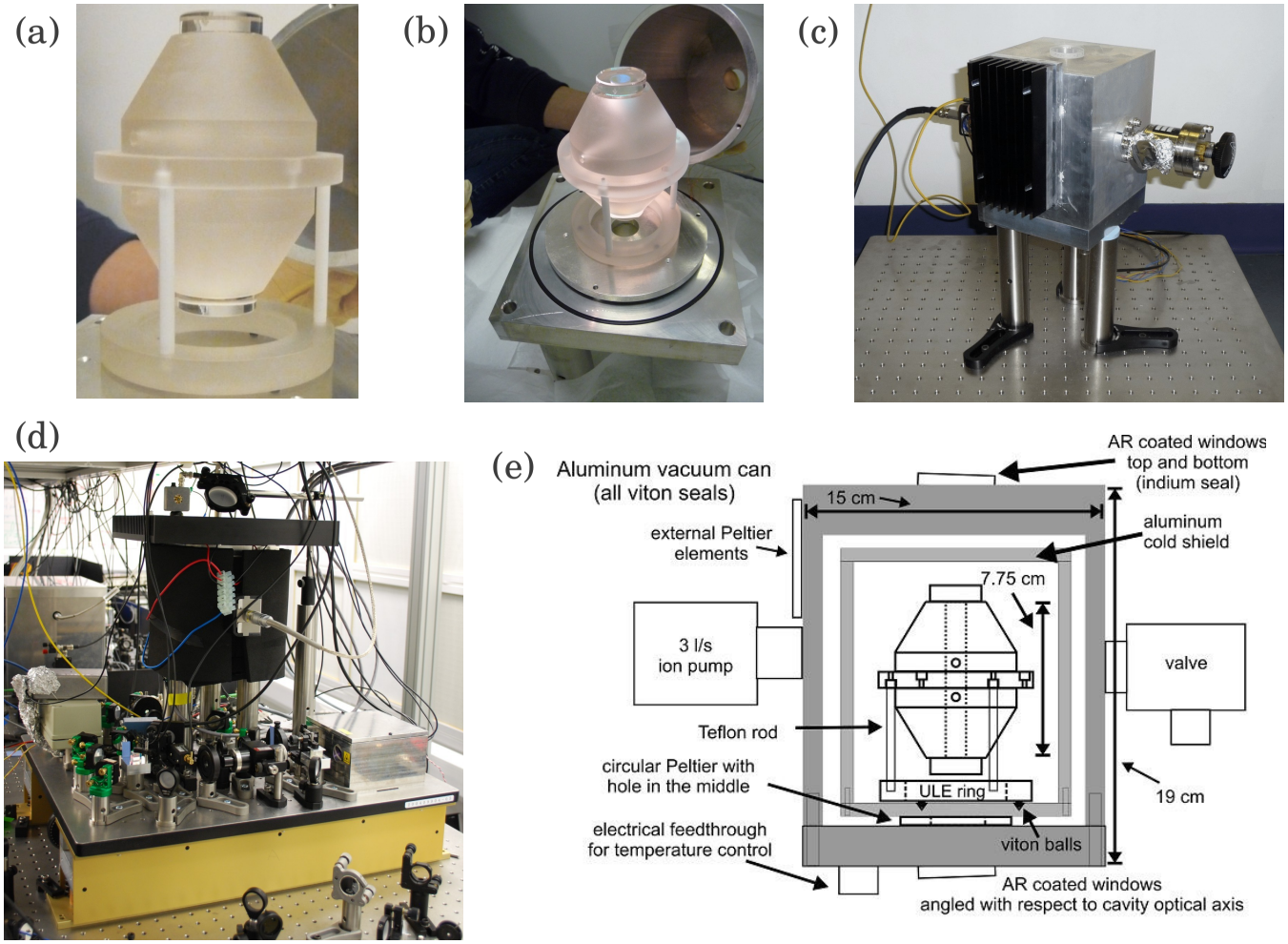

Figure 5.18: **All-aluminium cavity vacuum chamber # 1** - (a) and (b) photographs of the vertical cavity; (c) and (d) photographs of vacuum chamber on AVI, early and late in the build phase; (e) schematic of all-aluminium vacuum assembly.

before its first use in the vacuum system to remove grease from the surface, and solvents from the bulk of the material. This will reduce out-gassing rates and contamination of the vacuum system. It is standard to clean Viton in an ultrasonic bath with a detergent solution (Decon 90 or Neutracon and deionised water), followed by a thorough rinsing with deionised water and then methanol or isopropanol (acetone cannot be used with Viton). After this the Viton needs to be baked to remove the solvents it has just absorbed and the residual solvents from the manufacturing process. Baking can be done in air or a rough vacuum (vacuum bakes are quicker and more effective, but can contaminate the vacuum system and pump). The Viton can withstand temperatures of up to 120 °C without deforming. We chose to bake our Viton in air at just over 100 °C for 2 - 3 days and noticed a substantial reduction in initial out-gassing rate after completing this process. More information on Viton in vacuum can be found on various websites; the author particularly recommends the Vacuum Lab article [162].

After cleaning, constructing, and pumping down the all-aluminium vacuum system using our oil-free turbo-molecular pump it underwent a series of vacuum bakes:

1. Bake empty at 100 °C for a few days;
2. Attach inner peltier (with thermally conducting, vacuum compatible epoxy) and inner temperature shield; re-pump and bake at 50 °C (temperature limited by the peltier) for about a week;
3. Place in all remaining items except for the cavity and bake at 50 °C for about a week. Power cycle the ion pump at elevated temperatures to reduce contamination;
4. Place the cavity in the vacuum for the final bake at 50 °C for about a week. After this reduce the temperature. Once cold turn on the ion pump and

close the valve.

This procedure allows us to reach vacuum pressures in the range of 10^{-6} mbar with a Varian 2 l/s ion pump. Trial and error lead us to discover that the long baking times, Viton pre-baking and an all-metal valve (to replace our original Viton valve) were essential to achieve a vacuum pressure that the small ion pump could maintain. Our first attempt had less baking and pre-baking, a Viton valve and a Lesker 3 l/s ion pump, the pressure started at $\sim 5 \times 10^{-6}$ mbar and crept up until the ion pump failed about a year later. The current configuration has been under vacuum for over a year and is reasonably stable having increased from $\sim 4 \times 10^{-6}$ mbar to $\sim 7 \times 10^{-6}$ mbar.

The problems we have experienced with maintaining an acceptable vacuum in this chamber and the contamination of the cavity mirrors possibly caused by the Viton (see section 5.3.3.1) has lead us to design a second vacuum system containing only all-metal seals. The only Viton remaining in the new vacuum system is the three balls supporting the ULE ring, see figure 5.18. Other changes include the peltier mounting; it is no longer affixed with epoxy but clamped using bolts made from PEEK (polyether ether ketone), because one of the original peltiers broke and the epoxy made it difficult to remove. The vacuum chamber is now made from 304 stainless steel with mainly ConFlat flanges. We have kept the inner temperature shield the same because we wish to benefit from the aluminium's high thermal conductivity; the only alteration we have made is to polish the inside surface to decrease the emissivity, which increases the radiative time constant to the cavity. The new all-metal vacuum chamber design is shown in figure 5.19.

The windows on both vacuum systems are indium sealed, wedged, anti-reflection coated fused silica (1.5" diameter, 0.25" thick, 0.5 degree wedge, Melles Griot part

Figure 5.19: **All-metal cavity vacuum chamber # 2** - The main body is a custom-made DN160CF – DN16CF cross. The top and bottom are custom-made DN160CF flange; one side has the DN160CF knife edge, the other side has an angled wedge for mounting the indium sealed window and M6 bolt holes for attaching the legs. This chamber was designed in-house, and made by LewVac.

number W2-IF-1525-UV-670-1064-0). We chose to use indium seals because they maintain a good UHV (ultra-high vacuum) seal when the compression clamp is removed, meaning the window doesn't have uneven strains across it distorting the refractive index (and the laser beam polarisation). This mounting method also allows us to angle the surfaces to which we are attaching the windows. Ensuring this mounting surface angle is orthogonal to the angle of the window wedge means there are no parallel window surfaces, eliminating possible parasitic etalons (see section 5.2.2.2).

5.3.4.3 Implementing temperature stabilisation

The two optical reference cavities are intended to be temperature stabilised to better than a millikelvin at the temperature of their minimum coefficient of thermal expansion (CTE). The temperature of minimum CTE depends on the ULE material and varies from batch to batch. Based on data from other groups and information we had been given, we were expecting our minimum CTE to fall between about 7 °C and 13 °C [151]. We used thermo-electric coolers (TECs,

also known at Peltier coolers/heaters) to control the temperature of our two layers of temperature shielding. The outside of the vacuum chamber is cooled to around 17 °C using four TECs in series (RS part number 618-730) sandwiched between the top of the vacuum chamber and a large heatsink (RS part number 264-670). The inner temperature shield is cooled further to ∼8 °C, in the first instance, using a ring-shaped TEC (RS part number 490-1294). The temperature is controlled and stabilised using a two channel temperature controller designed by Chris Edwards at NPL. The controller is able to drive ±16 V, ±3 A from each channel, providing adequate power to stabilise at the temperatures we require. Each channel has two Wheatstone bridge amplifier circuits, one for in-loop servo control and a second for high signal-to-noise monitoring of the temperature. The bridge resistor R_C (see figure 5.4) is placed with the thermistors in the temperature stabilised environment, this aids with temperature stability of the vacuum chamber by reducing temperature induced changes in the Wheatstone bridge component resistances (see section 5.1.1.1).

To enable good temperature stabilisation the PID gains need to be carefully chosen, too much or too little P, I or D gain will result in oscillating or drifting temperatures. The Ziegler-Nichols closed-loop method [163] was used to tune the PID parameters of this controller. This method involves finding the ultimate gain point where, with proportional only feedback, the system undergoes constant amplitude and period temperature oscillations. The ultimate gain, $K_u (= R_f/R_{in})$, is recorded, along with the period of the oscillations, T_u. From these values the ideal P, PI, or PID gain values can be calculated using the coefficients given in table 5.2. The Ziegler-Nichols gain parameters are often found to be a bit too harsh, resulting in some ringing of the temperature as it reaches set-point. Tyreus and Luyben modified Ziegler and Nichols' method with the result of faster settling

	Proportional $K_p = \frac{R_f}{R_{in}}$	Integral $K_i = \frac{1}{R_i C_i}$	Derivative $K_d = R_d C_d$
P controller (ZN)	$0.5K_u$		
PI controller (ZN)	$0.45K_u$	$1.2K_p/T_u$	
PI controller (TL)	$0.31\,K_u$	$0.\dot{4}\dot{5}K_p/T_u$	
PID controller (ZN)	$0.6K_u$	$2K_p/T_u$	$K_pT_u/8$
PID controller (TL)	$0.\dot{4}\dot{5}K_u$	$0.\dot{4}\dot{5}K_p/T_u$	$K_pT_u/6.3$

Table 5.2: **Ziegler-Nichols (ZN) and Tyreus-Luyben (TL) ideal PID coefficients** - from the Ziegler-Nichols closed-loop tuning method [163; 164].

systems [164], the modified coefficients are also given in table 5.2. The resistor and capacitor values needed to provide these gain parameters are calculated based on the set-up of the operational amplifier(s), the details for our controller are given in figure 5.20, with the equations used in table 5.2.

The Ziegler-Nichols and Tyreus-Luyben methods allow the user to get close to the desired PID parameters, then further tweaking is required to optimise. Usually from here a heuristic method is used, each parameter is tweaked in turn to see how the system responds and tuned accordingly. The aim is to have the system behave as a near-critically damped oscillator, so that it reaches its set-point quickly without too much ringing or being too heavily damped. There are plenty of sources of information on PID loop tuning including, but not exclusively: [165; 166].

The ultimate gains and ultimate oscillation periods for our all-aluminium vacuum chamber and inner temperature shield, along with the final chosen gains are detailed in table 5.3.

Using the optimised gain parameters detailed in table 5.3 the all-aluminium vacuum chamber has a long-term, out of loop temperature stability of $< 5\,\mathrm{mK}$ over 24 hours and $< 10\,\mathrm{mK}$ over a week, at $\sim 17\,^{\circ}\mathrm{C}$. The inner temperature shield

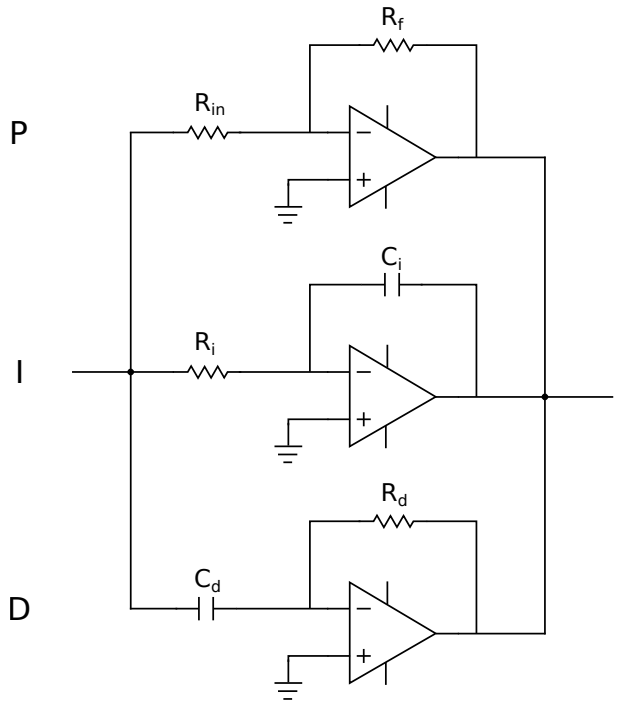

Figure 5.20: **Cavity temperature control PID** - Schematic of PID configuration used for the caivty vacuum chamber temperature controllers.

	Bridge gain	K_u	T_u (s)	K_p	K_i	K_d
All-aluminium vacuum chamber	99	15.1	116	$0.58\,K_u$	$0.82\,K_p/T_u$	$K_pT_u/20$
Inner temperature shield	395	6.7	690	$0.35K_u$	$0.49K_p/T_u$	-

Table 5.3: **Chosen PID gain parameters** - for vertical cavity all-aluminium vacuum chamber and inner temperature shield.

has a long-term, out of loop temperature stability of $< 1\,\text{mK}$ over 24 hours and $< 3\,\text{mK}$ over a week, at a temperature of $\sim 25\,^{\circ}\text{C}$.

5.4 Finding cavity CTE minimum

In section 5.3.1.1 we demonstrate by calculation the importance of stabilising our cavity temperature to that of zero CTE, T_c. The method we use to find T_c is similar to that used in [151] in that we have two independent lasers locked to two independent cavities, one of which we vary the temperature of and observe the change in beat frequency between the two locked lasers. Our 698 nm laser # 1 is locked to vertical cavity # 1; this set-up is all on one AVI, as shown on AVI 1 in figure 5.21 and the photographs in figure 5.18. This cavity has the less-than-ideal finesse value of $43\,000 \pm 1\,000$ (equivalent to a cavity mode FWHM of $(45 \pm 1)\,\text{kHz}$); it is housed in an all-aluminium vacuum chamber at a pressure of $\sim 7 \times 10^{-6}\,\text{mbar}$, and is usually temperature stable to 1 mK over a 24 hour period under normal laboratory conditions. The laser frequency is PDH stabilised to the centre of the cavity mode, with fast PID feedback to the laser diode current and slow PIIID feedback to the drive voltage of the piezo stack on the ECDL arm housing the diffraction grating. A pick-off beam is fibre-coupled onto the second AVI where it is co-aligned with a pick-off from the second laser (both pick-offs are before the PDH modulation is applied) onto an avalanche photodiode to measure the beat frequency (see figure figure 5.21).

Since having our finesse problems and the need to re-design the vacuum chamber for vertical cavity # 2, this cavity was not available for the T_c measurement. Instead we used the stability of the horizontally mounted 689 nm cavity as our reference. This has a finesse of $65\,000 \pm 2\,000$ (equivalent to a cavity mode FWHM of $(23.1 \pm 0.7)\,\text{kHz}$) at 689 nm, and is assumed to be similar for 698 nm, although

it has not been measured. This cavity has a single layer of temperature stabilisation, which is stable to better than 10 mK over a 24 hour period, but the cavity is believed to be about 22 °C from its zero-CTE temperature. This equates to a worst case frequency deviation of < 400 kHz between measurements, which is better than the ~ 1 MHz frequency certainty we require to calculate a precise T_c value. The second laser, ECDL # 2, is housed on the second AVI with the first half of the optics required for locking. After the light is phase-modulated by the EOM, it is coupled into a 50 cm long APC (angle polished cut) polarisation maintaining optical fibre to take the light from the AVI onto the main optical table, where the cavity is housed. The cavity alignment mirrors and the pick-off for the PDH error signal are on the main optical table close to the cavity (see figure figure 5.21).

Cavity # 2 and laser # 2 remain at a constant temperature and frequency, respectively, throughout the data-set; the TEM_{00} mode frequency is (429 227 690 $\pm$ 2) MHz as measured on our High Finesse wavemeter (calibrated to the frequency of the clock laser from the Sr^+ laboratory) at a cavity temperature of ~ 22.5 °C. The temperature of the inner temperature shield around vertical cavity # 1 is set, the cavity is allowed to settle for a couple of days (allowing for settling of the temperature servo loop, and then sufficient delay for the cavity temperature to equilibrate), and a series of beat frequencies are taken throughout the day to get an idea of how much the frequency is drifting. Once we are happy that we have enough data to be confident of our measured beat frequency the temperature is changed to the next set-point and the process repeated. The data are shown in figure 5.22 with the best quadratic fit (found by least squared analysis). The error bars for each data-point are small compared to the scale of

the graph and are roughly $\pm 0.1\,^{\circ}\mathrm{C}$ and $\pm 0.3\,\mathrm{MHz}$. The fit follows the form:

$$f_{\mathrm{beat}} = f_{\mathrm{laser}} \times C\,(T - T_c)^2 + f_0 \tag{5.24}$$

where $f_{\mathrm{laser}} = (429\,228\,015 \pm 5)\,\mathrm{MHz}$, $C = (-6.63 \pm 0.01) \times 10^{-10}\,/\,^{\circ}\mathrm{C}^2$, $T_c = (25.7 \pm 0.1)\,^{\circ}\mathrm{C}$, and $f_0 = (319.7 \pm 0.1)\,\mathrm{MHz}$. Showing the temperature of zero-CTE for this cavity to be at $(25.7 \pm 0.1)\,^{\circ}\mathrm{C}$ with good certainty.

5.5 Optical frequency comb measurements

Before the zero CTE temperature was found we were under the impression that our vertical cavities were from the same ULE batch as those detailed in [151], indicating they would have a zero-CTE temperature in the $\sim 7\,^{\circ}\mathrm{C}$ to $13\,^{\circ}\mathrm{C}$ range, so we started with our cavity temperature at $\sim 8\,^{\circ}\mathrm{C}$, where we took a day of frequency measurements with the optical frequency comb referenced to the hydrogen maser. This data showed a surprisingly high drift rate (assuming we were close to T_c, and given that our temperature drifted by less than a maximum of 3 mK during the measurement) of 350 mHz/s, indicating that either we had large lock errors (varying offsets causing our lock point to change) or that we were not close to T_c. After measuring our T_c and stabilising the cavity temperature there, a further hydrogen-maser-referenced optical frequency comb measurement was taken, during which the cavity temperature drifted by less than 1 mK. This frequency measurement showed a much improved drift rate of $< 450\,\mathrm{Hz}$ in 4 hours, equivalent to $\sim 30\,\mathrm{mHz/s}$, this is equal to or better than expected, and compares well to low drift cavities in other laboratories at NPL. To estimate the worst case thermal drift contribution to the measured drift, we assume our cavity is $0.3\,^{\circ}\mathrm{C}$ from T_c and drifts by 1 mK during the measurement period, this gives us

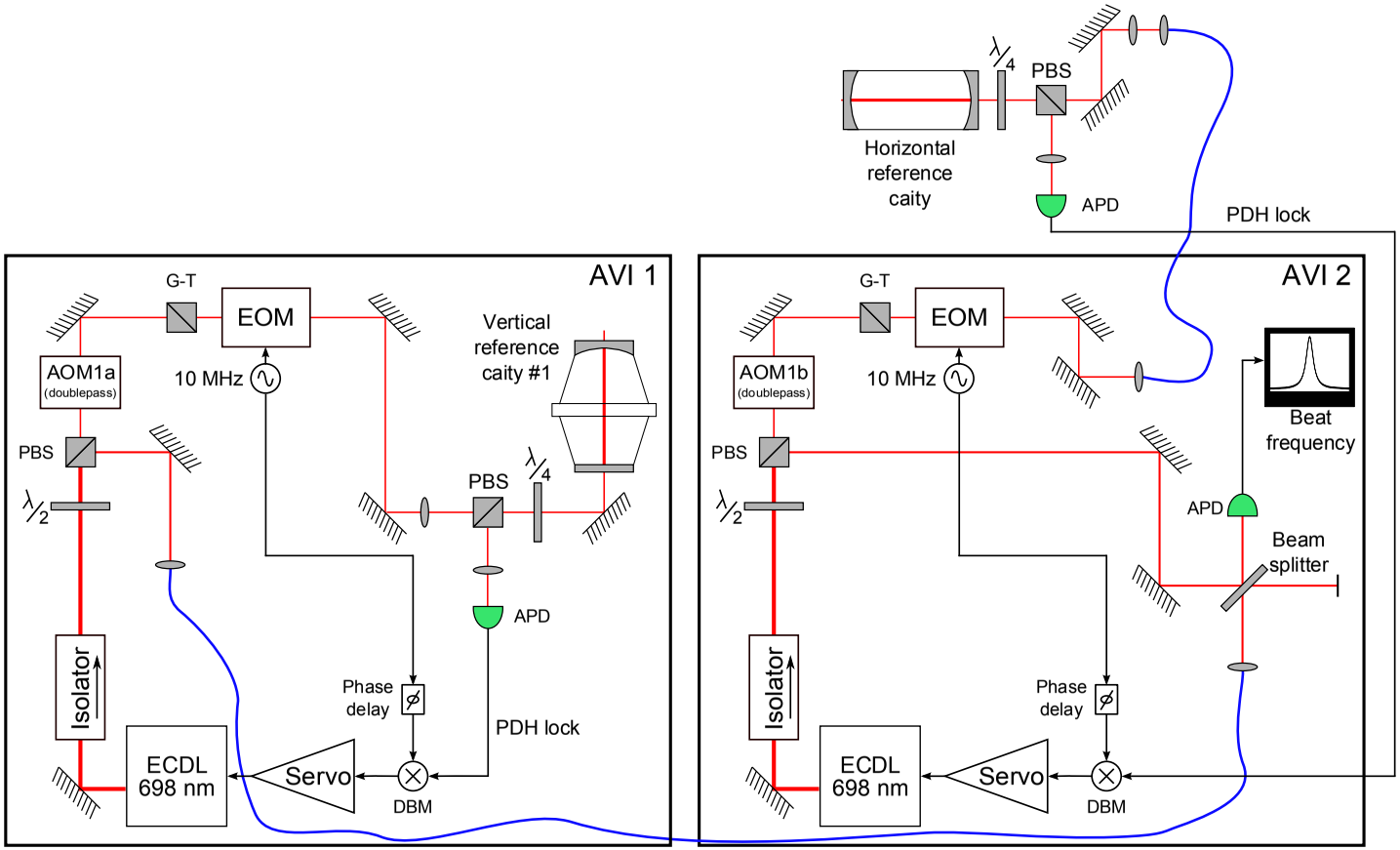

Figure 5.21: **Optical set-up for finding the zero-CTE temperature of cavity # 1** - Shows experimental set-up for taking the beat frequency data shown in figure 5.22. AVI 1 houses the laser, optics, and optical reference cavity # 1 for the first clock laser set-up. The second laser and optics are on AVI 2, with the horizontally orientated optical reference cavity on the main optical table. The beat frequency between the two locked clock lasers is measured for a range of temperatures of cavity # 1.

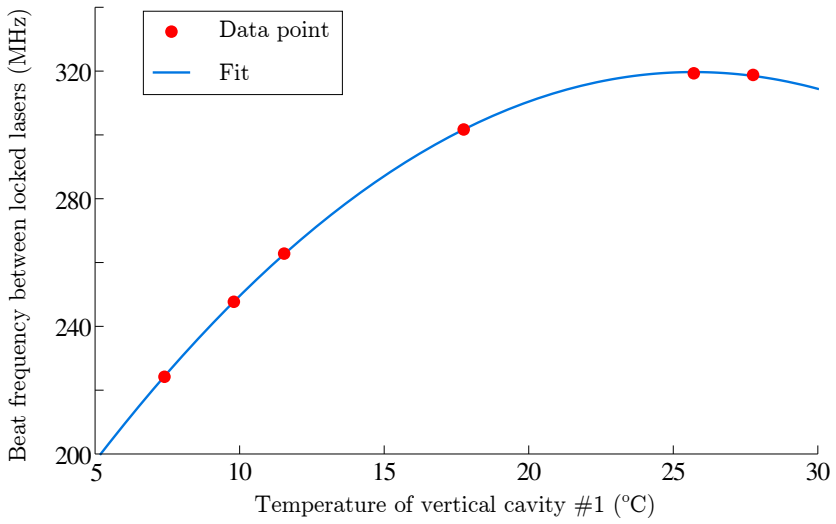

Figure 5.22: **Data for locating zero-CTE temperature of cavity #1** - Beat frequency between vertical cavity #1 at given temperatures and 689 nm horizontal reference cavity at a fixed temperature. The experimental set-up is shown in figure 5.21. The error bars for each data-point are small compared to the scale of the graph and are roughly $\pm 0.1\,^{\circ}\mathrm{C}$ and ± 0.3 MHz. The turning point of curve indicates temperature of zero-CTE, T_c. The fit follows equation 5.24, where $T_c = (25.7 \pm 0.1)\,^{\circ}\mathrm{C}$.

a maximum frequency drift of 170 Hz. This is a very cautious estimate, a more likely value would be < 30 Hz. The remainder of the drift is due to lock errors and creep of the cavity material as it settles in its vacuum environment. Cavity creep is a small contraction of the cavity material as it ages and impurities in the glass diffuse out under vacuum conditions, the creep is usually approximately linear, but reduces with material age and time under vacuum.

The frequency vs. time graph from the second optical frequency comb measurement is shown in figure 5.23, it shows the drift described above, with a linear fit, and the residuals between the fit and the data. The residuals show a maximum of ± 100 Hz deviation of the data from the linear fit expected from the cavity creep. This small frequency jitter at medium time-scales is most likely to be due to PDH lock errors, either optical or electronic, causing the lock point to drift from the centre of the cavity fringe (more on this explained in section 5.2.2).

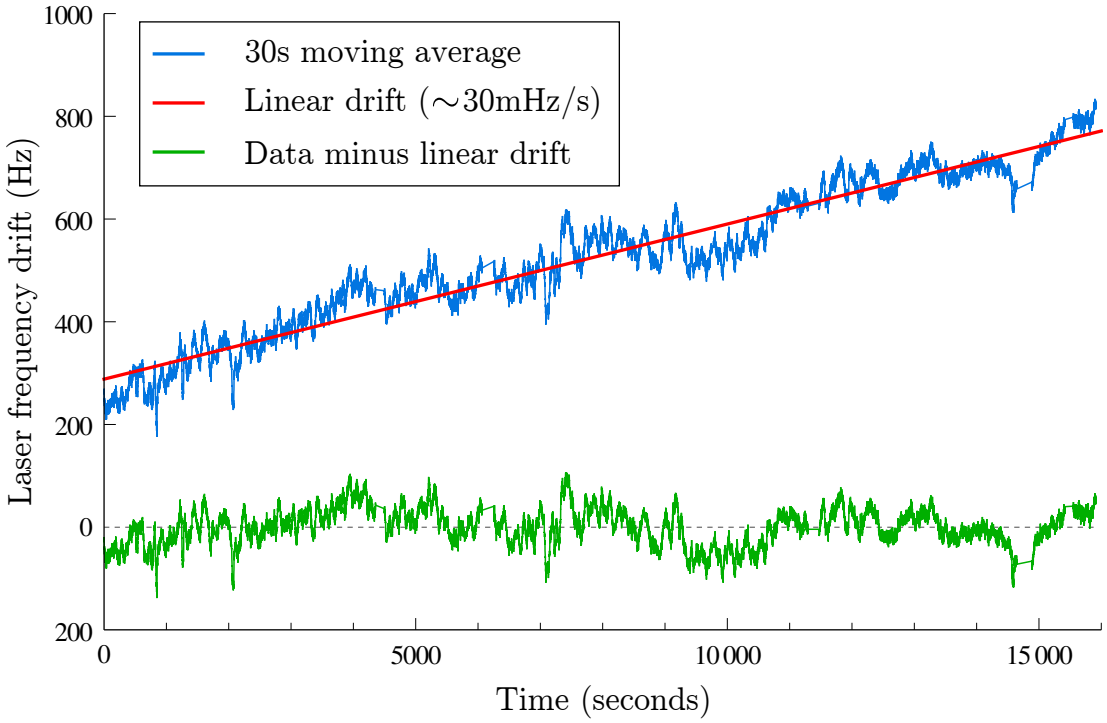

Figure 5.23: **Optical frequency comb measurement (drift)** - Frequency drift vs. time data of locked laser when cavity temperature is at T_c. Frequency is measured with the optical frequency comb referenced to the hydrogen maser. Data taken in one second bins, then a 30 second moving average taken to reduce the short-term frequency noise (mostly from the maser). A linear drift is fitted to this data, which shows a drift rate of 30 mHz/s, and the residuals from this linear fit and the data shown in green. The residuals show a deviation of a maximum of ± 100 Hz from the fit over the whole > 4 hour run.

This is often seen on new laser systems before they are fully optimised, the effect is larger in our system due to the 10 times larger cavity mode linewidth than usual, causing the frequency deviations to be 10 times larger also. This jitter will be reduced once the cavity mirrors are cleaned, increasing the cavity finesse, and we would expect to see the linear drift with around $\pm 10\,\mathrm{Hz}$ deviation. The following steps to reduce this further would be to put a box around the optical set-up to reduce air currents and increase the temperature stability, followed by temperature stabilisation of our EOM crystal. Temperature changes in the EOM crystal can cause varying residual amplitude modulation (RAM), which causes PDH lock errors, see section 5.2.2.1. RAM can be measured with a pick-off to a photodiode feeding a double balanced mixer, the signal from which can feed a PI servo control of the EOM temperature. This technique has been shown to reduce the RAM from around 180 ppm with fixed EOM temperature to below 25 ppm with feedback to the EOM temperature [128].

For details of how an optical frequency comb works there is a brief explanation in section 1.3 with more detailed descriptions in literature such as [14; 15; 167]. In order to take the measurements detailed here the hydrogen-maser-referenced optical frequency comb takes frequency measurements of our laser in 1 second bins. We can either look at this data as frequency vs. time, as in figure 5.23, or we can plot the Allan deviation, as in figure 5.24, which shows the fractional frequency instability at different time scales (as previously discussed in section 2.3.2.3). As predicted by our discussion in section 2.3.2.3 and the graph in figure 2.3 the maser stability determines the measurement fractional frequency instability at short time-scales, starting at around 5×10^{-13} at 1 second and falling as $\sim 1/\tau$. On longer time-scales ($> 1000\,\mathrm{s}$) the fractional frequency instability is set by the drift of the optical reference cavity to which the laser is locked. For

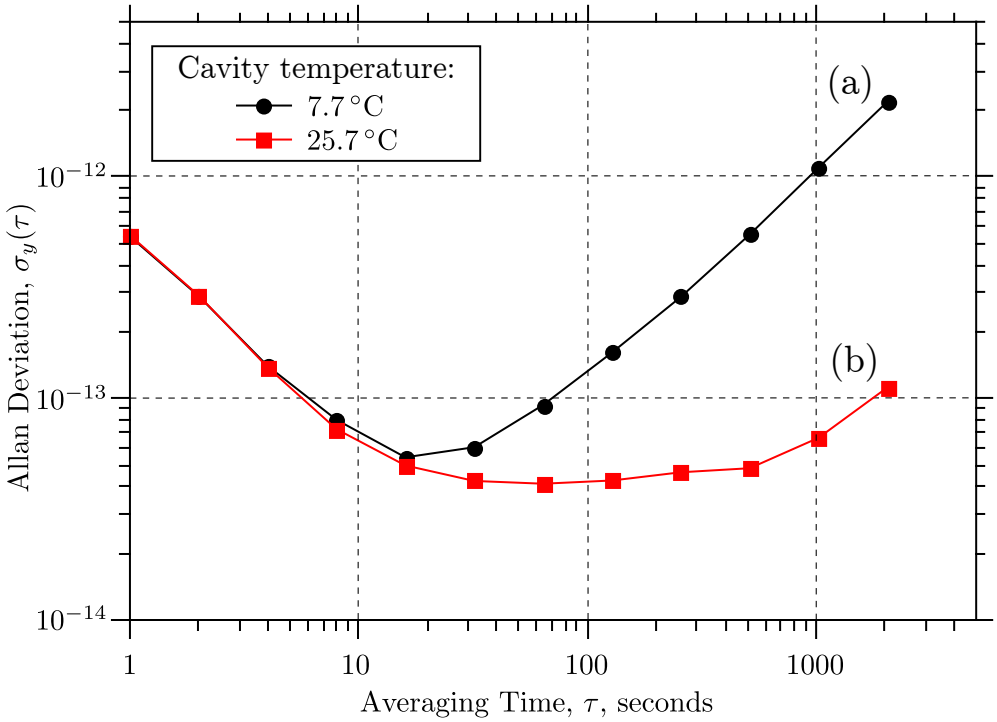

Figure 5.24: **Allan deviation of optical frequency comb measurements** - Fractional frequency instability vs. measurement time of locked clock laser when cavity #1 temperature is stabilised at (a) $(7.7 \pm 0.1)\,°\mathrm{C}$ and (b) $T_c = (25.7 \pm 0.1)\,°\mathrm{C}$. These Allan deviation plots nicely demonstrate the importance of stabilising the cavity to T_c, its temperature of zero coefficient of thermal expansion. Curve (a) has a drift rate over an order of magnitude higher than curve (b) for a similar level of temperature stability.

example from figure 5.24 (b) a fractional frequency instability of 6.64×10^{-14} at 1024 seconds is equivalent to 28 mHz/s drift rate, which is comparable to what we measure with our linear fit in figure 5.23. The shape of the Allan deviation between ~ 10 s and ~ 1000 s is usually defined by the quality of the laser lock, a very tight laser lock would make more of a v-shape than we see here. Our Allan deviation is flatter than ideal between 10 s and 1000 s, this is due mostly to the jitter noise we see in figure 5.23. As we explained before, a higher finesse cavity with decreased lock errors would reduce this instability on medium time-scales.

5.6 Locked laser linewidth

We have built a system to lock a laser to an optical reference cavity and have made a measurement of the frequency over a few thousand seconds, but we still know very little about the linewidth of the locked laser. From the frequency instability plot shown in figure 5.24 we can infer that the laser stability is equal to or better than that of the hydrogen maser on short time-scales, so we can estimate our instability at 1 s to be better than ~ 240 Hz. To make a better estimate of the linewidth we can look at the in-loop error signal of the locked laser and calibrate the measured voltage deviations into frequency deviations. This would give us an indication of the laser linewidth, but it would not show up any drifting lock errors (electrical or optical offsets) or cavity induced noise, such as that from vibrations or temperature fluctuations. The only way to truly measure a laser linewidth is to use a narrower frequency line, such as that of the atomic clock transition or a narrower linewidth laser to beat ours against. Failing this we can use a laser with approximately the same linewidth and infer the noise distribution between the two lasers. It is for this purpose that we have been building a second clock laser system.

By co-aligning two laser beams of similar frequency and directing them onto a photo-detector we can observe the beat frequency between the two lasers, the linewidth of which allows us to estimate the linewidth of our lasers. Assuming both lasers have near equal linewidths and frequency profiles that are approximately Gaussian, we can estimate the linewidth of each laser to be $\sim 1/\sqrt{2}$ times the linewidth of the beat. Any common noise between the two lasers systems will not show up on the beat, so it is important that the systems are as independent as possible, for example two separate lasers locked to two independent cavities, mounted on two different optical tables. Ideally we would take advantage of two

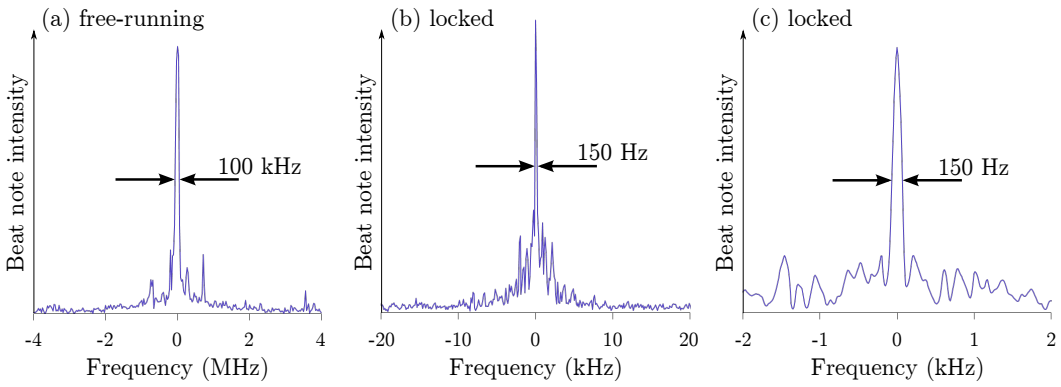

Figure 5.25: **Beat note for laser linewidth estimation** - Clock laser linewidth estimated by beat note comparison of (a) two free-running 698 nm lasers, (b) and (c) two 698 nm lasers locked to high finesse optical reference cavities. Measurement time for (b) and (c) is 10 ms for the width of the peak. The beat frequency offsets have been removed to show the beats around 0 Hz.

different cavity geometries to reduce noise from common vibrations.

Due to the finesse problems we had with vertical cavity # 1 and the subsequent delay of redesigning our second vacuum chamber we did not have the second cavity under vacuum in time to make this linewidth measurement. Instead we set up the laser, optics and electronics for the second system and utilised the horizontal cavity, which is usually used for the 689 nm laser locking. The locked lasers are overlapped onto an APD and the beat frequency observed on a spectrum analyser. The optical set-up is shown in figure 5.21. We observed a locked laser beat linewidth of ~ 300 Hz at one second, which equates to an individual laser linewidth of ~ 212 Hz at one second, if we assume the lasers have equal linewidth. Figure 5.25 shows examples of the unlocked and locked beat signals with the beat frequency offset removed[1].

[1]The beats shown in (b) and (c) show laser linewidths of 150 Hz at a 10 ms measurement time, rather than the 300 Hz at one second quoted above. Unfortunately on the day we had access to the spectrum analyser for saving the data, the second laser was struggling to maintain a good lock, so the linewidth at one second was very jittery. We would like to have saved good traces of the linewidth at one second, which we will do when the second cavity is under vacuum, but we have not reached this point yet.

The measured linewidth is just under 0.5 % of the cavity fringe width, which is getting close to the rule of thumb target of 0.1 %. Applying the same laser and lock techniques to a cavity with a ten times narrower resonant mode (ten times higher finesse), such as the second vertical cavity we are working towards implementing, should result in a ten times narrower linewidth. The frequency fluctuations we see in figure 5.23 are mainly due to lock errors (varying offsets) that will scale with cavity linewidth, so we also expect these to reduce to the ± 10 Hz level. The linear drift rate will remain the same. Once we have two lasers with ~ 10 Hz linewidth we can systematically go through the systems to identify sources of noise. We can optimise the optical power to the cavity, the lock gains and bandwidth, we will implement intensity stabilisation to the cavity, and temperature control of the EOM. We are also building a large box to go around the two systems to reduce perturbations due to air currents, temperature fluctuations, and acoustic vibrations. We are well prepared for each of these implementations, so once we have cleaned the first cavity mirrors and have both high finesse cavities under vacuum we will be well under-way to achieving our goal of sub-hertz linewidth clock lasers.

5.7 Clock laser summary and outlook

Significant progress has been made on the development of two narrow-linewidth clock laser systems, with the majority of the work having been completed or planned in detail. Unfortunately technical problems have slowed progress, and we have not yet reached our goal of two sub-hertz linewidth lasers, although we anticipate it is not too far away. The next steps are to place vertical cavity # 2 under vacuum and lock the laser to it. Once we have ascertained the vacuum level is good and the cavity still demonstrates a high finesse we can clean the

mirrors of vertical cavity #1 and build a new vacuum system for it, identical to that for cavity #2. With two lasers locked to two high finesse optical reference cavities we should be able to measure laser linewidths of a few Hertz via beat frequency comparison, and the lock optimisations outlined in sections 5.2 and 5.6 will be implemented. We see no reason why the laser systems we have built will not be able to achieve the desired sub-hertz linewidths.

Chapter 6

Conclusions and Outlook

This thesis presents the considerations towards the design of the strontium optical lattice frequency standard at the National Physical Laboratory (NPL) and focuses on the experimental details of selected parts of the set-up. During the course of this D.Phil. studentship the experiment grew from a small collection of articles perched on top of cupboards in a shared laboratory, to a wealth of functioning lasers, optical reference cavities, and vacuum systems, filling a large optical table in a new laboratory. A considerable amount of time has been invested in the development and construction of the many laser systems, associated control electronics, and the accompanying environmentally-stabilised optical reference cavities, required for clock operation, and represents a large portion of the work for this studentship and the project as a whole.

6.1 Thesis conclusions

We have designed, built and characterised a strontium vapour source and a range of permanent magnet Zeeman slowers, and demonstrated we can use these to slow, trap and cool strontium atoms in a magneto-optical trap (MOT) at 461 nm. We have demonstrated our source, slower and MOT combination works equivalently well for the four naturally abundant isotopes of strontium (^{84}Sr, ^{86}Sr, ^{87}Sr and

^{88}Sr). Without the aid of repump lasers we typically load $\sim 2 \times 10^{-7}$ ^{88}Sr atoms at a temperature of a few millikelvin in the first-stage MOT, and we have demonstrated atom number enhancements by the addition of repump lasers at 679 nm and 707 nm. For more details see chapter 3.

The permanent magnet Zeeman slowers, of both transverse and longitudinal magnetic field orientations, have been shown to provide effective and efficient cooling of strontium atoms without the added mass and power consumption necessary to run a typical tapered solenoid Zeeman slower. The transverse-field Zeeman slowers have a mass of just 2 kg and are very easy to design, build and tune the magnetic field profile for efficient slowing, however they do require twice the laser power of an equivalent longitudinal-field Zeeman slower. The permanent magnet Zeeman slowers and their results are detailed in sections 3.2.1 and 3.3.2.

The repump lasers at 707 nm and 679 nm have been built and locked to a HighFinesse WSU-10 wavemeter and a tunable optical reference cavity respectively. They have been shown to enhance the ^{88}Sr atom number in the first-stage MOT by a factor of 3, with the 707 nm laser, and 17, with both the 707 nm and 679 nm lasers. The repump lasers and their results are detailed in sections 3.3.1 and 3.3.3.2.

The 689 nm laser system for second-stage cooling of the strontium atoms in the second-stage MOT has been designed and built. The 689 nm ECDL is locked to a temperature stabilised, high finesse, ULE optical reference cavity. A very conservative estimate gives the locked laser linewidth to be less than a few kilohertz, which is ideal for driving the 7.5 kHz wide transition. Unfortunately the high drift rate (~ 2 Hz/s) of the optical reference cavity mode frequencies, due to the cavity not being stabilised at its temperature for zero coefficient of thermal expansion, means that the locked laser will drift off resonance from the atomic

transition within just one hour. The easiest way to solve this problem is to lock the 689 nm laser to the second clock optical reference cavity which is stabilised at its zero coefficient of thermal expansion and has demonstrated a drift rate of ~ 30 mHz/s. See section 4.1 for more details on the 689 nm laser set-up.

We have presented preliminary fluorescence spectroscopy of the 689 nm transition in the thermal atomic beam, where we were able to see fluorescence peaks from the ^{86}Sr and ^{88}Sr isotopes. Sub-doppler spectroscopy revealed a linewidth of 1.5 MHz, which we attribute to the linewidth of the resonant laser beam. We would like to be able to take this spectroscopy again with the 689 nm laser locked to the optical reference cavity, in which case we would expect to be able to see feature linewidths (at low probe beam powers) as low as ~ 100 kHz, limited by transit time broadening. This work is detailed in section 4.1.3.

The 813 nm ECDL for the magic wavelength lattice has been built, and will be locked to the same tunable optical reference cavity as the 679 nm repump laser and the 922 nm laser light, which is doubled to produce the 461 nm light for first-stage laser cooling of the atoms. We propose to reference this cavity to one of the extremely low-drift-rate clock cavities to provide more than adequate long term stability. See section 4.2 for more details.

An apparatus for measuring and characterising the black-body-radiation-induced Stark shift on the clock transition has been designed and partially installed. We propose to use two independently controllable black-body radiation (BBR) tubes, which can be stabilised to different temperatures. This set-up should allow us to make measurements of the clock transition frequency in two well-known temperature environments, and from this derive an experimentally realised measurement of the BBR shift coefficient. More details on this part of the experiment are given in sections 2.4.1.2 and 4.3

The two clock laser systems have been designed and built and are in the process of being characterised and optimised. They each consist of an ECDL locked to an optical reference cavity, all mounted on an active vibration isolation (AVI) platform. We have found the temperature of zero coefficient of thermal expansion of the first cavity to be at $T = (25.7 \pm 0.1)\,^{\circ}\mathrm{C}$; the method and data for this experiment is presented in section 5.4. After stabilising the cavity at $T = 25.7\,^{\circ}\mathrm{C}$ we use an optical frequency comb to measure the drift rate of the frequency of the 698 nm laser locked to the cavity. We find the drift rate to be suitably low, at around 30 mHz/s, and approximately linear (suggesting it is due to relaxation of the ULE material, an expected effect of material ageing). For details on this part of the experiment see section 5.5.

We have performed heterodyne beat frequency comparison of two independent 698 nm lasers locked to two independent optical reference cavities. This work is described in section 5.6. We measure a locked laser linewidth of less than 300 Hz at one second. This is less than ideal and needs optimising, but contamination on the optical reference cavity mirrors have delayed this process. Information on our optical reference cavities, and details of these laser linewidth results, can be found in sections 5.3 and 5.6 respectively.

6.2 The imminent future

The next steps for the NPL strontium optical lattice experiment are to begin loading the cold atoms into the narrow-line MOT to achieve lower temperatures and increased atomic density. From there the atoms can be loaded into the 'magic' lattice for initial 'clock' tests or into the transport lattice, allowing them to be moved in to the black-body radiation tubes. The second clock laser system needs to be completed and the mirrors of the first optical reference cavity cleaned. We

should then have two narrow linewidth laser systems ready for the final round of characterisation and optimisation. At this point we intend to have all the infrastructure necessary to start measuring the frequency of the clock transition and assessing the systematic frequency shifts and their uncertainties.

The future for neutral atom optical lattice clocks is arguably as short-term highly-stable oscillators, with the ion standards providing the long-term stable reference, mimicking today's arrangement of hydrogen maser oscillator and caesium fountain reference. Only time will tell if the fractional frequency uncertainties of neutral atom clocks can be reduced to the level of the best ion clocks. At present Stark shifts due to black-body radiation (BBR) dominate the uncertainty budget, but better knowledge of the physics behind the shift and characterisation of the BBR emission within the atomic environment is key to the reduction of the uncertainty associated with it. There is an, as yet, untapped area of science in terms of using Rydberg atoms and their ultra-high sensitivity to electric fields as local atomic sensors to detect the BBR [168] and static electric fields [169; 170] in the region of the clock atoms. One can envisage Rydberg atoms of the same atomic species being used to characterise the environment prior to, or interleaved between, clock transition frequency measurements. This would require the addition of only a small number of laser systems. The alternative approach, as we have mentioned earlier in section 2.4.1.2, is to house the atoms at cryogenic temperatures, where knowledge of the temperature to $\sim 1\,\mathrm{K}$ (a realistic limit) equates to a frequency measurement uncertainty of approximately 10^{-18}. For today's current uncertainty budget this bodes well, but could once again become a limiting factor in the future, especially considering the impracticalities of having a cryogenic system in space. A more worth-while pursuit might be to take the same approach as for the aluminium ion clock and build clocks using other atomic

species, such as cadmium, mercury, magnesium and zinc, that have clock states which are less sensitive to BBR [171].

6.3 A broader outlook

Looking further into the future, we may see a continuation of the trend, in that we look for clocks at even higher frequencies. A promising candidate for this is a $\sim 160\,\text{nm}$ nuclear transition in thorium [172] [173]. This transition frequency can be reached with today's laser technology and is insensitive to external electric and magnetic fields due to shielding from the core electrons [173]. Thorium ions could be held in an ion trap and directly or sympathetically laser-cooled, or a more exciting alternative is to use a thorium-doped crystal. The crystal would need to be transparent to the $\sim 160\,\text{nm}$ clock transition light, and perturb the frequency of the clock transition in a characterisable way [174]. The potential for this technique is huge; it could lead to an ultra-stable, ultra-precise clock at room temperature with no need for cooling lasers or a vacuum system. Observation of this nuclear transition is yet to be confirmed, but is being searched for my many laboratories, and a positive result could be reported very soon.

References

[1] D. Sobel. *Longitude*. Fourth Estate, London, 1998. 2

[2] C.W. Chou, D.B. Hume, J.C.J. Koelemeij, D.J. Wineland, and T. Rosenband. Frequency Comparison of Two High-Accuracy Al^+ Optical Clocks. *Physical Review Letters*, 104(7):070802, Feb 2010. 3, 11, 12, 14

[3] L. Essen and J.V.L. Parry. An Atomic Standard of Frequency and Time Interval: A Caesium Resonator. *Nature*, 176(4476):280–282, August 1955. 3

[4] L. Essen and J.V.L. Parry. The Caesium Resonator as a Standard of Frequency and Time. *Philosophical Transactions of the Royal Society A: Mathematical, Physical and Engineering Sciences*, 250(973):45–69, August 1957. 3

[5] D.B. Sullivan, J.C. Bergquist, J.J. Bollinger, R.E. Drullinger, W.M. Itano, S.R. Jefferts, W.D. Lee, D. Meekhof, T.E. Parker, F.L. Walls, and D.J. Wineland. Primary Atomic Frequency Standards at NIST. *Journal of Research of the National Institute of Standards and Technology*, 106:47–63, 2001. 3

[6] R. Li, K. Gibble, and K. Szymaniec. Improved accuracy of the NPL-CsF2

primary frequency standard: evaluation of distributed cavity phase and microwave lensing frequency shifts. *Metrologia*, 48:283, 2011. 3

[7] S.N. Lea. Limits to time variation of fundamental constants from comparisons of atomic frequency standards. *Reports on Progress in Physics*, 70(9):1473–1523, 2007. 6

[8] V.A. Dzuba and V.V. Flambaum. Atomic calculations and search for variation of the fine structure constant in quasar absorption spectra. *Canadian Journal of Physics*, 87:15, 2009. 6

[9] V.V. Flambaum. Astrophysical evidences for the variation of fundamental constants and proposals of laboratory tests. In *International Conference of Atomic Physics*, 2012. 6

[10] E. Peik, B. Lipphardt, H. Schnatz, T. Schneider, C. Tamm, and S.G. Karshenboim. Limit on the Present Temporal Variation of the Fine Structure Constant. *Physical Review Letters*, 93:170801, 2004. 6

[11] T. Rosenband, D.B. Hume, P.O. Schmidt, C.W. Chou, A. Brusch, L. Lorini, W.H. Oskay, R.E. Drullinger, T.M. Fortier, J.E. Stalnaker, S.A. Diddams, W.C. Swann, N.R. Newbury, W.M. Itano, D.J. Wineland, and J.C. Bergquist. Frequency Ratio of Al^+ and Hg^+ Single-Ion Optical Clocks; Metrology at the 17th Decimal Place. *Science*, 319(5871):1808–1812, March 2008. 6

[12] H. Schnatz, B. Lipphardt, J. Helmcke, F. Riehle, and G. Zinner. First Phase-Coherent Frequency Measurement of Visible Radiation. *Physical Review Letters*, 76:18–21, 1996. 7

[13] Th. Udem, J. Reichert, R. Holzwarth, and T.W. Hänsch. Absolute Optical Frequency Measurement of the Cesium D1 Line with a Mode-Locked Laser. *Physical Review Letters*, 82:3568, 1999. 8

[14] S.A. Diddams, D.J. Jones, J. Ye, S.T. Cundiff, J.L. Hall, Ranka J.K., R.S. Windeler, T. Holzwarth, R. Udem, and T.W. Hnsch. Direct link between microwave and optical frequencies with a 300 THz femtosecond laser comb. *Physical Review Letters*, 84:5102–5, 2000. 8, 180

[15] F. Riehle. *Frequency Standards: Basics and Applications*. Wiley-VCH, 2004. 8, 130, 132, 180

[16] P.G. Westergaard, J. Lodewyck, L. Lorini, A. Lecallier, E.A. Burt, M. Zawada, J. Millo, and P. Lemonde. Lattice-Induced Frequency Shifts in Sr Optical Lattice Clocks at the 10^{-17} Level. *Physical Review Letters*, 106(21):210801, May 2011. 12, 34, 35

[17] M Takamoto, T. Takano, and H. Katori. Frequency comparison of optical lattice clocks beyond the Dick limit. *Nature Photonics*, 5:288–292, 2011. 12

[18] P.G. Westergaard, J. Lodewyck, and P. Lemonde. Minimizing the dick effect in an optical lattice clock. *Ultrasonics, Ferroelectrics and Frequency Control, IEEE Transactions on*, 57(3):623 –628, March 2010. 12, 27, 28

[19] M.D. Swallows, M.J. Martin, M. Bishof, C. Benko, Y. Lin, S. Blatt, A.M. Rey, and J. Ye. Operating a ^{87}Sr Optical Lattice Clock With High Precision and at High Density. *IEEE Transactions on Ultrasonics, Ferroelectrics and Frequency Control*, 59:416–425, 2012. 12, 32, 149, 156

[20] T.L. Nicholson, M.J. Martin, J.R. Williams, B.J. Bloom, M. Bishof, S.L. Swallows, M.D. ad Campbell, and J. Ye. Comparison of two independent

Sr optical clocks with 1×10^{-17} stability at 10^3 s. *arXiv:1210.0064*, 2012. 12, 14, 27

[21] A.D. Ludlow, T. Zelevinsky, G.K. Campbell, S. Blatt, M.M. Boyd, M.H.G. de Miranda, M.J. Martin, J.W. Thomsen, S.M. Foreman, Jun Ye, T.M. Fortier, J.E. Stalnaker, S.A. Diddams, Y.Le Coq, Z.W. Barber, N. Poli, N.D. Lemke, K.M. Beck, and C.W. Oates. Sr lattice clock at 1x10^{-16} fractional uncertainty by remote optical evaluation with a Ca clock. *Science*, 319:1805, 2008. 12, 14, 15, 32, 35

[22] M.D. Swallows, M. Bishof, Y. Lin, S. Blatt, M.J. Martin, A.M. Rey, and J. Ye. Suppression of Collisional Shifts in a Strongly Interacting Lattice Clock. *Science*, 331:1043, 2011. 12, 32, 34

[23] T. Middelmann, C. Lisdat, S. Falke, J.S.R.V. Winfred, F. Riehle, and U. Sterr. Tackling the Blackbody Shift in a Strontium Optical Lattice Clock. *Instrumentation and Measurement, IEEE Transactions on*, 60(7):2550 – 2557, July 2011. 12, 36, 37, 38

[24] T. Middelmann, S. Falke, C. Lisdat, and U Sterr. High accuracy correction of blackbody radiation shift in an optical lattice clock. *arXiv:1208.2848v1*, 2012. 12, 37, 38, 39, 40

[25] C.W. Oates, F. Bondu, R.W. Fox, and L. Hollberg. A diode-laser optical frequency standard based on laser-cooled Ca atoms: Sub-kilohertz spectroscopy by optical shelving detection. *European Physical Journal D*, 7(3):449–460, 1999. 13

[26] C.W. Oates, E.A. Curtis, and L. Hollberg. Improved short-term stability of

optical frequency standards: approaching 1 Hz in 1 s with the Ca standard at 657 nm. *Optics Letters*, 25(21):1603, November 2000. 13

[27] H. Katori. Spectroscopy of strontium atoms in the Lamb-Dicke confinement. *Proceedings of the 6th Symposium in Frequency Standards and Metrology*, pages 323–330, 2001. 13

[28] R. Dicke. The Effect of Collisions upon the Doppler Width of Spectral Lines. *Physical Review*, 89(2):472–473, January 1953. 14

[29] D. Leibrfried, R. Blatt, C. Monroe, and D. Wineland. Quantum dynamics of single trapped ions. *Reviews of Modern Physics*, 75:281 – 324, 2003. 14, 24

[30] Marianna Safronova, Mikhail Kozlov, and Charles W. Clark. Precision Calculation of Blackbody Radiation Shifts for Metrology at the 18th Decimal Place. In *CLEO:2011 - Laser Applications to Photonic Applications*, page CFC3. Optical Society of America, 2011. 14

[31] M. Takamoto, F.-L. Hong, R. Higashi, and H. Katori. An optical lattice clock. *Nature*, 435(7040):321–324, May 2005. 15, 34, 104

[32] R. Le Targat, X. Baillard, M. Fouché, A. Brusch, O. Tcherbakoff, G. Rovera, and P. Lemonde. Accurate Optical Lattice Clock with Sr87 Atoms. *Physical Review Letters*, 97(13):130801, September 2006. 15

[33] N. Poli, M.G. Tarallo, M. Schioppo, C.W. Oates, and G.M. Tino. A simplified optical lattice clock. *Applied Physics B*, 97(1):27–33, April 2009. 15

[34] S. Falke, H. Schnatz, J.S.R. Vellore Winfried, T. Middelmann, S. Vogt, S. Weyers, B. Lipphardt, G. Grosche, F. Riehle, U. Sterr, and C. Lisdat.

The ^{87}Sr optical frequency standard at PTB. *Metrologia*, 48:399–407, April 2011. 15, 26, 32, 65

[35] E.M. Bridge, I.R. Hill, Y.B. Ovchinnikov, G.P. Barwood, E.A. Curtis, and P. Gill. Progress towards a strontium optical lattice clock at NPL. In *Proc. European Frequency and Time Forum*, 2010. 15

[36] S-K. Wang, Q. Wang, Y. Li, Y-G. Lin, M-M. W, B-K Lin, Y Zhao, E-J Zang, T-C Li, and Z-J. Fang. The Progress of Strontium Optical Lattice Clock at NIM. In *Proc. European Frequency and Time Forum*, 2010. 15

[37] Ole. Kock, S. Johnson, Y. Singh, and K. Bongs. Portable frequency standard with strontium in optical lattices. In *Proc. of International Conference of Atomic Physics*, 2012. 15

[38] S. Slusarev, A. Kostin, S. Barychev, K Khabarova, S. Stralkin, S. Donchenko, V. Palchikov, and A. Krasavin. Towards Russian optical clock with cold strontium atoms, present status and performance. In *Proc. of International Conference of Atomic Physics*, 2012. 15

[39] N.D. Lemke, A.D. Ludlow, Z.W. Barber, T.M. Fortier, S.A. Diddams, Y. Jiang, S.R. Jefferts, T.P. Heavner, T.E. Parker, and C.W. Oates. Spin-1/2 Optical Lattice Clock. *Physical Review Letters*, 103(6):063001, Aug 2009. 15

[40] T. Kohno, M. Yasuda, K. Hosaka, H. Inaba, Y. Nakajima, and F.-L. Hong. One-Dimensional Optical Lattice Clock with a Fermionic ^{171}Yb Isotope. *Applied Physics Express*, 2(7):072501, 2009. 15

[41] N. Poli, Z.W. Barber, N.D. Lemke, C.W. Oates, L.S. Ma, J.E. Stalnaker, T.M. Fortier, S.A. Diddams, L. Hollberg, J.C. Bergquist, A. Brusch, S. Jef-

ferts, T. Heavner, and T. Parker. Frequency evaluation of the doubly forbidden $^1S_0 - {}^3P_0$ transition in bosonic ^{174}Yb. *Physical Review A*, 77(5):050501, 2008. 15

[42] T. Akatsuka, M. Takamoto, and H. Katori. Optical lattice clocks with non-interacting bosons and fermions. *Nature Physics*, 4(12):954–959, December 2008. 15, 34

[43] X. Baillard, M. Fouché, R. Le Targat, P.G. Westergaard, A. Lecallier, Y. Le Coq, G.D. Rovera, S. Bize, and P. Lemonde. Accuracy evaluation of an optical lattice clock with bosonic atoms. *Optics Letters*, 32(13):1812–1814, 2007. 15

[44] J.J. McFerran, L. Yi, S. Mejri, S. Di Manno, W. Zhang, J. Guena, Y. Le Coq, and S. Bize. Neutral Atom Frequency Reference in the Deep Ultraviolet with Fractional Uncertainty $= 5.7 \times 10^{-15}$. *Physical Review Letters*, 108:183004, 2012. 15

[45] H. Hachisu, K. Miyagishi, S.G. Porsev, A. Derevianko, V.D. Ovsiannikov, V.G. Palchikov, M. Takamoto, and H. Katori. Trapping of Neutral Mercury Atoms and Prospects for Optical Lattice Clocks. *Physical Review Letters*, 100(5):053001, February 2008. 15, 36, 37

[46] G. Wilpers, C.W. Oates, S.A. Diddams, A. Bartels, T.M. Fortier, W.H. Oskay, J.C. Bergquist, S.R. Jefferts, T.P. Heavner, T.E. Parker, and L. Hollberg. Absolute frequency measurement of the neutral ^{40}Ca optical frequency standard at 657 nm based on microkelvin atoms. *Metrologia*, 44:146–151, 2007. 15

[47] C. Degenhardt, H. Stoehr, C. Lisdat, G. Wilpers, H. Schnatz, B. Lipphardt,

T. Nazarova, P.-E. Pottie, U. Sterr, J. Helmcke, and F. Riehle. Calcium optical frequency standard with ultracold atoms: Approaching 10^{-15} relative uncertainty. *Physical Review A*, 72(6):062111, Dec 2005. 15

[48] V. Grishina. *Blue laser for prescision spectroscopy: toward optical frequency standard referenced to laser cooled calcium atoms.* PhD thesis, University of Western Australia, 2008. 15

[49] J. Friebe, A. Pape, M. Riedmann, K. Moldenhauer, T. Mehlstubler, N. Rehbein, C. Lisdat, E.M. Rasel, W. Ertmer, H. Schnatz, B. Lipphardt, and G. Grosche. Absolute frequency measurement of the magnesium intercombination transition $^1S_0 - ^3P_1$. *Physical Review A*, 78:033830, 2008. 15

[50] A. Pape, S. Ruhmann, T. Wubbena, A. Kulosa, H. Kelkar, D. Fim, K. Zipfel, W. Ertmer, and E.M. Rasel. Interrogation laser with 5×10^{-16} instability for a magnesium optical lattice clock. In *European Frequency and Time Forum*, 2012. 15

[51] A.V. Taichenachev, V.I. Yudin, C.W. Oates, C.W. Hoyt, Z.W. Barber, and L. Hollberg. Magnetic Field-Induced Spectroscopy of Forbidden Optical Transitions with Application to Lattice-Based Optical Atomic Clocks. *Physical Review Letters*, 96(8), March 2006. 20

[52] M.M. Boyd, T. Zelevinsky, A.D. Ludlow, S.M. Foreman, S. Blatt, T. Ido, and Jun Ye. Optical Atomic Coherence at the 1-Second Time Scale. *Science*, 314(5804):1430–1433, December 2006. 20, 22

[53] J.E. Sansonetti and G. Nave. Wavelengths , Transition Probabilities , and Energy Levels for the Spectrum of Neutral Strontium Sr I. *Journal of Physical and Chemical Reference Data*, 39(3), 2010. 20, 22

[54] M. Yasuda, T. Kishimoto, M. Takamoto, and H. Katori. Photoassociation spectroscopy of ^{88}Sr : Reconstruction of the wave function near the last node. *Physical Review A*, 73(1):011403, Jan 2006. 22

[55] I.R. Hill. *Development of an Apparatus for a Strontium Optical Lattice Optical Frequency Standard*. PhD thesis, Imperial College London, 2012. 22, 33, 39, 43, 45, 46, 60, 104, 108, 111, 119

[56] L.R. Hunter, W.A. Walker, and D.S. Weiss. Observation of an Atomic Stark-Electric-Quadrupole Interference. *Physical Review Letters*, 56:823–826, 1986. 22

[57] K.R. Vogel. *Laser Cooling on a Narrow Atomic Transition and Measurement of the Two-Body Cold Collision Loss Rate in a Strontium Magneto-Optical Trap*. PhD thesis, University of Colorado, 1999. 22, 42

[58] C.W. Bauschlicher, S.R. Langhoff, and H. Partridge. The radiative lifetime of the $^1D_2$ state of Ca and Sr : a core-valence treatment. *Journal of Physics B (Atomic and Molecular Physics)*, 18:1523, 1985. 22, 23

[59] X. Baillard, M. Fouché, R. Le Targat, P.G. Westergaard, A. Lecallier, F. Chapelet, M. Abgrall, G.D. Rovera, P. Laurent, P. Rosenbusch, S. Bize, G. Santarelli, A. Clairon, P. Lemonde, G. Grosche, B. Lipphardt, and H. Schnatz. An optical lattice clock with spin-polarized ^{87}Sr atoms. *The European Physical Journal D - Atomic, Molecular, Optical and Plasma Physics*, 48(1):11–17, June 2008. 24

[60] M. Takamoto, F.-L. Hong, R. Higashi, Y. Fujii, M. Imae, and H. Katori. Improved Frequency Measurement of a One-Dimensional Optical Lattice

Clock with a Spin-Polarized Fermionic ^{87}Sr Isotope. *Journal of the Physical Society of Japan*, 75(10):104302, 2006. 24

[61] C.J. Foot. *Atomic Physics*. Oxford University Press, 2005. 24, 52, 102

[62] G. Dick. Local oscillator induced instabilities in trapped ion frequency standards. In *Precise Time and Time Interval*, pages 133–147, Redondo Beach, 1987. 27

[63] A. Quessada, R.P. Kovacich, I. Courtillot, A. Clairon, G. Santarelli, and P. Lemonde. The Dick effect for an optical frequency standard. *Journal of Optics B: Quantum and Semiclassical Optics*, 5(2):S150–S154, 2003. 27

[64] J. Lodewyck, P.G. Westergaard, and P. Lemonde. Non-destructive measurement of the transition probability in a Sr optical lattice clock. *Physical Review*, 79, February 2009. 27, 28

[65] P.G. Westergaard. *Horloge à r eseau optique au Strontium : en quete de la performance ultime*. PhD thesis, l'Edite de Paris, 2010. 28

[66] D.W. Allan. Time and frequency (time-domain) characterization, estimation, and prediction of precision clocks and oscillators. *IEEE transactions on ultrasonics, ferroelectrics, and frequency control*, 34:647–654, 1987. 29

[67] H.S. Margolis. Private communications. 29, 30

[68] K. Szymaniec, W. Chalupczak, P.B. Whibberley, S.N. Lea, and D. Henderson. Evaluation of the primary frequency standard NPL-CsF1. *Metrologia*, 42:49–57, 2005. 30

[69] A. Brusch, R. Le Targat, X. Baillard, M. Fouche, and P. Lemonde. Hyper-

polarizability Effects in a Sr Optical Lattice Clock. *Physical Review Letters*, 96(10):103003, 2006. 34, 104

[70] M.M. Boyd. *High Precision Spectroscopy of Strontium in an Optical Lattice: Towards a New Standard for Frequency and Time*. PhD thesis, University of Colorado, 2007. 34, 35, 93, 104

[71] M. Takamoto, H. Katori, S.I. Marmo, V.D. Ovsiannikov, and V.G. Pal'chikov. Prospects for Optical Clocks with a Blue-Detuned Lattice. *Physical Review Letters*, 102(6):63002, 2009. 34, 35

[72] S.G. Porsev and A. Derevianko. Multipolar theory of blackbody radiation shift of atomic energy levels and its implications for optical lattice clocks. *Physical Review A*, 74(2):4–7, August 2006. 36, 37, 38

[73] J.A. Sherman, N.D. Lemke, N. Hinkley, M. Pizzocaro, R.W. Fox, A.D. Ludlow, and C.W. Oates. High-accuracy measure of atomic polarizability in an optical lattice clock. *Physical Review Letters*, 108:053001, 2012. 37, 40

[74] K. Beloy, J.A. Sherman, N.D. Lemke, N. Hinkley, C.W. Oates, and A.D. Ludlow. Determination of the $5d6s\,^3\mathrm{D}_1$ state lifetime and blackbody radiation clock shift in Yb. *arXiv:1208.0552*, 2012. 38, 39

[75] C.B. Alcock, V.P. Itkin, and M.K. Horrigan. Vapour Pressure Equations for the Metallic Elements: 298 - 2500 K. *Canadian Metallurgical Quarterly*, 23:309, 1984. 42

[76] C.L. Yaws. *Chemical Properties Handbook*. McGraw-Hill, New York, 1999. 42

[77] J.A. Neuman, P. Wang, and A. Gallagher. Robust high temperature sapphire cell for metal vapors. *Review of Scientific Instruments*, 66(4):3021 –3023, apr 1995. 42

[78] Y. Li, T. Ido, T. Eichler, and H. Katori. Narrow-line diode laser system for laser cooling of strontium atoms on the intercombination transition. *Applied Physics B: Lasers and Optics*, 78:315–320, 2004. 42

[79] E.M. Bridge, J. Millen, C.S. Adams, and M.P.A. Jones. A vapor cell based on dispensers for laser spectroscopy. *Review of Scientific Instruments*, 80(1):013101 –013101–3, jan 2009. 43, 49

[80] D.A. Reay and P.A. Kew. *Heat Pipes: Theory, Design and Applications*. Elsevier, 5th edition, 2006. 43

[81] C.R. Vidal. *Atomic, Molecular, and Optical Physics: Atoms and Molecules*, volume 29B. Academic Press, 1996. 43

[82] M. Schioppo, N. Poli, M. Prevedelli, St. Falke, and Ch. Lisdat. A compact and efficient strontium oven for laser-cooling experiments. *Review of Scientific Instruments*, 83:103101, 2012. 44, 46, 84, 85

[83] N.F. Ramsey. *Molecular Beams*. Oxford University Press, 1956. 48

[84] K. Bongs. Private communication. 49

[85] M.P.A. Jones. Private communication. 49

[86] T. Hansch and A. Schawlow. Cooling of gases by laser radiation. *Optics Communications*, 13(1):68–69, January 1975. 50

[87] D.J. Wineland and H.G. Dehmelt. Proposed $10^{14}\ \Delta\nu\ <\ \nu$ laser fluorescence spectroscopy on $T1^{+}$ mono-ion oscillator III. *Bulletin of the American Phyiscal Society*, 20:637, 1975. 50

[88] W.D. Phillips. Nobel Lecture: Laser cooling and trapping of neutral atoms, 1997. 50

[89] H.J. Metcalf and P. van der Straten. *Laser Cooling and Trapping*. Springer-Verlag, New York, 1999. 52

[90] W. Ertmer, R. Blatt, J.L. Hall, and M. Zhu. Laser Manipulation of Atomic Beam Velocities: Demonstration of Stopped Atoms and Velocity Reversal. *Physical Review Letters*, 54:996–999, 1985. 52

[91] W.D. Phillips and H. Metcalf. Laser Deceleration of an Atomic Beam. *Physical Review Letters*, 48:596–599, Mar 1982. 53

[92] Y.B. Ovchinnikov. A Zeeman slower based on magnetic dipoles. *Optics Communications*, 276(2):261–267, August 2007. 55, 56, 66

[93] Y.B. Ovchinnikov. A permanent Zeeman slower for Sr atomic clock. *European Physical Journal Special Topics*, 163:95–100, 2008. 56, 68

[94] Y.B. Ovchinnikov. Longitudinal Zeeman slowers based on permanent magnetic dipoles. *Optics Communications*, 285:1175–1180, 2012. 56, 69

[95] M.M. Boyd, T. Zelevinsky, A.D. Ludlow, S. Blatt, T. Zanon-Willette, S.M. Foreman, and Jun Ye. Nuclear spin effects in optical lattice clocks. *Physical Review A*, 76(2):022510, Aug 2007. 58

[96] E.L. Raab, M. Prentiss, A. Cable, S. Chu, and D.E. Pritchard. Trapping of

Neutral Sodium Atoms with Radiation Pressure. *Physical Review Letters*, 59:2631–2634, Dec 1987. 58

[97] A. Derevianko. Feasibility of Cooling and Trapping Metastable Alkaline-Earth Atoms. *Physical Review Letters*, 87(2):023002, Jun 2001. 62

[98] R.W.P. Drever, J.L. Hall, F.V. Kowalski, J. Hough, G.M. Ford, A.J. Munley, and H. Ward. Laser phase and frequency stabilization using an optical resonator. *Applied Physics B: Lasers and Optics*, 31:97–105, 1983. 10.1007/BF00702605. 63, 92, 116, 125, 146

[99] N. Poli, R.E. Drullinger, G. Ferrari, J. Leonard, F. Sorrentino, and G.M. Tino. Cooling and trapping of ultracold strontium isotopic mixtures. *Physical Review A*, 71(6):61403 – 1, 2005. 64

[100] P.G. Mickelson, Y.N. Martinez de Escobar, P. Anzel, B.J. DeSalvo, S.B. Nagel, A.J. Traverso, M. Yan, and T.C. Killian. Repumping and spectroscopy of laser-cooled Sr atoms using the (5s5p) $^3P_2$ - (5s4d) $^3D_2$ transition. *Journal of Physics B: Atomic, Molecular and Optical Physics*, 42(23):235001, 2009. 65

[101] T.P. Dinneen, K.R. Vogel, E. Arimondo, J.L. Hall, and A. Gallagher. Cold collisions of Sr*-Sr in a magneto-optical trap. *Physical Review A*, 59:1216, 1999. 65, 89

[102] S. Nagel, C. Simien, S. Laha, P. Gupta, V. Ashoka, and T. Killian. Magnetic trapping of metastable $^3P_2$ atomic strontium. *Physical Review A*, 67(1):1–4, January 2003. 65

[103] A.R.L. Caires, G.D. Telles, M.W. Mancini, L.G. Marcassa, V.S. Bagnato, D. Wilkowski, and R. Kaiser. Intensity Dependence for Trap Loss Rate

in a Magneto-Optical Trap of Strontium. *Brazilian Journal of Physics*, 34:1504–1509, 2004. 65

[104] I.R. Hill, Y.B. Ovchinnikov, E.M. Bridge, S. Donnellan, E.A. Curtis, and P. Gill. A Simple, Configurable, Permanent Magnet Zeeman Slower for Sr. In *Proceedings of the European Frequency and Time Forum*, 2012. 67

[105] P. Gill, H. Margolis, E.A. Curtis, H. Klein, S.N. Lea, S.A. Webster, and P. Whibberley. Optical Atomic Clocks for Space. Technical report, National Physical Laboratory, 2008. 67

[106] M. Schioppio, G.M. Tino, N. Poli, M.G. Tarallo, D.V. Sutyrin, Ch. Lisdat, J.S.R. Vellore Winfred, S. Falke, U. Sterr, T. Legero, and F. Riehle. Development of a transportable laser cooled strontium source for future applications in space. In *Proceedings of the European Frequency and Time Forum*, 2010. 67

[107] S. Mauger, J. Millen, and M.P.A. Jones. Spectroscopy of strontium Rydberg states using electromagnetically induced transparency. *Journal of Physics B (Atomic and Molecular Physics)*, 40:F319–F325, 2007. 88

[108] G. Ferrari, P. Cancio, R. Drullinger, G. Giusfredi, N. Poli, M. Prevedelli, C. Toninelli, and G. M. Tino. Precision Frequency Measurement of Visible Intercombination Lines of Strontium. *Physical Review Letters*, 91(24):2–5, December 2003. 92, 99, 100

[109] I. Courtillot, A. Quessada-Vial, A. Brusch, D. Kolker, G.D. Rovera, and P. Lemonde. Accurate spectroscopy of Sr atoms. *European Physical Journal D*, 33:161, 2005. 92, 99

[110] T. Ido, T.H. Loftus, M.M. Boyd, A.D. Ludlow, K.W. Holman, and J. Ye. Precision Spectroscopy and Density-Dependent Frequency Shifts in Ultracold Sr. *Physical Review Letters*, 94:153001, 2005. 92, 99

[111] T.H. Loftus, T. Ido, M.M. Boyd, A.D. Ludlow, and Jun Ye. Narrow line cooling and momentum-space crystals. *Physical Review A*, 70:063413, Dec 2004. 93

[112] H. Katori, T. Ido, Y. Isoya, and M. Kuwata-Gonokami. Magneto-Optical Trapping and Cooling of Strontium Atoms down to the Photon Recoil Temperature. *Physical Review Letters*, 82:1116–1119, Feb 1999. 93

[113] T. Mukaiyama, H. Katori, T. Ido, Y. Li, and M. Kuwata-Gonokami. Recoil-Limited Laser Cooling of ^{87}Sr Atoms near the Fermi Temperature. *Physical Review Letters*, 90:113002, 2003. 93, 94

[114] A.D. Ludlow. *The Strontium Optical Lattice Clock: Optical Spectroscopy with Sub-Hertz Accuracy*. PhD thesis, University of Colorado, 2008. 93

[115] G.M. Tino, M. Barsanti, M. de Angelis, L. Gianfrani, and M. Inguscio. Spectroscopy of the 689 nm Intercombination Line of Strontium Using an Extended-Cavity InGaP/InGaAlP Diode Laser. *Applied Physics B*, 55:397–400, 1992. 99

[116] A.E. Siegman. *Lasers*. University Science Books, 1986. 102

[117] J.A. Giordmaine and T.C. Wang. Molecular Beam Formation by Long Parallel Tubes. *Journal of Applied Physics*, 31(3):463–471, 1960. 102

[118] P. Lemonde and P. Wolf. Optical lattice clock with atoms confined in a shallow trap. *Physical Review A*, 72(3):033409, Sep 2005. 109

[119] A.V. Taichenachev, V.I. Yudin, V.D. Ovsiannikov, and V.G. Pal'chikov. Optical Lattice Polarization Effects on Hyperpolarizability of Atomic Clock Transitions. *Physical Review Letters*, 97(17):173601, 2006. 116

[120] J. Ye. Precision metrology and many-body quantum physics. In *International Conference of Atomic Physics*, 2012. 116, 150

[121] L. Nilse, H.J. Davies, and C.S. Adams. Synchronous Tuning of Extended Cavity Diode Lasers: The Case for an Optimum Pivot Point. *Applied Optics*, 38(3):548–553, Jan 1999. 119

[122] E.D. Black. An introduction to PoundDreverHall laser frequency stabilization. *American Journal of Physics*, 69:79–87, 2001. 125

[123] E.D. Black. Notes on the Pound-Drever-Hall technique. Online, www.ligo.caltech.edu/docs/T/T980045-00.pdf. 125, 130, 134

[124] R.W. Fox, C.W. Oates, and L.W. Hollberg. *Experimental Methods in the Physical Sciences: Stabilising Diode Lasers to High Finesse Cavities*, volume 40. Elsevier Science (USA), 2003. 125, 132

[125] H. Kogelnik and T. Li. Laser Beams and Resonators. *Applied Optics*, 5(10):1550, October 1966. 127

[126] L.-S. Ma, P. Jungner, J. Ye, and J.L. Hall. Delivering the same optical frequency at two places: accurate cancellation of phase noise introduced by an optical fiber or other time-varying path. *Optics Letters*, 19(21):1777–9, November 1994. 129

[127] E.A. Whittaker, M. Gehrtz, and G.C. Bjorklund. Residual amplitude modulation in laser electro-optic phase modulation. *Journal of the Optical Society of America B*, 2:1320–1326, 1985. 131, 140

[128] L. Li, F. Lui, C. Wang, and L. Chen. Measurement and control of residual amplitude modulation in optical phase modulation. *Review of Scientific Instruments*, 83:043111, 2012. 139, 140, 141, 180

[129] J. Sathian and E. Jaatinen. Intensity dependent residual amplitude modulation in electro-optic phase modulators. *Applied Optics*, 51:3684–3691, 2012. 140

[130] N.C. Wong and J.L. Hall. Servo control of amplitude modulation in frequency-modulation spectroscopy: demonstration of shot-noise-limited detection. *Journal of the Optical Society of America B*, 2:1527 – 1533, 1985. 141

[131] T.C. Briles, D.C. Yost, A. Cingöz, J. Ye, and T.R. Schibli. Simple piezoelectric-actuated mirror with 180 kHz servo bandwidth. *Optics Express*, 18:9739–9746, 2010. 146

[132] B. Young, F. Cruz, W. Itano, and J. Bergquist. Visible Lasers with Subhertz Linewidths. *Physical Review Letters*, 82(19):3799–3802, May 1999. 146, 152

[133] S.A. Webster, M. Oxborrow, and P. Gill. Subhertz-linewidth Nd:YAG laser. *Optics Letters*, 29(13):1497, 2004. 146

[134] A.D. Ludlow, X. Huang, M. Notcutt, T. Zanon-Willette, S.M. Foreman, M.M. Boyd, S. Blatt, and Jun Ye. Compact, thermal-noise-limited optical cavity for diode laser stabilization at 1×10^{-15}. *Optics Letters*, 32(6):641–3, March 2007. 146, 152

[135] Y.Y. Jiang, A.D. Ludlow, N.D. Lemke, R.W. Fox, J.A. Sherman, L.-S. Ma, and C.W. Oates. Making optical atomic clocks more stable with 10^{-16}-level

laser stabilization. *Nature Photonics*, 5(3):158–161, March 2011. 147, 149, 150, 156

[136] T. Kessler, C. Hagemann, C. Grebing, T. Legero, U. Sterr, F. Riehle, M.J. Martin, L. Chen, and J. Ye. A sub-40 mHz linewidth laser based on a silicon single-crystal optical cavity. *arXiv:1112.3854v2*, 2012. 147, 148, 149

[137] A. Preston, B. Balaban, G.T. Boothe, and Mueller G. Stable Materials and Bonding Techniques for Space-Based Optical Systems. In *NASA Spase-based Technologies Conference*, 2007. 148

[138] J.W. Berthold III and S.F. Jacobs. Ultraprecise thermal expansion measurements of seven low expansion materials. *Applied Optics*, 15:2344, 1976. 148, 150, 151

[139] Corning website: ULE® (Corning Code 7972) product page. Online: www.corning.com/specialtymaterials/products_capabilities/ULE.aspx. 148

[140] K. Numata, A. Kemery, and J. Camp. Thermal-Noise Limit in the Frequency Stabilization of Lasers with Rigid Cavities. *Physical Review Letters*, 93(25):1–4, December 2004. 148, 149

[141] T. Legero, T. Kessler, and U. Sterr. Tuning the thermal expansion properties of optical reference cavities with fused silica mirrors. *Journal of the Optical Society of America B*, 27:914, 2010. 148, 149, 150

[142] C.T. Taylor, M. Notcutt, E.K. Wong, A.G. Mann, and D.G. Blain. Measurement of the coefficient of thermal expansion of a cryogenic, all-sapphire, Fabry-Perot optical cavity. *Optics Communications*, 131:311, 1996. 148

[143] M. Nagel and A. Peters. Towards an ultra-stable optical sapphire cavity system for testing Lorentz invariance. *arXiv:1112.3623v1*, 2011. 148

[144] C. Hagemann, C. Grebing, T. Kessler, S. Falke, C. Lisdat, H. Schnatz, F. Riehle, and U Sterr. Providing 10^{16} short-term stability of a 1.5 μm laser to optical clocks. *arXiv:1208.1634*, Aug., 2012. 148

[145] S. Webster and P. Gill. Low-thermal-noise optical cavity. In *International Frequency Control Symposium*, 2010. 149, 156

[146] H. Katori. Prospects for frequency caomparison of optical lattice clocks towards 10^{-18} fractional uncertianties. In *European Frequency and Time Forum: invited talk*, 2012. 149, 156

[147] M. Bondarescu, O. Kogan, and Y. Chen. Optimal light beams and mirror shapes for future LIGO interferometers. *Physical Review D*, 78:082002, 2008. 149

[148] G. Harry, T.P. Bodiya, and R. DeSalvo, editors. *Optical coatings and thermal noise in precision measurement*. Cambridge University Press, 2012. 149

[149] R.W. Fox. Temperature analysis of low-expansion Fabry-Perot cavities. *Optics Express*, 17:15023, 2009. 149, 150, 151

[150] T. Kessler, T. Legero, and U. Sterr. Thermal noise in optical cavities revisited. *Journal of the Optical Society of America B*, 29:178–184, 2012. 150

[151] J. Alnis, A. Matveev, N. Kolachevsky, Th. Udem, and T.W. Hänsch. Subhertz linewidth diode lasers by stabilization to vibrationally and thermally compensated ultralow-expansion glass Fabry-Pérot cavities. *Physical Review A*, 77:053809, May 2008. 152, 170, 174, 176

[152] M. Notcutt, C.T. Taylor, A.G. Mann, R. Gummer, and D.G. Blair. Cryogenic system for a sapphire Fabry-Perot optical frequency standard. *Cryogenics*, 36:13, 1996. 152

[153] M. Notcutt, L.-S. Ma, Jun Ye, and J.L. Hall. Simple and compact 1-Hz laser system via an improved mounting configuration of a reference cavity. *Optics Letters*, 30(14):1815–1817, 2005. 152

[154] J. Millo, D.V. Magalhaes, C. Mandache, Y. Le Coq, E.M.L English, P.G. Westergaard, J. Lodewyck, S. Bize, P. Lemonde, and G. Santarelli. Ultrastable lasers based on vibration insensitive cavities. *Physical Review A*, 79:053829, 2009. 152

[155] T. Nazarova, F. Riehle, and U. Sterr. Vibration-insensitive reference cavity for an ultra-narrow-linewidth laser. *Applied Physics B*, 83(4):531–536, May 2006. 153

[156] S.A. Webster, M. Oxborrow, and P. Gill. Vibration insensitive optical cavity. *Physical Review A*, 75(1), January 2007. 153

[157] D.R. Leibrandt, M.J. Thorpe, M. Notcutt, R.E. Drullinger, T. Rosenband, and J.C. Bergquist. Spherical reference cavities for frequency stabilization of lasers in non-laboratory environments. *Optics Express*, 19(4):3471–3482, Feb 2011. 153

[158] S.A. Webster and P. Gill. Force-insensitive optical cavity. *Optics Letters*, 36(18):3572–3574, 2011. 153

[159] W. Demtröder. *Laser Spectroscopy*. Springer, 1996. 155

[160] S.A. Webster. Private communications: advice based on a proceedure successfully completed on a previous optical reference cavity. 2012. 163

[161] Kaye & Laby. Table of Physical & Chemical Constants: 2.5.7 Refractive index of gases. Online: http://www.kayelaby.npl.co.uk/general_physics/2_5/2_5_7.html. 164

[162] P. Danielson. Gas Loads from Elastomer and Metal Seals. Online: www.vacuumlab.com/Articles/Gas Loads Elastomer-Metal Seals.pdf. 168

[163] J.G. Ziegler, N.B. Nichols, and N.Y. Rochester. Optimum Settings for Automatic Controllers. *American Society of Mechanical Engineers*, November, 1942. 171, 172

[164] B.D. Tyreus and L.L. Luyben. Tuning PI Controllers for Integrator/Dead Time Processes. *Industrial & Engineering Chemistry Research*, 31:2625–2628, 1992. 172

[165] T.R. Kuphaldt. *Lessons in Industril Instrumentation*. Creative Commons Attribution 3.0 licensed, 2009. 172

[166] D. Xue, Y.Q. Chen, and D.P. Atherton. *Linear Feedback Control*. Society for Industrial and Applied Mathematics, 2007. 172

[167] J. Ye and S.T. Cundiff, editors. *Femtosecond Optical Frequency Comb: Principle, Operation, and Applications*. Kluwer Academic Publishers / Springer Norwell, MA, 2005. 180

[168] V.D. Ovsiannikov, A. Derevianko, and K. Gibble. Rydberg Spectroscopy in an Optical Lattice: Blackbody Thermometry for Atomic Clocks. *Physical Review Letters*, 107(9):093003, 2011. 190

[169] J. Lodewyck, M. Zawada, L. Lorini, M. Gurov, and P. Lemonde. Observation and cancellation of a perturbing dc stark shift in strontium optical

lattice clocks. *IEEE Transactions on Ultrasonics, Ferroelectrics and Frequency Control*, 59(3):411–415, 2012. 190

[170] G. Lochead, D. Boddy, D.P. Sadler, C.S. Adams, and M.P.A. Jones. Number-resolved imaging of excited-state atoms using a scanning autoionization microscope. *arXiv:1212.3270*, 2012. 190

[171] J. Mitroy, M.S. Safronova, and C.W. Clark. Theory and applications of atomic and ionic polarizabilities. *Journal of Physics B (Atomic, Molecular and Optical Physics)*, page 202001, 2010. 191

[172] E. Peik and C. Tamm. Nuclear laser spectroscopy of the 3.5 eV transition in Th-229. *Europhysics Letters*, 61(2):181–186, 2003. 191

[173] E. Peik, K. Zimmermann, M. Okhapkin, and C. Tamm. Prospects for a Nuclear Optical Frequency Standard Based on Thorium-229. *arXiv:0812.3548v2*, 2009. 191

[174] W.G. Rellergert, D. DeMille, R.R. Greco, M.P. Hehlen, J.R. Torgerson, and E.R. Hudson. Optical transition of the ^{229}Th nucleus in a solid-state environment. *arXiv:0905.2230*, 2009. 191